Jordan Journal of
PHYSICS
An International Peer-Reviewed Research Journal

Volume 17, No. 4, Oct. 2024, Rabi' al-Thani 1446 H

Jordan Journal of Physics (*JJP*): An International Peer-Reviewed Research Journal funded by the Scientific Research and Innovation Support Fund, Jordan, and published quarterly by the Deanship of Research and Graduate Studies, Yarmouk University, Irbid, Jordan.

Manuscripts should be submitted to:

Prof. Mahdi Salem Lataifeh
Editor-in-Chief, Jordan Journal of Physics
Deanship of Research and Graduate Studies
Yarmouk University-Irbid-Jordan
Tel. 00 962 2 7211111 Ext. 2075
E-mail: *jjp@yu.edu.jo*
Website: *http://Journals.yu.edu.jo/jjp*

Jordan Journal of
PHYSICS
An International Peer-Reviewed Research Journal

Volume 17, No. 4, Oct. 2024, Rabi' al-Thani 1446 H

The Hashemite Kingdom of Jordan

Yarmouk University

Jordan Journal of PHYSICS

An International Peer-Reviewed Research Journal

Funded by the Scientific Research and Innovation Support Fund

Volume 17, No. 4, Oct. 2024, Rabi' al-Thani 1446 H

Instructions to Authors

Instructions to authors concerning manuscript organization and format apply to hardcopy submission by mail, and also to electronic online submission via the Journal homepage website (http://jjp.yu.edu.jo).

Manuscript Submission

Manuscripts are submitted electronically through the journal's website:

https://jjp.yu.edu.jo/index.php/jjp

Original *Research Articles*, *Communications* and *Technical Notes* are subject to critical review by minimum of two competent referees. Authors are encouraged to suggest names of competent reviewers. *Feature Articles* in active Physics research fields, in which the author's own contribution and its relationship to other work in the field constitute the main body of the article, appear as a result of an invitation from the Editorial Board, and will be so designated. The author of a *Feature Article* will be asked to provide a clear, concise and critical status report of the field as an introduction to the article. *Review Articles* on active and rapidly changing Physics research fields will also be published. Authors of *Review Articles* are encouraged to submit two-page proposals to the Editor-in-Chief for approval. Manuscripts submitted in *Arabic* should be accompanied by an Abstract and Keywords in English.

Organization of the Manuscript

Manuscripts should be typed double spaced on one side of A4 sheets (21.6 x 27.9 cm) with 3.71 cm margins, using Microsoft Word 2000 or a later version thereof. The author should adhere to the following order of presentation: Article Title, Author(s), Full Address and E-mail, Abstract, PACS and Keywords, Main Text, Acknowledgment. Only the first letters of words in the Title, Headings and Subheadings are capitalized. Headings should be in **bold** while subheadings in *italic* fonts.

Title Page: Includes the title of the article, authors' first names, middle initials and surnames and affiliations. The affiliation should comprise the department, institution (university or company), city, zip code and state and should be typed as a footnote to the author's name. The name and complete mailing address, telephone and fax numbers, and e-mail address of the author responsible for correspondence (designated with an asterisk) should also be included for official use. The title should be carefully, concisely and clearly constructed to highlight the emphasis and content of the manuscript, which is very important for information retrieval.

Abstract: A one paragraph abstract not exceeding 200 words is required, which should be arranged to highlight the purpose, methods used, results and major findings**.**

Keywords: A list of 4-6 keywords, which expresses the precise content of the manuscript for indexing purposes, should follow the abstract.

PACS: Authors should supply one or more relevant PACS-2006 classification codes, (available at http://www.aip.org/pacs/pacs06/pacs06-toc.html)

Introduction: Should present the purpose of the submitted work and its relationship to earlier work in the field, but it should not be an extensive review of the literature (e.g., should not exceed 1 ½ typed pages).

Experimental Methods: Should be sufficiently informative to allow competent reproduction of the experimental procedures presented; yet concise enough not to be repetitive of earlier published procedures.

Results: should present the results clearly and concisely.

Discussion: Should be concise and focus on the interpretation of the results.

Conclusion: Should be a brief account of the major findings of the study not exceeding one typed page.

Acknowledgments: Including those for grant and financial support if any, should be typed in one paragraph directly preceding the References.

References: References should be typed double spaced and numbered sequentially in the order in which they are cited in the text. References should be cited in the text by the appropriate Arabic numerals, enclosed in square brackets. Titles of journals are abbreviated according to list of scientific periodicals. The style and punctuation should conform to the following examples:

1. Journal Article:

a) Heisenberg, W., Z. Phys. 49 (1928) 619.
b) Bednorz, J. G. and Müller, K. A., Z. Phys. B64 (1986) 189
c) Bardeen, J., Cooper, L.N. and Schrieffer, J. R., Phys. Rev. 106 (1957) 162.
d) Asad, J. H., Hijjawi, R. S., Sakaji, A. and Khalifeh, J. M., Int. J. Theor. Phys. 44(4) (2005), 3977.

2. Books with Authors, but no Editors:

a) Kittel, C., "Introduction to Solid State Physics", 8th Ed. (John Wiley and Sons, New York, 2005), chapter 16.
b) Chikazumi, S., C. D. Graham, JR, "Physics of Ferromagnetism", 2nd Ed. (Oxford University Press, Oxford, 1997).

3. Books with Authors and Editors:

a) Allen, P. B. "Dynamical Properties of Solids", Ed. (1), G. K. Horton and A. A. Maradudin (North-Holland, Amsterdam, 1980), p137.
b) Chantrell, R. W. and O'Grady, K., "Magnetic Properities of Fine Particles" Eds. J. L. Dormann and D. Fiorani (North-Holland, Amsterdam, 1992), p103.

4. Technical Report:

Purcell, J. "The Superconducting Magnet System for the 12-Foot Bubble Chamber", report ANL/HEP6813, Argonne Natt. Lab., Argonne, III, (1968).

5. Patent:

Bigham, C. B., Schneider, H. R., US patent 3 925 676 (1975).

6. Thesis:

Mahmood, S. H., Ph.D. Thesis, Michigan State University, (1986), USA (Unpublished).

7. Conference or Symposium Proceedings:

Blandin, A. and Lederer, P. Proc. Intern. Conf. on Magnetism, Nottingham (1964), P.71.

8. Internet Source:

Should include authors' names (if any), title, internet website, URL, and date of access.

9. Prepublication online articles (already accepted for publication):

Should include authors' names (if any), title of digital database, database website, URL, and date of access.

For other types of referenced works, provide sufficient information to enable readers to access them.

Tables: Tables should be numbered with Arabic numerals and referred to by number in the Text (e.g., Table 1). Each table should be typed on a separate page with the legend above the table, while explanatory footnotes, which are indicated by superscript lowercase letters, should be typed below the table.

Illustrations: Figures, drawings, diagrams, charts and photographs are to be numbered in a consecutive series of Arabic numerals in the order in which they are cited in the text. Computer-generated illustrations and good-quality digital photographic prints are accepted. They should be black and white originals (not photocopies) provided on separate pages and identified with their corresponding numbers. Actual size graphics should be provided, which need no further manipulation, with lettering (Arial or Helvetica) not smaller than 8 points, lines no thinner than 0.5 point, and each of uniform density. All colors should be removed from graphics except for those graphics to be considered for publication in color. If graphics are to be submitted digitally, they should conform to the following minimum resolution requirements: 1200 dpi for black and white line art, 600 dpi for grayscale art, and 300 dpi for color art. All graphic files must be saved as TIFF images, and all illustrations must be submitted in the actual size at which they should appear in the journal. Note that good quality hardcopy original illustrations are required for both online and mail submissions of manuscripts.

Text Footnotes: The use of text footnotes is to be avoided. When their use is absolutely necessary, they should be typed at the bottom of the page to which they refer, and should be cited in the text by a superscript asterisk or multiples thereof. Place a line above the footnote, so that it is set off from the text.

Supplementary Material: Authors are encouraged to provide all supplementary materials that may facilitate the review process, including any detailed mathematical derivations that may not appear in whole in the manuscript.

Revised Manuscript and Computer Disks

Following the acceptance of a manuscript for publication and the incorporation of all required revisions, authors should submit an original and one more copy of the final disk containing the complete manuscript typed double spaced in Microsoft Word for Windows 2000 or a later version thereof. All graphic files must be saved as PDF, JPG, or TIFF images.

Allen, P.B., "…….", in: Horton, G.K., and Muradudin, A. A., (eds.), "Dynamical…….", (North……..), pp….

Reprints

Twenty (20) reprints free of charge are provided to the corresponding author. For orders of more reprints, a reprint order form and prices will be sent with the article proofs, which should be returned directly to the Editor for processing.

Copyright

Submission is an admission by the authors that the manuscript has neither been previously published nor is being considered for publication elsewhere. A statement transferring copyright from the authors to Yarmouk University is required before the manuscript can be accepted for publication. The necessary form for such transfer is supplied by the Editor-in-Chief. Reproduction of any part of the contents of a published work is forbidden without a written permission by the Editor-in-Chief.

Disclaimer

Opinions expressed in this Journal are those of the authors and neither necessarily reflects the opinions of the Editorial Board or the University, nor the policy of the Higher Scientific Research Committee or the Ministry of Higher Education and Scientific Research. The publisher shoulders no responsibility or liability whatsoever for the use or misuse of the information published by JJP.

Indexing

JJP is currently indexing in:

Scopus	**Emerging Sources Citation Index (ESCI)** Journal Impact Factor 2022 0.7
ULRICHSWEB GLOBAL SERIALS DIRECTORY	

Jordan Journal of
PHYSICS
An International Peer-Reviewed Research Journal

Volume 17, No. 4, Oct. 2024, Rabi' al-Thani 1446 H

Table of Contents:

Volume 17, Number 4, 2024. pp. 383-394

Jordan Journal of Physics

ARTICLE

TomoTherapy Hi-Art Machine Matching: Verification and Quality Assurance

Hazim A. Jaradat[a] and **Abd Alghany Jaradat**[b]

[a]*Department of Physics, University of Tabuk, Tabuk, KSA.*
[b]*Department of Physics, Yarmouk University, Irbid 21163, Jordan.*

Doi: **https://doi.org/10.47011/17.4.1**
Received on: 06/04/2022; *Accepted on: 21/05/2023*

Abstract: This work aims to check the similarities between two TomoTherapy machines: TomoTherapy I and TomoTherapy II (TomoTherapy Inc. Madison, WI). A strategy to match the two machines is developed to facilitate patient transfer between them. Ensuring smooth patient transfer between the two machines improves clinic workflow and reduces the time needed to complete treatments as scheduled. It also reduces the risk of errors during patient transfer between machines.
Keywords: Tomotherapy, Radiation therapy, Twinning, Treatment planning.

PACS: 87.56.-v.

1. Introduction

In a busy clinical department with multiple radiation treatment machines, it is sometimes necessary to transfer patients from one machine to another due to unavoidable machine downtime. When the treatment machines within the same clinic have matching beam characteristics and identical treatment delivery accessories, such as multi-leaf collimators (MLC), the treatment plan transfer is assumed to be straightforward. This allows for efficient patient transfer between machines, optimizing daily clinical operations.

The TomoTherapy Hi-Art system is an advanced inverse-planning radiation treatment system designed to deliver image-guided intensity-modulated radiation therapy (IG-IMRT) [1,2]. The system uses a large number of beam projections to achieve an exceptionally conformal dose distribution. Several studies have shown that tomotherapy treatment plans provide favorable dose distribution compared to conventional IMRT [3-7]. After a clinic acquires a second TomoTherapy system, it would be logical to generate cross-backup plans for both machines. These backup plans ensure that patients receive consistent treatment plan quality, and eliminate the need for re-simulation. More importantly, the calculation of compound dose across treatment planning systems (from one Hi-Art to another) is easily achievable.

However, creating backup plans between TomoTherapy systems using current methods and resources, is time-consuming and requires significant personnel and computing resources. Based on our experience, with an average of one new start per day per TomoTherapy machine, given that each tomotherapy plan requires about 8.5 hours to complete, including patient QA on the planning system, and since each TomoTherapy machine can be serviced with only one planning system, generating duplicate tomotherapy plans would require extending working hours to 17 hours per day. In order to address some of the above-stated issues, we

Corresponding Author: Hazim A. Jaradat **Email**: hjaradat@ut.edu.sa

developed a procedure that enables one to verify that two TomoTherapy machines are identical in terms of delivering radiation beams with identical characteristics within acceptable tolerances. This procedure allows the transfer of treatment plans from one machine to another without the need for a lengthy optimization process and enables one to verify that the transferred plan can be delivered with acceptable accuracy [8,9].

2. Materials and Methods

Two TomoTherapy Hi-ART machines were used: TomoTherapy I running TomoTherapy software version 2.1.0.2 on both the operator and planning stations and TomoTherapy II running version 2.2.1.2 on both stations. The differences between the two planning software versions, 2.1.0.2 and 2.2.1.2, include minor changes in the user interfaces of the operator and planning stations, along with additional software fixes in the operator station.

A tomotherapy treatment machine delivers a given MLC sinogram, synchronized with the couch speed and gantry rotation period. The MLC sinogram is a two-dimensional array (64 leaves by the number of projections), where each entry is either 0 (closed leaf) or 1 (open leaf). The couch speed is a real number, while the gantry rotational period is an integer between 15 and 60 seconds. The MLC file format, as well as the couch speed and the gantry rotational period, are consistent across both software versions. The TomoTherapy planning system has been previously detailed [10-12].

A tomotherapy beam scanning system was used to check the beams on both machines. This system consists of a two-dimensional water tank, two A1SL ion chambers, a TomoElectrometer (Standard Imaging, Middleton, WI.), and beam analysis software (TomoTherapy Inc. Madison, WI). Additionally, the TomoTherapy planning system was used for comparing treatment plans. The delivery quality assurance (DQA) module of the TomoTherapy planning software was used to compare the delivered dose (measured with film in the Tomo phantom) to the calculated dose from the plans [13].

The matching of two TomoTherapy machines was accomplished through the following procedure:

i. Three commissioned field widths (1.05, 2.5, and 5.02 cm) were verified to match on both machines.
ii. Beam matching between the two machines was performed by comparing the longitudinal and transverse profiles and the percent depth dose of the beams.
iii. The MLC tongue-and-groove and MLC leakage were verified to be identical within measurement uncertainties.
iv. Gantry rotational speed was confirmed to be within acceptable tolerances at different planned speeds on both machines.
v. Couch drive speed was verified to be within acceptable tolerances at different planned speeds on both machines.

2.1 The Beam Model

Once the beams on the two TomoTherapy machines had been verified to be identical, the beam model on TomoTherapy I was changed to the beam model used on TomoTherapy II. This step was essential since the planning system uses the field widths specified in the beam model to calculate the couch speed during delivery and the total couch translation while the MLC is in active delivery status. Since the pitch controls the couch drive during MLC delivery, and therefore the field width, any mismatch in the field widths would result in either shorter or longer treatment lengths.

2.2 Patient Plan Transfer

The TomoTherapy planning system does not allow any modifications to a treatment plan after final acceptance. If changes to a patient's treatment plan are required post-acceptance, a new plan and a full re-optimization must be conducted. It is not unusual for clinicians to request prescription changes after treatment has already begun. These changes may be as simple as adding a fraction or combining the last two fractions into one biologically equivalent fraction. To accommodate such modifications without the need for replanning, we routinely archive all treatment plans just before the final acceptance step. At this stage, most treatment plan adjustments can be made quickly without re-optimization. When transferring a treatment plan from one TomoTherapy unit to another, we transfer these archived plans to the second machine. Once the archived plan is restored on the second TomoTherapy planning system, it can be finally accepted on that machine, making it

available for treatment. This archive transfer and final acceptance process takes between 5 and 10 minutes.

Once the treatment plan has been transferred and accepted by the second machine, it can be delivered as if it were originally planned on that system. Delivery quality assurance for the plan can also be performed on the second system as usual. Delivery quality assurance setup on the planning system, treatment delivery on the machine onto a phantom with films and ion chamber measurements, and film analysis on the planning system are used to verify the dose distribution agreement between the plan and delivery.

The DQA analysis is used to validate the process of transferring patient plans from TomoTherapy I to TomoTherapy II. The validation process is done by completing the following steps [13-15]:

I. Transferring an existing pre-final accepted patient archive from TomoTherapy I to TomoTherapy II and finalizing the plan for TomoTherapy II.

II. Setting up the DQA on TomoTherapy II using the same cheese phantom and setup as used on TomoTherapy I.

III. Delivering the DQA plan on TomoTherapy II using extended dose range (EDR) film in the phantom's central coronal plane and placing three ion chambers in the phantom's central sagittal plane.

IV. Delivering the DQA plan on TomoTherapy II using extended dose range (EDR) film in the phantom's central sagittal and three ion chambers in the phantom-central coronal plane.

V. Processing the films using a Kodak processor and digitizing the scan using a Vidar scanner and TomoTherapy scanning software.

VI. Transferring the digitized film files to the TomoTherapy II planning system for analysis.

VII. Performing the DQA analysis on the TomoTherapy II planning system by comparing the delivered dose distribution to the planned dose distribution on both the coronal and sagittal film planes. The ion chamber measurements are used to obtain the absolute dose distribution on the films and to compare with the point dose from the planning system.

To validate the reverse transfer process (i.e., transferring from TomoTherapy II to TomoTherapy I) the same steps are followed, swapping TomoTherapy I and TomoTherapy II.

2.3 Intra-Fraction Patient Transfer

Although small, but still finite, there remains a possibility that a patient may need to be transferred between machines during the delivery of the same fraction. This could occur, for example, during a mid-fraction interruption of stereotactic body radiation therapy (SBRT) or stereotactic radiosurgery (SRS), where the timely completion of the entire treatment is essential. To accommodate this possibility, the validation process outlined above was followed with no modifications to step IV. In this case, the DQA treatment delivery on TomoTherapy II was intentionally interrupted mid-treatment. The phantom, ion chambers, and films were transferred to TomoTherapy I, where the treatment resumed from the point where it had stopped on TomoTherapy II. By doing this, we delivered the same plan onto the same film on both machines. This was done for sagittal and coronal films. Any mismatch between the two machines or any issue in continuing the treatment delivery after the transfer would be easily detected on one or more of the films.

3. Results and Discussion

3.1 Verifying the Beams

The tomotherapy beam scanning system was used to measure the longitudinal, transverse, and percent depth dose profiles on both machines. Figure 1 shows the longitudinal beam profiles for the 1.05 cm field, with dotted points representing TomoTherapy I and solid lines representing TomoTherapy II. The profiles are taken at depths of 15, 50, 100, 150, and 200 mm. Figure 2 displays the longitudinal beam profiles for the 2.5 cm field. Again, the dotted points represent TomoTherapy I and solid lines represent TomoTherapy II, with the same depth measurements. Figure 3 shows the longitudinal beam profiles for the 5.02 cm field. The dotted points are from TomoTherapy I and the solid lines are from TomoTherapy II, measured at the same depths (15, 50, 100, 150, and 200 mm). Figure 4 presents the normalized percent depth

doses for the three fields: the 1.05 cm field (blue points for TomoTherapy I and solid blue line for TomoTherapy II), the 2.5 cm field (yellow points for TomoTherapy I and solid yellow line for TomoTherapy II), and the 5.02 cm field (red points for TomoTherapy I and solid red line for TomoTherapy II.

3.2 Longitudinal Beam Profile Match

The longitudinal beam profiles for the three commissioned fields (1.05, 2.5, and 5.02 cm, shown in Figs. 1-3, respectively) demonstrated a very good match between the two machines (discrete points from TomoTherapy I and solid lines from TomoTherapy II). Despite intrinsic differences in components and design between the two machines, the final beam profiles can be matched since they depend on the geometry of the jaws and source, as well as the energy of the photons produced. The apparent mismatch at the center of the field at different depths (Figs. 1-3) is an artifact of the tomotherapy beam scanning system. The scanning software assumes that the ion chamber used for scanning the beam always runs at the same speed, even though it starts from rest and ends at rest for each segment of the beam profile. The ion chamber travels in the opposite direction through consecutive depths which is why the center of the field seems to move back and forth for different depth profiles. Different tests are used for field alignment with the gantry rotation plane. These tests are done during routine machine quality assurance. What is relevant here is that the profiles at different depths for the three commissioned fields match for both machines. The field width at half maximum was also calculated and verified to be within acceptable tolerances for both machines.

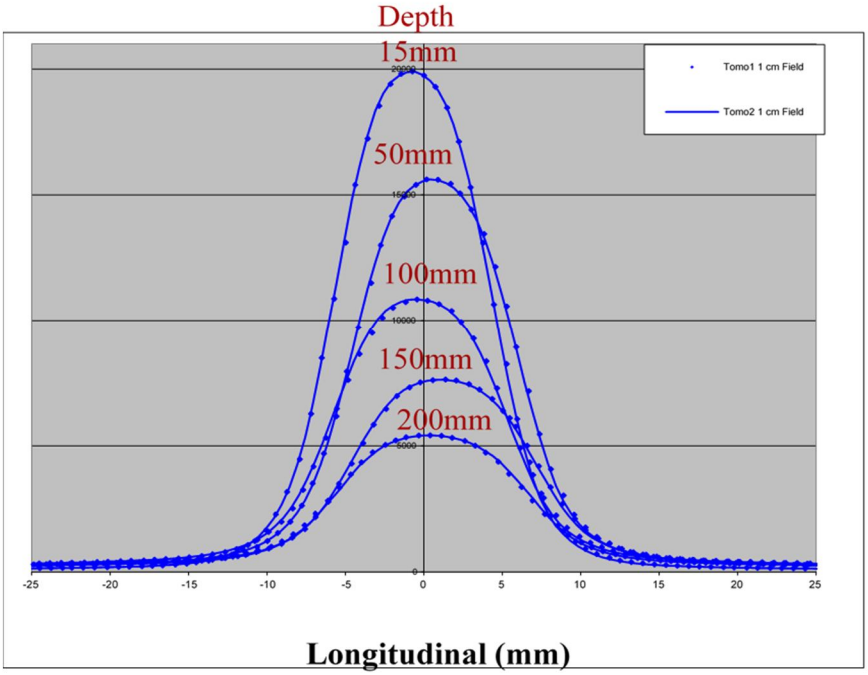

FIG. 1. Longitudinal profiles at five different depths for TomoTherapy I (discrete points) and TomoTherapy II (solid lines) for the 1.02 cm field.

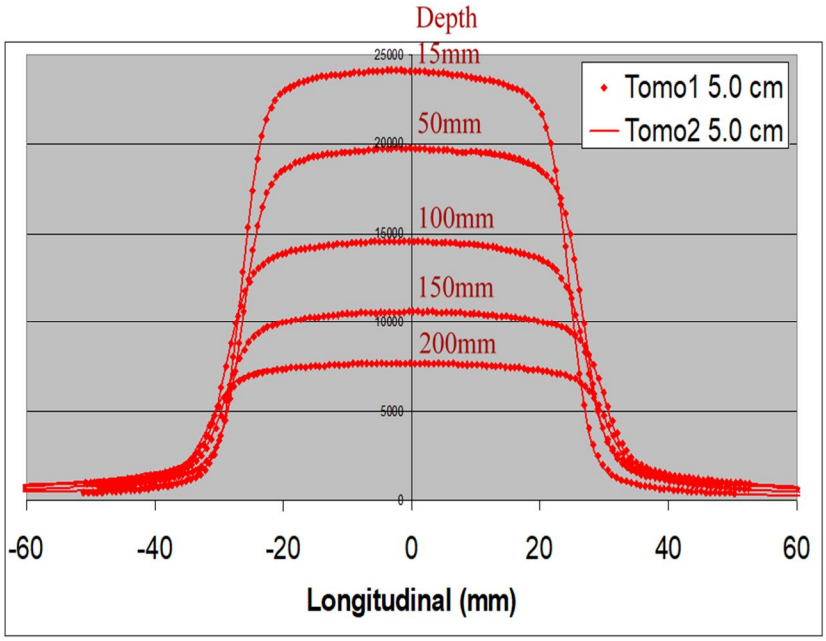

FIG. 2. Longitudinal profiles at five different depths for TomoTherapy I (discrete points) and TomoTherapy II (solid lines) for the 2.5 cm field.

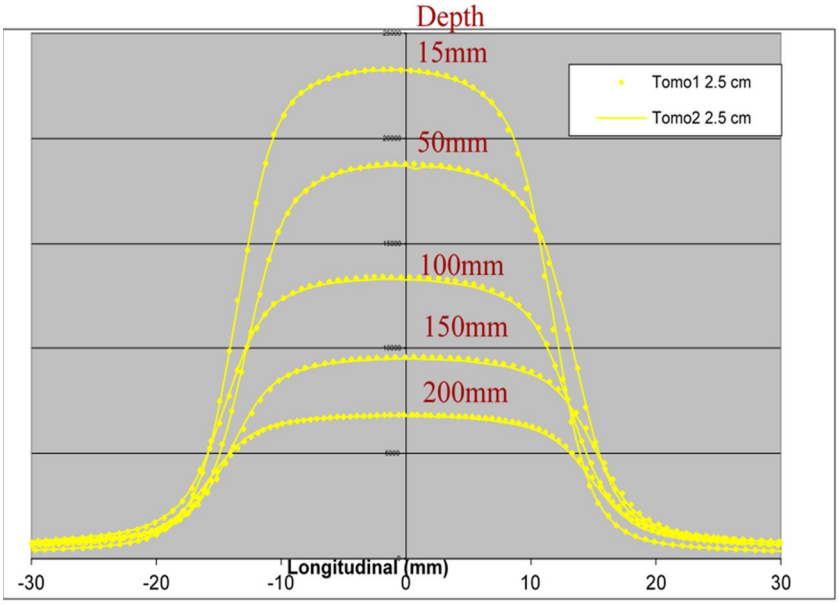

FIG. 3. Longitudinal profiles at five different depths for TomoTherapy I (discrete points) and TomoTherapy II (solid lines) for the 5.02 cm field.

3.3 Transverse Beam Profile Match

Figures 4 through 6 show the transverse beam profiles for the three commissioned fields (1.05, 2.5, and 5.02 cm, respectively), with the yellow solid line representing TomoTherapy I and the blue solid line representing TomoTherapy II. The agreement between the curves shows a very good match between the two machines.

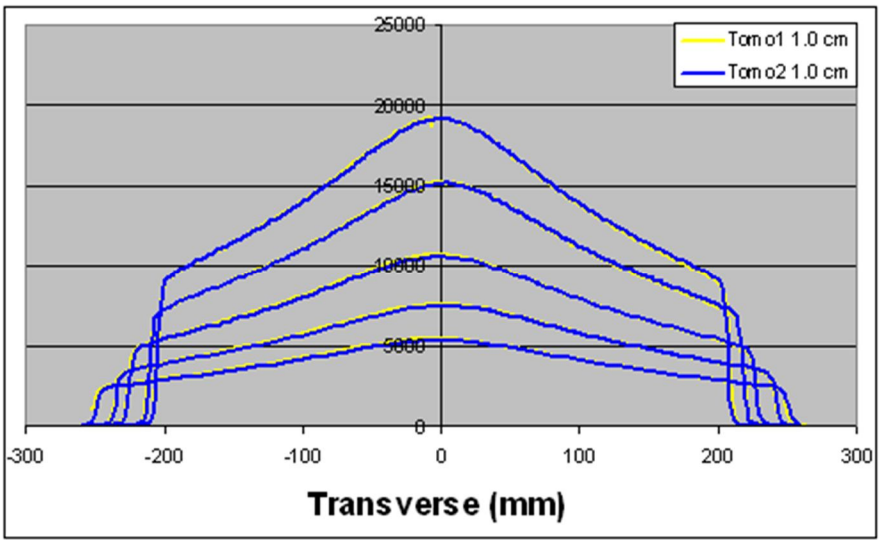

FIG. 4. Transverse profiles at five different depths for TomoTherapy I (yellow lines) and TomoTherapy II (blue lines) for the 1.05 cm field.

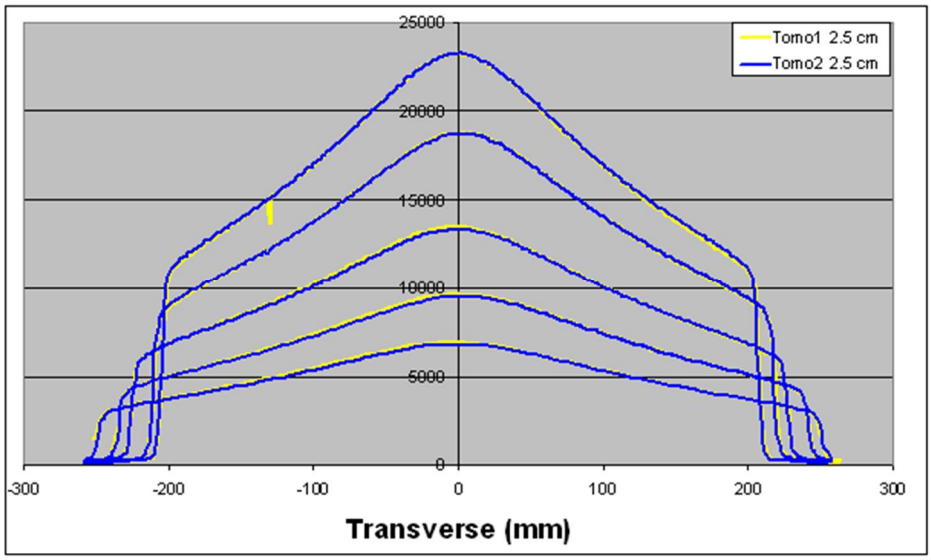

FIG. 5. Transverse profiles at five different depths for TomoTherapy I (yellow lines) and TomoTherapy II (blue lines) for the 2.5 cm field.

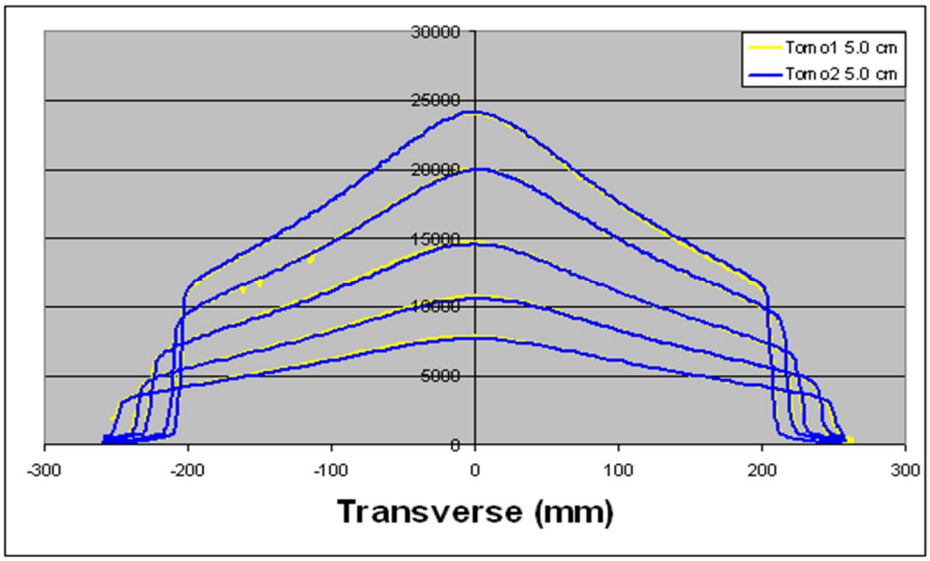

FIG. 6. Transverse profiles at five different depths for TomoTherapy I (yellow lines) and TomoTherapy II (blue lines) for the 5.02 cm field.

3.4 Percent Depth Dose

The TomoTherapy Hi-ART treatment machines use a single 6 MV energy, typically normalized at a depth of 1.6 cm. The normalized percent depth dose curves for the three commissioned fields on both machines, shown in Fig. 7 (discrete points representing TomoTherapy I and solid lines representing TomoTherapy II), are in good agreement. This agreement is expected since both machines produce the same energy photons and have identical field widths. The small differences between the TomoTherapy I and TomoTherapy II normalized percent depth dose are within acceptable measurement errors and are actually a result of expected uncertainties when measuring a 1 cm field with the A1Sl ion chamber. Therefore, treatment plan transfer can be accomplished regardless of the software version.

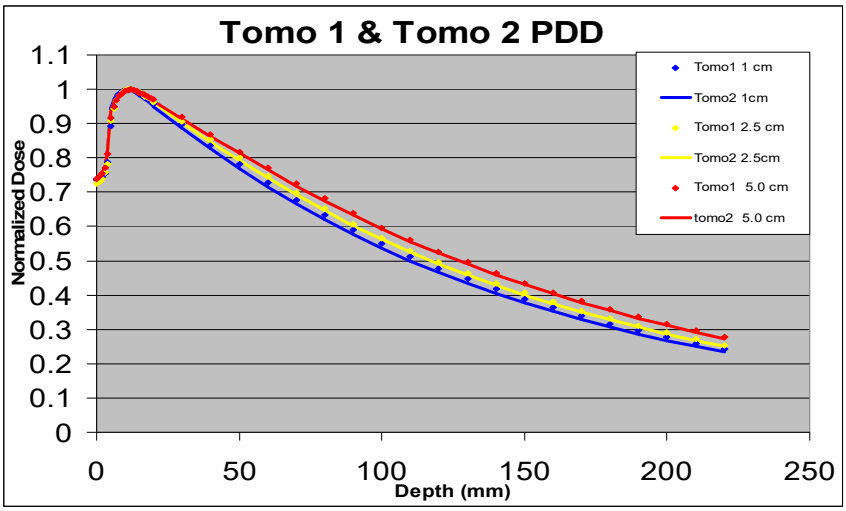

FIG. 7. Normalized percent depth dose for the two TomoTherapy machines: TomoTherapy I (points) and TomoTherapy II (solid lines).

3.5 Validation

Multiple patient DQA procedures were performed across the two TomoTherapy machines to validate the process of matching the machines. In this section, only three cases are discussed in detail: a prostate case, a stereotactic body radiotherapy (SBRT) case for the lung, and a pelvis case.

3.5.1 Example: Prostate Cancer

The first case presented here is a prostate case where 98% of the PTV volume was prescribed to receive 70.0 Gy in 28 fractions, while minimizing the dose to the rectal wall, bladder, femoral heads, and penile bulb. A typical prostate planning protocol was used, with a field width of 2.5 cm, a pitch of 0.215, and a final modulation factor of 1.81. The plan was computed on TomoTherapy II and transferred to TomoTherapy I where it was verified for plan matching between the two planning systems and for plan and delivery matching.

To verify that the transferred plan matched the original, the dose volume histogram (DVH) curves were first visually compared between the two planning systems. Then, for an accurate quantitative comparison, DVH statistics, including maximum, minimum, median, average dose, standard deviation, and physical volume, were compared between the two planning systems for the PTV and all critical structures, as reported in the plan. These statistics showed complete agreement between the planning systems, with the maximum difference being 0.06%.

To verify that the delivered dose matched the transferred plan, the dose delivered to a phantom was verified using the DQA procedure. The DQA analysis is shown in Fig. 8. Figures 8(a)-8(d) show good agreement between the planned dose distribution and the delivered dose distribution. Figure 8(a) displays the gamma map superimposed on a coronal film passing through the PTV within the cylindrical phantom. The white background corresponds to the high-dose region. The gamma index, introduced by Low *et al* [16], uses a combined ellipsoidal test of dose difference and distance-to-agreement (DTA). A gamma value of one for any pixel means that the measured pixel value matches the planned pixel value within an ellipsoid with radii of 3mm and

3% of the planned dose. The profile in Fig. 8(b), corresponding to the horizontal line in Fig. 8(a) and lateral measured and planned profiles on the film, shows a good agreement between the measured delivered and planned doses. Figure 8(c) shows good isodose line agreement between the planned and delivered doses on the coronal plane going through the center of the target. The longitudinal measured and planned profiles in the coronal plane going through the center of the target are shown in Fig. 8(d), which shows a good agreement.

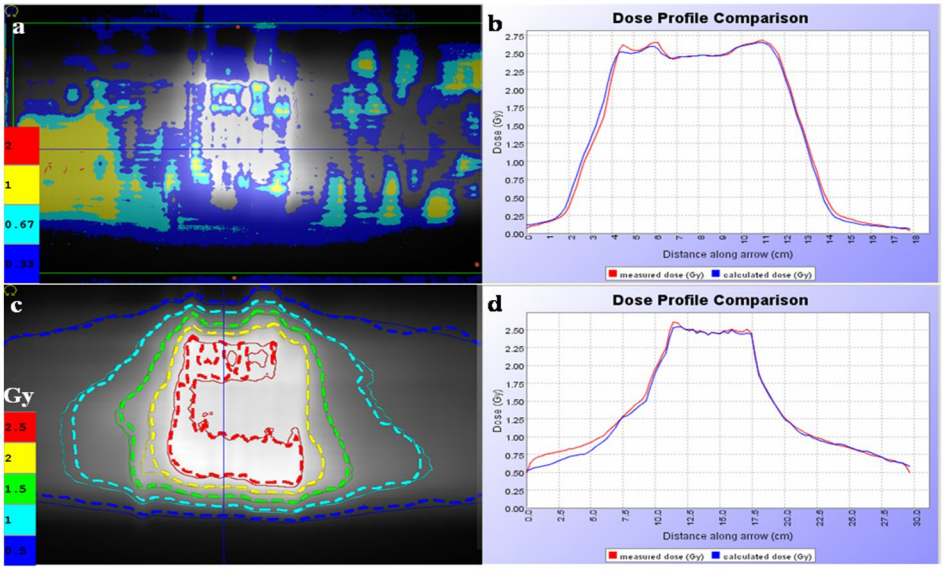

FIG. 8. (a) Gamma map superimposed on a coronal film passing through the PTV within the cylindrical phantom. The white background correlates to the high-dose region. (b) Lateral profile going through the PTV along the horizontal line in Fig. 8(a). (c) Film isodose lines (dashed lines) and plan isodose lines (solid lines) superimposed on a coronal film passing through the PTV. (d) Longitudinal profile going through the PTV along the vertical line in Fig. 8(c).

Figures 9(a)-9(d) show the analysis of a sagittal film placed at the center of the prostate PTV within the cylindrical phantom. The gamma distribution, AP profile, isodose lines, and longitudinal profile all support the good agreement between the planned and delivered dose distribution for the transferred plan between the two TomoTherapy machines.

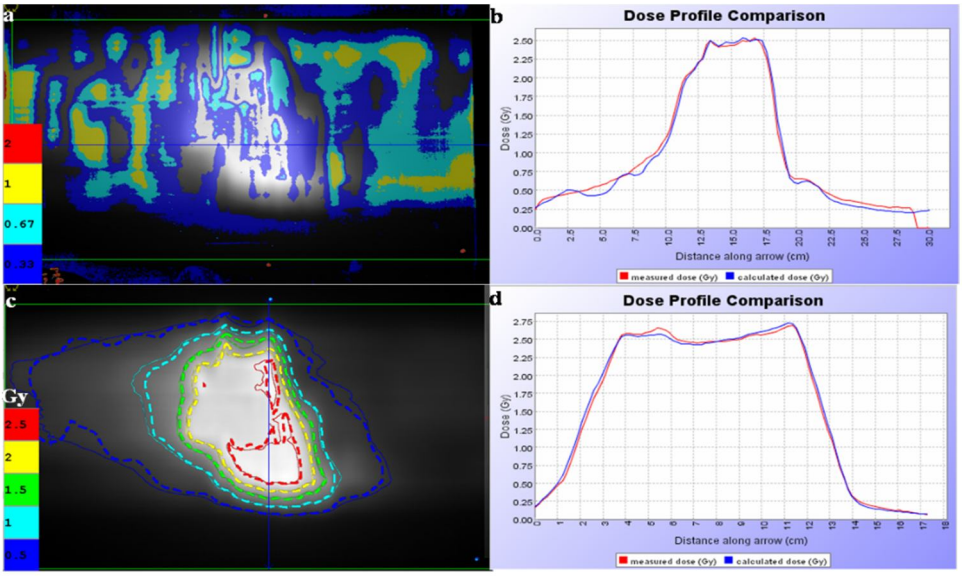

FIG. 9. (a) Gamma map superimposed on a sagittal film passing through the prostate PTV within the cylindrical phantom. The white background correlates to the high-dose region. (b) AP profile going through the PTV along the horizontal. (c) Film isodose lines (dashed lines) and plan isodose lines (solid lines) superimposed on a sagittal film passing through the PTV. (d) Longitudinal profile going through the PTV along the vertical line in Fig. 9(c).

3.5.2 Stereotactic Body Radiotherapy (SBRT) for Lung Cancer

The second case presented is a lung SBRT case, where 98% of the PTV volume was prescribed to receive 60.0 Gy in 5 fractions, while minimizing the dose to the residual lung, spinal cord, heart, esophagus, bronchus, and brachial plexus. A typical lung SBRT planning protocol was followed, with a field width of 2.5 cm, a pitch of 0.123, and a final modulation factor of 1.31. The plan was computed on TomoTherapy I and transferred to TomoTherapy II, where it was verified for plan matching between the two planning systems and plan and delivery matching.

The transferred plan was verified to match the original plan using the same method described above. When comparing all statistics for all ROIs between the original and transferred plans, there was no difference between the two plans. The DQA analysis is shown in Fig. 10. Figures 10(a)-10(d) show good agreement between the planned dose distribution and the delivered dose distribution. Figure 10(a) shows the gamma map superimposed on a coronal film passing through the SBRT PTV. The white background correlates to the high-dose region. The profile shown in Fig. 10(b) corresponds to the horizontal line in Fig. 10(a), displaying the lateral measured and planned profiles on the film. Figure 10(c) shows good isodose line agreement between the planned and delivered doses in the coronal plane going through the center of the target. The longitudinal measured and planned profiles in the coronal plane through the center of the target are shown in Fig. 10(d).

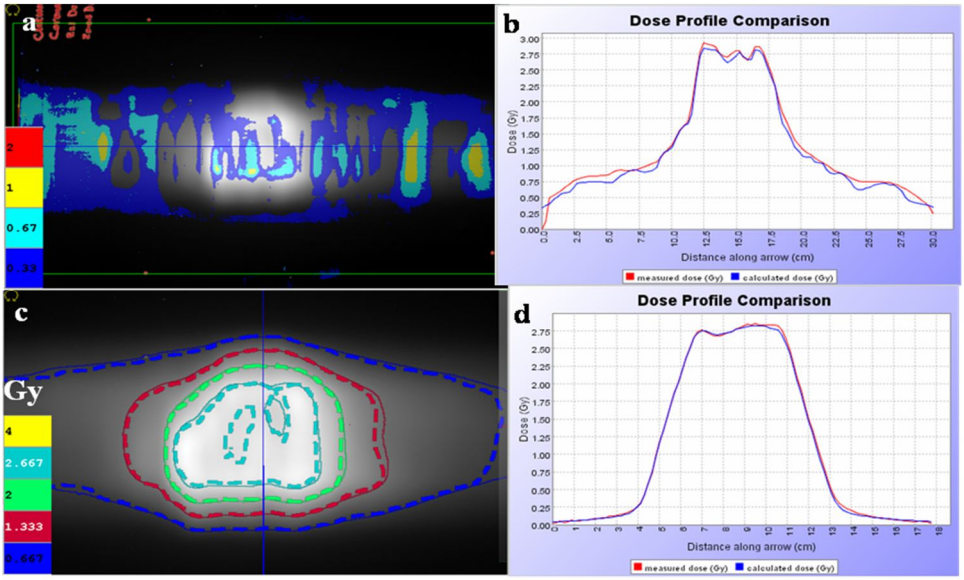

FIG. 10. (a) Gamma map superimposed on a coronal film passing through the SBRT PTV within the cylindrical phantom. The white background correlates to the high-dose region. (b) The lateral profile going through the PTV along the horizontal line in Fig. 10(a). (c) Film isodose lines (dashed lines) and plan isodose lines (solid lines) superimposed on the coronal film. (d) Longitudinal profile going through the PTV along the vertical line in Fig. 10(c).

Figures 11(a)-11(d) show good agreement between the planned dose distribution and the delivered dose distribution. Figure 11(a) shows the gamma map superimposed on a sagittal film passing through the SBRT PTV. The white background correlates to the high-dose region. The profile in Fig. 11(b) corresponds to the horizontal line in Fig. 11(a), showing the lateral measured and planned profiles on the film. Figure 11(c) illustrates good isodose line agreement between the planned and delivered doses in the sagittal plane going through the center of the target. The longitudinal measured and planned profiles in the sagittal plane going through the center of the target are shown in Fig. 11(d).

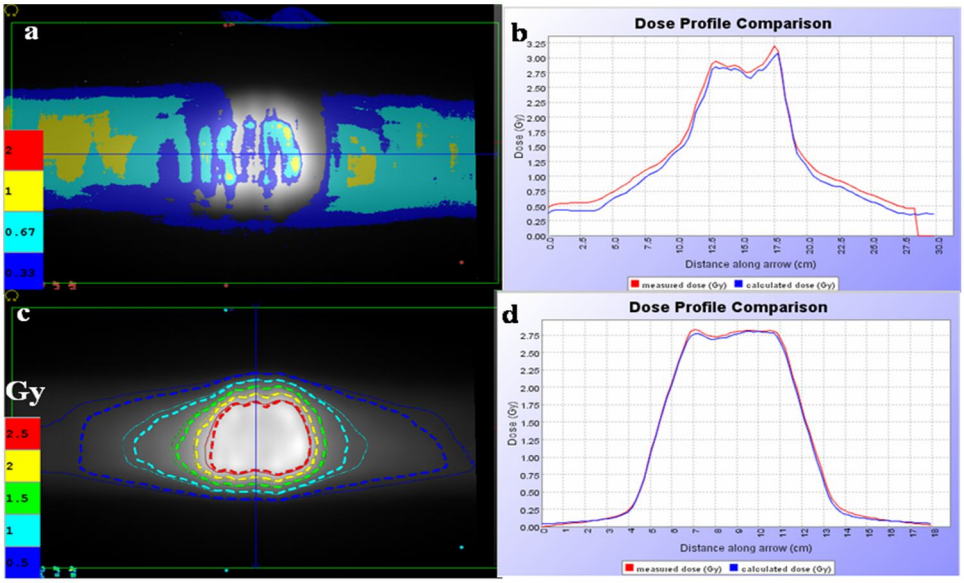

FIG. 11. (a) Gamma map superimposed on a sagittal film passing through the SBRT PTV within the cylindrical phantom. The white background correlates to the high-dose region. (b) AP profile going through the PTV along the horizontal line in Fig. 11(a). (c) Film isodose lines (dashed lines) and plan isodose lines (solid lines) superimposed on the sagittal film. (d) Longitudinal profile going through the PTV along the vertical line in Fig. 11(c).

3.5.3 Head and Neck Cancer

The third case presented is a head and neck case where 98% of the PTV volume was prescribed to receive 60.0 Gy, while the nodal PTV received 50.0 Gy in 30 fractions. Critical structures to avoid included the residual parotid, spinal cord, brainstem, larynx, and oral cavity. A typical head and neck planning protocol was used, with a field width of 2.5 cm, a pitch of 0.172, and a final modulation factor of 2.421. The plan was computed on TomoTherapy II and transferred to TomoTherapy I where it was verified for plan matching between the two planning systems. To test delivery matching in scenarios where a patient may need to switch machines mid-treatment (for example, to complete a fraction that was started on one machine and finished on the other), the DQA procedure was manually interrupted mid-treatment and completed on the second machine. This process verified the accuracy of interrupted treatments between machines.

The transferred plan was verified to match the original plan using the same method described above. When comparing all statistics for all ROIs between the original and transferred plans, we didn't find any differences. The DQA analysis, shown in Figs. 12 and 13, were designed to demonstrate that an interrupted treatment on one machine can be safely completed on the other machine. The top half of the film in Fig. 12(a) was delivered on TomoTherapy II. The treatment was manually interrupted after the first half. The phantom and film were transferred to TomoTherapy I where the second half of the treatment was delivered. Figure 12 shows the film dose compared to the planned dose on TomoTherapy I. The gamma distribution within the reliable region of the film (green rectangle) in Fig. 12(a) is well within the acceptable limits of 3% of the prescribed dose and 3 mm distance to agreement. The direction of treatment progression is along the vertical line (top to bottom) in Fig. 12(a). The measured and planned profiles along this line are shown in Fig. 12(b). Any mismatch between the two machines during treatment would be presented as a discontinuity (a peak or a dip) in the measured profile. The lack of such discontinuity shows that an interrupted treatment on one machine can be safely completed on the other machine. Isodose lines and AP profiles for the same sagittal film are shown in Figs. 12(c) and 12(d).

The same film analyzed on TomoTherapy II is shown in Fig. 13. The good agreement between the planned and delivered dose distributions, as shown by the gamma map, isodose lines, and profile agreement, assures that the transferred plan and the deliveries are identical across the two machines.

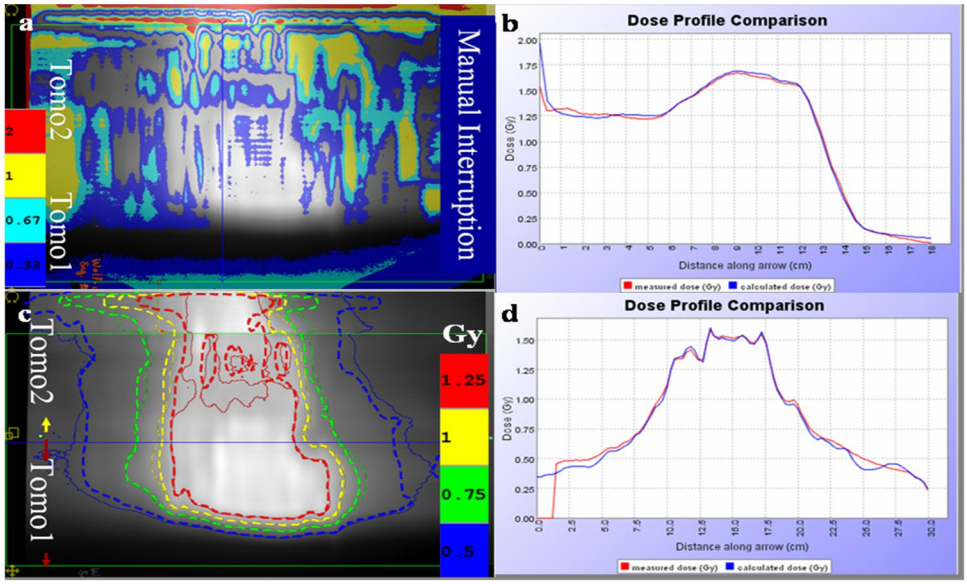

FIG. 12. The dose on the film was delivered on both TomoTherapy machines and analyzed on TomoTherapy I. (a) Gamma map superimposed on a sagittal film passing through the H& N PTV. The film was delivered on both TomoTherapy machines. (b) Longitudinal profile going through the PTV along the vertical line in Fig. 12(a). (c) Film isodose lines (dashed lines) and plan isodose lines (solid lines) superimposed on the sagittal film. (d) AP profile going through the PTV along the horizontal line in Fig. 12(c).

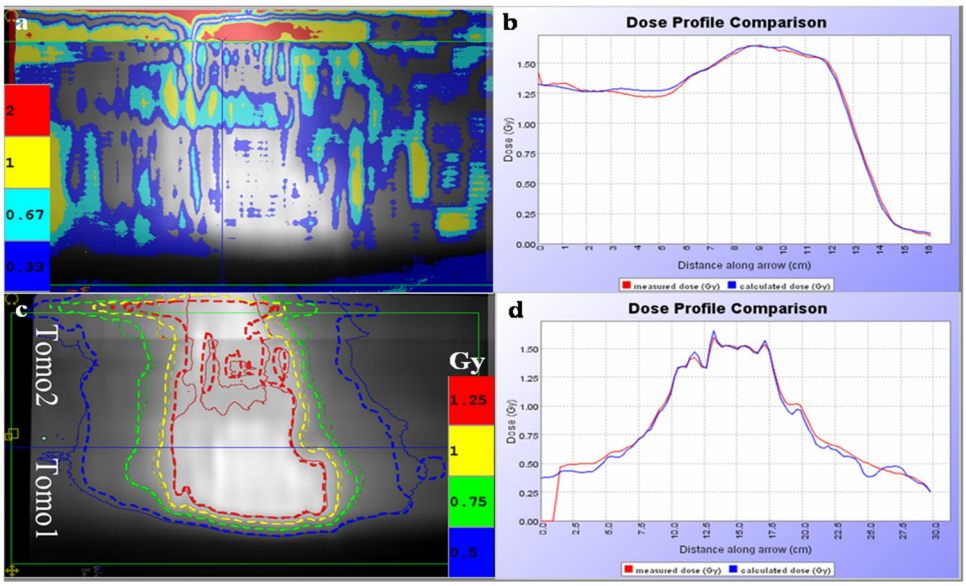

FIG. 13. The dose on the film was delivered on both TomoTherapy machines and analyzed on TomoTherapy II. (a) Gamma map superimposed on a sagittal film passing through the H& N PTV. The film was delivered on both TomoTherapy machines. (b) Longitudinal profile going through the PTV along the vertical line in Fig. 13(a). (c) Film isodose lines (dashed lines) and plan isodose lines (solid lines) superimposed on the sagittal film. (d) AP profile going through the PTV along the horizontal line in Fig. 13(c).

The beams from the two TomoTherapy machines were checked and verified to be identical within measurement uncertainties. No physical modifications on either of these two tomotherapy delivery machines resulted from this study. Both machines still have their original gold standard files. The beam model on the TomoTherapy I planning system was replaced with the beam model from TomoTherapy II. This adjustment was necessary to deliver identical plans and does not have any effect on treatment planning since the two beams were verified to be the same. Comprehensive tests using film and ion chamber dosimetry show that both beam models are correct models for both machines within the limits of measurement uncertainty.

4. Conclusion

A comprehensive methodology to check the similarities between two TomoTherapy machines — TomoTherapy I and TomoTherapy II (TomoTherapy Inc. Madison, WI) — has been described. A strategy was developed to match the two machines, facilitating patient transfers between them. Using this approach, the two UW TomoTherapy machines were found to be similar and capable of delivering the same treatment plans within the tolerances acceptable for IMRT treatments. On several occasions, tomotherapy treatment plans were transferred between the two TomoTherapy machines to avoid treatment cancellations. Tomotherapy treatment plan transfers were accomplished within a reasonable time frame (5-10 minutes per plan) without changing the outcome of the plans.

Interrupted treatments on one machine can be safely completed on the second machine within 10 to 15 minutes. This can be useful in SRS or SBRT cases where the delivery of the treatment or fraction within a short time is essential.

The procedure of matching the two TomoTherapy machines can be applied to more machines within the same clinic or across clinics. When having two TomoTherapy machines, this procedure eliminates the need for backup planning which requires additional planning clusters and additional dosimetry staff time.

Disclaimer

The procedures and methods presented here were solely developed by the Institute's physics team for internal use. TomoTherapy Inc. did not participate in this study, and they neither support nor recommend the procedures presented here.

Acknowledgments

This work is partially supported by NIH Grant 5 PO1 CA088960-04.

References:

[1] Kraus, K.M., Kampfer, S., Wilkens, J.J., Schüttrumpf, L., and Combs, S.E., Sci. Rep., 10 (1) (2020) 4928.

[2] Kurosaki, H., Hirayama, K., Takahashi, M., Uematsu, M., and Tate, E., Cureus, 14 (10) (2022).

[3] Hong, T.S., Tome, W.A., Jaradat, H., Raisbeck, B.M., and Ritter, M.A., Int. J. Radiat. Oncol. Biol. Phys., 63 (2005) S61.

[4] Mañon, R.R., Jaradat, H., Patel, R., Zhang, T., Fenwick, J., Tomé, W., ... and Mehta, M., Clin. Lung Cancer, 7 (2) (2005) 107.

[5] Orton, N., Jaradat, H., Welsh, J., and Tomé, W., Med. Dosim., 30 (3) (2005) 162.

[6] Aoyama, H., Westerly, D.C., Mackie, T.R., Olivera, G.H., Bentzen, S.M., Patel, R.R., ... and Mehta, M.P., Int. J. Radiat. Oncol. Biol. Phys., 64 (3) (2006) 962.

[7] Khuntia, D., Jaradat, H., Orton, N., Tomé, W., Mehta, M.P., and Welsh, J.S., Int. J. Radiat. Oncol. Biol. Phys., 64 (4) (2006) 1288.

[8] Mackie, T.R., Phys. Med. Biol., 51 (13) (2006) R427.

[9] Thondykandy, B.A., Swamidas, J.V., Agarwal, J., Gupta, T., Laskar, S.G., Mahantshetty, U., ... and Deshpande, D.D., J. Med. Phys., 40 (4) (2015) 233.

[10] Mackie, T.R., Holmes, T., Swerdloff, S., Reckwerdt, P., Deasy, J.O., Yang, J., ... and Kinsella, T., Med. Phys., 20 (6) (1993) 1709.

[11] Shepard, D.M., Olivera, G.H., Reckwerdt, P.J., and Mackie, T.R., Phys. Med. Biol., 45 (1) (2000) 69.

[12] Grigorov, G., Kron, T., Wong, E., Chen, J., Sollazzo, J., and Rodrigues, G., Phys. Med. Biol., 48 (13) (2003) 1933.

[13] Garcia-Fernandez, L.M., Doctoral Dissertation, Carleton University, (2010).

[14] Wang, H., Feng, X., Shi, B., Liang, W., Chen, Y., Wang, J., and Li, X., Rev. Sci. Instrum., 89 (9) (2018) 093114.

[15] Engelsman, M., Mazal, A., and Jaffray, D.A., "Proton and Charged Particle Radiotherapy", (2008) 57.

[16] Low, D.A., Harms, W.B., Mutic, S., and Purdy, J.A., Med. Phys., 25 (5) (1998) 656.

Volume 17, Number 4, 2024. pp. 395-402

Jordan Journal of Physics

ARTICLE

Solution of the Woods-Saxon Potential and its Application for Study of Thermodynamic Properties

Derar Altarawneh[a], **Abdullah Atef Shukri**[b] and **Akpan N. Ikot**[c,d]

[a] *Department of Applied Physics, Tafila Technical University, Tafila, 66110, Jordan.*

[b] *Department of Physics, Yarmouk University, Irbid, Jordan.*

[c] *Theoretical Physics Group, Department of Physics, University of Port Harcourt, Port Harcourt, Nigeria.*

[d] *Western Caspian University, Baku, Azerbaijan.*

Doi: **https://doi.org/10.47011/17.4.2**

Received on: 20/11/2022; *Accepted on: 26/04/2023*

Abstract: This work presents an exact analytical solution for the Schrödinger equation with the Woods-Saxon potential. To achieve this, the factorization method is utilized with the Pekeris approximation applied to the centrifugal potential for arbitrary l states. The resulting solution provides both the wave functions of the potential expressed in the hypergeometric function and the energy eigenvalues. Additionally, the study calculates the thermodynamic properties of the Woods-Saxon potential in its classical limit, including the vibrational partition function, mean vibrational energy, vibrational specific heat, vibrational mean free energy, and vibrational entropy.

Keywords: Woods-Saxon Potential, Schrodinger equation, Thermodynamic properties, Factorization method.

PACS numbers: 11.15.Ha, 12.38.Gc.

Introduction

The Schrödinger equation is a crucial tool for investigating quantum mechanical systems and making predictions. Since it encodes all the necessary information about these systems, particularly in physics and chemistry, its solution has attracted considerable interest [1, 2, 3, 4]. However, exact solutions are only feasible for a small number of potentials, prompting the development of approximation methods for tackling complex cases, such as those involving arbitrary angular momentum quantum numbers l. Several such methods have been proposed, including the factorization method [5, 6], the asymptotic iteration method [7, 8, 9], the super-symmetric quantum mechanics approach [10, 11], the Nikiforov-Uvarov method, and the factorization method [12]. The factorization method involves transforming a second-order homogeneous linear differential equation into a hypergeometric equation using appropriate transformations. In this study, we employ the factorization method to determine the nonrelativistic energy states of the standard Woods-Saxon potential [13].

The Woods-Saxon potential is a widely used short-range potential in nuclear, particle, and atomic physics that has contributed significantly to the field's development over the past several decades. This potential has been instrumental in the understanding of numerous experimental observations, including proton scattering and neutron interactions with heavy nuclei. Additionally, it is a popular model for systems of

Corresponding Author: Derar Altarawneh **Email**: derar@ttu.edu.jo

confined particles within a potential well enclosed by a potential barrier, such as protons and neutrons in atomic nuclei, electrons in metals, and nuclear fusion and fission. Researchers have shown considerable interest in solving the Schrödinger equation for the Woods-Saxon potential, with numerous studies conducted to determine the associated wave function and energy states [7, 9, 13, 14, 15, 16, 17, 18, 19, 20,21]. Studying thermodynamic functions has also garnered much attention in the last few decades, with researchers utilizing various methods to evaluate the thermodynamic properties of physical systems under different potentials [22, 23, 24].

This paper focuses on the study of the Schrödinger equation with the Woods-Saxon potential, specifically for an arbitrary angular momentum quantum number l, using the factorization method. The aim is to obtain energy levels and wave functions and subsequently apply the canonical partition function in the classical limit to analyze the thermodynamic properties of nonrelativistic particles. The paper is organized into several sections. Section I provides an introduction to the topic. Section II presents the energy states and wave function of the Woods-Saxon potential. Section III covers the thermodynamic properties of the potential, including free energy, specific heat, mean energy, and entropy. The discussion and conclusion of the paper are presented in Sections IV and V, respectively.

Energy States and Wave Function of Woods-Saxon Potential

The standard Woods-Saxon potential [1] is defined as:

$$V(r) = -\frac{V_0}{1+\exp(\frac{r-R_0}{a})}, a \ll R_0. \quad (1)$$

Here, V_0 represents the potential well depth, a is the surface thickness of the nucleus, and R_0 is the nuclear radius.

The radial part of the Schrodinger equation is:

$$\frac{d^2\psi(r)}{dr^2} + \frac{2m}{\hbar^2}[E_{nl} - V(r) - \frac{l(l+1)\hbar^2}{2mr^2}]\psi(r) = 0 \quad (2)$$

By substituting the Woods-Saxon potential, the Schrodinger equation becomes:

$$\frac{d^2\psi(r)}{dr^2} + \frac{2m}{\hbar^2}[E_{nl} + \frac{V_0}{1+\exp(\frac{r-R_0}{a})} - \frac{l(l+1)\hbar^2}{2mr^2}]\psi(r) = 0 \quad (3)$$

The equation cannot be analytically solved for $l \neq 0$, leading to the use of the Pekeris approximation to address this limitation. This approach enables the expression of the centrifugal term as:

$$\frac{l(l+1)\hbar}{2mr^2} = \alpha[S_0 + \frac{S_1}{1+exp(\frac{r-R_0}{a})} + \frac{S_1}{(1+exp(\frac{r-R_0}{a}))^2}], \quad (4)$$

where

$$\frac{l(l+1)\hbar}{2mR_0^2} = \alpha \quad (5)$$

By using Taylor expansion around $r = R_0$, the values of S_0, S_1, and S_2 are found to be:

$$\left.\begin{aligned} S_0 &= 1 - \frac{4a}{R_0} + \frac{12a^2}{R_0^2} \\ S_1 &= \frac{8a}{R_0} - \frac{48a^2}{R_0^2} \\ S_2 &= \frac{48a^2}{R_0^2} \end{aligned}\right\} \quad (6)$$

The solution presented in this study focuses on the point where the Woods-Saxon potential weakens and higher-order terms are not considered. The Woods-Saxon potential has a short range, which means that the expansion presented above is applicable only to low-energy states. With this in mind, Eq. (3) can be written as:

$$\psi''(z) + \frac{[1-2z]}{[z(1-z)]}\psi'(z) + \frac{\epsilon^2+\chi^2 z-\gamma^2 z^2}{z(z-1)^2}\psi(z) = 0 \quad (7)$$

Here, we insert the Pekeris approximation into the equation and we change the variables $r \to z$ by applying the mapping function $z = (1 + e^{\frac{r-R_0}{a}})^{-1}$. The parameters ϵ,χ, and γ are defined as:

$$\left.\begin{aligned} \epsilon^2 &= \frac{2ma^2}{\hbar^2}[E_{nl} - \alpha S_0] \\ \chi^2 &= \frac{2ma^2}{\hbar^2}[V_0 - \alpha S_1] \\ \gamma^2 &= \frac{2ma^2\alpha S_2}{\hbar^2} \end{aligned}\right\} \quad (8)$$

By using the boundary conditions of the wave functions $\psi(z)$, we obtain:

$$\left.\begin{aligned} \psi(z) \to 0 \quad \text{when} \quad z \to 1 \\ \psi(z) \to 0 \quad \text{when} \quad z \to 0 \end{aligned}\right\} \quad (9)$$

Thus, we can write the wave function as:

$$\psi(z) = z^{\mu}(1-z)^{\phi} f(z) \quad (10)$$

By substituting Eq. (10) into Eq. (7), we obtain the following equation:

$$z(1-z)f''(z)+[1+2\mu-(2\mu+2\phi+2)z]f'(z)-[(\mu+\phi)^2+(\mu+\phi)-\gamma^2]f(z)+[\frac{-\epsilon^2+\mu^2}{z(1-z)}+\frac{\phi^2-\mu^2+\chi^2-\gamma^2}{1-z}]f(z)=0 \quad (11)$$

Equation (10) becomes a Gauss hypergeometric equation if and only the following equations vanish:

$$-\epsilon^2+\mu^2=0 \text{ and } \phi^2-\mu^2+\chi^2-\gamma^2=0 \quad (12)$$

Equation (11) becomes:

$$z(1-z)f''(z)+[1+2\mu-(2\mu+2\phi+2)z]f'(z)-[(\mu+\phi+\frac{1}{2}+\sqrt{\frac{1}{4}+\gamma^2})((\mu+\phi+\frac{1}{2}-\sqrt{\frac{1}{4}+\gamma^2})]f(z)=0 \quad (13)$$

Equation (13) is compared with the hypergeometric differential equation which has the following form:

$$z(1-z)f''(z)+[c-(a+b+1)z]f'(z)-abf(z)=0 \quad (14)$$

We find that:

$$\left.\begin{aligned} a &= \mu+\phi+\frac{1}{2}+\sqrt{\frac{1}{4}+\gamma^2} \\ b &= \mu+\phi+\frac{1}{2}-\sqrt{\frac{1}{4}+\gamma^2} \\ c &= 1+2\mu \end{aligned}\right\} \quad (15)$$

With the help of the Gauss hypergeometric function, a solution to Eq. (14) is given by:

$$f(z)={}_2F_1(a,b;c;z)=\frac{\Gamma(c)}{\Gamma(a)\Gamma(b)} \quad (16)$$

By substituting Eqs. (15) and (16) into Eq. (10), the wave function becomes:

$$\psi(z)=z^{\mu}(1-z)^{\phi}{}_2F_1(a,b;c;z) \quad (17)$$

The hypergeometric function appearing in Eq. (16) can be reduced into a polynomial of degree n when either a or b equals a negative integer $-n$. Under this condition, the wave function can asymptotically vanish.

$$\left.\begin{aligned} \mu+\phi+\frac{1}{2}+\sqrt{\frac{1}{4}+\gamma^2}&=-n \\ \mu+\phi+\frac{1}{2}-\sqrt{\frac{1}{4}+\gamma^2}&=-n \end{aligned}\right\} \quad (18)$$

By using Eqs. (12) and (18), one can find the non-relativistic energy spectrum as:

$$E_{nl}=\frac{-\hbar^2}{2ma^2}[\frac{(\omega-n)}{2}-\frac{(\gamma^2-\chi^2)}{2(\omega-n)}]^2+\alpha S_0 \quad (19)$$

where

$$\omega=((\sqrt{\frac{1}{4}+\gamma^2}-\frac{1}{2}) \quad (20)$$

Using Eqs. (8) and (9), one can get:

$$\epsilon=\frac{1}{2}[(\omega-n)+\frac{\gamma^2-\chi}{(\omega-n)}] \quad (21)$$

Since for the bound states ($\epsilon>0$), one can get that $(\omega-n)>0$ and $\omega\neq n$. Here, the index n is a non-negative integer and describes the quantization of the bound states and the energy spectrum. This result shows a perfect agreement with previous results

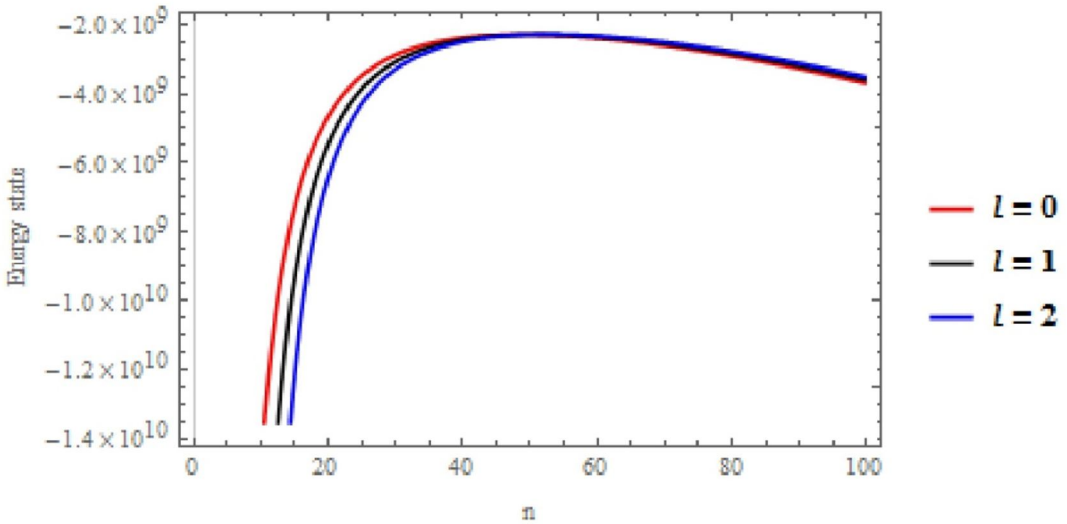

FIG. 1. Energy states (eV) versus radial quantum number (n) for different values of l.

Thermodynamic Properties

For studying the thermodynamic properties of the Woods-Saxon potential, we first obtain the vibrational partition function which is defined as:

$$Z_{vib}(\beta) = \sum_{n=0}^{\lambda} e^{-\beta E_{nl}} \tag{22}$$

where $\beta = 1/k_b T$, k_b is the Boltzmann constant, and λ is the upper-bound vibrational quantum number. At high temperature T (classical limit) the sum can be converted to an integral. By substituting the energy state, one can find:

$$Z_{vib}(\beta) = \int_0^{\lambda} e^{-\beta E_{nl}}\, dn = \frac{1}{2}\sqrt{b\beta}\left(2\sqrt{\pi}\left(\text{erfi}\left(\frac{\sqrt{b\beta}}{\lambda}\right)+1\right) - \frac{2\lambda e^{\frac{b\beta}{\lambda^2}}}{\sqrt{b\beta}}\right) e^{\beta\left(c+P(\omega-n)^2\right)} \tag{23}$$

where:

$$\text{erfi}(x) = \frac{\text{erf(x)}}{i} = \frac{2}{\pi}\int_0^x e^{t^2}\, dt \tag{24}$$

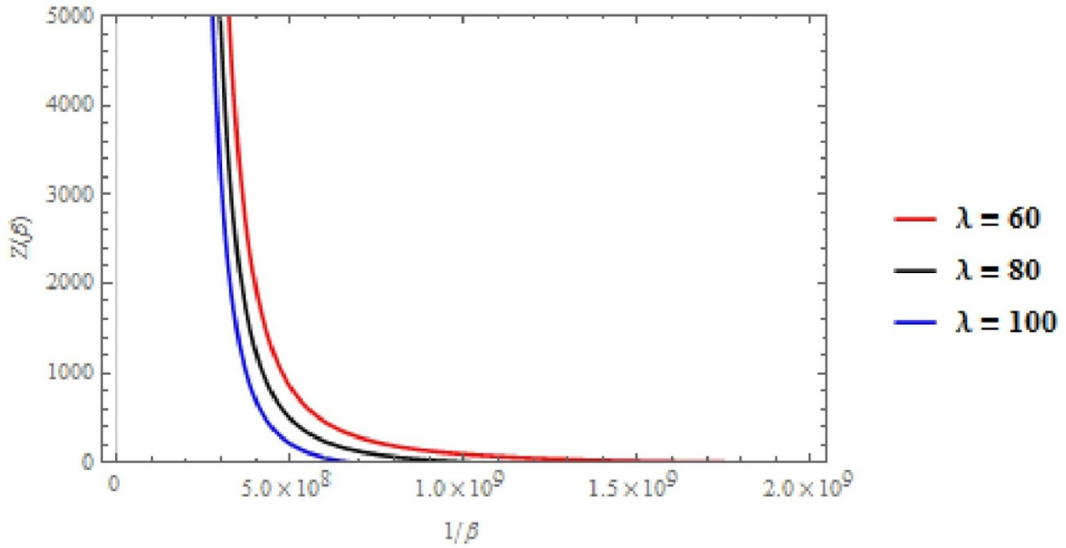

FIG. 2. Vibrational partition function Z versus $\frac{1}{\beta}$.

Having determined the vibrational partition function, we can easily obtain the thermodynamic properties for the Woods-Saxon as follows:

$$U(\beta) = -\frac{\partial}{\partial\beta}\ln Z_{vib}(\beta) \tag{25}$$

After substituting Eq. (22) into Eq. (25), the vibrational mean energy will have the form:

1. The Vibrational Mean Energy U:

$$U(\beta) = -\frac{2e^{-\beta(c+P(\omega-n)^2)}\left(\frac{b\left(2\sqrt{\pi}\left(\text{erfi}\left(\frac{\sqrt{b\beta}}{\lambda}\right)+1\right)-\frac{2\lambda e^{\frac{b\beta}{\lambda^2}}}{\sqrt{b\beta}}\right)e^{\beta(c+P(\omega-n)^2)}}{4\sqrt{b\beta}}\right)}{\sqrt{b\beta}\left(2\sqrt{\pi}\left(\text{erfi}\left(\frac{\sqrt{b\beta}}{\lambda}\right)+1\right)-\frac{2\lambda e^{\frac{b\beta}{\lambda^2}}}{\sqrt{b\beta}}\right)}$$

$$+\frac{2e^{-\beta(c+P(\omega-n)^2)}\left(\frac{1}{2}\sqrt{b\beta}\left(2\sqrt{\pi}\left(\text{erfi}\left(\frac{\sqrt{b\beta}}{\lambda}\right)+1\right)-\frac{2\lambda e^{\frac{b\beta}{\lambda^2}}}{\sqrt{b\beta}}\right)(c+P(\omega-n)^2)e^{\beta(c+P(\omega-n)^2)}+\frac{\lambda e^{\frac{b\beta}{\lambda^2}+\beta(c+P(\omega-n)^2)}}{2\beta}\right)}{\sqrt{b\beta}\left(2\sqrt{\pi}\left(\text{erfi}\left(\frac{\sqrt{b\beta}}{\lambda}\right)+1\right)-\frac{2\lambda e^{\frac{b\beta}{\lambda^2}}}{\sqrt{b\beta}}\right)} \tag{26}$$

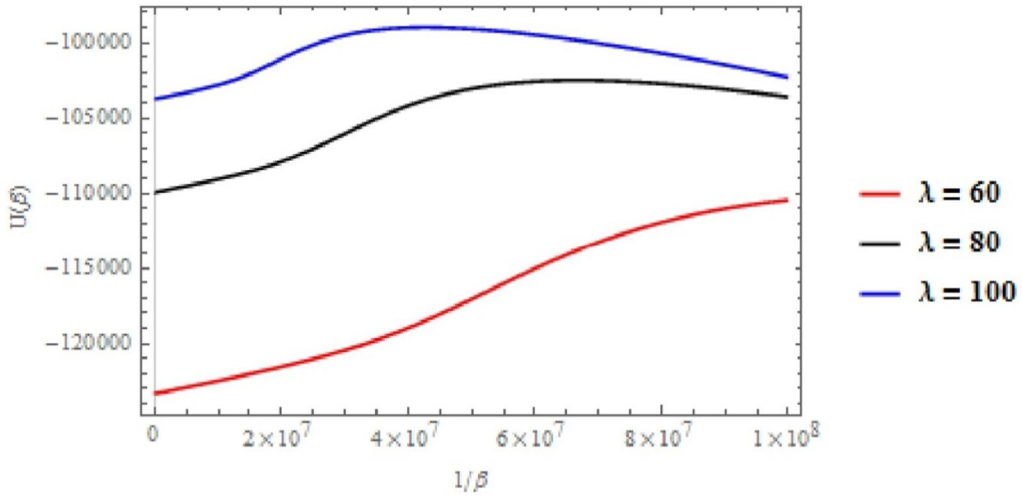

FIG. 3. Mean vibrational energy $U(cm^{-1})$ versus $\frac{1}{\beta}(K)$ for different values of λ.

2. *Mean Free Energy* F**:**

$$F = -\frac{1}{\beta}\ln Z_{vib}(\beta) = -\frac{\log\left(\frac{1}{2}\sqrt{b\beta}\left(2\sqrt{\pi}\left(\operatorname{erfi}\left(\frac{\sqrt{b\beta}}{\lambda}\right)+1\right)-\frac{2\lambda e^{\frac{b\beta}{\lambda^2}}}{\sqrt{b\beta}}\right)e^{\beta(c+P(\omega-n)^2)}\right)}{\beta} \tag{27}$$

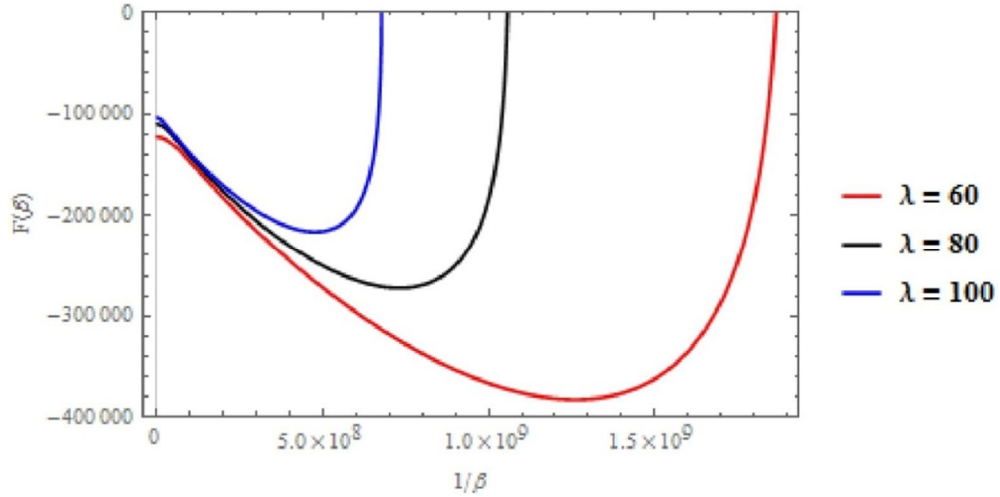

FIG. 4. Mean vibrational free energy $F(cm^{-1})$ versus $\frac{1}{\beta}(K)$ for different values of λ.

3. Vibrational Specific Heat C*:*

$$C = -K_b\beta^2\frac{\partial}{\partial\beta}U$$

$$C = -K_b\beta^2\frac{\partial}{\partial\beta}U$$

$$C = -\beta^2\left(\frac{be^{-\beta\left(P(\omega-n)^2+c\right)}\left(\frac{e^{\left(P(\omega-n)^2+c\right)\beta+\frac{b\beta}{\lambda^2}}\lambda}{2\beta}+\frac{be^{\beta\left(P(\omega-n)^2+c\right)}\left(2\sqrt{\pi}\left(\operatorname{erfi}\left(\frac{\sqrt{b\beta}}{\lambda}\right)+1\right)-\frac{2e^{\frac{b\beta}{\lambda^2}}\lambda}{\sqrt{b\beta}}\right)}{4\sqrt{b\beta}}-\frac{1}{2}\sqrt{b\beta}e^{\beta\left(P(\omega-n)^2+c\right)}\left(P(\omega-n)^2+c\right)\left(2\sqrt{\pi}\left(\operatorname{erfi}\left(\frac{\sqrt{b\beta}}{\lambda}\right)+1\right)-\frac{2e^{\frac{b\beta}{\lambda^2}}\lambda}{\sqrt{b\beta}}\right)\right)}{(b\beta)^{3/2}\left(2\sqrt{\pi}\left(\operatorname{erfi}\left(\frac{\sqrt{b\beta}}{\lambda}\right)+1\right)-\frac{2e^{\frac{b\beta}{\lambda^2}}\lambda}{\sqrt{b\beta}}\right)}\right)$$

$$+\beta^2\left(\frac{2e^{-\beta\left(P(\omega-n)^2+c\right)}\left(-P(\omega-n)^2-c\right)\left(\frac{e^{\left(P(\omega-n)^2+c\right)\beta+\frac{b\beta}{\lambda^2}}\lambda}{2\beta}+\frac{be^{\beta\left(P(\omega-n)^2+c\right)}\left(2\sqrt{\pi}\left(\operatorname{erfi}\left(\frac{\sqrt{b\beta}}{\lambda}\right)+1\right)-\frac{2e^{\frac{b\beta}{\lambda^2}}\lambda}{\sqrt{b\beta}}\right)}{4\sqrt{b\beta}}-\frac{1}{2}\sqrt{b\beta}e^{\beta\left(P(\omega-n)^2+c\right)}\left(P(\omega-n)^2+c\right)\left(2\sqrt{\pi}\left(\operatorname{erfi}\left(\frac{\sqrt{b\beta}}{\lambda}\right)+1\right)-\frac{2e^{\frac{b\beta}{\lambda^2}}\lambda}{\sqrt{b\beta}}\right)\right)}{\sqrt{b\beta}\left(2\sqrt{\pi}\left(\operatorname{erfi}\left(\frac{\sqrt{b\beta}}{\lambda}\right)+1\right)-\frac{2e^{\frac{b\beta}{\lambda^2}}\lambda}{\sqrt{b\beta}}\right)}\right)$$

$$+\beta^2\left(\beta^2 k_b\left(\frac{be^{-\beta\left(P(\omega-n)^2+c\right)}\left(\frac{e^{\left(P(\omega-n)^2+c\right)\beta+\frac{b\beta}{\lambda^2}}\lambda}{2\beta}+\frac{be^{\beta\left(P(\omega-n)^2+c\right)}\left(2\sqrt{\pi}\left(\operatorname{erfi}\left(\frac{\sqrt{b\beta}}{\lambda}\right)+1\right)-\frac{2e^{\frac{b\beta}{\lambda^2}}\lambda}{\sqrt{b\beta}}\right)}{4\sqrt{b\beta}}-\frac{1}{2}\sqrt{b\beta}e^{\beta\left(P(\omega-n)^2+c\right)}\left(P(\omega-n)^2+c\right)\left(2\sqrt{\pi}\left(\operatorname{erfi}\left(\frac{\sqrt{b\beta}}{\lambda}\right)+1\right)-\frac{2e^{\frac{b\beta}{\lambda^2}}\lambda}{\sqrt{b\beta}}\right)\right)}{(b\beta)^{3/2}\left(2\sqrt{\pi}\left(\operatorname{erfi}\left(\frac{\sqrt{b\beta}}{\lambda}\right)+1\right)-\frac{2e^{\frac{b\beta}{\lambda^2}}\lambda}{\sqrt{b\beta}}\right)}\right)\right)$$

$$+\beta^2\left(\frac{2e^{-\beta\left(P(\omega-n)^2+c\right)}\left(-P(\omega-n)^2-c\right)\left(\frac{e^{\left(P(\omega-n)^2+c\right)\beta+\frac{b\beta}{\lambda^2}}\lambda}{2\beta}+\frac{be^{\beta\left(P(\omega-n)^2+c\right)}\left(2\sqrt{\pi}\left(\operatorname{erfi}\left(\frac{\sqrt{b\beta}}{\lambda}\right)+1\right)-\frac{2e^{\frac{b\beta}{\lambda^2}}\lambda}{\sqrt{b\beta}}\right)}{4\sqrt{b\beta}}-\frac{1}{2}\sqrt{b\beta}e^{\beta\left(P(\omega-n)^2+c\right)}\left(P(\omega-n)^2+c\right)\left(2\sqrt{\pi}\left(\operatorname{erfi}\left(\frac{\sqrt{b\beta}}{\lambda}\right)+1\right)-\frac{2e^{\frac{b\beta}{\lambda^2}}\lambda}{\sqrt{b\beta}}\right)\right)}{\sqrt{b\beta}\left(2\sqrt{\pi}\left(\operatorname{erfi}\left(\frac{\sqrt{b\beta}}{\lambda}\right)+1\right)-\frac{2e^{\frac{b\beta}{\lambda^2}}\lambda}{\sqrt{b\beta}}\right)}\right)$$

$$-\beta^2\left(\frac{2e^{\frac{b\beta}{\lambda^2}-\beta\left(P(\omega-n)^2+c\right)}\lambda\left(\frac{e^{\left(P(\omega-n)^2+c\right)\beta+\frac{b\beta}{\lambda^2}}\lambda}{2\beta}+\frac{be^{\beta\left(P(\omega-n)^2+c\right)}\left(2\sqrt{\pi}\left(\operatorname{erfi}\left(\frac{\sqrt{b\beta}}{\lambda}\right)+1\right)-\frac{2e^{\frac{b\beta}{\lambda^2}}\lambda}{\sqrt{b\beta}}\right)}{4\sqrt{b\beta}}-\frac{1}{2}\sqrt{b\beta}e^{\beta\left(P(\omega-n)^2+c\right)}\left(P(\omega-n)^2+c\right)\left(2\sqrt{\pi}\left(\operatorname{erfi}\left(\frac{\sqrt{b\beta}}{\lambda}\right)+1\right)-\frac{2e^{\frac{b\beta}{\lambda^2}}\lambda}{\sqrt{b\beta}}\right)\right)}{b\beta^2\left(2\sqrt{\pi}\left(\operatorname{erfi}\left(\frac{\sqrt{b\beta}}{\lambda}\right)+1\right)-\frac{2e^{\frac{b\beta}{\lambda^2}}\lambda}{\sqrt{b\beta}}\right)^2}\right)$$

(28)

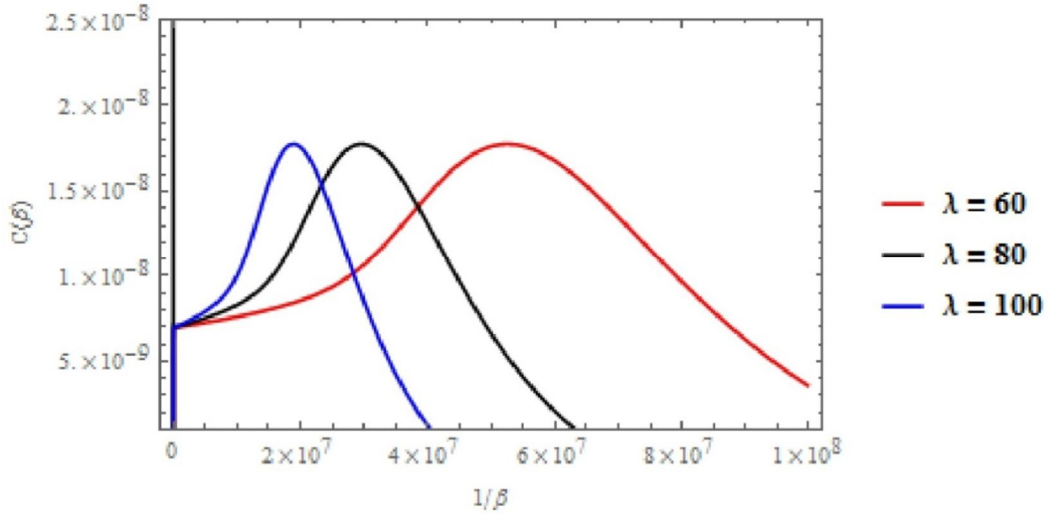

FIG. 5. Vibrational specific heat capacity $C(cm^{-1}K^{-1})$ versus $\frac{1}{\beta}(K)$ for different values of λ.

4. The Vibrational Entropy S:

$$S = k_b\beta^2\frac{\partial}{\partial\beta}F = \beta^2 k_b\left(\frac{\log\left(\frac{1}{2}\sqrt{b\beta}\left(2\sqrt{\pi}\left(\operatorname{erfi}\left(\frac{\sqrt{b\beta}}{\lambda}\right)+1\right)-\frac{2\lambda e^{\frac{b\beta}{\lambda^2}}}{\sqrt{b\beta}}\right)e^{\beta\left(c+P(\omega-n)^2\right)}\right)}{\beta^2}\right)$$

$$-\beta^2 k_b\left(\frac{2e^{-\beta(c+P(\omega-n)^2)}\left(\frac{b(2\sqrt{\pi}(\operatorname{erfi}(\frac{\sqrt{b\beta}}{\lambda})+1)-\frac{2\lambda e^{\frac{b\beta}{\lambda^2}}}{\sqrt{b\beta}})e^{\beta(c+P(\omega-n)^2)}}{4\sqrt{b\beta}}\right)}{\beta\sqrt{b\beta}(2\sqrt{\pi}(\operatorname{erfi}(\frac{\sqrt{b\beta}}{\lambda})+1)-\frac{2\lambda e^{\frac{b\beta}{\lambda^2}}}{\sqrt{b\beta}})}\right)$$

$$+\beta^2 k_b\left(\frac{2e^{-\beta(c+P(\omega-n)^2)}\left(\frac{1}{2}\sqrt{b\beta}(2\sqrt{\pi}(\operatorname{erfi}(\frac{\sqrt{b\beta}}{\lambda})+1)-\frac{2\lambda e^{\frac{b\beta}{\lambda^2}}}{\sqrt{b\beta}})(c+P(\omega-n)^2)e^{\beta(c+P(\omega-n)^2)}+\frac{\lambda e^{\frac{b\beta}{\lambda^2}+\beta(c+P(\omega-n)^2)}}{2\beta}\right)}{\beta\sqrt{b\beta}(2\sqrt{\pi}(\operatorname{erfi}(\frac{\sqrt{b\beta}}{\lambda})+1)-\frac{2\lambda e^{\frac{b\beta}{\lambda^2}}}{\sqrt{b\beta}})}\right)$$

(29)

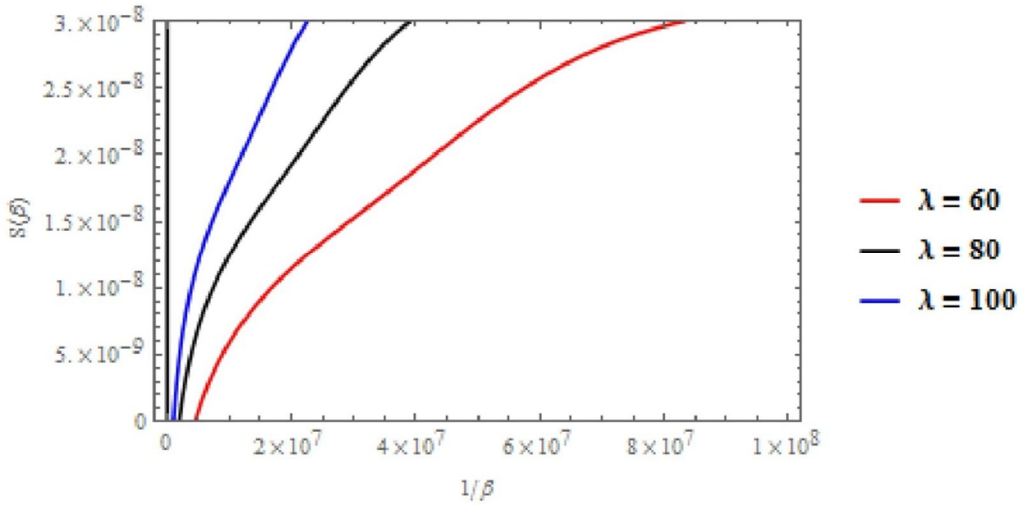

FIG. 6. Vibrational entropy $S(cm^{-1}K^{-1})$ versus $\frac{1}{\beta}(K)$ for different values of λ.

The study focused on the Woods-Saxon potential, with energy states calculated first, followed by the determination of the vibrational partition function at high temperatures. From this, various thermodynamic properties were derived using specific values for parameters including $\hbar = 6.582119 \times 10^{-16}\, eV.s$, $k_b = 8.6177 \times 10^{-5}\frac{eV}{K}$, $m = 51amu$, $V_0 = 2300Mev$, $R = 1.285fm$, $1cm = 1.2398 \times 10^{-4}eV$, and $a = 0.65fm$. Figure 1 displays the relationship between energy states and temperature for different l values. This figure illustrates that the energy spectrum approaches zero as n values increase. The second figure, labeled as Fig. 2, demonstrates that the vibrational partition function of the Woods-Saxon potential drps considerably after $\frac{1}{\beta} = 1 \times 10^8$ for all values of λ. This partition function serves as a foundation for evaluating a range of thermodynamic properties. Another figure, Fig. 3, displays the alteration of the vibrational free energy of the Woods-Saxon potential. Additionally, the internal energy of the potential is linear across all λ values until $\frac{1}{\beta} = 4 \times 10^7$, which matches the vibrational specific heat capacity in Fig. 5. In Fig. 4, the vibrational mean free energy decreases with temperature until it reaches a minimum value. Figure 5 shows that the vibrational specific heat capacity rises as temperature increases until it reaches a peak and then has a concave ascent until it reaches saturation. Finally, Fig. 6 displays the vibrational entropy for the Woods-Saxon potential. At low temperatures, the entropy is small, but it approaches infinity at very high temperatures.

Conclusion

Using the factorization method, the Schrödinger equation for the standard Woods-Saxon potential was solved, yielding eigenvalues and corresponding eigenfunctions in terms of hypergeometric functions. The results were found to agree perfectly with previous studies. In addition, the thermodynamic properties of the system were analyzed, including vibrational mean energy, vibrational free energy, vibrational specific heat capacity, and vibrational entropy. These properties were determined using the high-temperature vibrational partition function and were obtained within the classical limit. The behaviors of all the thermodynamic functions are presented through various plots.

References

[1] Woods, R.D. and Saxon, D.S., Phys. Rev., 95 (1954) 577.

[2] Schrödinger, E., Ann. Phys., 385 (1926) 437.

[3] Schrödinger, E., Ann. Phys., 384 (1926) 489.

[4] Oyewumi, K.D., J. Math. Chem., 50 (2012) 1039.

[5] Mir-Kasimov, R.M., Phys. Part. Nuclei, 44, (2013) 422.

[6] Pahlavani, H.R.M. and Ghezelbash, M., J. Microphys., 3 (2013) 1.

[7] Ikhdair, S.M., Falaye, B.J., and Hamzavi, M., Chin. Phys. Lett., 30 (2013) 020305.

[8] Ciftci, H., Hall, R.L., and Saad, N., J. Phys. A: Math. Gen., 36 (2003) 11807.

[9] Falaye, B.J., Hamzavi, M., and Ikhdair, S.M., Chin. Phys. Lett., 30 (2013) 020305.

[10] Ikot, A.N., Obong, H.P., Abbey, T.M., Zare, S., Ghafourian, M., and Hassanabadi, H., Few-Body Syst., 57 (2016) 807.

[11] Liang, H., Shen, S., Zhao, P., and Meng, J., Phys. Rev., C87 (2013) 014334.

[12] Jia, Y., Eur. Phys. J. D, 71 (2017) 3.

[13] Kumar, P.R. and Wong, B.R., AIP Conf. Proc., 1657 (2015) 160001.

[14] Badalov, V.H., Ahmadov, H.I., and Ahmadov, A.I., Int. J. Mod. Phys. E, 18 (2009) 631.

[15] Berkdemir, C., Berkdemir, A., and Sever, R., Phys. Rev., C72 (2005) 027001.

[16] Lütfüoğlu, B.C., Eur. Phys. J. Plus, 133 (2018) 309.

[17] Lütfüoğlu, B.C., Commun. Theor. Phys., 69 (2018) 23.

[18] Lütfüoğlu, B.C., Commun. Theor. Phys., 71 (2019) 267.

[19] Lütfüoğlu, B.C., Can. J. Phys., 96 (2018) 843.

[20] Lütfüoğlu, B.C., Lipovský, J., and Kříž, J., Eur. Phys. J. Plus, 133 (2018) 17.

[21] Lütfüoğlu, B. C., Akdeniz, F., and Bayrak, O., J. Math. Phys., 57 (2016) 032103.

[22] Pacheco, M.H., Landim, R.R., and Almeida, C.A.S., Phys. Lett., A311 (2003) 93.

[23] Pacheco, M.H., Maluf, R.V., Almeida, C.A.S., and Landim, R.R., EPL, 108 (2014) 10005.

[24] Yahya, W.A. and Oyewumi, K.J., J. Assoc. Arab Univ. Basic Appl. Sci., 21 (2016) 53.

Volume 17, Number 4, 2024. pp. 403-410

Jordan Journal of Physics

ARTICLE

The Many-Worlds Interpretation versus the Copenhagen Interpretation: A Case Discussion with the Hydrogen Atom

Rabah Ladj[a], **Nour El Houda Bensiradj**[b,c] and **Salah Eddine Aid**[d]

[a] *School of Physics, Education of Sciences and Mathematical Laboratory, E. N. S., Kouba, Algiers, Algeria.*

[b] *Computational and Photonic Theoretical Chemistry Laboratory, Faculty of Chemistry, USTHB BP32, 16111 El Alia, Algiers, Algeria.*

[a] *Laboratoire, N–corps & Structure de la Matière, Département Sciences Physiques, E. N. S., Kouba. Alge, Algeriar.*

[b] *Post Graduate Student, School of Physics, E. N. S., Kouba, Algiers, Algeria.*

Doi: **https://doi.org/10.47011/17.4.3**

Received on: 19/12/2022; *Accepted on: 18/05/2023*

Abstract: The main objective of this work is to compare the interpretations of the hydrogen atom spectrum according to two famous schools in quantum mechanics: Copenhagen and many-worlds. The Schrodinger equation is solved using the many-worlds interpretation, and the results are then compared to those obtained using the Copenhagen interpretation. While the energy spectra are similar in both cases, the interpretations of these results differ. In the many-worlds interpretation, the eigenvectors are entangled across multiple worlds, whereas, in the Copenhagen interpretation, they are superimposed. The hydrogen atom, being a system of only one electron and without electron-electron interaction, serves as a clear and accessible example for comparing these interpretations. In this case, the wave function depends on independent coordinates and is written as a tensor product of independent functions, even before solving the Schrödinger equation. In more complex systems where there are electron-electron, electron-nucleus, nucleus-nucleus, and other interactions, the wave function should be written as a tensor product of entangled states after solving the Schrodinger equation. The aim of this study is to demonstrate to physics and chemistry teachers and students that there are different ways to view the quantum world. The many-worlds interpretation is simply another way of interpreting the solutions of the Schrodinger equation, rather than a new mathematical approach. The present work emphasizes the importance of understanding different interpretations of quantum mechanics and their implications for understanding the physical world.

Keywords: Hydrogen atom spectrum, Schrodinger equation, Copenhagen school, Many-worlds interpretation.

1. Introduction

The meaning of quantum mechanics, both in concept and description, has been the subject of various interpretations, leading to debates between different schools of thought. Although the exact number of interpretations is not precisely defined, there are about sixteen commonly discussed schools of interpretation. Hugh Everett proposed the many-worlds interpretation in 1957, suggesting the existence of multiple parallel universes. This interpretation is universally considered the second most significant interpretation and has received

Corresponding Author: Nour El Houda Bensiradj **Email**: nourelhouda.bensiradj@gmail.com

support from notable physicists and philosophers, including Nobel Prize laureates Stephen Hawking, Murray Gell-Mann, and Richard Feynman.

According to Everett's concept, the universe branches into multiple copies, each corresponding to a different possible outcome of that measurement. These branches, or "worlds", exist independently and are not directly observable or accessible to one another [1]. In the many-worlds interpretation, the universe consists of multiple worlds. Each world follows deterministic and reversible laws, with no non-deterministic or irreversible wavefunction. Consequently, there is no collapse of wave functions associated with scaling [2]. Everett considered the wavefunction to be a real entity, suggesting that all possible outcomes of a quantum measurement exist as separate branches or parallel universes. This interpretation can be seen as a departure from the traditional collapse of the wavefunction and a return to a view where all mathematical entities in a physical theory are considered real [3]. Similar to how Maxwell's electromagnetic fields and Dalton's atoms were treated in classical physics, Everett treated the wavefunction as a real object. He assumed that the wavefunction obeyed the same equation during observation as it did at all other times [4].

In the Everett interpretation, quantum systems, such as particles, become entangled when they interact. According to this interpretation, any system can be considered an observer, and when it interacts with another system, it effectively performs a measurement or observation. As a result of this interaction, the observer system and the observed system split into multiple copies or branches. Each branch corresponds to one of the possible outcomes of the measurement, and each copy of the observer perceives only one specific outcome while remaining unaware of the other possible outcomes [1].

Interactions between systems and their environments lead to communication between observers. This communication transmits correlations and induces the splitting, or decoherence, of the universal wavefunction into multiple branches. These branches represent equally real but mutually unobservable worlds. Unlike in other interpretations, the wavefunction does not collapse at the moment of observation. Instead, it continues to evolve deterministically, encompassing all possibilities within it [5]. The outcomes exist simultaneously but do not interfere further with each other; every single prior world has split into mutually unobservable but equally real worlds.

Everett demonstrated that once there is a possibility that an object is in any state, the universe of that object transforms into a series of parallel universes equal to the number of possible states in which this object can exist, each universe containing a single possible state of this object. It should be noted that Everett was not entirely comfortable with talking about “many worlds”; it seemed less important to him how this language described pure wave mechanics. Rather, his emphasis was on the empirical understanding and cognitive implications of his theory [6].

Several recent works on Everett’s interpretation, viewed as a realist interpretation of quantum formalism, highlight how it can benefit from advances in the metaphysics of dispositions [7], removing action at a distance and randomness from quantum theory [8]. There is also a work on the discussion of the possibility of multiverses beyond the universe we live in and the alternatives to the multi-world interpretation, as proposed by Christianto *et al*. [9].

The Copenhagen interpretation, developed by Bohr [10] and Heisenberg [11] is the most famous interpretation of quantum mechanics, which is still used and followed in the teaching of quantum mechanics worldwide. However, it is not a deterministic interpretation. Despite the preponderance of the Copenhagen reading of quantum phenomena, numerous questions concerning the interpretation of quantum mechanics continue to be the subject of energetic debates, affirming that its fundamental basis is far from being definitively settled [12].

The Copenhagen interpretation proposed by Bohr *et al*. is based on a dualistic core idea: the description of the microscopic world by quantum mechanics must be supplemented by an external classical world, which causes the wave packet collapse [13]. However, Albert Einstein and Erwin Schrodinger did not agree with the Copenhagen school [14].

Currently, many physicists find quantum theory to be full of contradictions and paradoxes that are difficult to resolve consistently. The

disagreement focuses primarily on the problem of describing observations [9]. This leads to the question of what happens when quantum theory is applied unrestrictedly to the entire universe. Some argue that if we allow unlimited application of Schrödinger's equation, assuming the quantum state is something physically real, contradictions may arise.

In this context, our original work is based on the discussion of the hydrogen atom's spectrum treated according to two famous schools: the many-worlds interpretation and the Copenhagen interpretation. Before proceeding with this research, it is important to note that the key difference between these schools lies in how they interpret measurement results. Therefore, we would like to recall some important definitions from algebra, which are necessary to clarify this work.

2. Measurements

Measurements in general are a "function" of application, between observers and observables, in order to determine a certain physical quantity of the observable, such as its position, its momentum, its energy, etc.

2.1 Functions

A function is defined as a relation "application", that assigns each element of group "A" to only one element of group "B". Both sets "A" and "B" must be non-empty. Thus, "f: A → B" is a function of this type; for each element $a_i \in A$, there is a unique corresponding " image" element $b \in B$ [15].

2.2 Types of Functions:

a) Subjective Function

It is a function that assigns two or more elements of "A" to the same element of set "B". The elements of "A" have the same figure in the other set. So for every b_i in the set "B", there is at least one "a_i" in the set "A" [15].

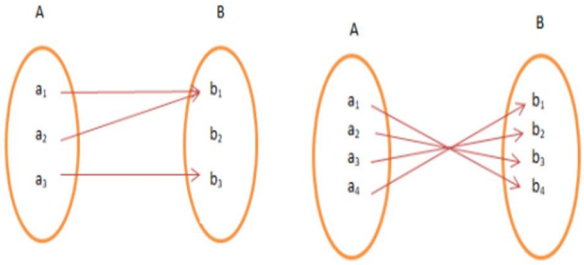

FIG. 1. Sets A and B.

b) Bijective Function

A function f is bijective if it links each element of "A" with a distinct element of "B" and each element of "B" has a pre-image in "A". In other words, for every "b_i" in set "B" there is exactly one "a_i" in set "A" [15]. In measurement, there is no meaning to many observers to observe or measure just one observable.

Now. we present the corresponding physical meanings of the mathematical definitions above. The measurement process is a relational process, or "application", that connects the group of observers "B" to the set of observables, set "A". In the quantum case, set "B" represents the different set of observes, $\{\widehat{H_i}\}$, where $\{\widehat{H_i}\}$ represents the Hamiltonian or energy operators in set "B"; its role is to measure its eigenvalues a_i in set "A".

In the Copenhagen interpretation, Bohr and his team considered that there is just one observer, $\widehat{H}$, in set "B" that observes various observables, $\{a_i\}$, in set "A", using a set of eigenfunctions that are "not necessary parallel". Conversely, in the many-worlds interpretation, it is assumed that multiple observes, ", depending on the existing potential, $\widehat{H_i}$ in set "B", "each observer observes just one observable", $\{a_i\}$, in set "A" using a different set of eigenfunctions, "which should be parallel".

In conclusion, in the Copenhagen school, the relationship between observers and observables is subjective, while in the many-worlds interpretation, this relationship is bijective.

Everett's view Copenhagen's view

FIG. 2. Everett's and Copenhagen's view.

3. Solving and Interpreting Schrodinger Equation for the Hydrogen Atom, According to the Many-Worlds Interpretation.

Before starting, we would like to present a summary of our modest modeling of entangled states according to the many-worlds interpretation [16]. Once there is a possibility of an object being in any state, the universe of that object turns or splits into a series of parallel "branched" universes equal to the number of possible states where the object can exist. Each universe contains one possible unique state for that object [1]. We symbolize the universe by $|\Psi\rangle$, and because of the parallel states, we write:

$$|\Psi\rangle = |\psi_1\rangle \otimes |\psi_2\rangle \ldots\ldots\ldots \otimes |\psi_n\rangle$$
$$|\Psi\rangle = \prod_{j=1}^{n\geq 2} |\psi_j\rangle \otimes |\psi_{j+1}\rangle, \quad j(\leq n) \qquad (1)$$

Parallel universes imply no interference (superposition) between them. Because of this, no information is exchanged between the states. Therefore, the universal wave function that describes the universal world is a tensor product of states or worlds.

When a measurement is taken in universe $|\Psi\rangle = \prod_{j=1}^{n\geq 2} |\psi_j\rangle \otimes |\psi_{j+1}\rangle$ using an observer, represented by an operator $\hat{A}_i$, this operator acts on $|\Psi\rangle$, measuring only its corresponding eigenvalue λ_i, and so on, for other observers $\hat{A}_k$, $k = 1,2,.. \neq i$. Each observer measures its specific eigenvalue $\lambda_k \neq \lambda_i$. The measurement operation for a single observer, $\hat{A}_j$, acting on $|\Psi\rangle$, is as follows:

$$\hat{A}_j \prod_{j=1}^{n} |\psi_j\rangle \otimes |\psi_{j+1}\rangle = \lambda_i \prod_{j=1}^{n} |\psi_j\rangle \otimes |\psi_{j+1}\rangle$$

The expectation value $\langle \hat{A}_j \rangle$ is given by $\Rightarrow$ (2)

$$\left\{\prod_{j=1}^{n} \langle \psi_{j+1}| \otimes \langle \psi_j| \right\} \hat{A}_j \left\{\prod_{j=1}^{n} |\psi_j\rangle \otimes |\psi_{j+1}\rangle\right\} = \lambda_j.$$

The normalisation of $|\Psi\rangle$ gives:

$$\langle\Psi|\Psi\rangle = 1 \Rightarrow \langle\psi_i|\psi_j\rangle = \delta_{i,j}$$

When measurements are taken by all observers ($\sum_{j=1}^{n} \hat{A}_j$), each observer $\hat{A}_j$ measures only its correspondent eigenvalue λ_j in its own world $|\psi_j\rangle$. Due to the parallel nature of these worlds, "there is no superposition of states". The general form of the universe $|\Psi\rangle$ as a function of all single universes $|\psi_j\rangle$ can be expressed as:

$$|\Psi\rangle = \prod_{j\neq i}^{n\geq 2} \sum_{i=1}^{n\geq 2} (-1)^{i-1} \alpha_i \alpha_j |\psi_i\rangle \otimes |\psi_j\rangle. \qquad (3)$$

The factor $(-1)^{i-1}$ is due to the mirroring (reflection) property.

In $\alpha_i \alpha_j |\psi_i\rangle \otimes |\psi_j\rangle \neq \alpha_i |\psi_i\rangle \otimes \alpha_j |\psi_j\rangle$, the first part, $\alpha_i \alpha_j |\psi_i\rangle \otimes |\psi_j\rangle$, indicates entangled states, while the second one, $\alpha_i |\psi_i\rangle \otimes \alpha_j |\psi_j\rangle$, refers to separated states. The coefficient $\alpha_{j,j+1}$ represents the entanglement factor. Since the universe, represented by the wave function $|\Psi\rangle$, is normalized to unity, we write:

$$\begin{aligned}\langle\Psi|\Psi\rangle &= \int_{-\infty}^{+\infty} \Psi^{*}\Psi\, dv = 1 \\ &= \prod_{j\neq i}^{n\geq 2} \sum_{i=1}^{n\geq 2} (-)^{i-1} |\alpha_i|^2 |\alpha_j|^2 = 1 \\ & i = 0,1,.....n\end{aligned} \quad . \tag{4}$$

where the entanglement factor $\alpha_i\, \alpha_{j,} = \sqrt{\frac{1}{n}}$.

All the wave functions are real and reversible, with no wave collapse and no eigenvalue degeneration. Due to state entanglement, once any observer measures its eigenvalue in its state, all other eigenvalues of the other states are instantly known, even though there is no exchange of information between them. As a result, the Hilbert space is constructed from the tensor product of vector states.

Application to the Hydrogen Atom Case

Our aim is to apply the many-worlds interpretation to solve the stationary Schrodinger equation for the hydrogen atom.

$$\hat{H}|\Psi\rangle = E|\Psi\rangle$$

The above equation in the hydrogen atom case, "independent coordinates", will take the following form under the many-worlds interpretation:

$$\hat{H}_i|\Psi\rangle = E_i|\Psi\rangle \tag{5}$$

The observer $\hat{H}_i$ in the entangled states can observe only its eigenvalue E_i on the world or branch $|\psi_i\rangle$. As previously discussed, Everett believed that the electron of the hydrogen atom, if it has the potential to exist in multiple states, will have its initial state divided into many other states, ($|\psi_1\rangle$, $|\psi_2\rangle$, $|\psi_3\rangle$,....). Each state $|\psi_i\rangle$ is composed of many other states, which we call "orbits", *(S_i, P_i, d_i...),* with each orbit containing a single electron copy.

Therefore, in the hydrogen atom case, we can write the state $|\psi\rangle$ as a tensor product of its different states or branches, even before solving the Schrodinger equation, as follows:

$$|\Psi\rangle = |\psi_1\rangle \otimes |\psi_2\rangle \otimes .... \otimes |\psi_i\rangle \otimes ..... \otimes |\psi_n\rangle \tag{6}$$

where $\hat{H}_i = -\frac{\hbar^2}{2m}\nabla^2 + V(r)$, and $V(r) = \frac{-q^2}{4\pi\varepsilon_0 r}$ is the potential due to the single hydrogen proton in the hydrogen nucleus at a distance r (considering the nucleus to be static). The observer (operator) $\hat{H}_i$ within $|\psi_i\rangle$ measures only the observable E_i. Consequently, Eqs. (1) and (5) are rewritten in the following form:

$$\begin{aligned}&\left\{-\frac{\hbar^2}{2m}\nabla^2 + \frac{-q^2}{4\pi\varepsilon_0 r}\right\}(|\psi_i\rangle \otimes |\psi_{i+1}\rangle) \\ &\otimes \left[\prod_{j=1}^{n} |\psi_j\rangle \otimes |\psi_{j+1}\rangle\right] \\ &= E_i(|\psi_i\rangle \otimes |\psi_{i+1}\rangle) \otimes \\ &\left[\prod_{j=1}^{n} |\psi_j\rangle \otimes |\psi_{j+1}\rangle\right] \quad j \neq i\end{aligned} \quad . \tag{7}$$

Since there is no superposition between states (referred to as "parallel states"), the above equation, after subtraction the term

$$|\psi_{i+1}\rangle \otimes \left[\prod_{j=1}^{n} |\psi_j\rangle \otimes |\psi_{j+1}\rangle\right]$$

takes the following form on both sides:

$$\left\{-\frac{\hbar^2}{2m}\nabla^2 + \frac{-q^2}{4\pi\varepsilon_0 r}\right\}|\psi_i\rangle = E_i|\psi_i\rangle \tag{8}$$

That means that observer $\hat{H}_i$ measures only the observable E_i on its state $|\psi_i\rangle$, which is entangled with other possible states:

$$\left[\prod_{j=1}^{n} |\psi_j\rangle \otimes |\psi_{j+1}\rangle\right] \quad i \neq j\,. \tag{9}$$

Note that Eq. (8) is the same as in the Copenhagen interpretation.

Because the hydrogen electron moves around the nucleus in different positions $\vec{r}_i$, we rewrite Eq. (8) using spherical coordinates as follows:

$$\begin{aligned}&-\frac{\hbar^2}{2m_e}\left[\frac{1}{r^2}\frac{\partial}{\partial r}\left(r^2\frac{\partial\psi_i}{\partial r}\right) + \frac{1}{r^2\sin\theta}\frac{\partial}{\partial\theta}\left(\sin\theta\frac{\partial\psi_i}{\partial\theta}\right) + \right. \\ &\left.\frac{1}{r^2(\sin\theta)^2}\frac{\partial^2\psi_i}{\partial^2\phi}\right] - \frac{e^2}{4\pi\varepsilon_0 r}\psi_i = E\psi_i\end{aligned} \tag{10}$$

The solutions to this equation in the Copenhagen interpretation are:

$$\psi_{ilm}(\vec{r},\theta,\varphi) = R_i(r)Y_{lm}(\theta,\varphi)$$

$$E_i = -\frac{me^4}{32\pi^2\varepsilon_0^2\hbar^2}.\frac{1}{i^2}(i = 1; 2; ..i \ldots; n) \qquad (11)$$

According to the many-worlds interpretation, each world « i » is described by the following wave function:

$$\psi_{ilm}(\vec{r},\theta,\varphi) = R_i(r)Y_{lm}(\theta,\varphi) \otimes \left[\prod_{j=1}^{n} \mathrm{R_j\ (r)Y_{lm}}(\theta,\phi) \otimes \mathrm{R_{j+1}\ (r)Y_{lm}}(\theta,\phi)\right] \quad j \neq i \qquad (12)$$

The combined wave function for all "worlds," representing all observers, is given by:

$$|\Psi\rangle = \prod_{j\neq i}^{n\geq 2} \sum_{i=1}^{n\geq 2} (\pm)^{i-1}\alpha_i\alpha_j\, |\psi_{ilm}(r,\theta,\phi)\rangle_i \otimes |\psi_{ilm}(r,\theta,\phi)\rangle_j \qquad (13)$$

4. Results and Interpretations According to the Many-Worlds School

The energy and its correspondent world are defined as:

$$E_i = -\frac{me^4}{32\pi^2\varepsilon_0^2\hbar^2}.\frac{1}{i^2}(i = 1; 2; ..i \ldots; n) \qquad (14)$$

$$\psi_{ilm}(\vec{r},\theta,\varphi) = R_i(r)Y_{lm}(\theta,\varphi) \otimes \left[\prod_{j=1}^{n} \mathrm{R_j\ (r)Y_{lm}}(\theta,\phi) \otimes \mathrm{R_{j+1}\ (r)Y_{lm}}(\theta,\phi)\right] \quad j \neq i \qquad (15)$$

This can be interpreted as follows: the observer in the world $\psi_{ilm}(\vec{r},\theta,\varphi)$, which is entangled with all the other possible worlds (states), notices or measures the energy:

$$E_i = -\frac{me^4}{32\pi^2\varepsilon_0^2\hbar^2}.\frac{1}{i^2}. \qquad (14)$$

To clarify how many worlds are interpreted, we assume that the hydrogen electron has the possibility to be in sp^3 worlds or orbits. In this case, the hydrogen electron simultaneously exists in $s,\ p_x,\ p_y,\ and\ p_z$ states without probability, contrasting with the Copenhagen interpretation. So, the observer in the s-world, which is entangled with the $p_x,\ p_y, and\ p_z$ worlds measures the energy:

$$E_{s1} = -\frac{mZ^2e^4}{32\pi^2\varepsilon_0^2\hbar^2}.\frac{1}{1^2} = -13.6\ eV\ ,$$

while its world expression is:

$$\psi_{1,0,0} = R_{1,0}(r)Y_{0,0}(\theta,\varphi) \otimes R_{2,0}(r)Y_{0,0}(\theta,\varphi) \otimes R_{2,1}(r)Y_{1,1}(\theta,\varphi) \otimes R_{2,1}(r)Y_{1,-1}(\theta,\varphi) \otimes R_{2,1}(r)Y_{1,0}(\theta,\varphi)$$

$$= 2\left(\frac{1}{a_0}\right)^{3/2}\exp\left(-\frac{r}{a_0}\right)Y_{0,0} \otimes \left(\frac{1}{2a_0}\right)^{\frac{3}{2}}\left(2 - \frac{r}{a_0}\right).\exp\left(-\frac{r}{2a_0}\right)Y_{0,0} \otimes \left(\frac{1}{2a_0}\right)^{\frac{3}{2}}\frac{r}{\sqrt{3}a_0}\exp\left(-\frac{r}{2a_0}\right)Y_{1,1}(\theta,\varphi) \otimes \left(\frac{1}{2a_0}\right)^{\frac{3}{2}}\frac{r}{\sqrt{3}a_0}\exp\left(-\frac{r}{2a_0}\right)Y_{1,-1}(\theta,\varphi) \otimes \left(\frac{1}{2a_0}\right)^{\frac{3}{2}}\frac{r}{\sqrt{3}a_0}\exp\left(-\frac{r}{2a_0}\right)Y_{1,0}(\theta,\varphi). \qquad (16)$$

Observers in the worlds $(s_2, p_x,\ p_y,\ p_z)$ measure the same energy:

$$E_{s2} = E_{p_x} = E_{p_y} = E_{p_z} = -\frac{mZ^2e^4}{32\pi^2\varepsilon_0^2\hbar^2}.\frac{1}{2^2} = -3.4\ eV$$

Their mathematical representations are as follows:

$$\psi_{2,0,0} = \left(\frac{1}{2a_0}\right)^{\frac{3}{2}}\left(2 - \frac{r}{a_0}\right).\exp\left(-\frac{r}{2a_0}\right)Y_{0,0} \otimes \left(\frac{1}{2a_0}\right)^{\frac{3}{2}}\frac{r}{\sqrt{3}a_0}\exp\left(-\frac{r}{2a_0}\right)Y_{1,1}(\theta,\varphi) \otimes \left(\frac{1}{2a_0}\right)^{\frac{3}{2}}\frac{r}{\sqrt{3}a_0}\exp\left(-\frac{r}{2a_0}\right)Y_{1,-1}(\theta,\varphi) \otimes \left(\frac{1}{2a_0}\right)^{\frac{3}{2}}\frac{r}{\sqrt{3}a_0}\exp\left(-\frac{r}{2a_0}\right)Y_{1,0}(\theta,\varphi) \otimes 2\left(\frac{1}{a_0}\right)^{3/2}\exp\left(-\frac{r}{a_0}\right)Y_{0,0}$$

$$\psi_{2,1,1} = \left(\frac{1}{2a_0}\right)^{\frac{3}{2}}\frac{r}{\sqrt{3}a_0}\exp\left(-\frac{r}{2a_0}\right)Y_{1,1}(\theta,\varphi) \otimes \left(\frac{1}{2a_0}\right)^{\frac{3}{2}}\frac{r}{\sqrt{3}a_0}\exp\left(-\frac{r}{2a_0}\right)Y_{1,-1}(\theta,\varphi) \otimes \left(\frac{1}{2a_0}\right)^{\frac{3}{2}}\frac{r}{\sqrt{3}a_0}\exp\left(-\frac{r}{2a_0}\right)Y_{1,0}(\theta,\varphi) \otimes \left(\frac{1}{2a_0}\right)^{\frac{3}{2}}\left(2 - \frac{r}{a_0}\right).\exp\left(-\frac{r}{2a_0}\right)Y_{0,0} \otimes 2\left(\frac{1}{a_0}\right)^{3/2}\exp\left(-\frac{r}{a_0}\right)Y_{0,0}$$

$$\psi_{2,1,-1} = \left(\frac{1}{2a_0}\right)^{\frac{3}{2}}\frac{r}{\sqrt{3}a_0}\exp\left(-\frac{r}{2a_0}\right)Y_{1,-1}(\theta,\varphi) \otimes \left(\frac{1}{2a_0}\right)^{\frac{3}{2}}\frac{r}{\sqrt{3}a_0}\exp\left(-\frac{r}{2a_0}\right)Y_{1,1}(\theta,\varphi) \otimes \left(\frac{1}{2a_0}\right)^{\frac{3}{2}}\frac{r}{\sqrt{3}a_0}\exp\left(-\frac{r}{2a_0}\right)Y_{1,0}(\theta,\varphi) \otimes \left(\frac{1}{2a_0}\right)^{\frac{3}{2}}\left(2 - \frac{r}{a_0}\right).\exp\left(-\frac{r}{2a_0}\right)Y_{0,0} \otimes 2\left(\frac{1}{a_0}\right)^{3/2}\exp\left(-\frac{r}{a_0}\right)Y_{0,0}$$

$$\psi_{2,,1,0} = \left(\frac{1}{2a_0}\right)^{\frac{3}{2}} \frac{r}{\sqrt{3}a_0} \exp\left(-\frac{r}{2a_0}\right) Y_{1,0}(\theta,\varphi) \otimes \left(\frac{1}{2a_0}\right)^{\frac{3}{2}} \frac{r}{\sqrt{3}a_0} \exp\left(-\frac{r}{2a_0}\right) Y_{1,1}(\theta,\varphi) \otimes \left(\frac{1}{2a_0}\right)^{\frac{3}{2}} \frac{r}{\sqrt{3}a_0} \exp\left(-\frac{r}{2a_0}\right) Y_{1,-1}(\theta,\varphi) \otimes \left(\frac{1}{2a_0}\right)^{\frac{3}{2}} \left(2-\frac{r}{a_0}\right).\exp\left(-\frac{r}{2a_0}\right) Y_{0,0} \otimes 2\left(\frac{1}{a_0}\right)^{3/2} \exp\left(-\frac{r}{a_0}\right) Y_{0,0} \quad (17)$$

The wave function describing the entirety of these worlds is:

$$|\Psi\rangle = \sqrt{\frac{1}{5}}\ \psi_{1,0,0} - \sqrt{\frac{1}{5}}\ \psi_{2,0,0} + \sqrt{\frac{1}{5}}\ \psi_{2,1,1} - \sqrt{\frac{1}{5}}\ \psi_{2,1,-1} + \sqrt{\frac{1}{5}}\ \psi_{2,,1,0}$$

The results indicate that when the hydrogen electron of $|\Psi_{1,0,0}\rangle$ world, or $|s\rangle$, has the potential to be in other states (for example, in the $|sp^3\rangle$ worlds), the initial world $|s\rangle$ splits into $|sp^3\rangle$ worlds. Each $|sp^3\rangle$ world contains a copy of the electron, and each observer in each state measures only the energy corresponding to their respective state (see the figure below).

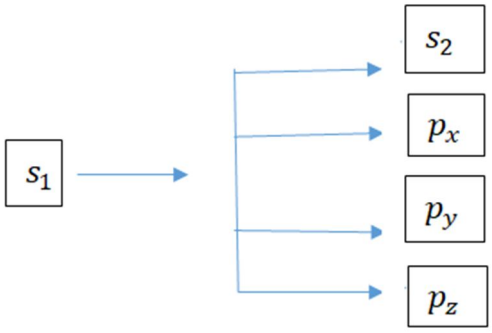

FIG. 3. Electron states.

According to the Copenhagen school, the general wave function is represented by the following relation:

$$\Psi(r,\theta,\varphi) = \sum_{n,l,m} c_{n,l,m}\psi_{n,lm}(r,\theta,\varphi); where,$$

$$c_{n,l,m} = \langle \Psi(r,\theta,\varphi) | \psi_{n,l,m}(r,\theta,\varphi) \rangle,$$

$$and\ |c_{nl,m}|^2\ present\ the\ probability$$

$$E_n = -\frac{m_e Z^2 e^4}{8\varepsilon_0^2 h^2 n^2}, \quad n = 1,2,...i....$$

The results mean that before any measurement, the hydrogen electron, as observed by a single observer, exists in a superposition of all possible states, represented by a combination of wave functions. This concept is discussed in the works of Held [17] and Saxon [18]

$$\Psi(r,\theta,\varphi) = \sum_{n,l,m} c_{n,l,m}\psi_{n,lm}(r,\theta,\varphi), \quad n = 1,2,...i...,.$$

Upon measurement by the observer, the general wave function, $\Psi(r,\theta,\varphi) = \sum_{n,l,m} c_{n,l,m}\psi_{n,lm}(r,\theta,\varphi)$, collapses into a single state:

$$\psi_{i,l,m}(r,\theta,\varphi). \quad (18)$$

5. Conclusion

In classical mechanics, the determinism principle implies that the observer's presence does not affect the observables; measurements in classical physics are deterministic.

However, many interpretation schools have emerged in quantum mechanics, some fundamentally differing from classical mechanics' determinism.

The Copenhagen interpretation, one of the most influential schools, is based on the indeterminism principle. It does not require an observer-induced wave packet collapse, nor does it prioritize the observer's perspective, rejecting ideas of subjectivism and positivism in measurement.

Conversely, deterministic schools such as Hugh Everett's "many-worlds interpretation" hold that quantum mechanics follows a deterministic framework similar to classical mechanics. According to the many-worlds interpretation, there is no action at a distance. Instead, this theory gives a set of local descriptions that wholly describe the entire physical universe. It provides metaphysical neutrality between observers' perspectives on different branches of the universal wave function, as opposed to one-world theories that give a privileged perspective on reality to an observer.

Many students have no idea about these different interpretations at the microscopic scale

and cannot explain why some interpretations are deterministic while others are not.

This paper aims to explore these two interpretations in the context of the hydrogen atom's spectrum. By solving the Schrödinger equation under the many-worlds interpretation, our results are compared to those derived from the Copenhagen interpretation. Our findings underscore the mathematical viability of the deterministic school in explaining quantum mechanics because it resolves most paradoxes like the collapse of the quantum wave.

Finally, the many-worlds interpretation presents itself as a reasonable interpretation of quantum mechanics. However, it is necessary to work on the problem of probability and consider modifications to the standard theory.

Compliance with ethical standards

Conflict of interest

The authors declare that they have no conflict of interest.

References

[1] Everett, H., Rev. Mod. Phys., 29 (1957) 254.

[2] Griffiths, R. B., "Consistent Quantum Theory", (Cambridge University Press, 2003), pp. 201-219.

[3] Kent, A., "One World Versus Many: The Inadequacy of Everettian Accounts of Evolution, Probability and Scientific Confirmation", In: Saunders et al. (2010), 307–54.

[4] Duwel, A., Philos. Sci., 74 (2009) 1007.

[5] Bradley, D. J. Brit. J. Philos. Sci., 62 (2011) 323.

[6] Barrett, J. A.. Eur. J. Philos. Sci., 1 (2011) 277.

[7] Boge, F. J., Stud. Hist. Philos. Sci. B, 66 (2019) 135.

[8] Vaidman, L., Quantum Rep., 4 (2022) 264.

[9] Christianto, V., Sci. GOD J., 9 (6) (2018) 435.

[10] Bohr, N., Philos. Mag. Ser. 6, 26 (1913) 1.

[11] Heisenberg, W., "The development of the interpretation of the quantum theory", In: Ed. W. Pauli, "Niels Bohr and the Development of Physics", (London: Pergammon, 1955).

[12] Vieira, A. L., Rev. Bras. Hist. Cienc., 6 (2) (2013) 248.

[13] Sun, C., Bull. Chin. Acad. Sci., 36 (3) (2021).

[14] Gribbin, J. R., Phys. Perspect., 15 (2013) 502.

[15] Robinson, D. J. S., "An Introduction to Abstract Algebra", Chapter 1: "Sets, Relations, Functions", (Walter de Gruyter, Berlin, NewYork, 2003), pp 1-12.

[16] Ladj, R., Lat. Am. J. Phys. Educ., 11 (2017) 4.

[17] Held, C., Stud. Hist. Philos. Sci., 25 (1994) 222.

[18] Saxon, D.S., "Elementary Quantum Mechanics", (University of California, Los Angeles, HOLDEN-DA San Francisco, Dusseldorf, Johannedburg, London, Panama, Singapore, Sydney, Toronto, 1968) pp 270-280.

Volume 17, Number 4, 2024. pp. 411-422

Jordan Journal of Physics

ARTICLE

Calculation the Low Orbits and More Stable for a Satellite around Mars

Duaa Deyaa Abood and **Abdulrahman H. Saleh**

Department of Astronomy and Space, College of Science, University of Baghdad, Iraq.

Doi: **https://doi.org/10.47011/17.4.4**

Received on: 15/12/2022; *Accepted on: 25/06/2023*

Abstract: This research examines various types of orbits around Mars. The effects of Mars's non-spherical shape, atmospheric drag, and solar attraction on these orbits were included in the calculations. The objective was to determine the optimal orbital elements to obtain a stable orbit of a satellite around Mars. The values of angles w and Ω were taken as 40° and 20°, respectively, while the orbit inclination was examined at three experimental values: i = 88°, 89°, and 90°. The perigee height above the Martian surface was assessed at three altitudes (hp = 50, 100, and 150 km) considering all perturbations except atmospheric drag. The orbital eccentricity was tested at values of e = 0.01, 0.02, 0.05, 0.08, and 0.1. The findings indicate that the most stable orbit was achieved with a low-altitude perigee (hp = 50 km), low eccentricity (e = 0.05), and an inclination of i = 90°.

Keywords: Mars, Orbiting spacecraft, Orbital elements, Inclination, Eccentricity.

1. Introduction

When a spacecraft moves around Mars, the perturbation forces must be accounted for. The most significant perturbation is due to the non-spherical shape of Mars, which introduces periodic variations in the orbit. By applying relationships between Keplerian orbital elements and Cartesian coordinates, orbital perturbations in the position and velocity vectors can be measured [1].

Spacecraft exploring the solar system often orbit various planets before escaping and re-entering an orbit around Earth. These spacecraft are transferred to their targets and follow orbits around the Sun as they travel between planets. When a spacecraft is close to its target, the planet's gravitational field deflects it into a modified orbit, causing it to either gain or lose energy.

To enter an orbit around a planet, the spacecraft or satellite's relative velocity must be reduced using a rocket when the satellite is near to its new orbit. This step allows the spacecraft to be captured into an elliptical orbit. Finally, to return to Earth, the spacecraft must gain enough momentum to complete the process in the opposite direction successfully [2].

2. The Orbital Elements of the Elliptical Orbit

An orbit is called an ellipse when its plane is inclined, and it is characterized by six orbital elements: semi-major axis (a), eccentricity (e), inclination (i), argument of perigee (w), right ascension of ascending node (Ω), and mean anomaly (M). To decrease the size of the transfer orbit and achieve a stable final orbit for a satellite around Mars, it is necessary to increase the height of the perigee (hp) while decreasing both the semi-major axis (a) and an eccentricity (e) [3].

Corresponding Author: Duaa Deyaa Abood **Email**: Duaa.abood1107@sc.uobaghdad.edu.iq

The inclination (i) is the angle between the orbital plane and the plane of the equator, calculated as:

$$i = tan^{-1}\frac{\sqrt{h_x^2+h_y^2}}{h_z} \quad (1)$$

The argument of perigee (w) is the angle between the ascending node and the perigee, calculated as:

$$w = tan^{-1}\frac{zh}{yh_x - xh_y} \quad (2)$$

The right ascension of the ascending node (Ω) is the angle between the vernal equinox and the ascending node on the equatorial plain, calculated as:

$$\Omega = tan^{-1}(-\frac{h_x}{h_y}) \quad (3)$$

Equations (1), (2), and (3), known as the Euler angles, describe the orbit's direction in space. Here, hx, hy, and hz are the angular momentum components of x, y, and z directions, and h is given by:

$$h = \sqrt{h_x^2 + h_y^2 + h_z^2}$$

The mean anomaly (M) is calculated from perigee to the position of the satellite. It is defined as the fraction of an orbit period and is measured by the equation:

$$M = E - e\,sinE \quad (4)$$

or

$$M = n(t - t_p) \quad (5)$$

where E is the eccentric anomaly, n is the mean motion, t is epoch time, and tp is the time at which the satellite passes the perigee point [3, 4].

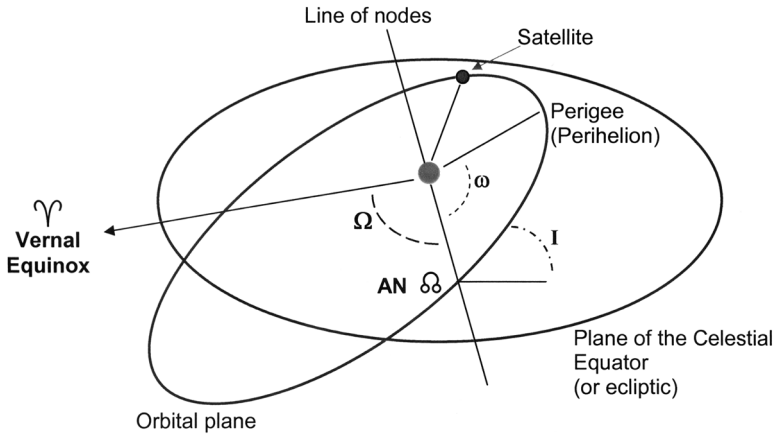

FIG. 1. The orbital elements of a satellite during it is spin around a planet [5].

TABLE 1. The main six orbital elements and their coefficients for Mars orbit around the Sun for the year 1900 [6].

Orbital element	a_0	a_1	a_2	a_3
L	293.737334	+19141.69551	+0.0003107	---------
a	1.5236883	----------	---------	---------
e	0.09331290	+0.000092064	- 0.000000077	---------
i	1.850333	-0.0006750	+0.0000126	---------
w	285.431761	+1.0697667	+0.0001313	+0.00000414
Ω	48.786442	+0.7709917	-0.0000014	-0.00000533

The orbital elements = $a_0+a_1T+a_2T^2+a_3T^3$ (6)

where $T = \frac{JD-2415020.0}{36525}$ (7)

JD = INT(365.25 y) + INT(30.6001(m+1)) + DD.dd + 1720994.5 + B (8)

where Y, m, and DD.dd are the year, month, and day with time, respectively. B is the Gregorian correction on the date, where B = 0 before 15/10/1582 AD.

The longitude of the perihelion point (α) is calculated as:

$$\alpha = w + \Omega \quad (9)$$

The mean anomaly of the planets is calculated as:

$$M = L - w - \Omega \quad (10)$$

For the major axis:

$$2a = r_p + r_a$$

where r_p is the perigee distance and, r_a is the apogee distance, calculated as:

$$r_p = a(1 - e) \quad (11)$$

$$r_a = a(1 + e) \quad (12)$$

TABLE 2. Mars Euler angles values for the year 2000 [6].

Euler angle	a_0	a_1	a_2	a_3
I	1.845113	-0.0081839	-0.00002305	-0.000000045
W	285.597172	+0.7385934	+0.00046647	+0.000006962
Ω	49.319212	-0.2940497	-0.00064435	-0.000008182

3. Perturbation Forces

3.1. Solar Radiation Pressure

Solar radiation pressure is a force exerted on a satellite due to the momentum flux of sunlight reaching Mars. For most satellites, this force acts radially away from the Sun. The magnitude of the resulting acceleration on the satellite is given by:

$$a_{srp} = k * p * \left(\frac{A}{m}\right) * \left(\frac{r_{mars} - r_{sat}}{R_{sun-mars}}\right) \quad (13)$$

where:

- asrp is solar radiation pressure acceleration,
- k is a constant = 1.3 and (p) is = 4.56 x 10^{-6} ,
- A/m is a cross-sectional area of the satellite,
- r_{mars} is the Mars position,
- r_{sat} is the satellite position,
- $R_{sun-mars}$ is the distance between the Sun and Mars.

In general, it is assumed that the sun-line a perpendicular to the cross-sectional area, because it is taken as the maximum cross-sectional area to calculate the worst possible case [5].

3.2. Atmospheric Drag

Assume that the cross-sectional area of the satellite (A/m) is perpendicular to its velocity vector, which maximizes the atmospheric drag force. By changing the satellite's orientation, we can adjust the atmospheric drag from zero to its maximum value. If we further assume that the only other force acting on the satellite is Mars's gravitational attraction, then as soon as the atmospheric drag on the satellite is set to zero, that satellite would rotate smoothly in an ideal Kepler orbit from its current position and velocity [7, 8].

The lower atmosphere of Mars extends from the planet's surface to about 7 km. Within this range, temperature (T) decreases linearly, and pressure (P) decreases exponentially. The relationships between T and P are as follows:

If h < 7 km, then, T = -31 – 0.000998 h, p = $0.699 * e^{-0.00009\,h}$

If h > 7 km, then, T = - 23.4 – 0.00222 h, p = $0.699 * e^{-0.00009\,h}$

$$\rho = p / (0.1921 * (T + 273.1)) \quad (17)$$

where ρ is density [4, 7].

The perturbing acceleration of the satellite can be represented as:

$$a_{Drag} = -\frac{1}{2} C_D \frac{A}{m} \rho v_{r\,(mag)}^2 \quad (18)$$

where $v_{r(mag)}$ is the relative speed between the satellite and the atmosphere, C_D is the drag coefficient, and ρ is the air density at the satellite's altitude [9].

A precise prediction of the satellite motion under the influence of drag involves a good density model of the upper atmosphere. An empirical atmospheric density model is used for this purpose. The velocity of the satellite relative to the atmosphere is defined as [10]:

$$v_r = v_{in} + r \times w_{Earth}$$

3.3. Planetary Oblateness

Planetary oblateness is a measure of how much a planet is flattened by its rotation. It is a unitless magnitude.

Several Martian satellites, such as MRO and MGS, are positioned in Sun-synchronous orbits (SSO).

Recent studies suggest that to achieve a stable, Martian frozen orbit, the initial values of eccentricity (e) and the angle of ascending node

(ω) should be carefully chosen based on given values for the semi-major axis (a) and inclination (i). For Mars, the J2 = 1.9555 × 10^{-3}, and J3= 3.14498 × 10^{-5} [5-7].

The J2 perturbation, which affects satellite orbits in three Cartesian components, is calculated using the following equation:

$$J2 = \left(2\frac{\epsilon_M}{3}\right) - \left(\frac{R_M^3 \omega_M^2}{3GM_M}\right) \quad (19)$$

where ε_M is Mars's oblateness, R_M is Mars's mean equatorial radius, ω_M is the Mars rotation rate, G is the universal gravitational constant, and M_M is Mars's mass.

3.4. Solar Gravity

The main external perturbations come from the Sun and the planet's moons. In this study, we focused only on the Sun's gravitational effect, excluding the perturbation effects from Mars's moons. The satellite receives a stronger gravitational pull when it is closer to these external influences. The gravitational attraction exerted by the Sun on a satellite around Mars is denoted by the symbol (Mus) and is calculated using Newton's universal law of gravitation [8]:

$$F(Mus) = G * \frac{M*m}{R^2} \quad (20)$$

Mus = 1.6100839093*10^{21} N.

4. Mars Coordinates from the Sun

To determine the coordinates of Mars relative to the Sun, the following results can be obtained using a MATLAB program:

$$l = 293.737334+19141.69551*T+0.0003107*T2 \quad (21)$$

$$a = 1.5236883 \quad (22)$$

$$e = 0.0933129+0.000092064*T-0.000000077*T^2 \quad (23)$$

$$i = 1.857806-0.0081565 * T_2 -0.00002304 * T_2^2 + 0.000000044 * T_2^3 \quad (24)$$

$$w = 285.762379 + 0.7387251 * T_2 + 0.00046551 * T_2^2 + 0.000006939 * T_2^3 \quad (25)$$

$$\Omega = 49.852347 - 0.2941821 * T_2 -0.00064344 * T_2^2 - 0.000008159 * T_2^3 \quad (26)$$

where $T = \frac{j3-2415020}{36525}$, $T_2 = \frac{j3-2451545.5}{36525}$, $j3 = \frac{j2+tp}{24*3600}$, and j2 is Julian date.

5. Practical Section and Discussion of Results

5-1. For a proposed satellite orbit around Mars, we analyzed orbits over 2000 periods with initial orbital elements set to Ω = 20°, ω = 40°, and i = 88°. Using eccentricity values e = 0.01, 0.02, 0.05, 0.08, 0.1 and altitudes above Mars's surface hp = 50, 100, and 150 km, we generated graphical data through MATLAB. Our analysis of these graphs identified that the most stable orbital configuration—characterized by minimal variations in orbital elements—occurred at a low altitude of 50 km from the Mars surface and with an eccentricity magnitude of 0.05, as shown in Fig. 2.

Note that not all the obtained graphs were included because it is not possible to include all of them in this research.

5-2. Further analysis was conducted using inclinations i = 89° and i = 90° while maintaining Ω = 20° and ω = 40° for 2000 periods. Eccentricities remained set to e = 0.01, 0.02, 0.05, 0.08, 0.1, and satellite altitudes above Mars were hp = 50, 100, and 150 km. By observing and comparing graphical outputs for each configuration, it was evident that the optimal stability was achieved with I = 90°, an altitude of 50 km, and an eccentricity of 0.05, as illustrated in Figs. 3-10.

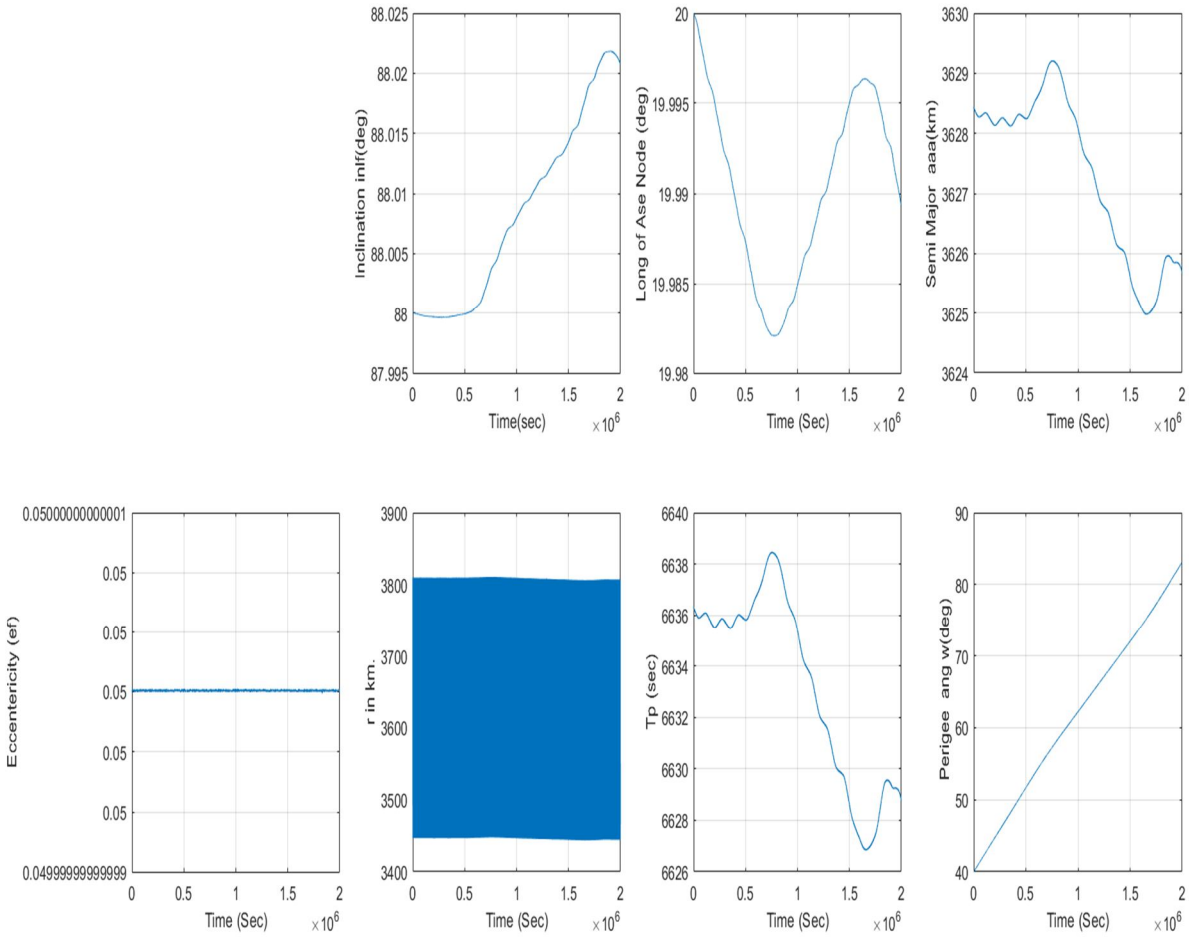

FIG. 2. The orbital elements of the satellite orbit around Mars at (e=0.05, hp=50km, i=88) for 2000 periods i=88 deg.

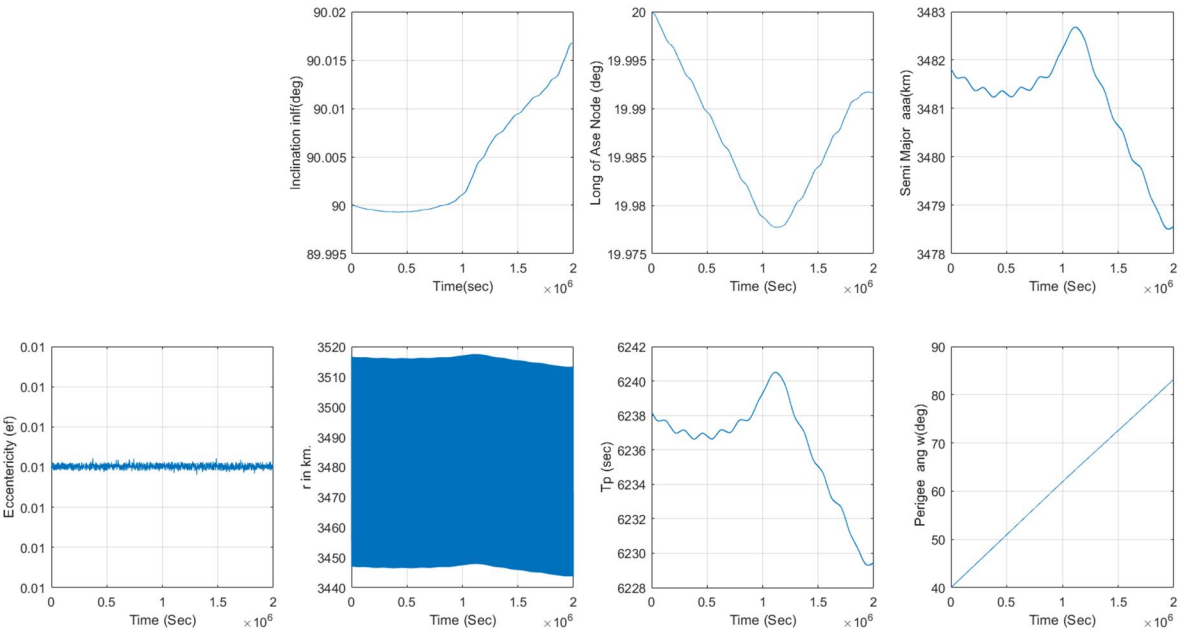

FIG. 3. The orbital elements of the satellite orbit around Mars at (e = 0.01, hp = 50 km, i = 90) for 2000 periods.

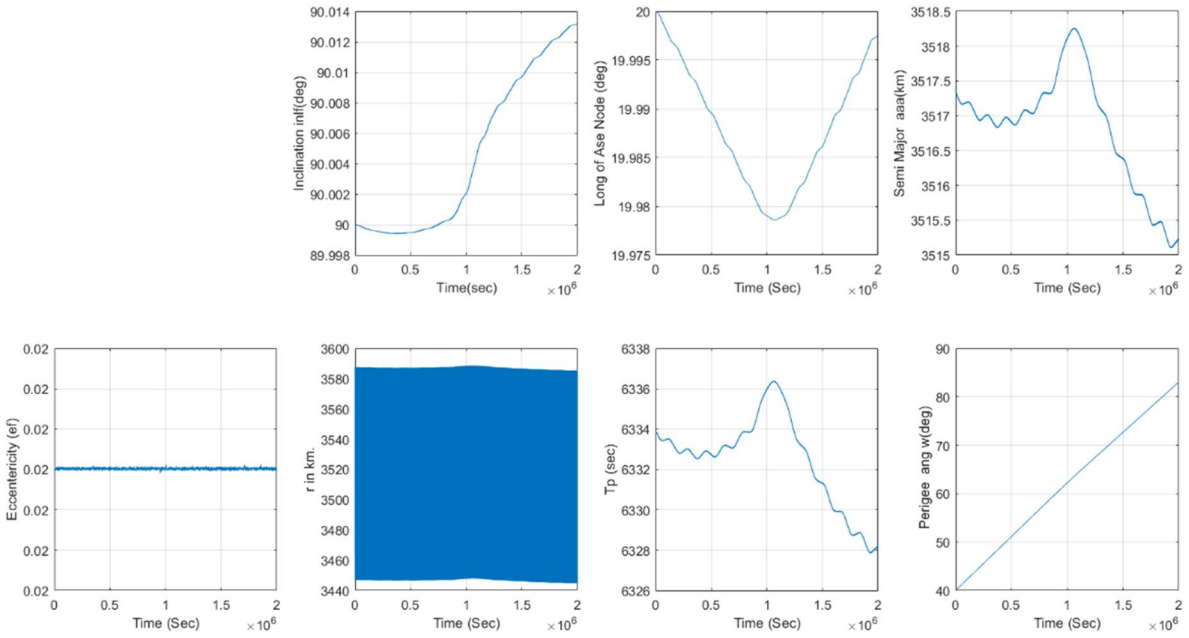

FIG. 4. The orbital elements of the satellite orbit around Mars at (e = 0.02, hp = 50 km, i = 90) for 2000 periods.

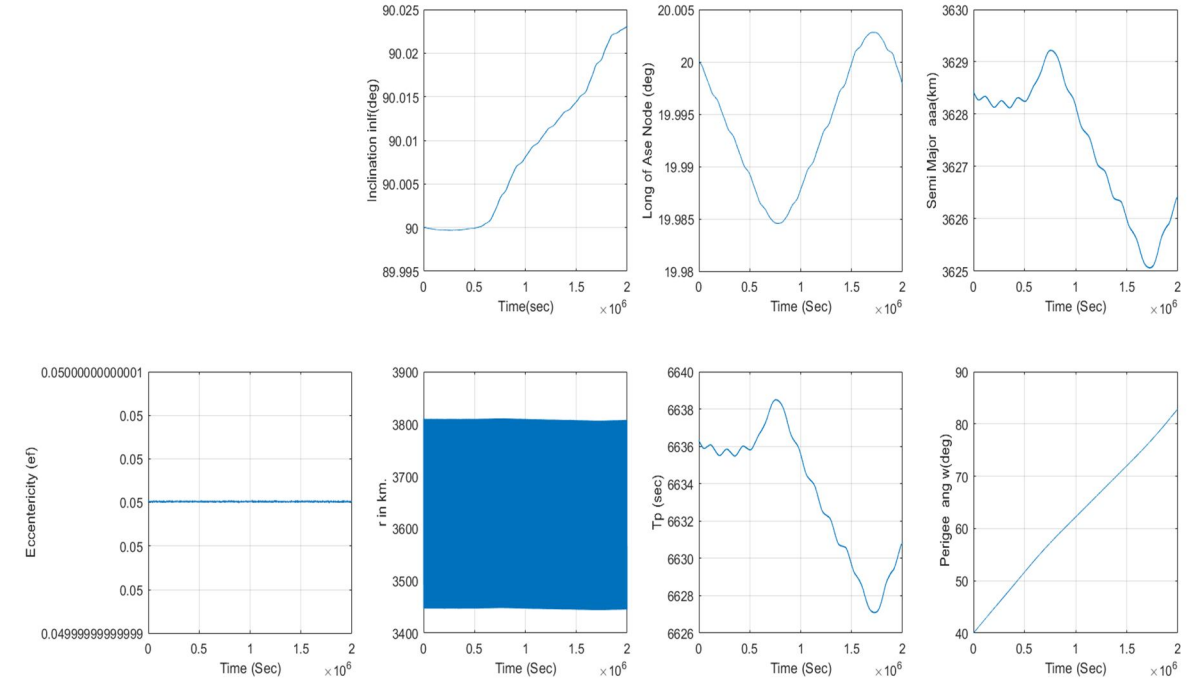

FIG. 5. The orbital elements of the satellite orbit around Mars at (e = 0.05, hp = 50 km, i = 90) for 2000 periods.

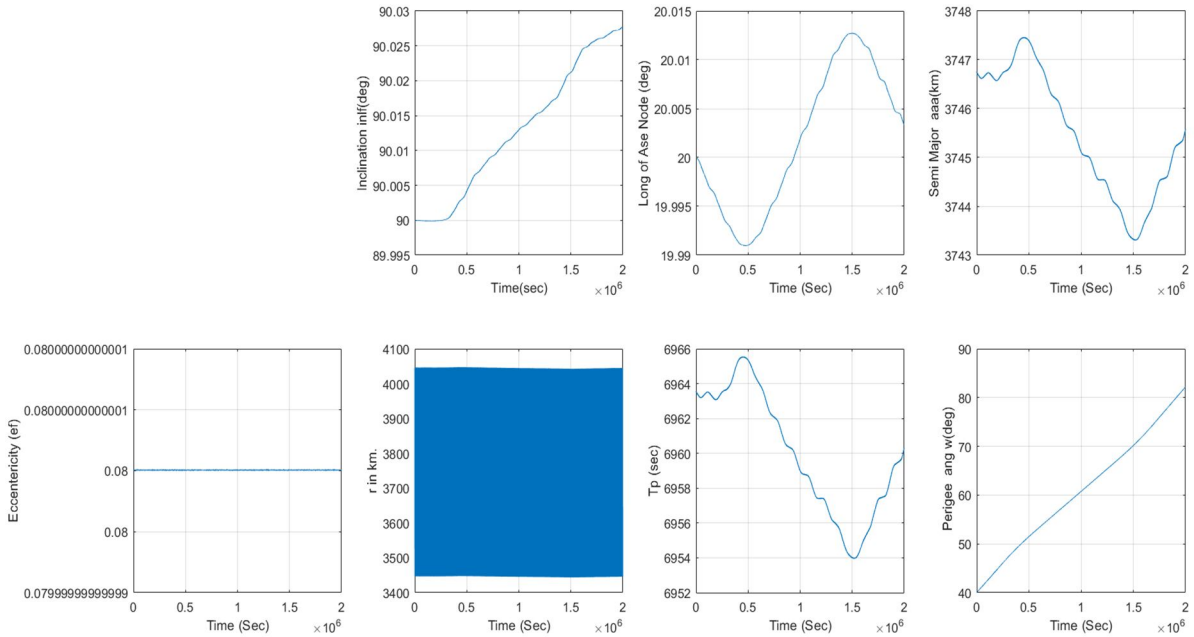

FIG. 6. The orbital elements of the satellite orbit around Mars at (e = 0.08, hp = 50 km, i = 90) for 2000 periods.

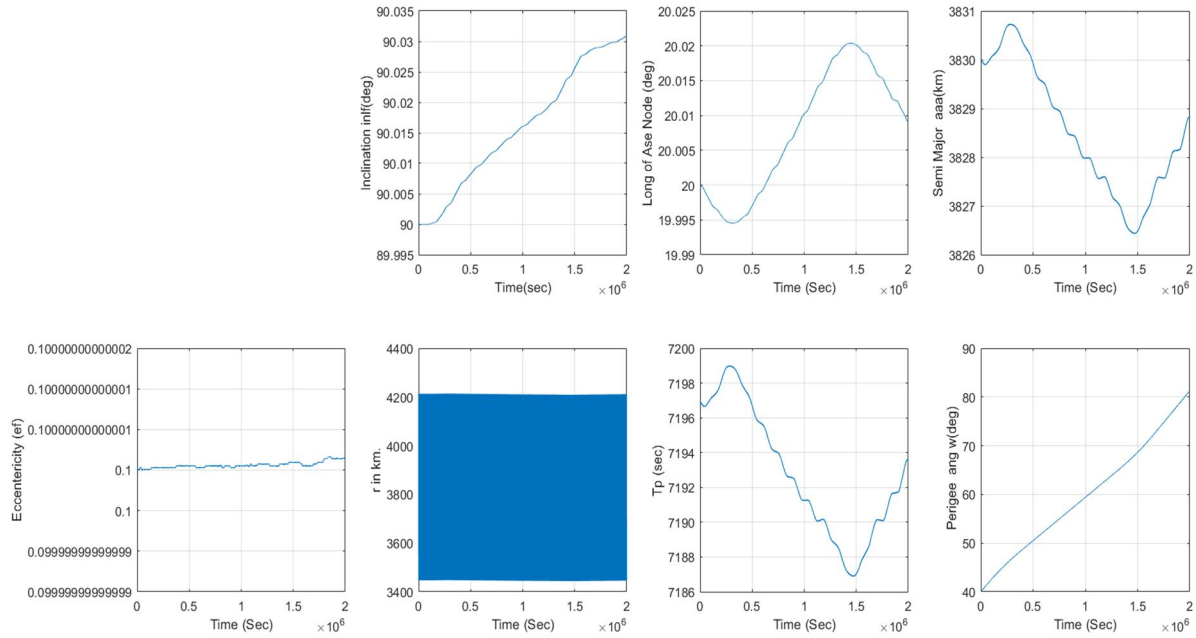

FIG. 7. The orbital elements of the satellite orbit around Mars at (e = 0.1, hp = 50 km, i = 90) for 2000 periods.

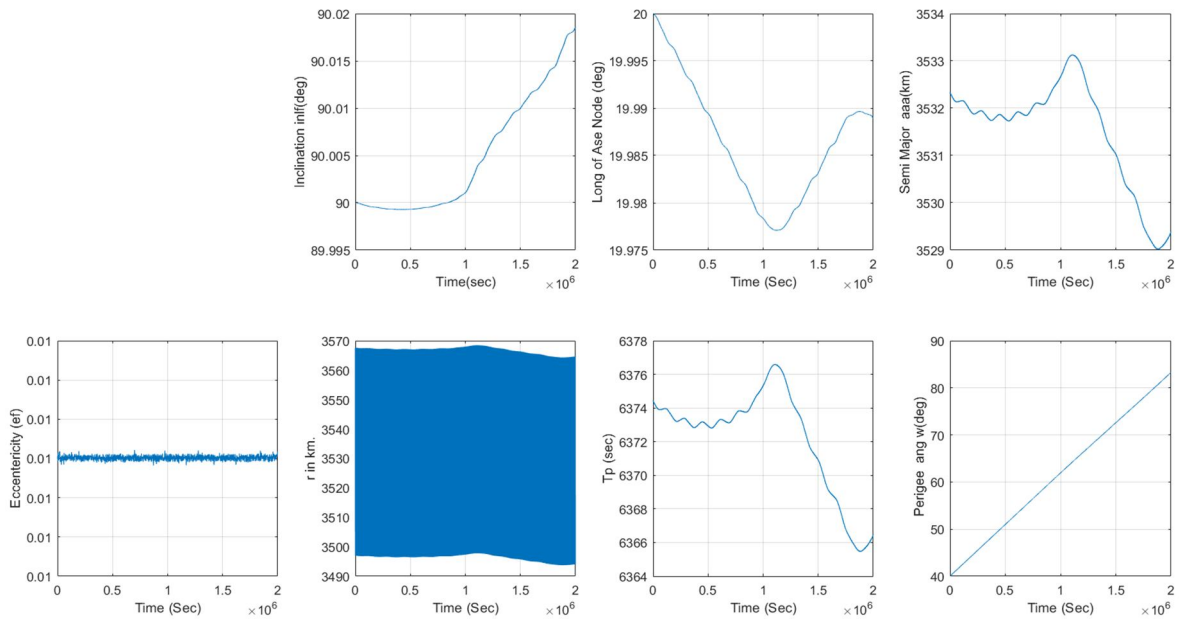

FIG. 8. The orbital elements of the satellite orbit around Mars at (e = 0.01, hp = 100 km, i = 90) for 2000 periods.

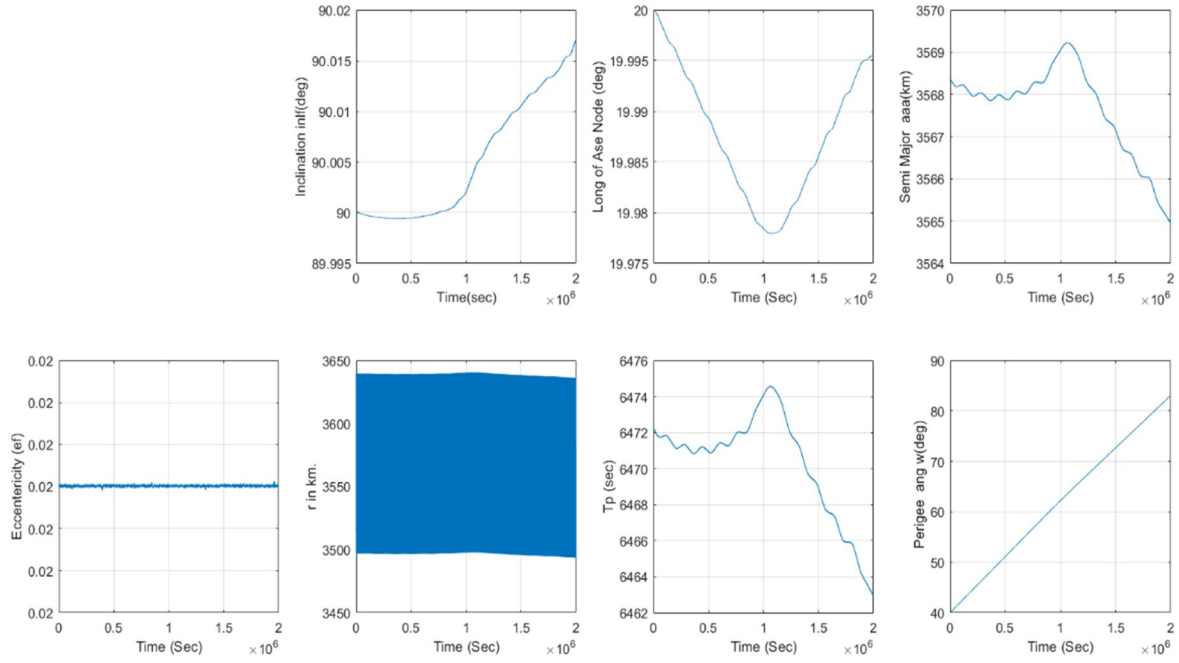

FIG. 9. The orbital elements of the satellite orbit around Mars at (e = 0.02, hp = 100 km, i = 90) for 2000 periods.

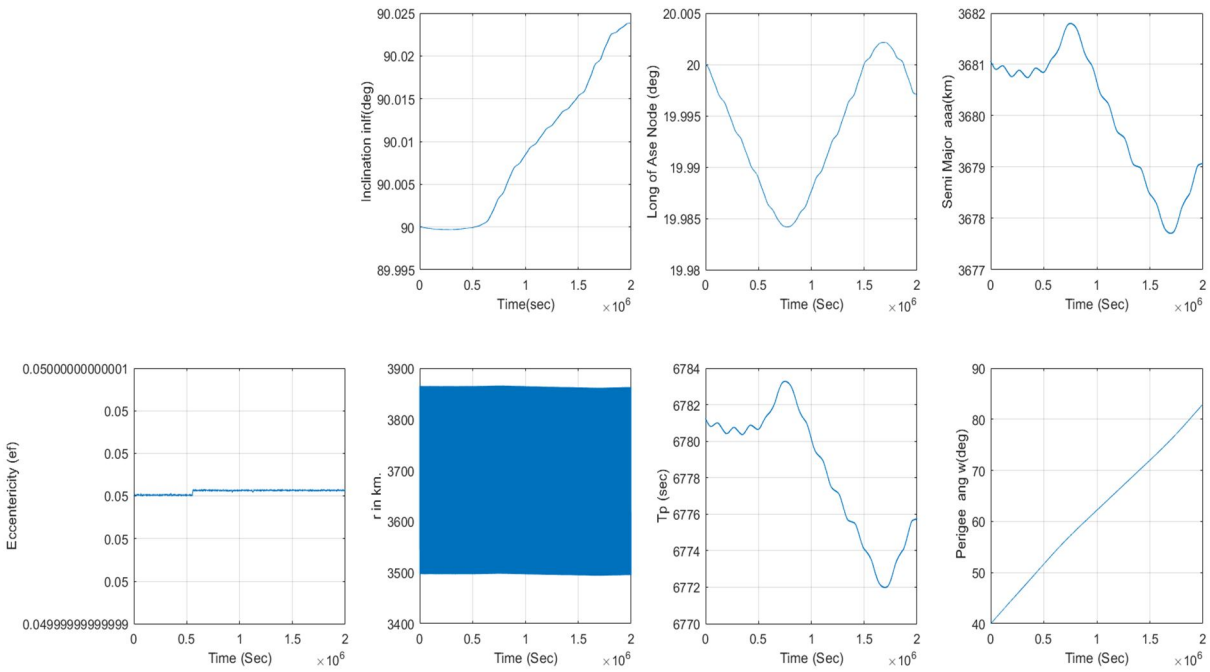

FIG. 10. The orbital elements of the satellite orbit around Mars at (e = 0.05, hp = 100 km, i = 90) for 2000 periods.

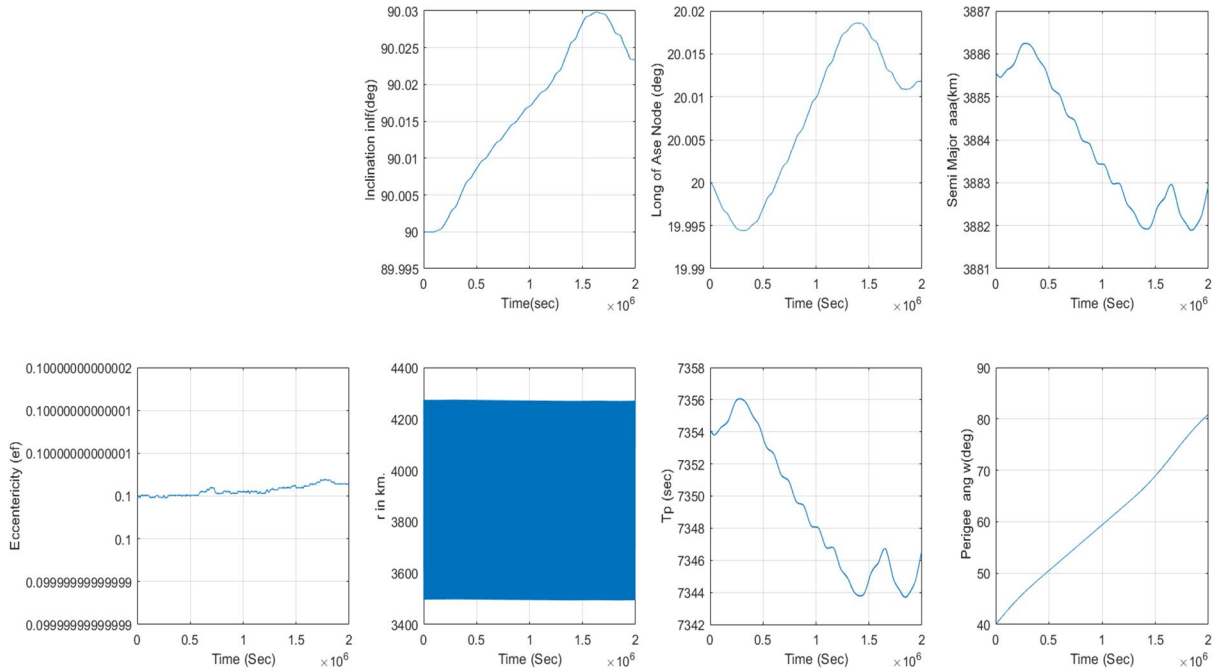

FIG. 11 The orbital elements of the satellite orbit around Mars at (e = 0.1, hp = 100 km, i = 90) for 2000 periods.

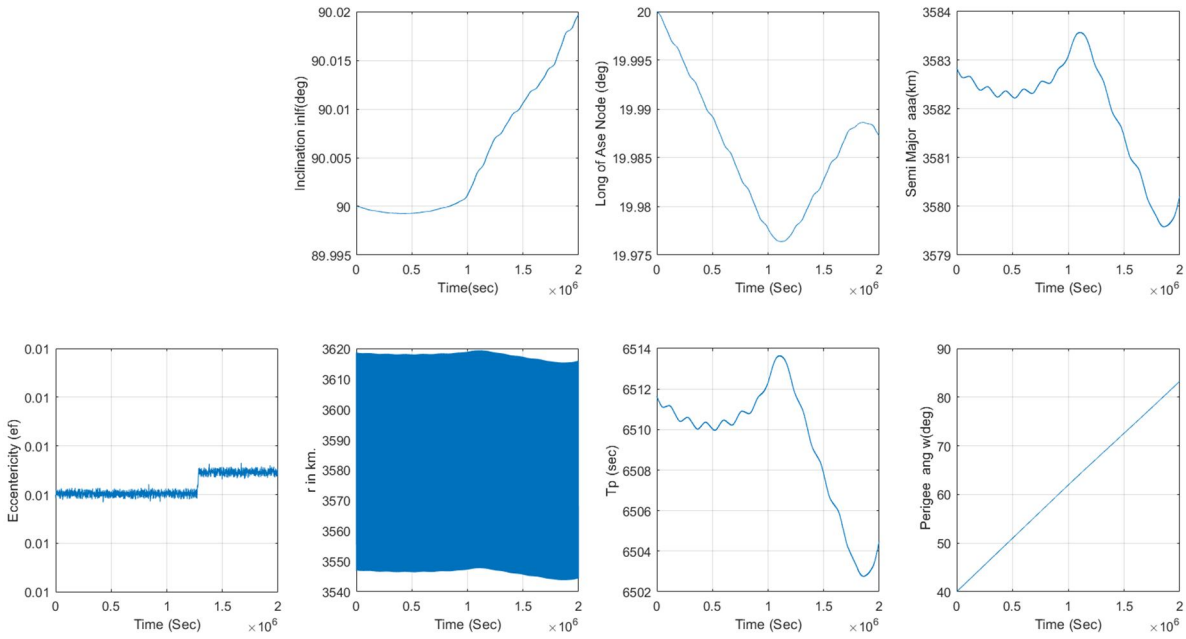

FIG. 12. The orbital elements of the satellite orbit around Mars at (e = 0.01, hp = 150 km) for 2000 periods.

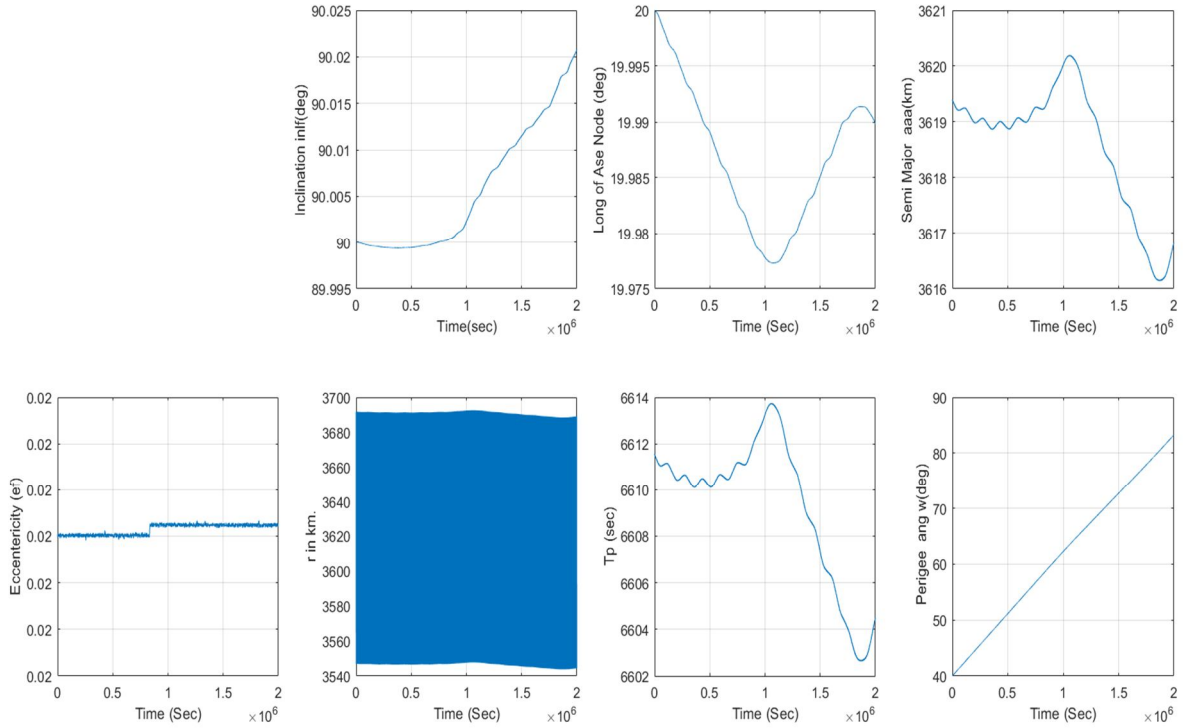

FIG. 13. The orbital elements of the satellite orbit around Mars at (e = 0.02, hp = 150 km, i = 90) for 2000 periods.

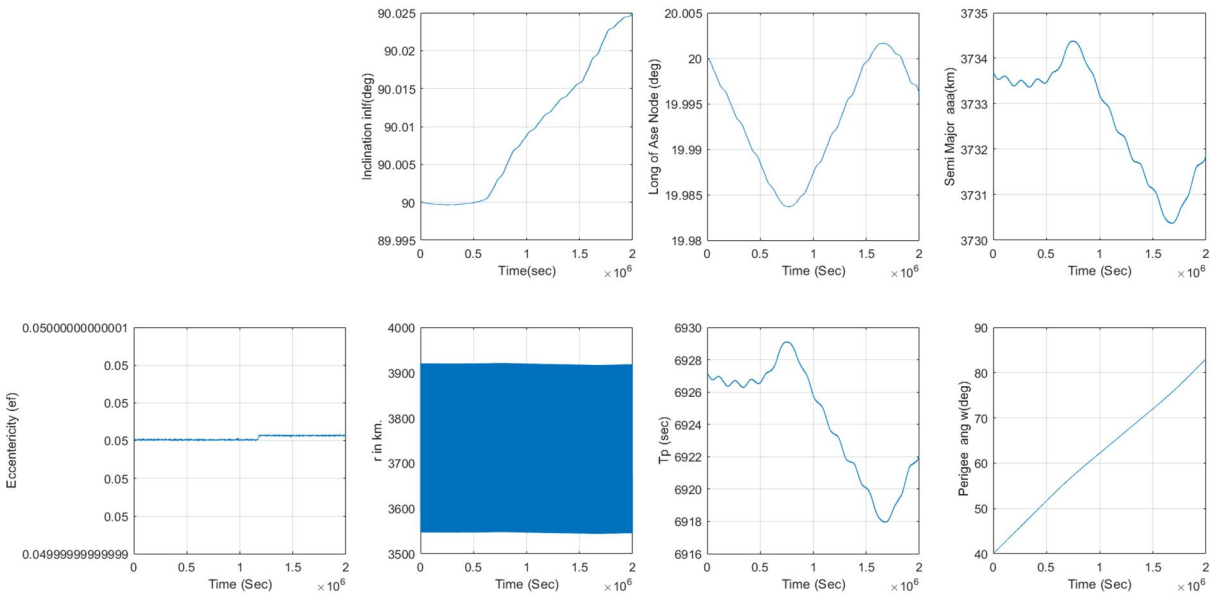

FIG. 14. The orbital elements of the satellite orbit around Mars at (e = 0.05, hp = 150 km, i = 90) for 2000 periods.

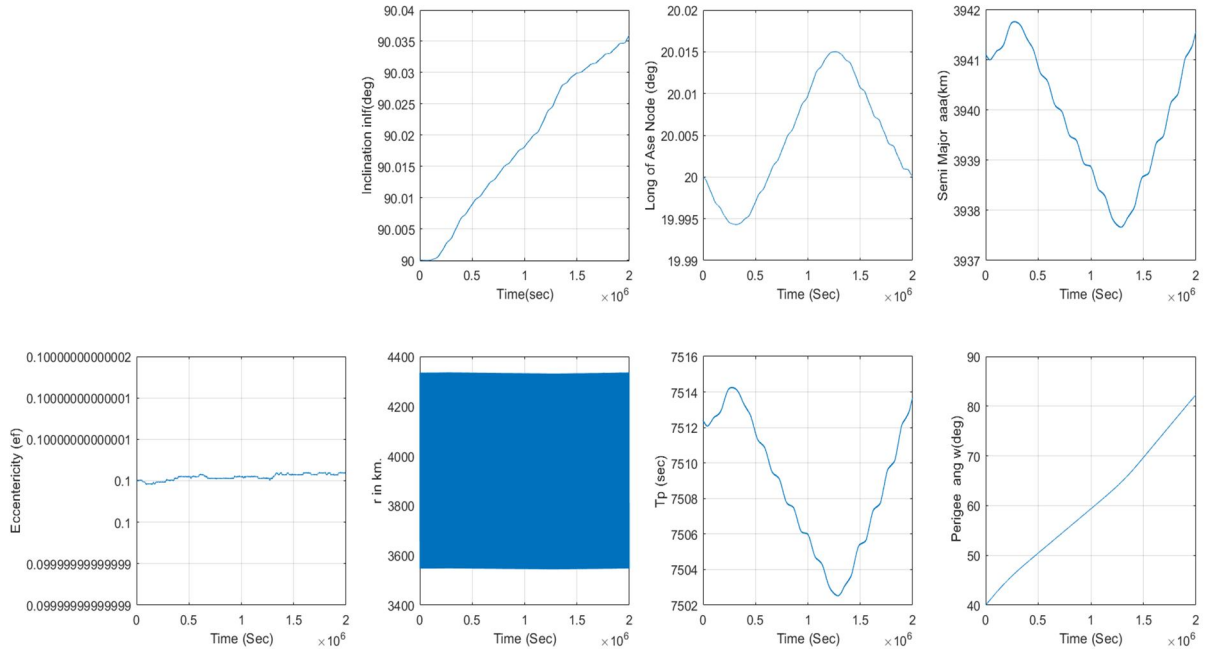

FIG. 15. The orbital elements of the satellite orbit around Mars at (e = 0.1, hp = 150 km, i = 90) for 2000 periods.

References:

[1] He, Z.-Z. and Huang, C.-L., Res. Astron. Astrophys. J., 15 (1) (2015) 107.

[2] https://courses.lumenlearning.com/astronomy/chapter/motions-of-satellites-and-spacecraft/.

[3] Fadhil, O. A. and Saleh, A. H., J. Phys.: Conf. Ser., 1664 (2020), 012005.

[4] Glenn Research Center, NASA, https://www.grc.nasa.gov/www/k-12/ airplane/ atmosmrm.html.

[5] Oliveira, A. C. et al., J. Phys.: Conf. Ser., 1365 (2019) 012028.

[6] Meeus, J., "Astronomical Formula for Calculators", 4th Ed., (Enlarged & Revised, 1988).

[7] Sinclair, A. T., Royal Astron. Soc., NASA Astrophys. Data Syst., I55 (1972) 249.

[8] Noullez, A. and Tsiganis, K., Adv. Space Res., 67 (2021) 477.

[9] Seeber, G., "Satellite Geodesy", 2nd Ed. (Walter de Gruyter, Berlin, NY, 2003).

[10] Montenbruck, O. and Gill, E., "Satellite Orbits Models Methods and Applications", 2nd Ed., (Springer-Verlag Berlin Heidelberg, 2001).

Volume 17, Number 4, 2024. pp. 423-436

Jordan Journal of Physics

ARTICLE

Spatial Variations of Particulate Matter in Mid-West Jordan

Enas M. Al-Hourani[a,b], **Shatha Suleiman Ali-Saleh**[c], **Mohammad A. Majali**[d], **Omar Al-Jaghbeer**[e], **Abdulrahman M. Shniekat**[a], **Mohammad A. Al-Qenneh**[a] and **Tareq Hussein**[a,e]

[a] *The University of Jordan, School of Science, Department of Physics, Environmental and Atmospheric Research Laboratory (EARL), Amman 11942, Jordan.*

[b] *Mu'tah University, College of Science, Department of Physics, Karak 61710, Jordan.*

[c] *National University College of Technology, Department of Basic Sciences, Amman 11191, Jordan.*

[d] *The Ministry of Education, Directorate of Education for the Karak Region, Karak, Jordan.*

[e] *University of Helsinki, Faculty of Science, Institute for Atmospheric and Earth System Research (INAR), PL 64, FI-00014 UHEL, Helsinki, Finland.*

Doi: **https://doi.org/10.47011/17.4.5**

Received on: 06/02/2023; *Accepted on: 27/03/2023*

Abstract: We evaluated aerosol concentrations in the northwestern region of Jordan (Amman, Salt, Madaba, Tafila, and Karak) using a simple mobile aerosol measurement setup during April 2022. The submicron particle number (PN_1) concentration was highest in Amman (4.6×10^4 m^{-3}) and lowest in Karak (2.0×10^4 cm^{-3}). The main roads connecting these cities exhibited PN_1 between 1.5×10^4 cm^{-3} and 6.6×10^3 cm^{-3}. The mean micron particle number (PM_{10-1}) concentration varied between 2 cm^{-3} and 5 cm^{-3} on roads and from 3 cm^{-3} to 5 cm^{-3} in cities. Micron particulate mass (PM_{10-1}) concentrations were higher in cities than on main roads, except for Amman-to-Karak road through Madaba, (~128 μg m^{-3}). Amman had the lowest PM_{10-1} concentrations (~34 μg m^{-3}). The average concentrations of $PM_{2.5}$ decreased as we moved southward from Amman. The outcomes of this study suggest that traffic emissions are the main sources of aerosols in cities. The southernmost locations (i.e. Karak) were mainly affected by dust aerosols due to local sand re-suspension from desert areas. As a recommendation, long-term aerosol measurements at multiple sites throughout the country, along with more extensive and repeated mobile measurements, are needed.

Keywords: Particle size distributions, Dust storms, Aerosol, Submicron particle, Particle mass.

1. Introduction

The climate impacts of aerosols can be realized in two ways: direct and indirect impacts. For example, aerosol particles are capable of absorbing and scattering solar radiation causing direct effects on the Earth's radiation balance. While aerosols reflect short-wavelength radiation back into space, which cools the Earth's atmosphere, they can also absorb long-wave terrestrial radiation. Aerosol particles can also affect the climate indirectly by forming cloud droplets. These droplets are formed in the troposphere by condensation of water vapor onto aerosol particles, cloud condensation nuclei, or what is called ice nuclei (CCN or IN) [1]. Besides the effects on the climate, aerosols also cause loss of visibility in urban areas.

Corresponding Author: Tareq Hussein **Email**: t.hussein@ju.edu.jo

In many Arab countries, environmental problems related to air pollution have not received sufficient scientific attention. Although monitoring stations in some Arab countries have been operating for more than two decades, active discussion and reporting of air pollution have lagged behind other regions of the world. Existing studies focus primarily on particulate matter, airborne dust (monitoring, source region, and transport), aerosol optical properties, chemical analysis, and gaseous pollution [2–16]. Very few studies focused on the measurement of size distributions and particle number concentrations [8, 13, 17, 18]. Recently advancements in aerosol measurement technology, particularly for particle size distribution of the particulate matter have gained importance within atmospheric science. Consequently, measuring particle number and mass size distributions has become a major research focus at the Environmental and Atmospheric Research Laboratory (EARL, University of Jordan) in Jordan [8–13, 19–22]. Besides our own research conducted at the EARL, only a few studies on air pollution in Jordan exist [23–26].

Urban aerosol measurements are important to establish proper linkages between air pollution and its harmful impacts on human health. Such measurements are also needed to assess the effectiveness of air quality regulations. Quantifying the particle size distributions (PSDs) of urban aerosols is essential to understanding the size-dependent mechanisms that regulate particle transport, transformation, and fate in the urban atmosphere [27].

This paper is a continuation of our efforts to measure and report particulate matter concentrations in Jordan, expanding coverage to the mid-western region (including Amman, Salt, Madaba, Tafila, and Karak). The experimental setup was based on a mobile arrangement of portable instruments that are capable of measuring the particulate matter concentrations across various particle size fractions and metrics (both number and mass concentrations in several size fractions from 0.01 to 25 μm in particle diameter). This study provided important preliminary information about particulate matter concentrations over a large geographic area in Jordan while accounting for diverse particle size fractions in the atmosphere of these governorates, with high accuracy regarding sampling time and location.

2. Materials and Methods

2.1. Description of the Measurement Campaign

The measurement campaign took place during April 10 – 28, 2022. During this period, we conducted three rounds of measurements in different governorates. We used portable instruments in a mobile setup to measure aerosol concentrations (number and mass) across several cities and along major routes in Jordan (Fig. 1).

First track (April 10): We started driving around 9:00 am from Amman (University of Jordan) and then headed west to Salt, where we made a full tour around Salt city before returning to Amman. The tour took 4 hours and the distance traveled was about 45 km.

Second track (April 12): Starting at around 10:00 am from Amman (University of Jordan), we headed south along the desert road to Karak Governorate, then turned west towards the Jordan Valley (Ghor Al Mazraa), the lowest point on Earth at 420 m below sea level. After that, we headed south along the Dead Sea until we reached Ghor Al Safi and Ghor Al Fifa. Then we headed east to Tafila Governorate, passing through the main street in Tafila City. After that, we headed north to Karak Governorate, where measurements were made in several areas of Karak Governorate, including the city of Karak, after which the tour ended. This route spanned about 317 km and lasted 8 hours.

Third track (April 28): We started driving at around 8:30 AM from Amman (University of Jordan) then headed southwest to Madaba Governorate, continuing southward to Madaba city and on to Dheban, passing Al Wala. Then we went to Karak Governorate passing Mujib Dam, where we made several measurements across the northern and central parts of the Karak Governorate. The tour took 8 hours, and the approximate distance traveled on this track was about 237 km.

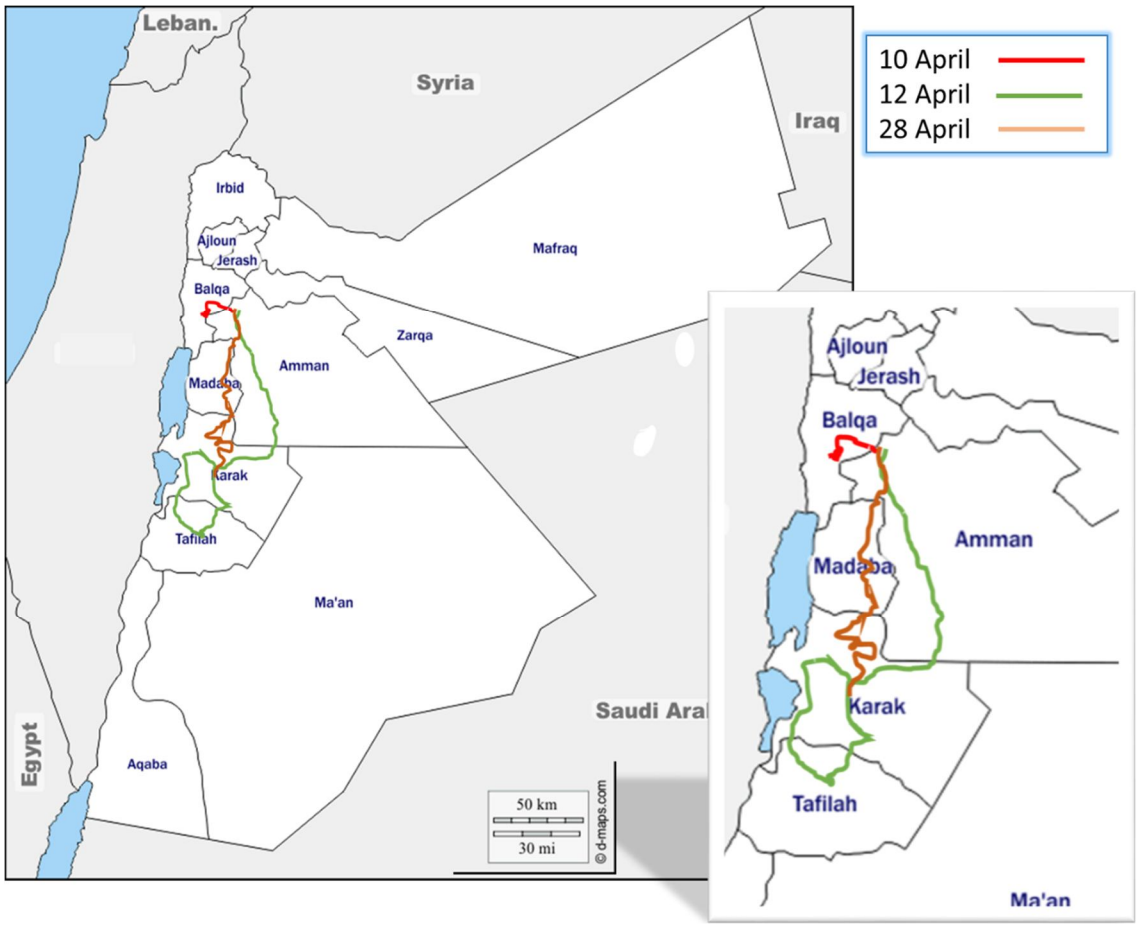

FIG. 1. Map of Jordan that shows the driving routes.

2.2. Mobile Experimental Setup

The mobile experimental setup included three portable instruments: two condensation particle counters (TSI CPC 3007-2 and P-Trak 8525) and a handheld optical particle counter (TSI AeroTrak 9306-V2).

The CPC and the P-Trak have cutoff particle diameters of 10 and 25 nm, respectively, and measure total sub-micron particle number concentrations up to a couple of microns in diameter. The maximum detectable concentrations for these counters are 10^5 cm^{-3} and 50×10^4 cm^{-3} (20% accuracy), respectively. The sampling flow rate was 0.1 L min^{-1} (inlet flow rate 0.7 L min^{-1}) in both counters.

The AeroTrak was used to measure size-specific particle number concentrations within an optical diameter range of 0.3–25 µm across six channels: 0.3–0.5, 0.5–1, 1–2.5, 2.5–5, 5–10, and 10–25 µm. The sampling time resolution was 1 s at a flow rate of 2.83 L min^{-1}.

Portable low-cost sensors (LCS, Panasonic assembled in-house by Nagoya University) were included in the mobile setup to measure particulate matter ($PM_{2.5}$) as a complementary setup alongside the portable counters. These LCS also recorded relative humidity (RH) and temperature (T) during the measurement.

We used a Garmin GPS (eTrex 32x) to record the speed and location of the mobile laboratory with a 1-second time resolution.

All instruments were situated on the back seat of a car (Jeep Cherokee, 2013). While driving, we kept the front windows and the back windows fully open. This guaranteed a high exchange rate between indoor and outdoor air, providing representative outdoor aerosol measurements. We, therefore, did not need special inlets for the aerosol instruments in this simple "mobile setup". Before each measurement session, we checked all devices for readiness and synchronized the instrument clocks.

2.3. Aerosol Data Handling

The raw data underwent a quality check and was then converted to a one-minute average database. We also calculated average concentrations during different periods: (1) periods spent crossing each city and (2) periods spent on the main roads between cities. In total, we visited five cities: Amman, Salt, Madaba, Tafila, and Karak. As for the main roads between cities, we traveled along nine roads: Amman–Salt, Amman–Madaba, Desert (between Amman and Qatrana), Qatrana-Karak, Madaba–Karak, Karak–Ghor, Jordan Valley (Dead Sea), Dead Sea (industrial area)–Tafila, and Tafila–Karak.

We obtained particle number concentrations (PN) in eight particle size fractions within the following diameter ranges: 10–25 nm (calculated from the difference between the concentrations measured with the CPC and the P-Trak), 25–300 nm (calculated from the difference between the concentrations measured with the P-Trak and the AeroTrak), 0.3–0.5 µm, 0.5–1 µm, 1–2.5 µm, 2.5–5 µm, 5–10 µm, and 10–25 µm. The last six particle size channels were measured directly with the AeroTrak.

The normalized particle number size distribution (n_N^0) was calculated by normalizing the particle number concentration (PN) in each size fraction to its corresponding particle diameter range:

$$n_N^0 = \frac{dN}{dlog(D_p)} = \frac{N}{log_{10}(D_{p2}) - log_{10}(D_{p1})} \quad (1)$$

where N is the size-specific particle number concentration and D_{p1} and D_{p2} are, respectively, the lower and upper particle diameter limits of that corresponding particle size-fraction.

The normalized particle mass size distribution (n_M^0) was calculated by assuming spherical particles with unit density:

$$n_M^0 = \frac{dM}{dlog(D_p)} = \frac{\frac{\pi}{6}\langle D_p\rangle^3 \rho_p N}{log_{10}(D_{p2}) - log_{10}(D_{p1})} = \frac{\pi}{6}\langle D_p\rangle^3 \rho_p n_N^0 \quad (2)$$

where $\langle D_p \rangle$ is the mean particle diameter of the particle size channel, ρ_p is the particle bulk density, and N is the size-specific particle number concentration, with D_{p1} and D_{p2} as diameter limits.

The particle number (PN) or mass (PM) concentration in any particle size fraction can be calculated by integration:

$$PN = \int_{D_{p1}}^{D_{p2}} n_N^0 dlog(D_p) \quad (3)$$

$$PM = \int_{D_{p1}}^{D_{p2}} n_M^0 dlog(D_p) \quad (4)$$

As such, the fine particle mass concentration ($PM_{2.5}$) can be calculated by integrating the normalized particle mass size distribution up to 2.5 µm:

$$PM_{2.5} = \int_{0.01}^{2.5} n_M^0 dlog(D_p) \quad (5)$$

The submicron particle number concentration can be calculated by integrating the normalized particle number size distribution up to 1 µm

$$PN_1 = \int_{0.01}^{1} n_N^0 dlog(D_p) \quad (6)$$

2.4. Weather Conditions

For this study's analysis, we included only temperature and relative humidity data collected from April 10 to April 28, 2022.

April, being part of the spring season, generally has moderate temperatures and variable relative humidity. These conditions guarantee accurate readings and do not lead to the failure of the devices, as high temperatures are not suitable for these devices. Sometimes, dust storms may occur during this season in several regions of Jordan, especially the eastern and southern regions. During all measurement campaigns, relative humidity mostly ranged from 12% to 55%, and temperatures varied between 12°C and 32°C, with a median of 22°C.

3. Results and Discussion

3.1. Particle Number Concentrations

3.1.1. Submicron Particle Number (PN_1) Concentrations

The mid-western region of Jordan was the main focus of this study. The spatial variation of PN_1 is shown in Fig. 2 and listed in Table 1. This data suggests that traffic emissions are the main reasons for high aerosol concentrations in Jordan. The measurements were taken in more than 20 sites within Karak. Most of these sites did not have intensive traffic activity. As discussed in this and the next subsections, the particle number size distribution also reflects the spatial variation in concentrations (Fig. 3).

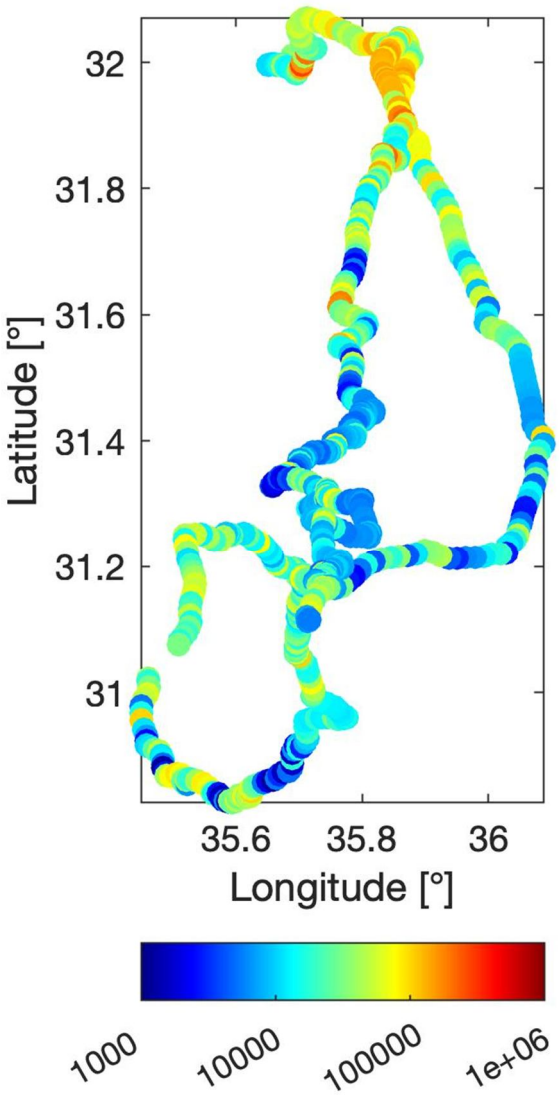

FIG. 2. Total particle number concentrations (PN_1) plotted on the measurement routes.

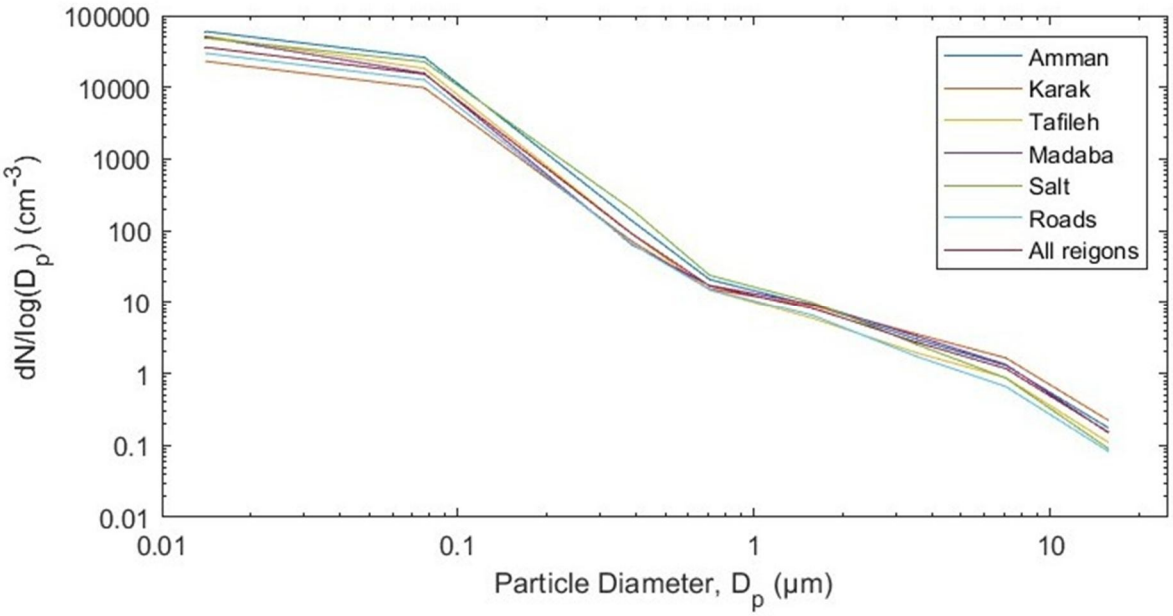

FIG. 3. Average particle number size distributions (n_N^0) derived from the merge of the three instruments: CPC, P-Trak, and AeroTrak.

TABLE 1. Average submicron particle number concentrations (PN_1 [cm^{-3}]).

	Size fraction	mean	Std.	min	5%	25%	Median	75%	95%	max	#
Cities	Amman	46000	42400	7500	8100	16300	31900	56300	131900	243700	284
	Salt	43900	49300	10600	11000	13300	32400	45700	147000	287600	74
	Madaba	37000	38000	2200	2900	11800	30500	47300	99400	184800	52
	Karak	19700	18400	1500	4500	7700	11000	27000	58900	134400	430
	Tafila	40500	25900	1100	2400	26700	36300	55100	90000	110100	31
Roads	Amman-Salt	66400	33100	34500	35900	41700	54500	84600	120200	137000	10
	Amman-Madaba	39000	29200	9100	12200	14100	34200	47500	80500	132600	21
	Madaba-Karak	6400	3600	2500	2600	3700	5500	7500	14400	17500	45
	Amman-Karak (Desert)	30600	30700	2600	4400	8700	16700	43200	89600	166800	71
	Qatrana-Karak	15800	13700	2400	2800	4400	11500	28200	37700	45200	21
	Karak-Dead sea	21300	17700	7900	8300	10400	14300	27100	52700	115200	74
	Dead sea industry	29100	20300	2400	8400	13700	22400	40400	63100	101100	50
	Dead sea-Tafila	31500	28600	1200	1500	6500	23800	46300	81700	91400	27
	Tafila-Karak	15500	11600	1200	1800	12200	13400	17600	38300	73000	65

TABLE 2. Average micron particle number concentrations (PN_{10-1} [cm^{-3}]) .

	Size fraction	mean	Std.	min	5%	25%	Median	75%	95%	max	#
Cities	Amman	5	3	2	2	3	4	6	9	18	284
	Salt	5	1	3	3	4	5	5	7	9	74
	Madaba	5	2	3	4	4	5	6	7	13	52
	Karak	5	3	2	3	4	5	6	9	31	430
	Tafila	3	1	2	2	3	3	3	7	8	31
Roads	Amman-Salt	4	1	3	3	4	4	4	5	5	10
	Amman-Madaba	5	1	4	4	5	5	5	7	8	21
	Madaba-Karak	5	1	2	2	4	5	5	8	9	45
	Amman-Karak (Desert)	2	1	2	2	2	2	3	5	9	71
	Qatrana-Karak	2	0	2	2	2	2	2	4	4	21
	Karak-Dead sea	2	0	2	2	2	2	2	4	6	74
	Dead sea industry	4	7	2	2	2	2	2	7	52	50
	Dead sea-Tafila	2	0	2	2	2	2	2	2	5	27
	Tafila-Karak	2	1	2	2	2	2	2	5	6	65

The PN_1 was the lowest in Karak (~1.97×10^4 cm^{-3}) among the regions studied. For example, it was ~4.6×10^4 cm^{-3} in Amman and ~4.4×10^4 cm^{-3} in Salt. These were the highest throughout this study. In Madaba it was ~3.7×10^4 cm^{-3} (measured during 10:00–11:30 on April 28) and ~3.7×10^4 cm^{-3} in Tafila (measured during 14:00–15:30 on April 12). Although Madaba and Tafila are small towns in Jordan, the relatively high PN_1 levels can be attributed to the measurements taken on the main roads with high traffic activities and related emissions (Table 1).

As for the main roads connecting cities, the overall average PN_1 was ~2.3×10^4 cm^{-3}. The concentration was the highest on the road between Amman and Salt (~6.6×10^4 cm^{-3}). The lowest concentrations were observed along the main roads connecting Karak and Madaba (less than 10^4 cm^{-3}). For instance, the PN_1 in the Dhiban area was about half of that reported in Madaba. On the desert road between Amman and Karak, the mean concentration was about 4×10^4 cm^{-3}. This road had active traffic of heavy-duty vehicles (e.g. trucks and lorries). As the traffic activity was low on the road between Al-Qatraneh and Karak, the concentration was considerably low (about 1.6×10^4 cm^{-3}), similar to the Tafila–Karak road, which winds through mountainous terrain near Al-Tanour Dam and resembles the conditions on the Madaba–Karak route through Dhiban. On the road passing by the southern part of the Dead Sea, the concentration was about 3×10^4 cm^{-3} (Table 1).

It is worth mentioning that the measurements were taken in Amman on different dates (April 10, 12, and 28) at various times and locations: Jubaiha, Sweileh, part of the airport road, Marj Al-Hamam, and Naour. All these measurements were taken during the morning period. This variability suggests that PN_1 concentrations in Amman can fluctuate significantly. For further context, Hussein *et al*. reported that PN_1 concentrations at an urban background location (University of Jordan campus) ranged between 15000 cm^{-3} and 40000 cm^{-3} [12]. Additionally, these results can be compared to the results of a study conducted in Amman in 2014, where the mean PN_1 concentration was 11×10^4 cm^{-3}. The reason for this increase is that the measurements were taken in many areas of Amman and included peak times.

3.1.2. Micron Particle Number (PN_{10-1}) Concentrations

The PN_{10-1} varied considerably from one location to another. The highest concentration was about 5 cm^{-3}, recorded in Amman, Salt, Madaba, and Karak. Interestingly, the concentration in Tafila was about 3 cm^{-3} (Table 2). The high concentrations of micron particles in these cities can be partly due to road dust re-suspension.

The overall average PN_{10-1} on the main roads was about 3 cm^{-3} and it varied between 2 cm^{-3} and 5 cm^{-3}. The highest concentration (~5 cm^{-3}) was observed on the road from Amman to Karak passing through Madaba. Concentrations on the Amman–Salt road and near the Dead Sea were about 4 cm^{-3}. The rest of the tested roads had a PN_{10-1} concentration of about 2 cm^{-3}.

Interestingly, the PN_{10-1} concentrations were more variable on roads than within cities. It can be due to the fact that on some roads traffic activity was not as high as on other roads. In cities, traffic activity remains relatively high throughout the day, and the road dust dispersed within the city reaches a rather steady-state concentration, which was considerably high (~5 cm^{-}).

3.2. Particulate Matter (PM) Concentrations

3.2.1. Micron and Super Micron Particulate Matter ($PM_{10-2.5}$ and PM_{25-10})

Amman had the lowest PM_{10-1} concentrations, which was ~22 µg m^{-3} (Table 3). This is because the studied areas in Amman (University of Jordan, Jubaiha, Marj Al-Hamam) are devoid of quarries and farms. The PM_{25-10} concentrations in Amman were about (~141 µg m^{-3}). This indicates that Amman is also clearly affected by sand and dust storm (SDS) episodes coming from the eastern and southern regions.

The mean concentration of PM_{10-1} increased to ~74 µg m^{-3} when we moved westward to the city of Salt, while the PM_{25-10} concentrations decreased to ~73 µg m^{-3}, reflecting Salt's distance from desert regions and reduced local dust storm impact.

The PM_{10-1} and PM_{25-10} concentrations in Madaba were 105 µg m^{-3} and 120 µg m^{-3}, respectively. The concentration of PM_{10-1} in the city center was high and then decreased when we moved south to Theban, whereas PM_{25-10} followed an opposite trend, confirming what we

discussed previously. Tafila showed a similar pattern, with the average concentration of PM_{10-1} and PM_{25-10} of 67 μg m^{-3} and 89 μg m^{-3}, respectively.

Karak had the highest PM_{10-1} and PM_{25-10} concentrations (~123 μg m^{-3} and ~180 μg m^{-3}, respectively), due to the large spread of quarries, crushers, and farms in the non-urban areas along the measurement path in addition to the effect of dust storms coming from the desert areas east of Karak.

The mean PM_{10-1} and PM_{25-10} concentrations on the Amman-Madaba road were high (~112 μg m^{-3} and 107 μg m^{-3}, respectively). This increase in the average PM_{10-1} and PM_{25-10} concentrations may be due to the presence of many farms west of the road (Table 4). This is repeated on the Jordan Valley road that borders the Dead Sea from the Ghor Al Mazraa to the Ghor Al Fifa, where the average PM_{10-1} and PM_{25-10} concentrations are also high (84 μg m^{-3} and 143 μg m^{-3}, respectively). In this area, there are also a large number of farms and some factories. This leads us to conclude that the average concentrations of PM_{10-1} and PM_{25-10} are high on roads with significant agricultural activities, and the average concentration is low on roads free of farms.

The particle mass size distribution can be best represented by eight particle size fractions: 10–25 nm, 25–300 nm, 0.3–0.5 μm, 0.5–2.5 μm, 2.5–5 μm, 5–10 μm, and 10-25 μm. The particle mass size distribution shows that the high concentrations in all regions of the 10–25 μm particle size-fraction is caused by dust (Fig. 4).

3.2.2. Submicron and Fine Particulate Matter

$PM_{1-0.3}$ concentrations were higher across the cities than on the main roads, except for Karak, where the $PM_{1-0.3}$ concentrations were the lowest (~5 μg m^{-3}), likely due to dilution from clean air in that area. Amman and Salt had the highest concentrations (~12 μg m^{-3} and ~11 μg m^{-3}, respectively), which can be attributed to higher traffic activity compared to other study areas. In Madaba and Tafila, $PM_{1-0.3}$ concentrations were ~7 μg m^{-3} and ~8 μg m^{-3}, respectively, and these concentrations decreased when we moved away from the main streets in the city centers in both regions (Table 3).

TABLE 3. Average particulate matter concentrations (μg/m^3) in different size fractions measured across the cities.

	Size fraction	mean	Std.	min	5%	25%	Median	75%	95%	max	#
Amman	$PM_{1-0.3}$	12	11	2	3	6	7	15	56	72	284
	PM_{10-1}	22	94	17	34	54	71	127	203	887	284
	PM_{25-10}	141	264	23	32	64	95	142	275	3000	284
Karak	$PM_{1-0.3}$	5	4	1	2	2	3	7	20	37	430
	PM_{10-1}	123	121	26	39	64	93	135	288	1200	430
	PM_{25-10}	180	265	8	36	68	104	190	488	2600	430
Madaba	$PM_{1-0.3}$	7	6	1	2	3	6	10	30	29	52
	PM_{10-1}	105	46	61	66	80	94	116	161	309	52
	PM_{25-10}	120	90	53	64	77	96	138	207	650	52
Tafila	$PM_{1-0.3}$	8	5	1	1	5	7	11	26	22	31
	PM_{10-1}	67	73	24	30	37	40	55	252	313	31
	PM_{25-10}	89	120	14	22	40	48	77	393	507	31
Salt	$PM_{1-0.3}$	11	11	4	4	5	9	11	45	68	74
	PM_{10-1}	74	44	39	43	52	60	75	151	282	74
	PM_{25-10}	73	79	19	29	40	52	70	185	544	74
All roads	$PM_{1-0.3}$	6	6	1	1	3	4	7	25	53	394
	PM_{10-1}	53	111	15	18	26	36	58	121	2100	394
	PM_{25-10}	67	249	6	11	21	35	61	149	4700	394
All regions	$PM_{1-0.3}$	7	8	1	1	3	5	8	32	80	1265
	PM_{10-1}	89	108	14	22	40	63	102	215	2100	1265
	PM_{25-10}	122	244	6	16	39	72	121	336	4700	1265

TABLE 4. Average particulate matter (µg/m^3) in different size fractions measured on main roads.

	Size fraction	mean	Std.	min	5%	25%	Median	75%	95%	max	#
Amman-Salt	$PM_{1-0.3}$	14	5	9	9	9	12	17	40	26	10
	PM_{10-1}	62	8	51	51	56	61	66	73	75	10
	PM_{25-10}	53	11	39	39	44	52	62	69	72	10
Amman-Madaba	$PM_{1-0.3}$	9	5	2	3	5	5	9	32	21	21
	PM_{10-1}	112	21	82	83	98	108	120	142	159	21
	PM_{25-10}	107	31	70	76	87	99	117	159	193	21
Madaba-Karak	$PM_{1-0.3}$	2	1	2	2	2	2	2	5	5	45
	PM_{10-1}	64	24	42	44	53	59	70	96	190	45
	PM_{25-10}	80	72	24	35	45	58	83	206	443	45
Amman-Karak (Desert)	$PM_{1-0.3}$	8	7	2	2	3	5	10	36	41	71
	PM_{10-1}	38	25	16	19	24	30	39	84	179	71
	PM_{25-10}	34	31	7	9	17	23	36	102	182	71
Qatrana-Karak	$PM_{1-0.3}$	4	3	2	2	2	3	5	15	12	21
	PM_{10-1}	31	14	16	17	21	26	38	59	68	21
	PM_{25-10}	31	45	7	8	13	16	28	75	215	21
Karak-Dead sea	$PM_{1-0.3}$	6	5	2	2	3	4	5	22	38	74
	PM_{10-1}	37	19	21	22	26	33	40	57	134	74
	PM_{25-10}	37	27	9	13	21	31	42	85	182	74
Dead sea industry	$PM_{1-0.3}$	6	4	1	2	4	6	8	20	21	50
	PM_{10-1}	84	291	17	22	27	32	42	151	2077	50
	PM_{25-10}	143	666	11	16	24	32	47	204	4743	50
Dead sea-Tafila	$PM_{1-0.3}$	5	0	4	4	4	5	5	14	6	27
	PM_{10-1}	53	83	17	20	25	28	41	109	449	27
	PM_{25-10}	30	60	6	7	11	13	21	63	319	27
Tafila-Karak	$PM_{1-0.3}$	4	2	1	1	4	4	5	12	13	65
	PM_{10-1}	55	55	18	22	28	40	57	191	291	65
	PM_{25-10}	84	116	7	14	27	47	95	306	670	65

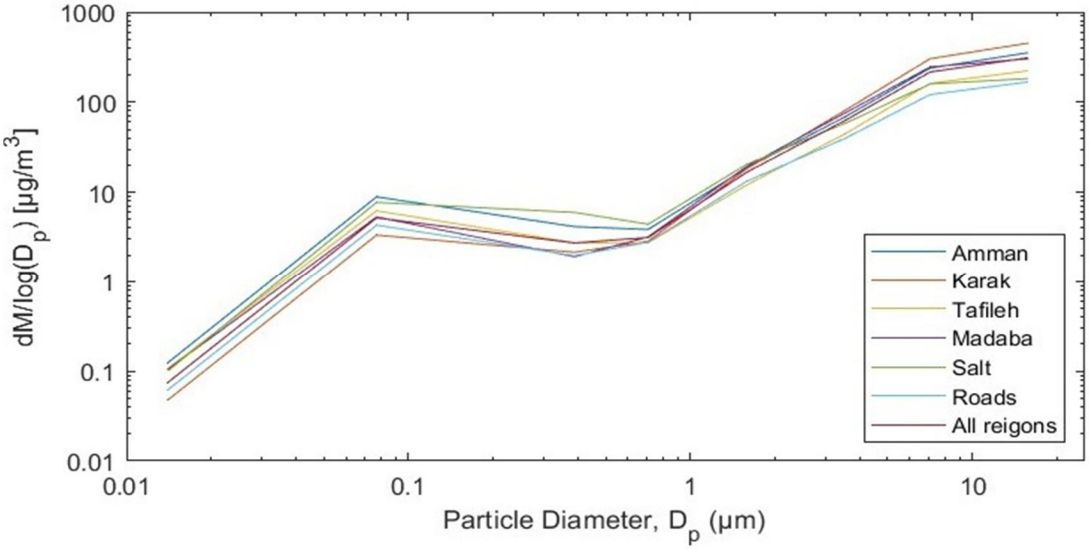

FIG. 4. Average particle mass size distributions (n_M^0) derived across cities and along main roads.

On the main roads, the highest average concentration was observed on the Amman-Salt Road (~15 µg m^{-3}), which connects two urban areas close to each other. Then there is the Amman-Madaba road and the Desert Road (~9 µg m^{-3}), which are sometimes exposed to dust

storms that occur during this period of the year. As for the lowest average concentration, it was on the Karak-Madaba road (~2 μg m^{-3}). On other roads, the average $PM_{1\text{-}0.01}$ concentrations ranged between (5 μg m^{-3} and 7 μg m^{-3}).

The average $PM_{2.5}$ concentration within Amman, especially near the University of Jordan and the areas around it, was about 19 μg m^{-3} (Table 5) This average increased as we went to the southwest side, where the average $PM_{2.5}$ concentration was 21 μg m^{-3} in Marj Al-Hamam, and 34 μg m^{-3} in Naour, likely due to nearby small industrial complexes and the movement of heavy machinery. This concentration did not decrease when we headed west to Salt (19 μg m^{-3}). In Madaba, the concentration was 15 μg m^{-3}. We observed that the concentration of $PM_{2.5}$ in the city center was high and then decreased when we moved south to Theban. The average concentrations continued to decrease as we moved south to Karak and Tafila (12 μg m^{-3} and 13 μg m^{-3}, respectively).

On the main roads, the highest concentrations were on the Amman-Salt road and the Amman-Madaba road (22 μg m^{-3} and 17 μg m^{-3}, respectively). The lowest concentrations (8 μg m^{-3}) were recorded on the road between Madaba and Karak, the Tafila-Karak road, and on the road between Ghor and Tafila, likely due to similar mountainous geography. The average concentrations on the road between Amman and Karak and the Dead Sea Road (industrial areas) were 13 μg m^{-3}. The reason for the increase in the average concentration is the presence of industrial complexes situated along these routes.

Comparison of $PM_{2.5}$ and PN_1 concentrations indicated a positive linear relationship (Fig. 5), suggesting that emissions of both $PM_{2.5}$ and PN_1 likely originate from similar sources.

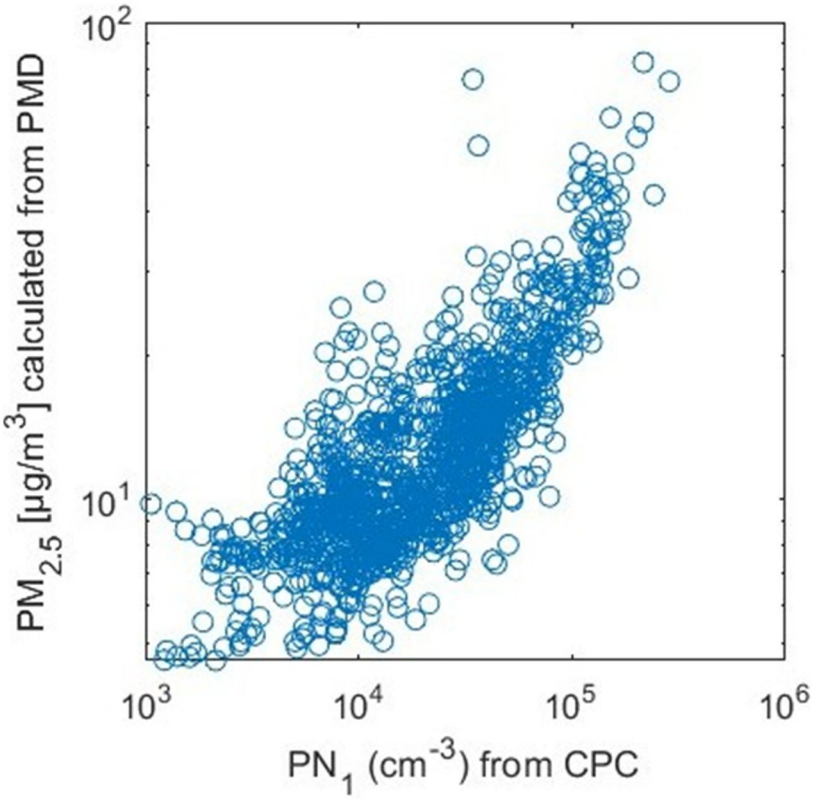

FIG. 5. A comparison between the PN_1 concentrations and calculated $PM_{2.5}$ concentrations.

Additionally, $PM_{2.5}$ concentrations were measured using the LCS device. The use of LCS devices in making measurements is a good addition to the study. In fact, three low-cost sensitive devices were used, and then the results of the three devices were averaged. This leads to more accurate results, as it was found that there is a variation in the levels of $PM_{2.5}$ concentrations from one region to another (Fig. 6). The average $PM_{2.5}$ concentrations measured with the LCS in Amman and Salt ranged between 11 µg m^{-3} and 13 µg m^{-3}, while in Karak and Madaba they ranged between 12 µg m^{-3} and 14 µg m^{-3}. The lowest concentration was in Tafila (~7 µg m^{-3}). On the main roads, the highest average concentration was on the Madaba-Karak road and the lowest on the Tafila-Karak road. This is largely consistent with the results of PMD.

Comparing the $PM_{2.5}$ concentrations calculated from the PMD with the $PM_{2.5}$ concentrations that were measured by the LCS devices in all regions included in the study showed a positive linear relationship (Fig. 7). In some areas, such as Karak, Madaba, and many areas within the governorates, and on some main and secondary roads, there was a match or convergence in the $PM_{2.5}$ concentrations measured by the LCS devices and the $PM_{2.5}$ concentrations calculated from the PMD. This means that the LCS devices can be relied upon to measure the $PM_{2.5}$ concentrations with the same efficiency as the AeroTrak device.

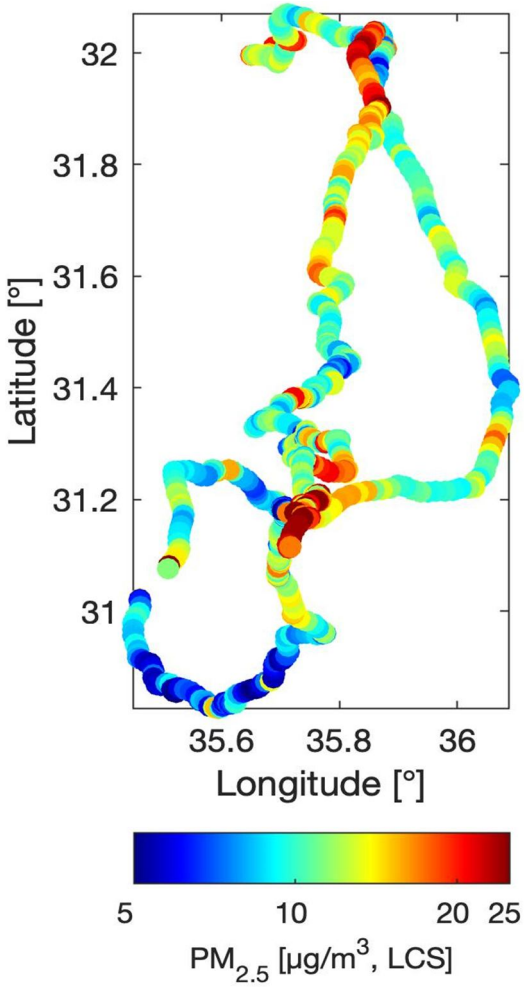

FIG. 6. Fine particulate matter ($PM_{2.5}$) concentrations plotted on the measurement routes.

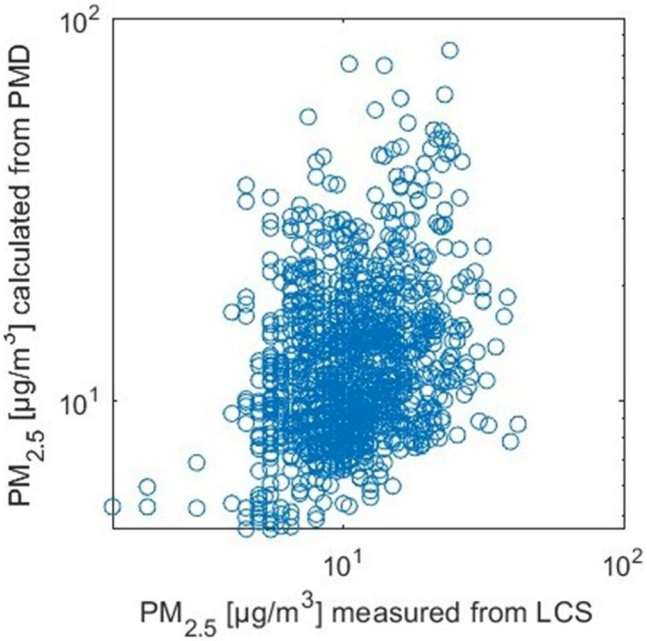

FIG. 7. A comparison between the $PM_{2.5}$ concentrations measured by the low-cost sensors (LCS) and calculated $PM_{2.5}$ concentrations.

TABLE 5. Average $PM_{2.5}$ concentrations measured by the LCS device compared to the calculated $PM_{2.5}$ concentrations (here marked as PMD).

Location			mean	Std.	min	5%	25%	Median	75%	95%	max	#
Cities	Amman	LCS	11	6	2	5	6	9	17	23	27	284
		PMD	19	12	5	8	11	15	22	45	82	284
	Karak	LCS	13	6	5	6	9	12	16	26	39	430
		PMD	12	5	7	8	9	11	14	21	55	430
	Madaba	LCS	14	3	10	10	12	13	16	19	22	52
		PMD	15	7	8	8	10	14	17	28	39	52
	Tafila	LCS	7	3	5	5	6	6	7	14	17	31
		PMD	13	5	5	7	10	12	16	20	25	31
	Salt	LCS	13	3	8	10	12	13	15	19	20	74
		PMD	19	10	13	14	14	15	20	35	75	74
Roads	Amman-Salt	LCS	11	1	10	10	10	11	11	12	13	10
		PMD	21	5	16	16	17	19	25	28	29	10
	Amman-Madaba	LCS	15	1	13	14	14	15	16	17	17	21
		PMD	17	5	10	11	14	15	21	26	27	21
	Madaba-Karak	LCS	10	2	7	8	9	10	12	13	14	71
		PMD	13	7	5	7	8	11	16	29	43	71
	R(Desert)	LCS	12	2	9	10	11	12	14	15	15	21
		PMD	9	3	5	6	6	8	10	14	15	21
	Qatrana-Karak	LCS	12	3	7	8	9	11	14	18	19	45
		PMD	8	1	7	7	7	8	8	10	11	45
	Karak-Dead sea	LCS	9	2	6	7	8	9	10	12	15	74
		PMD	10	5	6	7	7	9	11	21	37	74
	Dead sea industry	LCS	12	7	5	6	9	10	12	24	42	49
		PMD	13	10	5	6	8	11	15	20	76	50
	Dead sea- Tafila	LCS	6	1	5	5	5	6	6	8	9	26
		PMD	8	4	5	5	5	7	9	16	21	27
	Tafila-Karak	LCS	8	3	5	5	7	8	10	15	18	65
		PMD	8	2	5	5	7	8	9	13	17	65

4. Conclusion

We evaluated aerosol concentrations (including particle number, mass, and size distribution) in northwestern Jordan (Amman, Salt, Madaba, Tafila, and Karak) using a simple mobile setup during April 2022.

The submicron particle number (PN_1) concentration was highest in Amman (4.6×10^4 cm^{-3}), followed by Salt (4.4×10^4 cm^{-3}), Karak (2.0×10^4 cm^{-3}), and Tafila (4.1×10^4 cm^{-3}). On the main roads, the highest PN_1 was on Amman-Salt road (6.6×10^4 cm^{-3}), followed by the road between Amman and Salt (3.9×10^3 cm^{-3}). The lowest PN_1 (6.4×10^3 cm^{-3}) was observed on the road between Madaba and Karak via Dhiban. On other roads considered in this study, the concentrations varied between 1.5×10^4 cm^{-3} and 3.1×10^4 cm^{-3}. The mean micron particle number ($PM_{10\text{-}1}$) concentrations varied between 2 and 5 cm^{-3} on roads and 3–5 cm^{-3} in cities.

Similar to the PN concentrations findings, the micron particulate mass ($PM_{10\text{-}1}$) concentrations were higher across the cities than on main roads, except for the road between Amman and Madaba. Karak and Madaba had the highest $PM_{10\text{-}1}$ concentrations of ~128 μg m^{-3} and ~112 μg m^{-3}, respectively, whereas Amman had the lowest $PM_{10\text{-}1}$ concentrations of ~34 μg m^{-3}. The concentrations on the road between Amman and Madaba (mean value ~120 μg m^{-3}), were the highest, whereas the main road from Amman through Qatrana towards Karak had the lowest $PM_{10\text{-}1}$ concentrations (lower than 32 μg m^{-3}).

Karak had the highest $PM_{10\text{-}25}$ concentrations (~180 μg m^{-3}), whereas Salt had the lowest $PM_{10\text{-}25}$ concentrations (~73 μg m^{-3}). Concentrations were also high along the Jordan Valley road (~143 μg m^{-3}), but low on the main road from Amman through Qatrana towards Karak and the road between Al-Ghor and Al-Tafila (lower than 34 μg m^{-3}).

The average concentrations of $PM_{2.5}$ decreased as we moved southward from Amman. It was found that the topography and geographical nature, as well as the presence of industrial clusters, have a clear effect on the difference in concentrations from one region to another.

The PN and PM concentrations observed in this study suggest that traffic emissions are the main sources of aerosols in cities. The southernmost locations (i.e. Karak) were mainly affected by dust aerosols due to local sand re-suspension from desert areas.

This study's primary limitation is the short measurement duration. Further research is needed to improve understanding of the air pollution in Jordan. Currently, there is a lack of information about aerosol temporal and spatial variations, the impact of aerosols on weather and vice versa, and trends in dust outbreaks. Such information can be gathered via long-term measurements as well as extensive short-term measurement campaigns. Measurements of the particle size distribution are also needed to understand the dynamic behavior of particulate matter. Furthermore, physical and chemical characterizations are highly needed to better understand the toxicity and health effects, as well as the formation and transformation processes of air pollution.

For future research, we strongly recommend conducting long-term aerosol measurements at several sites throughout the country, complemented by extensive and repeated mobile measurement campaigns.

Acknowledgments

This study was supported by the Deanship of Scientific Research (DSR) at the University of Jordan. This work was conducted as part of a close collaboration between the University of Jordan and the Institute for Atmospheric and Earth System Research (INAR) at the University of Helsinki.

References

[1] Lohmann, U. and Feichter, J., Atmos. Chem. Phys., 5 (2005) 715.

[2] Boman, J., Shaltout, A. A., Abozied, A. M., and Hassan, S. K., X-Ray Spectrom., 42 (2013) 276.

[3] Rushdi, A. I., Al-Mutlaq, K. F., Al-Otaibi, M., El-Mubarak, A. H., and Simoneit, B. R. T., Arabian J. Geosci., 6 (2013) 585.

[4] Dada, L., Mrad, R., Siffert, S., and Saliba, N.A., J. Aerosol. Sci., 66 (2013) 187.

[5] Alam, K., Mukhtar, A., Shahid, I., Blaschke, T., Majid, H., Rahman, S., Khan, R., and Rahman, N., Aerosol. Air Qual. Res., 14 (2014) 1851.

[6] Alam, K., Trautmann, T., Blaschke, T., and Subhan, F., Remote Sens. Environ., 143 (2014) 216.

[7] Gherboudj, I. and Ghedira, H., Int. J. Climatol., 34 (2014) 3321.

[8] Hussein, T., Al-Ruz, R. A., Petäjä, T., Junninen, H., Arafah, D.-E., Hämeri, K., and Kulmala, M., Aerosol. Air Qual. Res., 11 (2011) 109.

[9] Hussein, T., Boor, B. E., dos Santos, V. N., Kangasluoma, J., Petäjä, T., and Lihavainen, H., Aerosol. Air Qual. Res., 17 (2017) 1875.

[10] Hussein, T. and Betar, A., Jordan J. Phys., 10 (2017) 51.

[11] Hussein, T., Dada, L., Hakala, S., Petäjä, T., and Kulmala, M., Atmosphere, 10 (2019) 710.

[12] Hussein, T., Saleh, S. S. A., dos Santos, V. N., Abdullah, H., and Boor, B.E., Atmosphere, 10 (2019) 323.

[13] Hussein, T., Halayaka, M., Al-Ruz, R. A., Abdullah, H., Mølgaard, B., and Petäjä, T., Jordan J. Phys., 9 (2016) 31.

[14] Basha, G., Phanikumar, D. V., Kumar, K. N., Ouarda, T. B. M. J., and Marpu, P. R., Remote Sens. Environ., 169 (2015) 404.

[15] Saliba, N. A., Kouyoumdjian, H., and Roumié, M., Atmos. Environ., 41 (2007) 6497.

[16] Roumie, M., Chiari, M., Srour, A., Sa'adeh, H., Reslan, A., Sultan, M., Ahmad, M., Calzolai, G., Nava, S., Zubaidi, Th., Rihawy, M. S., Hussein, T., Arafah, D.-E., Karydas, A. G., Simon, A., and Nsouli, B., Nucl. Instrum. Methods Phys. Res. B, 371 (2016) 381.

[17] Tadros, M. T. Y., Madkour, M., and Elmetwally, M., Renew. Energy, 174 (1999) 339.

[18] Moustafa, M., Mohamed, A., Ahmed, A.-R., and Nazmy, H., J. Adv. Res., 6 (2014) 827.

[19] Hussein, T., Juwhari, H., Al Kuisi, M., Alkattan, H., Lahlouh, B., and Al-Hunaiti, A., Arabian J. Geosci., 11 (2018) 617.

[20] Hussein, T., Li, X., Al-Dulaimi, Q., Daour, S., Atashi, N., Viana, M., Alastuey, A., Sogacheva, L., Arar, S., Al-Hunaiti, A., and Petäjä, T., Aerosol. Air Qual. Res., 20 (2020) 2780.

[21] Hussein, T., Atashi, N., Sogacheva, L., Hakala, S., Dada, L., Petäjä, T., and Kulmala, M., Atmosphere, 11 (2020) 79.

[22] Hussein, T., Li, X., Bakri, Z., Alastuey, A., Arar, S., Al-Hunaiti, A., Viana, M., and Petäjä, T., Atmosphere, 13 (2022) 197.

[23] Al-Momani, I. F., Daradkeh, A. S., Haj-Hussein, A. T., Yousef, Y. A., Jaradat, Q. M., and Momani, K.A., Atmos. Res., 73 (2005) 87.

[24] Jiries, A., Environmentalist, 23 (2003) 205.

[25] von Schneidemesser, E., Zhou, J., Stone, E. A., Schauer, J. J., Qasrawi, R., Abdeen, Z., Shpund, J., Vanger, A., Sharf, G., Moise, T., Brenner, S., Nassar, K., Saleh, R., Al-Mahasneh, Q. M., and Sarnat, J.A., Atmos. Environ., 44 (2010) 3669.

[26] Abdeen, Z., Qasrawi, R., Heo, J., Wu, B., Shpund, J., Vanger, A., Sharf, G., Moise, T., Brenner, S., Nassar, K., Sarnat, J. A., and Schauer, J. J., Sci. World J., 2014 (2014) 78704.

[27] Hussein, T., Puustinen, A., Aalto, P. P., Mäkelä, J. M., Hämeri, K. and Kulmala, M., Atmos. Chem. Phys., 4 (2004) 391.

Volume 17, Number 4, 2024. pp. 437-442

Jordan Journal of Physics

ARTICLE

Investigation of Electrochemically Modulated Fluorescent Cresyl Violet Molecules for Biosensing Application Using an Electrochemical Surface Plasmon Resonance

Aymen H. Qatamin

Department of Applied Physics, Tafila Technical University, Tafila 66110, Jordan.

Doi: **https://doi.org/10.47011/17.4.6**

Received on: 20/02/2023; *Accepted on: 17/04/2023*

Abstract: In this work, the potential-modulated fluorescent of cresyl violet molecules was investigated under an applied electric step potential using the electrochemical surface plasmon resonance (EC-SPR) technique. The EC-SPR device employed in the study consisted of two detection units: a reflected optical intensity detection unit and a fluorescence detection unit. Both units were used simultaneously to optimize the fluorescence signal and achieve the highest fluorescence intensity. The results show that the fluorescence intensity of the cresyl violet molecules changes during the step potential. This study demonstrates that cresyl violet molecules are suitable candidates for biosensing applications using the EC-SPR technique based on the detection of fluorescence differences between their reduced and oxidized states. This research opens up a new avenue to using this class of dyes in electrochemically modulated SPR fluorescence-based biosensors.

Keywords: Electrochemical surface plasmon resonance.

1. Introduction

Electrochemical surface plasmon resonance EC-SPR is a technique that combines the principles of surface plasmon resonance SPR and electrochemistry to detect and analyze chemical and biological interactions at the interface between a metal surface and an electrolyte solution [1, 2]. This technique has been widely used in various fields such as biosensing, bioelectronics, and materials science [3-7].

Recently, we have developed an EC-SPR approach for detecting immune responses, which employs a sandwich assay and utilizes a redox probe to generate an optically modulated electric signal [8]. This technique enables the identification of the H5N1 strain of avian influenza A virus, with a minimum detection limit of 300 pM. We posit that combining a sandwich assay with an electrochemically modulated SPR fluorescent sensor could yield significant benefits, potentially leading to a breakthrough in the field of EC-SPR sensing. As opposed to modulated absorbance measurements, the fluorescent intensity grows from the negligible background, and the SPR enhances the electromagnetic field to more effectively excite the fluorophores. Additionally, the metal film acts as an efficient blocker to reduce the background interference from the excitation light source.

In this work, we have investigated the use of electrochemically modulated fluorescent cresyl violet molecules as candidates for biomarkers in an EC-SPR device. Cresyl violet, a member of the oxazine class of dyes, has been found to have high fluorescence quantum yields and long-lived excited states, making it a potentially useful compound for energy and electron transfer

Corresponding Author: Aymen H. Qatamin **Email**: aymen.qatamin@ttu.edu.jo

reactions [9]. Additionally, cresyl violet has been observed to exhibit reversible redox behavior, undergoing a quasi-reversible reduction/ oxidation reaction in an aqueous solution [10, 11]. The platform of the device was created using a layer of gold (Au, 35 nm) and indium tin oxide (ITO, 10 nm). The Au film was chosen to improve the sensitivity of the SPR and to ensure the SPR platform's stability for spectroelectrochemical measurements. On the other hand, ITO was employed to prevent the metal surface from quenching the fluorescence.

2. Experimental Methods

2.1. Experimental Setup

Figure 1 illustrates the EC-SPR device with two detection units.

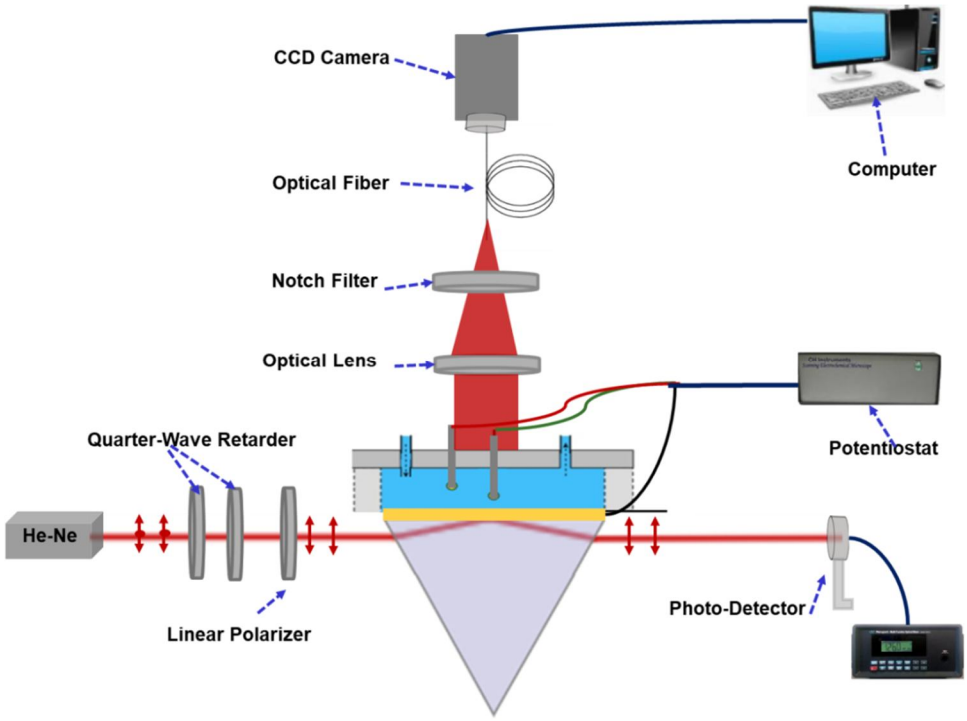

FIG. 1. Schematic of an EC-SPR device, where P-polarized light from a He-Ne laser is generated using two quarter-wave retarders and a linear polarizer to excite plasmons. The reflected optical intensity is measured by a photo-detector, and electrical control is achieved through a potentiostat with three electrodes. Additional setup for collecting fluorescence data includes a monochromatic CCD camera for spectrally resolved measurements.

An electrochemical flow cell was designed with three electrodes. The SPR surface served as the working electrode, while a platinum rod and silver/silver chloride (1 M potassium chloride) electrodes were utilized as the reference and counter electrodes. The flow cell was equipped with a 60-degree equilateral prism, which was optically connected to the SPR surface using index matching gel with a refractive index of 1.52. The setup was then fixed on a rotational stage to adjust the angle of incidence. A He-Ne laser beam with a wavelength of 595 nm (Newport Corporation, Irvine, CA USA) was utilized along with two quarter-wave retarders and a linear polarizing element to generate linearly polarized light with TM polarization. Then, the polarized light was directed towards the prism to excite the plasmon. This enables the fluorescent molecules close to the surfaces to be excited through the surface plasmons' evanescent field. The setup has two detection units: the reflected optical intensity detection unit and the fluorescence detection unit. The reflected optical intensity detection unit employed a photo-detector to monitor the reflected light at varying incidence angles. The fluorescence detection unit was mounted towards the base of the prism and rotated with the prism. The fluorescence emission from the sample surface was collected by a lens and passed through a notch filter to eliminate the transmitted laser light. The fluorescence emission was then directed to an optical fiber and coupled to the CCD camera (Hamamatsu, C5405-01). The electric potential applied to the working electrode was controlled by a potentiostat (CS350, CorrTest, China), and a computer with specialized software was used to acquire and process the data.

2.2. Preparation of the EC-SPR Surface

To assemble cresyl violet molecules on the surface, the surface was functionalized using self-assembled monolayers (SAMs) of MPA (3-mercaptopropionic acid from Sigma-Aldrich). Initially, the surface was immersed in a 10 mM MPA solution in ethanol for 48 hours [12, 13]. Afterward, the surface was rinsed with ethanol and DI water and then dried gently using N_2 gas. The surface coated with MPA was subsequently placed in an electrochemical flow cell. After that, to activate the carboxylate groups on the MPA coating, a mixture of 0.02 M EDC (1-ethyl-3-(3-dimethylaminopropyl)-carbodiimide hydrochloride obtained from Sigma-Aldrich) and 0.04 M NHS (N-hydroxysulfosuccinimide, also from Sigma-Aldrich) was flowed into the flow cell for 1 hour [14]. Subsequently, a solution of 500 nM cresyl violet molecules was injected and kept in the flow cell for half an hour, after which any unbound cresyl violet molecules were removed by rinsing with a solution of 2.0 M PBS pH = 6.2 (phosphate buffered saline from Sigma-Aldrich). Finally, the adsorbed cresyl violet molecules on the platform were stabilized using cyclic voltammetry (CV) in the potential range of -0.75 to 0.2 V at a scan rate of 0.03 V/s.

2.3 EC-SPR Measurements

The study focuses on three specific measurements. The first measurement involved using CV modulation to confirm the presence of immobilized cresyl violet molecules at the device interface. A modulation of the potential was performed on the surface, ranging from -0.75 V to 0.2 V at a rate of 0.03 V/s, while a photo-detector was used to observe the reflected light that was electrically modulated at a fixed angle. In the second measurement, angular reflectance experiments were performed to obtain the SPR curve, while the fluorescence detection unit was used for the optimization of the fluorescence signal and getting the highest fluorescence intensity. A rotation stage was used to control the incident angle of light, while the reflected light was monitored at different incidence angles with the photo-detector. Simultaneously, the fluorescence intensities were measured at six different incident angles. In the third measurement, fluorescence measurements were performed with modulated potential, while ensuring that the angle of incidence was set to maximize fluorescence intensity. The electric potential applied to the working electrode was regulated using a potentiostat, while the fluorescence detection unit monitored the fluorescence intensities at a fixed angle.

3. Results and Discussion

3.1 CV Scan

The immobilization of cresyl violet molecules in the EC-SPR surface was demonstrated using a CV technique with a potential range of -0.75 to 0.2 V at a scan rate of 0.03 V/s.

Figure 2 illustrates the reflectance response obtained for cresyl violet molecules absorbed onto the EC-SPR surface during the CV scans.

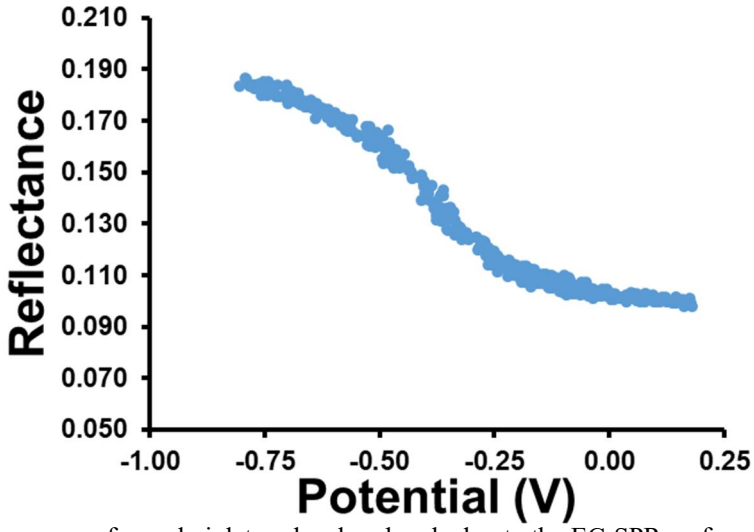

FIG. 2. Reflectance response of cresyl violet molecules absorbed onto the EC-SPR surface during a CV scan at a rate of 0.03 V/s.

The results demonstrate an evident and reversible change in the reflectance light when the modulation potential reaches the formal potential of cresyl violet molecules (around -0.35

V), providing evidence for the existence of immobilized cresyl violet molecules at the interface of the device.

3.2 Optimization of Fluorescence Detection

To optimize the SPR curve and enhance fluorescence detection, the reflected optical intensity and fluorescence detection units were used simultaneously. After demonstrating the successful immobilization of cresyl violet molecules in the EC-SPR surface, the SPR curve was determined. Figure 3 (left y-axis) shows the reflectance over a range of different incident angles.

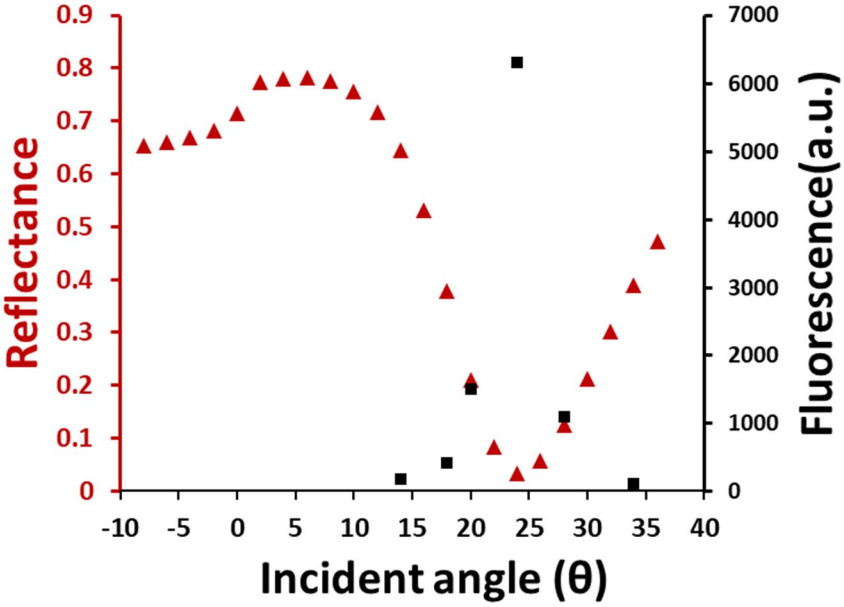

FIG. 3. The full curve of the SPR reflectance is shown on the left y-axis, while the fluorescence signal at six different incident angles is displayed on the right y-axis.

Then, the fluorescence signal at six different incident angles was measured. Figure 4 illustrates the measurement of fluorescence, covering a spectral range of 580 to 740 nm.

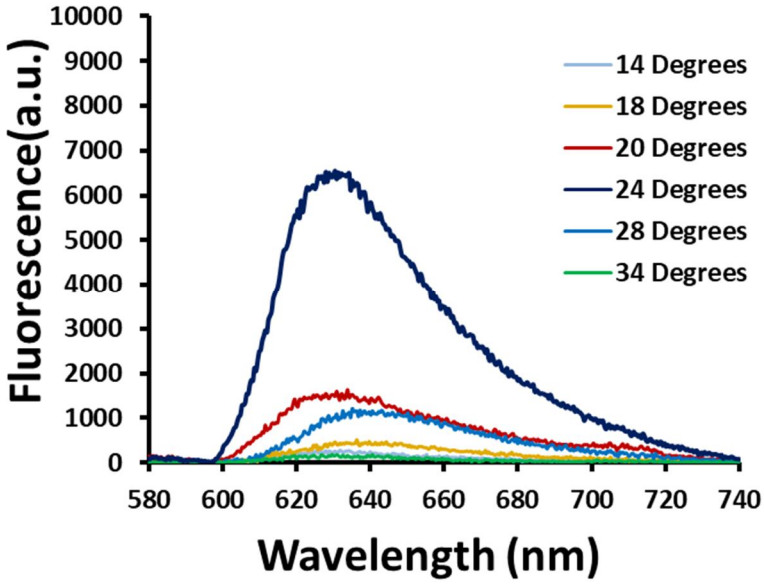

FIG. 4. Fluorescence signals at six different incident angles, covering a spectral range from 580 to 740 nm.

To better understand the relationship between the fluorescence intensity and the incident angle, the values of the highest intensity of fluorescence at six different incident angles were

plotted against the incidence angle on the same SPR curve graph (Fig. 3, right y-axis). The results demonstrate that the fluorescence intensity is influenced by the incident angle and that the highest value of the fluorescence signal was observed at the resonance angle (24 degrees). These findings confirm that maintaining a fixed incident angle at the resonance angle is crucial for improving and enhancing the sensitivity of fluorescence detection.

3.3 Potential-modulated Fluorescence Spectroscopy Using EC-SPR

To determine if cresyl violet molecules could potentially be used as a modulated fluorescent probe for biosensing applications, a potential step technique was applied. The incident angle was fixed at the resonance angle (24 degrees), which produces the highest fluorescence intensities. First, a 20 mM PBS pH 6.2 solution was introduced to the flow cell to measure the background, and the fluorescence spectrum was recorded. Next, a 500 nM cresyl violet solution in 20 mM PBS pH 6.2 was injected into the flow cell for half an hour. After rinsing the flow cell, fluorescence spectra were recorded at different electric potential values: 0.1, -0.1, -0.2, -0.3, and -0.6 V. Finally, the background was subtracted from the fluorescence spectrum at each specific electric potential step. The data are shown in Fig. 5.

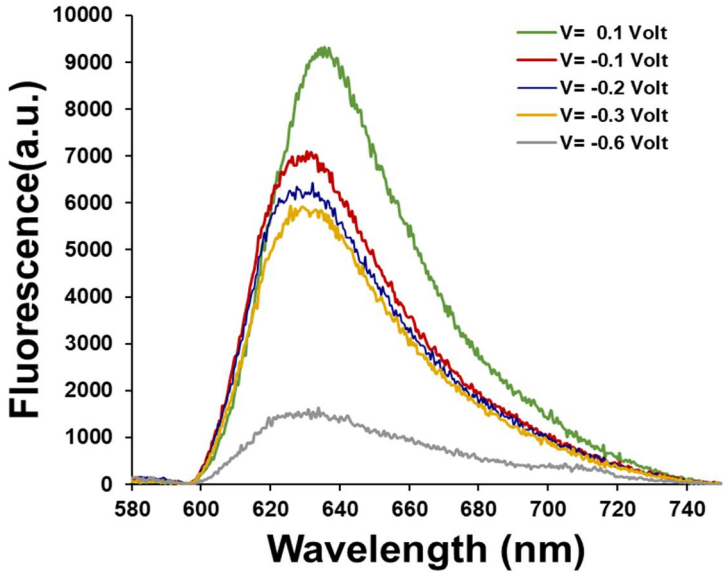

FIG. 5. Fluorescence spectrum of 500 nM cresyl violet under step potential modulation on EC-SPR surface.

The results indicated that the fluorescence intensity of cresyl violet changed during the potential step. A strong fluorescence spectrum was recorded at 0.1 V (green curve), indicating that most of the cresyl violet was in the oxidized state, as the oxidized state of cresyl violet produces very strong fluorescence [12]. In contrast, a weak fluorescence spectrum recorded at -0.6 V (grey curve) indicated that most of the cresyl violet molecules were in the reduced state, as the reduced state of cresyl violet produces very weak or no fluorescence.

The ability to detect and measure the change in fluorescence intensity of cresyl violet using the EC-SPR technique will establish a new technology for immuno-biosensor-based approach that allows for direct, highly sensitive detection of human pathogens with minimal background signal. This has the potential to be a significant contribution to the field of biosensing, as the ability to directly detect and quantify human pathogens can have important applications in medical diagnosis and public health. Additionally, reducing background signals can improve the sensitivity and specificity of biosensors, making them more reliable and accurate.

4. Conclusion

In conclusion, the study presents the investigation of electrochemically modulated fluorescence of cresyl violet molecules under applied electric step potentials. The results show that the fluorescence intensity of the cresyl violet molecules changes during the step potential, indicating the reversible redox behavior of these molecules. The capability of detecting a modulated fluorescence signal from the cresyl violet molecules makes them a promising candidate for bio-sensing applications using the EC-SPR technique.

References

[1] Lu, J., Wang, W., Wang, S., Shan, X., Li, J., and Tao, N., Anal. Chem., 84 (1) (2012) 327.

[2] Liang, W., Wang, S., Festa, F., Wiktor, P., Wang, W., Magee, M., LaBaer, J., and Tao, N., Anal. Chem., 86 (19) (2014) 9860.

[3] Fang, Y., Wang, W., Wo, X., Luo, Y., Yin, S., Wang, Y., Shan, X., and Tao, N., J. Am. Chem. Soc., 136 (36) (2014) 12584.

[4] Fang, Y., Wang, H., Yu, H., Liu, X., Wang, W., Chen, H.-Y., and Tao, N. J., Acc. Chem. Res., 49 (11) (2016) 2614.

[5] Shan, X., Díez-Pérez, I., Wang, L., Wiktor, P., Gu, Y., Zhang, L., Wang, W., Lu, J., Wang, S., Gong, Q., Li, J., and Tao, N., Nat. Nanotechnol., 7 (10) (2012) 668.

[6] Dallaire, A. M., Patskovsky, S., Vallée-Bélisle, A., and Meunier, M., Biosens. Bioelectron., 71 (2015) 75.

[7] Ribeiro, J. A., Sales, M. G. F., and Pereira, C. M., TrAC Trends Anal. Chem., 157 (2022) 116766.

[8] Qatamin, A. H., Ghithan, J. H., Moreno, M., Nunn, B. M., Jones, K. B., Zamborini, F. P., Keynton, R. S., O'Toole, M. G., and Mendes, S. B., Appl. Opt., 58 (11) (2019) 2839.

[9] Rurack, K. and Spieles, M., Anal. Chem., 83 (4) (2011) 1232.

[10] Kreller, D. I. and Kamat, P. V., J. Phys. Chem., 95 (11) (1991) 4406.

[11] Lei, C., Hu, D., and Ackerman, E. J., Chem. Commun. (Camb), (43) (2008) 5490.

[12] Michota-Kaminska, A., Wrzosek, B., and Bukowska, J., Appl. Spectrosc., 60 (7) (2006) 752.

[13] Mendes, R. K., Freire, R. S., Fonseca, C. P., Neves, S., and Kubota, L. T., J. Braz. Chem. Soc., 15 (2004) 849.

[14] Wilson, A. J., Molina, N. Y. and Willets, K. A., J. Phys. Chem. C, 120 (37) (2016) 21091.

Volume 17, Number 4, 2024. pp. 443-451

Jordan Journal of Physics

ARTICLE

Investigation Study on the Zn Doping Effect on the Structural and Morphological Characteristics of Fe_2O_3 Thin Films for Future Gas Sensor Applications

Jamal M. Rzaij, Wisam D. Jalal and **Ahmed M. Ahmed**

Department of Physics, College of Science, University Of Anbar, Ramadi, Iraq.

Doi: **https://doi.org/10.47011/17.4.7**

Received on: 17/02/2023; *Accepted on: 01/05/2023*

Abstract: In this work, thin films of undoped hematite (α-Fe_2O_3) and Fe_2O_3 doped with various concentrations of Zn (2, 4, 6, and 8 at.%) were deposited on a glass substrate using the chemical spray pyrolysis technique. The effect of Zn ions on the structural, topographical, morphological, and chemical properties of hematite was investigated. Structural analysis revealed hematite phase crystallization with a hexagonal crystal structure, with crystallite sizes ranging from 36.7 to 50.2 nm. Topographical analysis showed surface features where atoms aggregated to form hill- and plateau-like structures, free of cracks. Grain sizes ranged from 43 to 80 nanometers. As the concentration of Zn dopant increased, there was an observed increase in both surface roughness and root-mean-square values. Morphological analysis indicated a porous microstructure with surface porosity increasing as Zn concentration rose. The average particle size increased from 86 to 114 nm at a Zn concentration of 8 at.%. Therefore, it can be concluded that the hematite doped with Zn^{2+} exhibits promising characteristics for utilization in gas sensor devices.

Keywords: Thin film, Fe_2O_3, Zinc concentration, Doping effect, Structural, AFM, Spray pyrolysis.

PACs: 87.15.-v, 68.47.Pe.

Introduction

Nanocrystalline oxides have recently gained significant attention of researchers due to their high surface area-to-volume ratio, which enhances their ability to absorb a significant amount of radiation falling on the material and convert it into electric current, as in solar cells [1], or to adsorb oxygen atoms on the film surface and affect the electrical conductivity, as in gas sensor devices [2]. Hematite ferric oxide (α-Fe_2O_3) is one such semiconductor oxide, known for its low toxicity, biocompatibility, structural stability, and soft ferromagnetic properties at ambient temperatures [3, 4]. As a result, α-Fe_2O_3 applications in photocatalysts [5], solar cells [6], lithium-ion batteries [7], and gas sensors [8] have been widely investigated.

Several methods are used today to modify materials for their intended purposes [9]. These methods include ion doping, shape control, heterostructure construction, and catalyst addition. Ion doping and shape control are useful and effective methods to improve the physical and chemical characteristics of semiconductor oxide thin films [10]. Ti doping effect on Fe_2O_3 photoactive electrodes was presented by Zandi *et al.* [11]. They have found that the Ti dopant atoms improve the photoelectric properties of the Fe_2O_3 thin film in a study on the Ti doping role on the Fe_2O_3 photoelectrochemical performance. The sensing capability of the Zn-doped microcubes of Fe_2O_3 which were produced via the hydrothermal method was characterized by

Corresponding Author: Jamal M. Rzaij **Email**: sc.jam72al@uoanbar.edu.iq

Song *et al*. [12]. The results of the study indicate that the use of Zn makes it possible to adjust the Debye length of the fabricated sensor, increasing the sensitivity of the Fe_2O_3 thin film sensor. The hydrothermal synthesis of Sn-doped hematite nanoparticles was discussed by Lam *et al.* [13]. Their study outcomes revealed that the Sn-doped Fe_2O_3 has the imminent capability of effectively participating in the photocatalytic degradation of inorganic dyes, such as those found in wastewater.

Fe_2O_3 is an example of few semiconductors with a precise valence band position for the evolution or dissociation of oxygen, making it a promising catalytic material. However, due to the rapid recombination of charge carriers, the catalytic activity of α-Fe_2O_3 remains much lower, reducing its effectiveness in optoelectronic and sensing devices [5]. Numerous methodologies have been developed to address this challenge. One feasible approach involves doping α- Fe_2O_3 with additional metal ions as a way of reducing this limitation. Doping with metals like zinc (Zn), titanium (Ti), chromium (Cr), aluminum (Al), nickel (Ni), and cobalt (Co) at the Fe site influences hematite's physical and catalytic properties [14].

The impact of zinc cation on hematite's structural, electrical, and optical characteristics is emerging as a topic of scientific interest. Substituting Fe^{3+} with Zn^{2+} induces an electrical charge disparity within the crystal structure (hematite host lattice). To preserve charge neutrality, this substitution may trigger one or more mechanisms: conversion of Fe^{3+} to Fe^{2+}, generation of cation vacancies, and subsequent occupation of oxygen vacancies. According to a study conducted by Velev *et al.* [15], Zn^{2+} influences the electronic properties of hematite by producing a hole in the valence band of oxygen. The additional hole produced from the zinc ion with a charge of 2+ is positioned on the neighboring oxygen sites, thereby creating an acceptor level that is located below the Fermi energy level. The delocalization of this hole makes it a promising candidate for exhibiting high conductivity. Incorporating Zn 2+ ions facilitates the electron hopping mechanism through Fe^{3+}–Fe^{2+} pairs while altering the physical characteristics of α-Fe_2O_3. Moreover, zinc cation (Zn^{2+}) investigation has been frequently addressed due to its potential to enhance the carrier lifetime and expand the absorption range of hematite Fe_2O_3 catalysts by conducting Zn-doping [16].

Based on these principles, this study synthesizes undoped and Zn-doped Fe_2O_3 thin films via chemical spray pyrolysis to investigate the effects of varying Zn concentrations on the structural, topographical, morphological, and elemental properties of Fe_2O_3 thin films. Structural properties were analyzed using X-ray diffraction (XRD), surface topography was examined with atomic force microscopy (AFM), surface morphology was studied with scanning electron microscopy (SEM), and elemental composition was assessed with energy-dispersive X-ray spectroscopy (EDX).

Experimental Work and Procedure

Precursor solutions of undoped ferric oxide (Fe_2O_3) and Fe_2O_3 doped with various Zn concentration ratios (2, 4, 6, and 8 at.%) were prepared separately and deposited on glass substrates using the low-cost technique of chemical spray pyrolysis. All powders used in the study were purchased from BDH Chemical Ltd., Poole, England, with a purity of 99%.

A 0.01 molar iron chloride solution was prepared by dissolving 0.198 g of iron chloride dihydrate ($FeCl_3.2H_2O$) in 100 ml of distilled water. As a source of zinc ions, a 0.01 M zinc chloride solution was synthesized by dissolving 0.086 g of zinc chloride dihydrate ($ZnCl_2.2H_2O$) in 50 ml of distilled water. The ferric precursor solution was doped with the zinc precursor solution at different concentrations, and then the obtained solutions were mixed using the ultrasonic bath for 15 minutes at 30°C.

Glass substrates were cleaned using distilled water and ethanol before the prepared solutions were deposited under a set of controlled conditions: a deposition temperature of 350 °C, a spray time of 10 seconds, a stop time of 25 seconds, a distance of 3 ± 28 cm between the substrate and the atomizer nozzle, and a gas carrier (oxygen) pressure of 3 millibars with 2 ml per minute flow rate. The prepared films were then annealed for one hour at 450°C in air. Scanning electron microscopy images and ImageJ software were used to determine the thickness of the deposited films, which were measured as 180, 205, 228, 239, and 254 nm for the undoped and Fe_2O_3 films doped with 2, 4, 6, and 8 at.% Zn, respectively.

Result and Discussion

Structural Properties

The X-ray diffraction pattern of undoped and Fe_2O_3 doped with varying Zn concentrations thin films (Fe_2O_3:Zn) are shown in Fig. 1. The results demonstrate that the deposited Fe_2O_3 films are polycrystalline and indexed to hexagonal phase. The diffraction peaks at (104), (110), (113), (024), (116), (018), and (214) correspond to diffraction angles (2-theta) of 33.161º, 35.627º, 40.86º, 49.461º, 54.072º, 57.608º, and 62.432º, respectively, in accordance with the reference JCPDS 96-900-0140.

Additionally, it was shown that the (104) diffraction peak is the sharpest, indicating the dominating directionality of crystal growth, in agreement with the findings in the literature [17, 18]. The absence of diffraction peaks aside from those associated with hematite indicates that Zn atoms have been incorporated into the α-Fe_2O_3 matrix. Consequently, the presence of dopant atoms affects the crystallinity without altering the hexagonal structure of hematite.

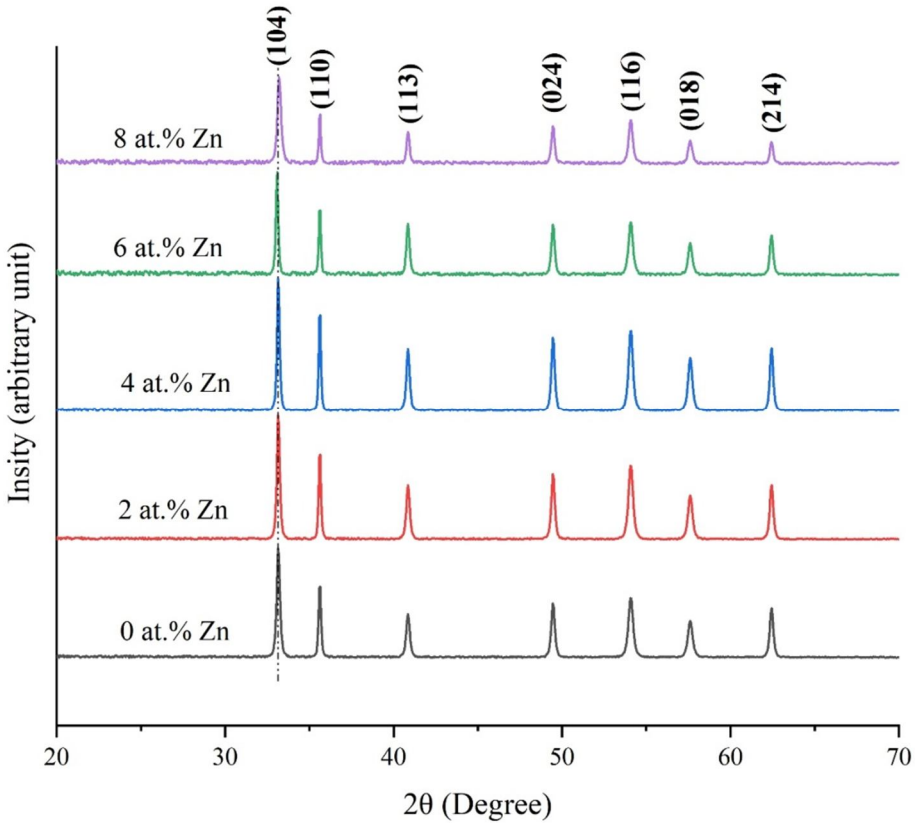

FIG. 1. XRD spectra of undoped Fe_2O_3 and Fe_2O_3 doped with 2, 4, 6, and 8 at.% Zn.

Figure 2 depicts the Rietveld refinement of the X-ray diffraction data, utilizing the full-pattern fitting method, for both undoped and Fe_2O_3 doped with 8 at.% Zn. The Rietveld refinement method is utilized to conduct a quantitative analysis of the Fe_2O_3 crystalline phase compared to the amorphous phases of the Fe_2O_3 structure or additional minor phases. The findings obtained from Rietveld refinement reveal that the X-ray diffraction pattern of the as-deposited Fe_2O_3 film, as depicted in Fig. 2(a), exhibits a high degree of conformity with the diffraction data of the standard lines. However, the degree of conformity is reduced for the sample doped with 8 at.% Zn, as illustrated in Fig. 2(b). This suggests that the doping process successfully altered the structural characteristics of the Fe_2O_3 film [19].

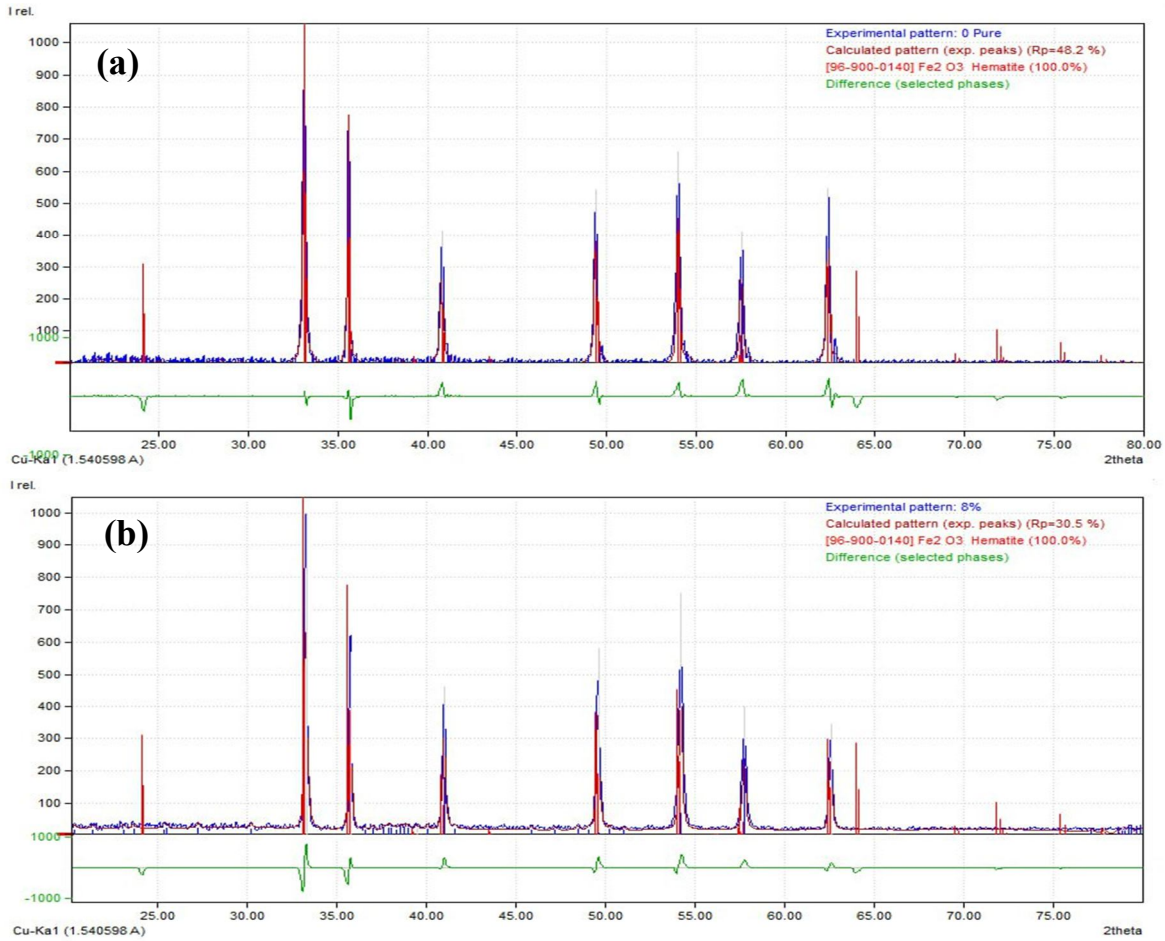

FIG. 2. Rietveld refinement of the XRD patterns of (a) as-deposited Fe_2O_3 and (b) 8 at.% Zn-doped Fe_2O_3.

XRD analysis indicates that the (104) diffraction peak experiences a shift towards the lower diffraction when Zn doping increases to 6 at.%, followed by a shift towards the higher diffraction angle at a Zn concentration of at. 8 %. The shift of XRD peaks results in variations in the lattice parameters (a and c) in addition to the unit cell volume (V), as presented in Table 1. This investigation suggests that at lower Zn doping levels (below 4 at.%), Zn atoms primarily occupy substitutional sites [20]. In comparison, higher doping concentrations of Zn occupy partial interstitial sites or segregate on the surface, distorting the host lattice structure. The incorporation of Zn^{2+} ions, which are larger than Fe^{3+} ions, into the host lattice is expected to result in distortion, resulting in stress within the system [21]. The stress (σ) is calculated by using Eq. (1) [21], with results listed in Table 1. The negative stress values obtained suggest the presence of compressive stress within the system [22].

$$\sigma = \frac{c - c_\circ}{c_\circ}, \quad (1)$$

where c and $c_\circ$ are, respectively, the lattice constant from the JCPDS standard card and the results of XRD.

TABLE 1. The structural parameters of undoped Fe_2O_3 and Zn-doped Fe_2O_3 thin films.

Samples	D (nm)	Lattice constant (Å)		σ ×10^{10}	δ ×10^{-4}	V (Å^3)
		a	c	dynes/cm^2	(lines/nm^2)	
0 at.% Zn	36.7	5.035	13.731	-11.63	74.24	301.45
2 at.% Zn	40.5	5.039	13.733	-10.18	60.96	301.97
4 at.% Zn	46.1	5.042	13.736	-8.001	47.05	302.40
6 at.% Zn	50.2	5.051	13.739	-5.81	39.68	303.54
8 at.% Zn	31.8	5.003	13.711	-26.18	98.88	297.19

Depending on the dominant diffraction peak (104), the crystallite size (D) was calculated using Scherrer's formula, Eq. (2). The findings indicate a correlation between the concentration of Zn dopant and the crystallite size: as Zn concentration increases up to 6 at.%, the crystallite size increases, then decreases when the Zn dopant concentration increases to 8 at.%, as demonstrated in Table 1.

$$D = \frac{k\lambda}{\beta \cos\theta}, \quad (2)$$

where $k \approx 0.9$ is the shape factor, λ = 1.54060 Å is the Cu kα radiation wavelength, β (measured in radians) is the full width at half maximum (FWHM) of the diffraction peak, and θ is Bragg's angle of the diffraction. The increase in crystallite size corresponds to the inclusion of Zn, which is a significant factor in the growth of crystals and Fe_2O_3 crystallization. The increase in crystallite size can be attributed to replacing Fe^{3+} ions with Zn^{2+} ions, which are comparatively larger. Thu trend observed in the crystallite size of Fe_2O_3 samples with higher Zn doping is consistent with the findings reported in earlier studies on ZnO doped with Y, CeO_2 doped with Mn, and ZnO doped with Mg [23–25]. Moreover, the evaluation of the dislocation density (δ) which is derived as ($\delta = 1/D^2$) offers additional insights into the defects in the prepared samples. The dislocation density for the 6 at.% Zn sample was relatively low, which indicates a high quantity of defects that can be used to improve the sensor sensitivity. However, the defects tend to be decreased at the doped sample of at. 8% Zn, as shown in Table 1. This suggests that, up to 6 at.% Zn, dopant atoms are well-integrated into the lattice, increasing crystallite size and reducing dislocation density. With a doping concentration of around 8 at.% of Zn, the size of the crystallites decreases as the number of dislocations density increases. This indicates that the dopant atoms pour into the interstitial lattice sites, making the crystal arrangement less regular and the dislocation density higher [26]. Through the changes in dislocation density and stress seen in the prepared samples, it could be inferred that the materials contain lattice structure defects, which impact the mechanical properties of the synthesized thin films. As crystallite size is crucial for the interaction of metal oxide thin films with gas molecules, optimizing crystallite structure and size can improve sensor response to target gases [27].

Atomic Force Microscopy (AFM)

The surface topography of the deposited thin films was analyzed using AFM to determine the topography of the films' surfaces, average grain size (Gs), average roughness (Ra), and root-mean-square roughness (Rs). Figure 3 displays 3D AFM images of Fe_2O_3 and Zn-doped Fe_2O_3 at various Zn concentrations. The AFM images reveal that the atoms are spread without cracks along the surface of the films, aggregating into a hill-and-plateau-like structure. The height of the hills grows as doping with zinc increases, which contributes to an increase in surface roughness rate [28]. High-roughness surfaces contribute to enhanced sensor performance by increasing surface area, increasing atom diffusion, and thereby creating more potential sites for surface reactions and oxygen molecule adsorption [29]. Table 2 confirms that the surface topography of Fe_2O_3 is strongly affected by Zn doping, which increases the Gs and Ra as the Zn at.% increases. The aggregation of smaller grains into larger grains is enhanced by increasing film thickness, increasing grain size, and, consequently, surface roughness [30]. Furthermore, the rise in root-mean-square roughness indicates that the grain growth on the glass substrates occurred perpendicular to the film's surface during the deposition process [31]. This is supported by the notable color variation observed in the 3D AFM images, which indicates that the deposited atoms exhibit variations in growth regarding their vertical positioning. Increases in particle size contribute to increased sensor response by increasing the area exposed to gas molecules, increasing the rate of interaction between the surface of the sensor film and the molecules of the target gas [32].

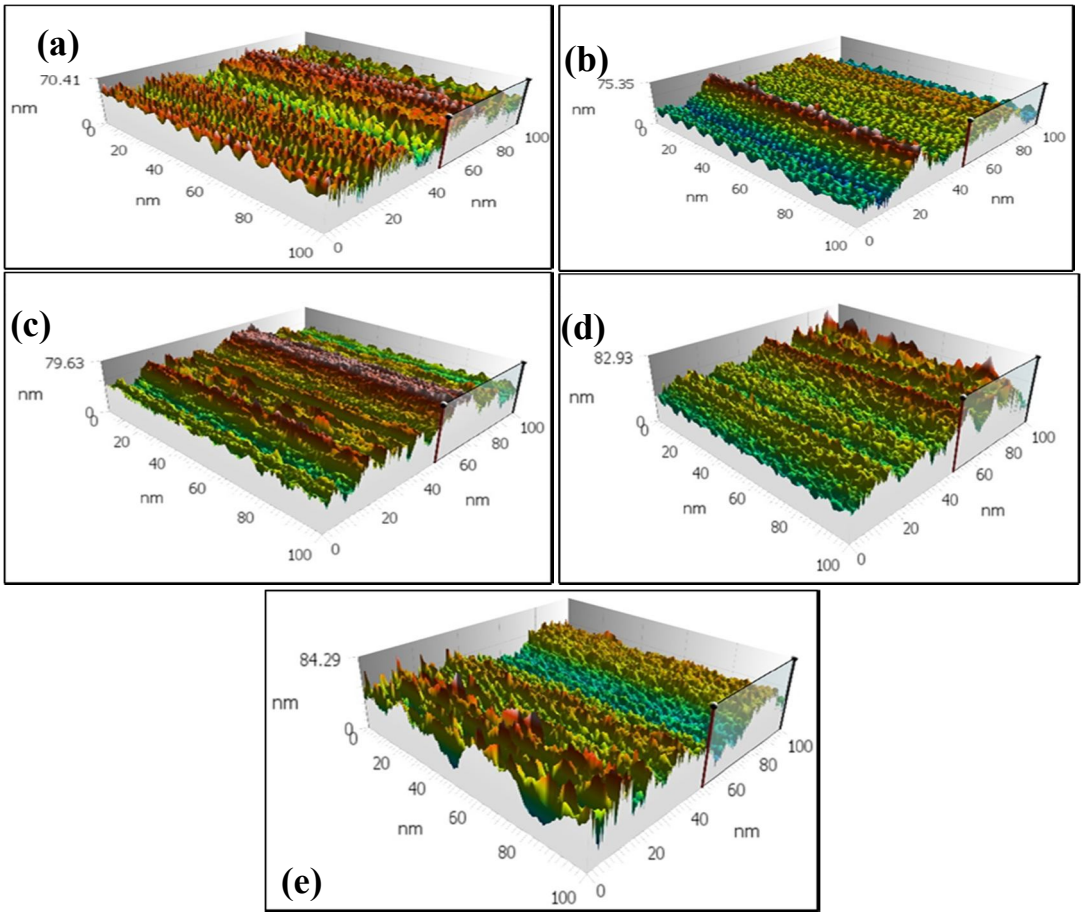

FIG. 3. AFM images of (a) Fe_2O_3 and Zn-doped Fe_2O_3: (b) 2 at.% Zn, (c) 4 at.% Zn, (d) 6 at.% Zn, and (e) 8 at.% Zn thin films.

TABLE 2. AFM Parameters of Fe_2O_3:Zn thin films.

Samples	Gs (nm)	Ra (nm)	Rs (nm)
0 at.% Zn	43	70.41	9.77
2 at.% Zn	48	75.35	10.92
4 at.% Zn	60	79.63	11.05
6 at.% Zn	67	82.93	12.06
8 at.% Zn	80	84.29	12.27

Morphological Analysis

SEM micrographs of undoped Fe_2O_3 and doped with various Zn concentrations are shown in Figs. 4 (a)-4(e). The microstructure of the film doped with 8 at.% Zn exhibits a significantly porous surface. It can be concluded that the porosity of films increases as the concentration of Zn doping increases. The high porosity of the film surface in gas sensor applications provides more accessibility to the bulk of the film, increasing the active area for gas adsorption on the film surface [27]. The average particle size of the samples was estimated using ImageJ software. According to the findings, the as-deposited Fe_2O_3 film exhibits an average particle size of 43 nm. However, the samples doped with varying concentrations of Zn, namely 2 at.%, 4 at.%, 6 at.%, and 8 at.%, exhibit average particle sizes of 68, 81, 97, and 114 nm, respectively. The doped film of 8 at.% Zn exhibits larger grains, contributing to its high porosity nature [33] and consequent increase in the average roughness. This observation is consistent with the results obtained from the AFM analysis. The findings indicate that zinc doping plays a crucial role in shaping the surface morphology of the deposited films.

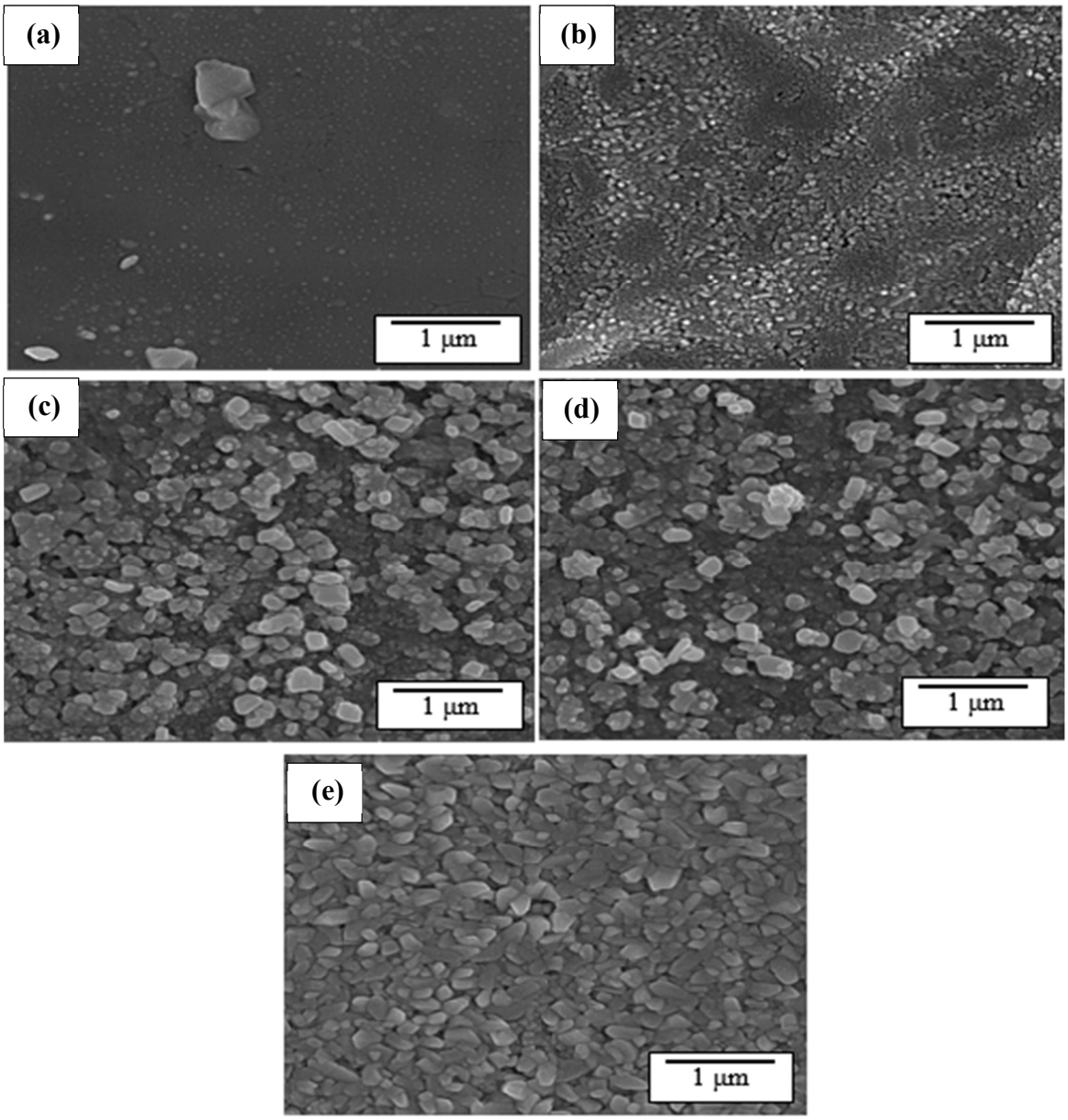

FIG. 4. SEM micrograph images of (a) as-deposited Fe_2O_3 and (b)-(e) Fe_2O_3:Zn thin films.

Energy Dispersive X-ray Spectroscopy (EDX)

Energy dispersive X-ray spectroscopy (EDX) measurements were conducted to verify the existence of Zn within the synthesized Fe_2O_3 thin film. Table 3 presents the elemental analysis results for Fe_2O_3:Zn nanostructured thin films, while Fig. 5 displays the EDX spectrum of Fe_2O_3 with 8 at.% Zn doping.

TABLE 3. EDX data of Zn-doped Fe_2O_3 thin films at various Zn at.%.

Samples	Percentage of the elements% (Wt%)			
	Fe	O	Zn	Zn/Fe ratio
0 at.% Zn	68.4	29.4	2.2	0.032
2 at.% Zn	65.5	27.7	5.8	0.089
4 at.% Zn	51.6	33.3	15.1	0.293
6 at.% Zn	57.8	26.0	22.07	0.382
8 at.% Zn	45.3	29.5	25.2	0.556

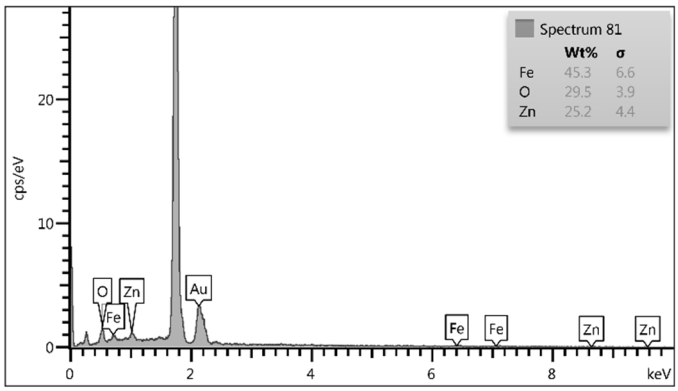

FIG. 5: EDX spectrum of Fe_2O_3 doped with 8 at.% Zn thin film.

The EDX spectrum indicates the absence of additional elements in the deposited thin films, except for the gold element. This finding verifies the high purity of the samples and the successful incorporation of zinc ions into the Fe crystal lattice. The gold coating used on non-conductive substrates for typical SEM applications may be responsible for the Au peak in the EDX spectrum. As shown in Table 3, increasing Zn concentrations corresponded to a decrease in the weight percentage of Fe and an increase in the weight percentage of Zn. This pattern further confirms the successful incorporation of Zn ions into the Fe matrix.

Conclusion

In summary, thin films of undoped Fe_2O_3 and Fe_2O_3 doped with different concentrations of Zn were developed on glass substrates by chemical spray pyrolysis. The synthesized films were characterized using XRD, AFM, SEM, and EDX to investigate the effects of Zn dopant on various Fe_2O_3 characteristics. XRD analysis confirmed that all the films showed a nanocrystalline hematite phase. Variations in diffraction peak intensity and crystallite size demonstrated the influence of zinc ions on the structural properties of the Fe_2O_3 film. AFM analysis showed that zinc doping increased film thickness, grain size, and surface roughness. SEM micrographs indicated that the porosity of the films exhibited an enhancement as the Zn doping concentration increased, with the film doped with 8 at.% Zn exhibiting the highest degree of porosity, providing an active surface area conducive to gas sensing applications. The findings suggest that the most optimal conditions for fabricating Fe2O3 thin films as sensor devices are achieved with 8 at.% Zn doping.

Conflict of Interest

The authors declare that they have no known competing financial interests or personal relationships that could have influenced the work reported in this paper.

References

[1] Fang, S., Chen, B., Gu, B., Meng, L., Lu, H., and Li, C.M., Mater. Adv., 11 (2) (2021) 3629.

[2] Hanfoosh, S.M. and Hassan, N.K., Iraqi J. Sci., 9 (60) (2019) 2009.

[3] Al-Haj, M. M., Jordan J. Phys., 2 (12) (2019) 133.

[4] Al-Hwaitat, E.S., Dmour, M.K., Bsoul, I., Albgour, A., Alsalti, T., Abuawad, R., Alajarmah, A., Al-Buqain, R., and Mahmood, S. H., Jordan J. Phys., 4 (14) (2021) 287.

[5] Suman, S.C., Kumar, A., and Kumar, P., Crystals, 4 (10) (2020) 273.

[6] Bouhjar, F., Mollar, M., Ullah, S., Marí, B., and Bessaïs, B., J. Electrochem. Soc., 2 (165) (2018) H30.

[7] Zhang, C., Chen, Z., Wang, H., Nie, Y., and Yan, J., ACS Appl. Nano Mater., 9 (4) (2021) 8744.

[8] Qin, Q., Olimov, D., and Yin, L., Chemosensors, 7 (10) (2022) 267.

[9] Mohsen, A. and Rzaij, J. M., J. Chem. Rev., 3 (2) (2020) 148.

[10] Chen, J., Xu, L., Li, W., and Gou, X., Adv. Mater., 5 (17) (2005) 582.

[11] Zandi, O., Klahr, B. M., and Hamann, T. W., Energy Environ. Sci., 2 (6) (2013) 634.

[12] Song, H., Sun, Y., and Jia, X., Ceram. Int., 10 (41) (2015) 13224.

[13] Lam, V.N., Vu, T.B., Do, Q.D., Le, T.T.X., Nguyen, T.D., Nguyen, T.-T.-B., Do, H.T., and Nguyen, T.T.O., J. Semicond., 12 (43) (2022) 122001.

[14] Wang, G., Ling, Y., Wheeler, D.A., George, K.E.N., Horsley, K., Heske, C., Zhang, J.Z., and Li, Y., Nano Lett., 8 (11) (2011) 3503.

[15] Velev, J., Bandyopadhyay, A., Butler, W.H., and Sarker, S., Phys. Rev. B, 20 (71) (2005) 205208.

[16] Lassoued, A., J. Mol. Struct., 1239 (2021) 130489.

[17] Mansour, S.A. and Ibrahim, M.M., J. Electron. Mater., 11 (46) (2017) 6502.

[18] Suresh, R., Giribabu, K., Manigandan, R., Stephen, A., and Narayanan, V., RSC Adv., 33 (4) (2014) 17146.

[19] Ibrahim, I.M., Rzaij, J.M., and Ramizy, A., Dig. J. Nanomater. Biostructures, 4 (12) (2017) 1187.

[20] Ibraheam, A.S., Rzaij, J.M., and Arshad, M. K. M., J. Electron. Mater., 1 (52) (2023) 414.

[21] Vijayalakshmi, K., Renitta, A., and Karthick, K., Ceram. Int., 4 (40) (2014) 6171.

[22] Rzaij, J. M., Sensors Actuators A Phys., 363 (2023) 114748.

[23] Kumar, P., Singh, V., Sharma, V., Rana, G., Malik, H.K., and Asokan, K., Ceram. Int., 5 (41) (2015) 6734.

[24] Kumar, P., Kumar, P., Kumar, A., Meena, R.C., Tomar, R., Chand, F., and Asokan, K., J. Alloys Compd., 672 (2016) 543.

[25] Kumar, P., Singh, J.P., Malik, H.K., Gautam, S., Chae, K.H., and Asokan, K., Superlattices Microstruct., 78 (2015) 183.

[26] Rzaij, J.M., Ibraheam, A.S., and Abass, A.M., Baghdad Sci. J., 2 (18) (2021) 401.

[27] Marei, J.M., Khalefa, A.A., Abduljabbar, Q.A., and Rzaij, J.M., J. Nano Res., 70 (2021) 41.

[28] Abduljabbar, Q.A., Radwan, H.A., Marei, J.M., and Rzaij, J.M., Eng. Res. Express, 1 (4) (2022) 015028.

[29] Liu, H., Shen, W., Chen, X., and Corriou, J.-P., J. Mater. Sci. Mater. Electron., 21 (29) (2018) 18380.

[30] Rzaij, J.M. and Habubi, N.F., J. Mater. Sci. Mater. Electron., 15 (33) (2022) 11851.

[31] Ma, X., Zhao, J., Du, W., Zhang, X., and Jiang, Z., J. Mater. Res. Technol., 3 (8) (2019) 3175.

[32] Jebur, K.H., J. Pet. Res. Stud., 1 (12) (2022) 226.

[33] Payton, R.L., Chiarella, D., and Kingdon, A., Sci. Rep., 1 (12) (2022) 7531.

Volume 17, Number 4, 2024. pp. 453-459

Jordan Journal of Physics

ARTICLE

Structural, Optical, and Electrical Properties of Undoped and Zn-Doped $CaSnO_3$ Nanoparticles Synthesized by the Co-Precipitation Method

V. Balasundaram[a], **V. Balasubramanian**[b], **J. Henry**[c], **T. Daniel**[d], **K. Mohanraj**[e,f] and **G. Sivakumar** [a]

[a]*CISL, Department of Physics, Annamalai University, Chidambaram, Tamil Nadu, India.*
[b]*Department of Science & Humanities, P.S.N. College of Engineering and Technology, Tirunelveli-627152, India.*
[c]*Department of Physics, School of Engineering & Technology, Dhanalakshmi Srinivasan University, Trichy – 621 112, India.*
[d]*Department of Physics, MVJ College of Engineering, Bengaluru, Karnataka-560067, India.*
[e]*Department of Physics, Manonmaniam Sundaranar University, Tirunelveli, Tamil Nadu, India.*
[f]*Department of Physics, School of Basic and Applied Sciences, Central University of Tamil Nadu Thiruvarur, Tami l Nadu 61 0 005, India.*

***Doi:*https://doi.org/10.47011/17.4.8**

Received on: 17/02/2023; *Accepted on: 18/06/2023*

Abstract: In this work, we studied the optical properties of undoped and Zn-doped $CaSnO_3$ nanoparticles. XRD patterns revealed the formation of the orthorhombic $CaSnO_3$ structure, with a pronounced shift for doped samples. Fourier-transform infrared spectroscopy identified the presence of Ca-O and Sn-O vibrations. The bandgap of CaSnO3 was found to be 4.5 eV, with variations observed upon doping. Scanning electron microscopy images showed a polygonal morphology with size variations. In Zn doped Zn-doped $CaSnO_3$, PL spectra showed a peak shift towards the visible region compared to the undoped sample. Among the Zn concentrations, 0.02M Zn-doped $CaSnO_3$ exhibited specific capacitance of 2880 F/g, as measured from the CV curve.

Keywords: Zn doped $CaSnO_3$, Co-precipitation, Structural properties, Optical properties, Electrical properties.

Introduction

Luminescent materials have attracted significant attention because of their potential applications in various fields, including photocatalysis, solar cells, and biomedicine. $CaSnO_3$ is a promising luminescent material due to its chemical stability, low cost, and non-toxicity. Luminescent properties of $CaSnO_3$have been enhanced by doping with several rare earth elements (e.g.Sm, Nd, Er, Eu, Tm, Yb, Pr, and Tb) [1-7]. In recent years, researchers have focused on $CaSnO_3$ particles doped with transition metals for applications such as batteries [8], efficient photocatalysts for the degradation of organic dye [9], piezoelectric properties for high-temperature applications [10], magnetic and electrochemical applications [11], photocatalytic activity [12], and memory devices [13]. Manoharan *et. al.,* recently reported that hafnium (Hf^{4+})-doped $CaSnO_3$ perovskites exhibit a co-existence of

Corresponding Author: G. Sivakumar **Email**: gskdopcisl@gmail.com

ferromagnetic and diamagnetic nature [14]. To the best of our knowledge, there are few studies available on supercapacitor applications of $CaSnO_3$ nanoparticles [15,16]. Hence, in the present work, we study the effect of doping by Zn on the structural, optical, morphological, and electrochemical properties of $CaSnO_3$ particles.

Experimental Methods

Undoped and Zn-doped $CaSnO_3$ nanoparticles (with various Zn concentrations of 0.01, 0.02, and 0.03 M) were prepared by the co-precipitation method using $CaCl_2$, $SnCl_2.2H_2O$, NaOH, and $ZnCl_2$ precursors. First, 0.4M $SnCl_2.2H_2O$ and 0.8M $CaCl_2$ were mixed well with the assistance of a magnetic stirrer. Next, a 4M NaOH solution was added dropwise to the former solution (pH 12). The whole solution was stirred at 65˚C for 45 min and then filtered, washed, and dried for 24 hours. The resulting product was at 900˚C for 6 hours. For Zn-doped $CaSnO_3$ appropriate amount of $ZnCl_2$ was added into the precursor solution.

The structural, molecular vibrational, surface, optical, and electrical properties of undoped and Zn doped $CaSnO_3$ nanoparticles were examined by PANalytical XPERT-PRO diffractometer (λ=1.5406 Å; 10˚-80˚) patterns, PerkinElmer FTIR spectrometer (Spectrum Two, Model C92107, resolution 4cm^{-1}) spectra, CARL ZEISS (EVO 18) scanning electron microscopy, Shimadzu (UV-2700) UV-visible spectroscopy (200-800 nm), and electrochemical workstation (CH 1604E; three-electrode system) CV, respectively.

Results and Discussion

The XRD pattern of Undoped $CaSnO_3$ nanoparticles, calcined at 900 ºC, is given in Fig. 1(a). The XRD pattern exhibits a prominent peak at 2θ=32.08°, corresponding to the (*112*) plane of the polycrystalline orthorhombic $CaSnO_3$, consistent with the JCPDS card No.77-1797. Some sharp peaks are detected at 2θ 46.04°(*004*), 22.57°(*002*), 56.60°(*132*), and 57.55°(*312*), which also match theJCPDS card No.77-1797. For Zn-doped samples, the major crystalline peak is shifted to a lower 2θ, indicating the incorporation of Zn into the $CaSnO_3$ lattice.

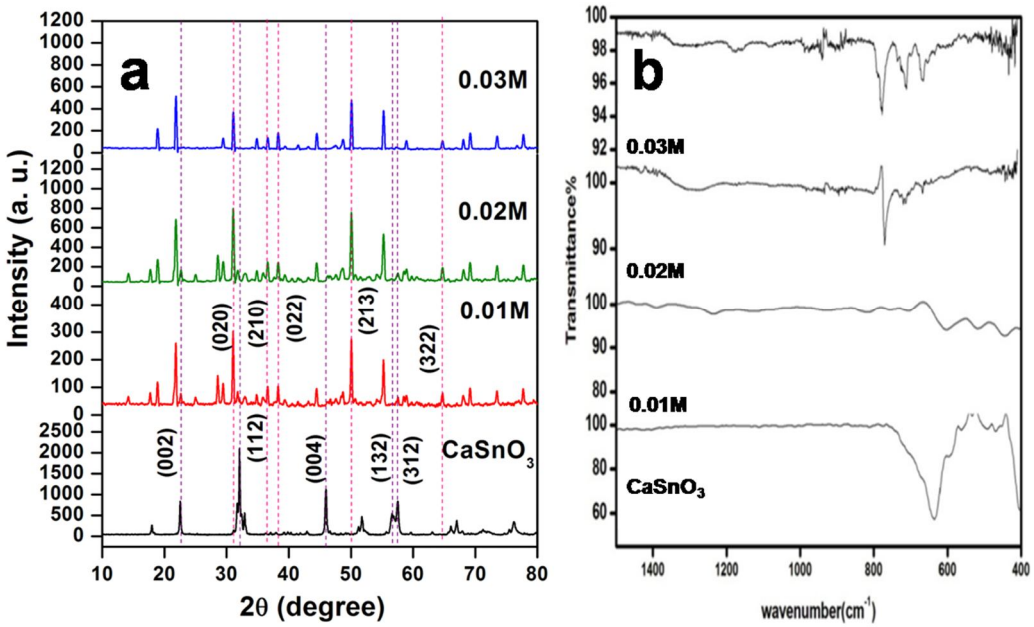

FIG.1. Zn-doped $CaSnO_3$ nanoparticles (a) XRD patterns and (b) FTIR spectra.

The average crystallite size (D) was calculated using the Scherrer formula [17]:

$$D = \frac{k\lambda}{\beta \cos\theta} \quad (1)$$

where k =0.9, λ =1.5406Å, β is the FWHM, and θ the diffraction angle.

Dislocations are imperfections in a crystal, associated with the misregistry of the lattice in one part of the crystal with respect to another part. Unlike vacancies and interstitial atoms, dislocations are not equilibrium imperfections [17]. In fact, the growth mechanism involving dislocations is a matter of importance. The

dislocation density (δ) was calculated by using the formula:

$$\delta = \frac{1}{D^2} \quad (2)$$

Stresses in the film are one of the most important unfavorable factors affecting the structural properties and can result from a geometric mismatch at boundaries between the crystalline lattices of the films and the substrate [18]. These stresses can cause microstrain (ε) in the films, calculated using the formula

$$\varepsilon = \frac{\beta cos\theta}{4} \quad (3)$$

The crystallite size was found to be 50 nm for undoped $CaSnO_3$, 0.01 M, and 0.02 M Zn-doped $CaSnO_3$ nanoparticles. For 0.03M Zn-doped $CaSnO_3$, however, it approximately doubled to 98 nm. The higher crystallite size is useful for photovoltaic applications. A similar trend is reflected in the dislocation density and microstrain values, as shown in Table 1. The dislocation density and microstrain increased with an increase in doping upto 0.02 M and then decreased for 0.03 M Zn-doping. This indicates improvement in the crystalline nature of the nanoparticles.

TABLE 1. Crystalline size, dislocation density, and microstrain in the undoped and Zn-doped $CaSnO_3$nanoparticles.

Sample	Concentration	Crystallite size (nm)	Dislocation density (10^{15})	Microstrain (10^{-3})
Undoped CaSnO3	-	50	0.39	0.68
Zn-doped CaSnO3	0.01M	50	0.40	0.68
	0.02M	49	0.41	0.69
	0.03M	98	0.10	0.34

The vibrational characteristics of the undoped and Zn-doped $CaSnO_3$ nanoparticles are shown in Fig. 1(b). Some weak bands appear around 400-670 cm^{-1} and a strong band is observed at 635 cm^{-1}, attributed to the presence of Sn-O stretching vibrations [19, 20]. The peak appearing at 564 $cm^{-1}$is due to Ca-O vibrations. FTIR analysis confirms the presence of metal oxide vibrations, consistent with findings in the literature. For 0.01 M Zn $CaSnO_3$ nanoparticles, FTIR peaks reappear around 630 cm^{-1}, 485 cm^{-1}, 1619 cm^{-1}, and 1286 cm^{-1},owing to SnO_6 vibrations, Zn-O stretching, C–H stretching vibration, and carbonate vibrations, respectively [20-22]. Similarly, 0.02 M and 0.03M Zn-doped $CaSnO_3$ nanoparticles show peaks around 485 and 670 cm^{-1}, due to the Zn-O vibrations, further confirming the incorporation of Zn into CaSnO3 lattice, as shown in the XRD patterns.

The optical characteristics of undoped and Zn-doped $CaSnO_3$ nanoparticles are shown in Fig. 2. It is observed that $CaSnO_3$ nanoparticles reach maximum absorbance at 245 nm. This result is in agreement with the report on $CaSnO_3$ nanoparticles [19]. Upon Zn doping, the absorption shifts toward shorter wavelengths, indicating a blue shift for all Zn concentrations compared to $CaSnO_3$. Additionally, the absorbance slightly decreases in the visible region.

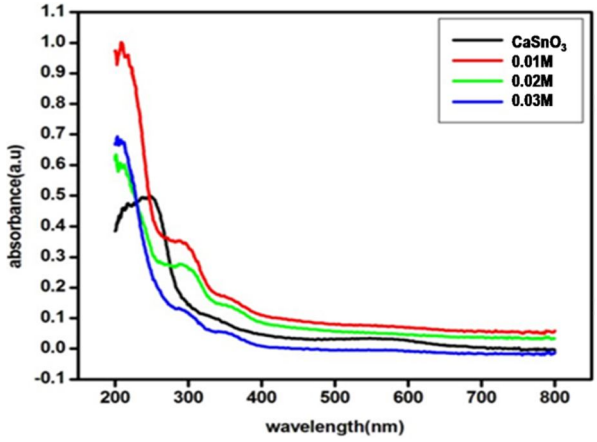

FIG.2. UV absorption spectrum for the undoped and Zn-doped $CaSnO_3$ nanoparticles.

The bandgap energy was calculated by the following equation:

$$(\alpha h\upsilon) = A\left(h\upsilon - E_g\right)^n \quad (4)$$

where 'a' is the absorption coefficient, 'hυ' is photon energy, 'A' is a parameter that depends on the transition probability, 'h' is Planck's constant, and the exponent 'n' depends on the nature of the transition during the absorption process. The value of n is 1/2, 3/2, 2, and 3 for direct allowed, direct forbidden, indirect allowed, and indirect forbidden transitions, respectively [23].

Previous experimental and theoretical studies indicated that $CaSnO_3$ is a direct bandgap semiconductor [24, 25]. Hence, in this work, we use n = ½, consistent with $CaSnO_3$ direct bandgap semiconductor nature. The bandgap of the $CaSnO_3$ sample was found to be 4.5 eV, aligning closely with the 4.2eV value reported by Mizoguchi *et al.* [26] and Sumithra *et al.* [27,]. For Zn-doped $CaSnO_3$ concentrations 0.01, 0.02, and 0.03 M, the bandgaps are approximately 4.9 , 3.7, and 5.0 eV, respectively. The spectra show a blue shift for all concentrations compared to undoped $CaSnO_3$ nanoparticles due to increased crystallite size. The blue shift is attributed to the Burnstein–Moss effect [28]. The donor Zn atoms provide additional carriers that shift the Fermi level into the conduction band so that the energy gap becomes larger. The optical absorption is slightly changed by increasing the Zn concentration as reflected in bandgap energy.

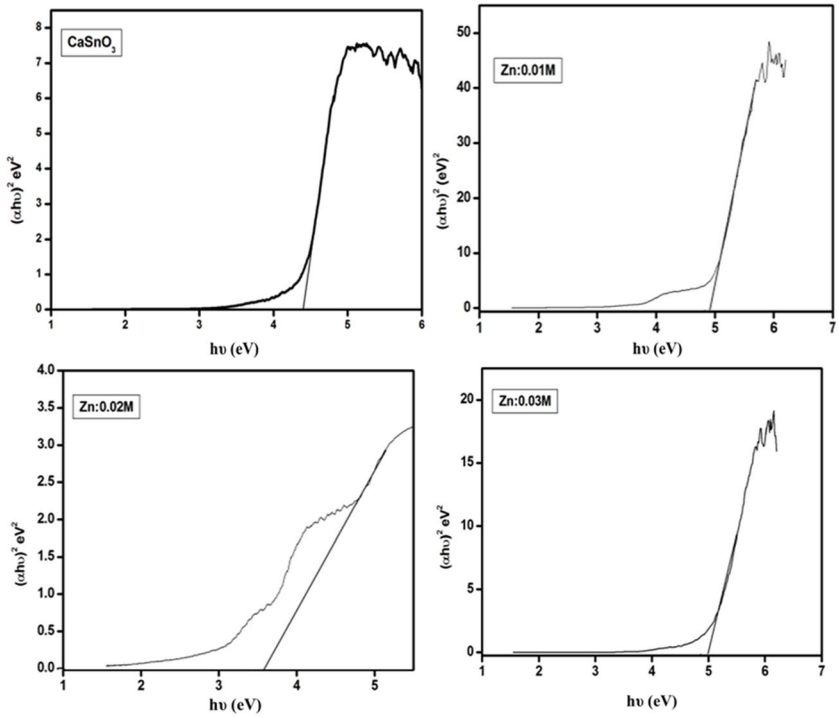

FIG. 3. Tauc plots for the undoped and Zn-doped $CaSnO_3$ nanoparticles.

SEM images of Zn-doped $CaSnO_3$ particles are shown in Fig. 4. All samples show a flower-flake-like morphology attached to each other. The average size is approximately 1.6 μm.

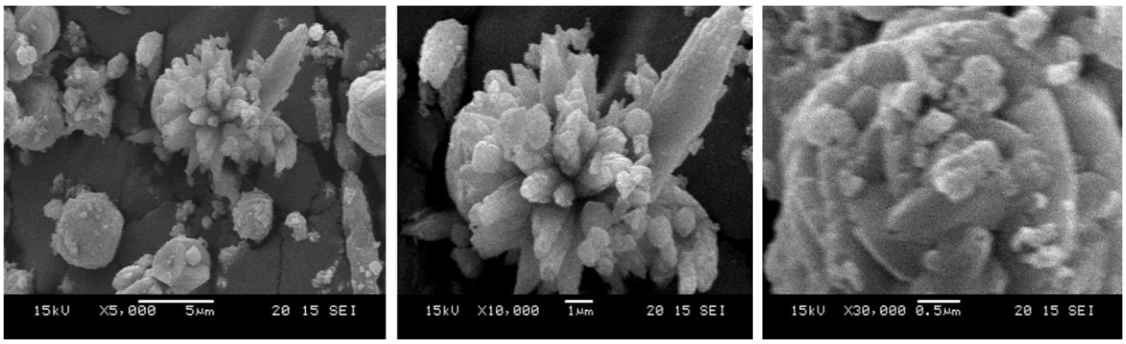

FIG. 4. SEM images of Zn-doped $CaSnO_3$ nanoparticles.

The photoluminescence (PL) properties, recorded with the excitation λ = 245nm, are shown in Fig. 5. An emission peak appears at 305 nm for the undoped $CaSnO_3$ nanoparticles. The possible defects that contribute to PL characteristics are oxygen vacancies. Secondary emission peaks at 408 and 431 nm, attributed to oxygen defects, exhibit blue emission properties [27]. For the Zn-doped samples, the emission peak is observed at 310 nm, showing a red shift compared to undoped $CaSnO_3$.

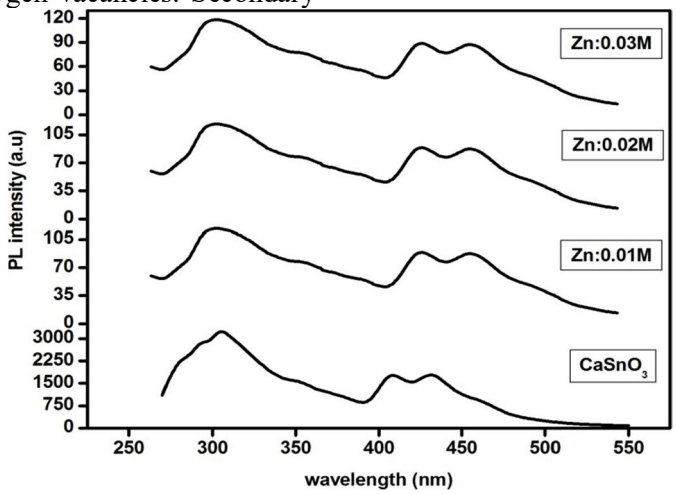

FIG.5. PL emission spectra of $CaSnO_3$ and Zn(0.01, 0.02, and 0.03M) doped CaSnO3 nanoparticles.

The CV measurements for Zn-doped $CaSnO_3$ nanoparticles (scan rates: 10, 50, 100,and 200 mV/s in 0.5M Na_2SO_4 solution; potential range: -1.6 to +1.6V vs Ag/AgCl electrode) are shown in Fig. 6. For the undoped sample (scan rate of 10 mVs^{-1}) an oxidation peak is observed at 0.92 V, and a redox peak is seen at -0.61 V. Anodic and cathodic peaks appear at -0.29 V and -0.63 V, respectively. It is noticed that the peak shifted towards a high potential with respect to scan rate. From the measurements, the specific capacitance was calculated according to the early report [29].

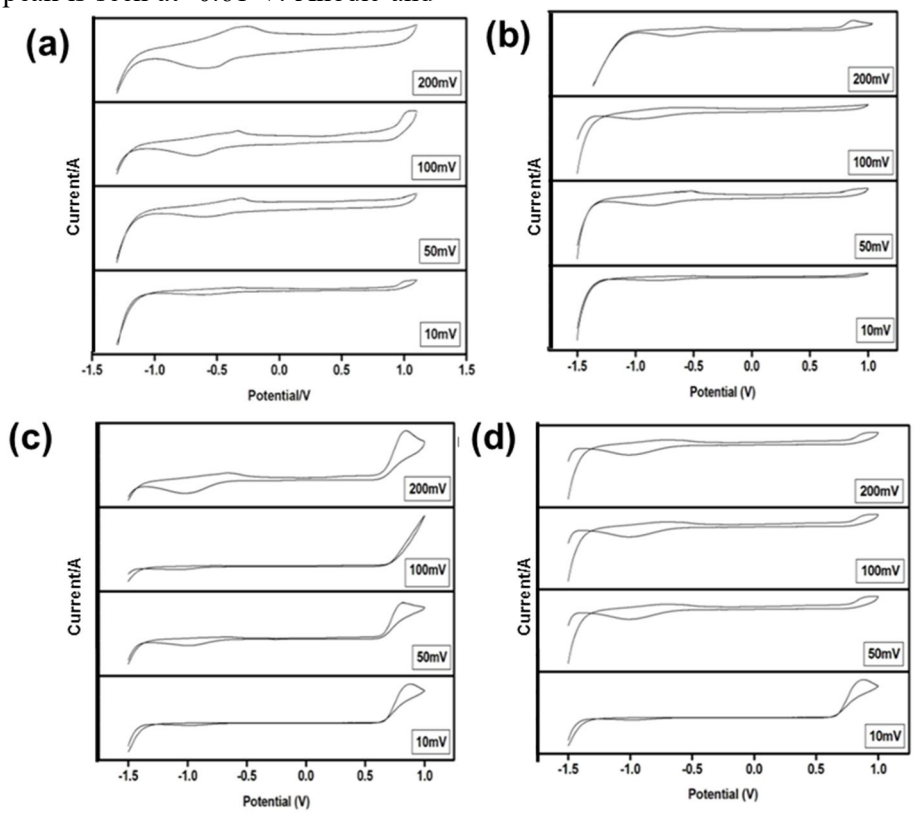

FIG.6. CV data of (a) $CaSnO_3$, (b) 0.01M, (c) 0.02M, and (d) 0.03M Zn-doped CaSnO3 nanoparticles.

At a scan rate of 10 mV s^{-1}, the $CaSnO_3$ nanoparticles have a specific capacitance of about 572 F/g, decreasing with increasing scan rates (167.2 F/g at 50mV/s, 94.6 F/g at100mV/s, and 71.1 F/g at 200mV/s). For Zn-doped $CaSnO_3$ (0.01, 0.02, and 0.03 M), the CV curves display varying loop shapes with changing Zn concentrations.The specific capacitances at 10 mV/s are 634 F/g, 2860 F/g, and 2880 F/g, respectively, decreasing similarly with higher scan rates. Among the samples, the 0.02 M and 0.03 M Zn-doped samples exhibit the highest capacitance values, suggesting that Zn-doped $CaSnO_3$ is an effective supercapacitor electrode material.

Conclusion

This paper reports on the structural, molecular vibrational, surface, optical, and electrical properties of Zn-doped $CaSnO_3$ nanoparticles synthesized via the co-precipitation method. XRD analysis confirms the formation of an orthorhombic $CaSnO_3$. The polycrystalline peak shift indicates the incorporation of Zn in the $CaSnO_3$ lattice. Fourier transform infrared spectroscopy identified the presence of Ca-O, Sn-O, and Zn-O vibrations at 564, 635, and 485 cm^{-1}, respectively. Optical absorption spectra show a blue shift across all Zn doped concentrations compared to the undoped sample, with absorption in the visible region decreasing as Zn concentration increases. The bandgap of for the $CaSnO_3$ is 4.5 eV, , while Zn doping yields bandgaps of 4.9, 3.7,and 5.0 eV for Zn concentrations of 0.01, 0.02, and 0.03 M, respectively. SEM images depict Zn-doped particles as flower-flake-like structures with an average size of 1.6µm. In Zn-doped $CaSnO_3$, PL spectra show a peak shift towards the visible region compared to the undoped $CaSnO_3$.CV analysis identifies Zn-doped $CaSnO_3$ with 0.02 M and 0.03 M Zn as optimal for use as supercapacitor electrodes.

References

[1] Gordo, V.O., Arslanli, Y.T., Canimoglu, A., Ayvacikli, M., Gobato, Y.G., Henini, M., and Can, N., Appl. Radiat. Isot., 99 (2015) 69.

[2] Saha, S., Das, S., Ghorai, U.K., Mazumder, N., Ganguly, D., and Chattopadhyay, K.K., J. Phys. Chem. C., 119 (2015) 16824.

[3] Pang, X.L., Jia, C.H., Li, G.Q., and Zhang, W.F., Opt. Mater., 34 (2011) 234.

[4] Stanulis, A., Katelnikovas, A., Bael, V.M., Hardy, A., Kareiva, A., and Justel, T., J. Lumin., 172 (2016) 323.

[5] Hu, Y., Zhou, F., Tian, X., Ji, C., Huang, Z., Wen, J., Luo, F., Chen, Z., Liu, X., and Peng, Y., Spectrochim. Acta A Mol. Biomol. Spectrosc., 243 (2020) 118799.

[6] Jin, Y., Hu, Y., Chen, L., Wang, X., Ju, G., and Mu, Z., J. Lumin., 138 (2013) 83.

[7] Stanulis, A., Katelnikovas, A., Enseling, D., Dutczak, D., Sakirzanovas, S., Bael, M.V., Hardy, A., Kareiva, A., and Justel, T., Opt. Mater., 36 (2014) 1146.

[8] Antonio, J.E., Rosas-Huerta, J.L., Cervantes, J.M., Flores, J.L., Romero, M., Carvajal, E., and Escamilla, R., Comput. Mater. Sci., 219 (2023) 112006.

[9] Venkatesh, G., Prabhu, S., Geerthana, M., Baskaran, P., Ramesh, R., and Prabhu, K.M., Optik, 212 (2020) 164716.

[10] Chen, X., Gao, P., Liu, C., Zhang, K., Huang, X., Zhang, H., Zhang, F., and Pu, Y., Céram. Int., 49 (2022) 1436.

[11] Bhat,A.A. and Tomar, R., J. Alloys Compd., 876 (2021) 160043.

[12] Wang, J., Asakura, Y., Hasegawa, T., and Yin, S., J. Environ. Chem. Eng., 10 (2022) 108169.

[13] Kumar,A., Khan,B., Singh,G., Dixit,A., Upendra Kumar, U., and Singh, M.K.,Phys. Scr., 95 (2020) 105807.

[14] Manoharan, A., Suresh, B., Kumari, A., Munisamy, M., and Krishnan, S., Solid State Commun., 360 (2023) 115033.

[15] Sharma, N., Shaju, K.M., Rao, G.S., and Chowdari,B.V.R., Electrochem. Commun.,12 (2002) 947.

[16] Sharma, Y., Sharma, N., Subba Rao, G.V., and Chowdari, B.V.R., Chem. Mater., 21 (2008), 6829.

[17] Turgut, G., Keskenler, E.F., Ayd, S., Dogan, S., Duman, S., Özçelik, S., Gürbulak, B., and Esen, B., Phys. Status Solidi A, 211 (2014) 580.

[18] Pradip, K.K., Sarma, B.K. and Das, H.L., Bull. Mater. Sci., 23 (2000) 313.

[19] Moshtaghi, S., Salavati-Niasari, M., and Ghanbari, D.,J. Nanostruct.,5 (2015) 169.

[20] Lucena, G.L., de Lima, L.C., Honório, L.M.C., de Oliveira, A.L.M., Tranquilim, R.L., Longo, E., and dos Santos, I.M.G., Cerâmica, 63(2017) 536.

[21] Parthasarathi, V. and Thilagavathi, G., Int. J. Pharm. Pharm. Sci., 3 (2011) 392.

[22] Kavitha, S., Dhamodaran, M., Prasad, R., and Ganesan, M., Int. Nano Lett., 7 (2017) 141.

[23] Hussein, H.F., Walailak J., Sci.& Tech., 11 (2014) 413.

[24] Shaili, H., Salmani, E., Beraich, M., Zidane, M., Taibi, M., Rouchdi, M., Ez-Zahraouy, H., Hassanain, N., and Mzerd, A., ACS Omega, 6 (2021) 32537.

[25] Tsega, M.and Dejene, F. B., Bull. Mater. Sci., 40(2017) 1347–1354.

[26] Mizoguchi, H., Eng, H.W., and Woodward, P.M., Inorg. Chem, 43 (2004) 1667.

[27] Sumithra, S. and Jaya, N.V., J. Mater. Sci. Mater. Electron., 29 (2018) 4048.

[28] Khan, M.A.M., Kumar, S., Khan, M.N., Ahamed, M. and Dwayyan, A.S.A., J. Lumin., 155 (2014) 275.

[29] Navale, S.T., Mali, V., Pawar, S.A., Mane, R.S., Naushad, M., Stadler, F.J., and Patil, V.B., RSC Adv., 5 (2015) 51961.

Volume 17, Number 4, 2024. pp. 461-468

Jordan Journal of Physics

ARTICLE

Effect of Strain Rate and Temperature on Mechanical Properties of Silicon Nanowire: MD Simulation Studies

S. Barik, C. Bhramarjal and **S. S. Sarangi**

Department of Physics, VSSUT, Burla, 768018, India.

Doi: **https://doi.org/10.47011/17.4.9**

Received on: 02/03/2023; Accepted on: 18/05/2023

Abstract: Silicon nanowires are of immense importance to the scientific community because of their unique properties and wide range of applications. In this work, MD simulations using MEAM potentials are employed to investigate the impact of temperature and strain rate on various mechanical properties of an ultra-thin silicon nanowire with a diameter of 3 nm. To characterize the effect of strain rate, the nanowire is subjected to strain rates varying from 0.0005 ps^{-1} to 0.05 ps^{-1} at 300 K, while the temperature effect is examined by varying it in the range of 10-700 K at a constant strain rate of 0.005 ps^{-1}. Young's modulus, yield strength, yield strain, and fracture strain of nanowire are calculated based on the variation of stress with strain. The study shows that both strain rate and temperature significantly influence the elastic and plastic characteristics of the nanowire. The strength of the silicon nanowire increases with higher strain rates and lower temperatures. To validate the chosen potential model, the Young's modulus of bulk silicon is estimated, showing good agreement with experimental values.

Keywords: MD simulations, Silicon, Nanowire, Strain rate, Young's modulus.

PACS: 68.35.Fx; 68.35.Ja.

1. Introduction

Nanoscale structures have drawn significant attention due to their unique mechanical, magnetic, electrical, optical, thermal, and other properties [1-8]. Nanoscale structures, such as nanowires (NWs), exhibit properties distinct from bulk materials due to their high surface-to-volume ratios. At these nano-dimensions, surface stresses and crystal orientations are the key factors in defining the properties. Silicon nanowire (Si NW) is one of the sought-after semiconductor NWs which has a broad spectrum of applications including in biosensors [9, 10], resonators [11], transistors [12], thermoelectric [13, 14], and electrode materials for various energy storage devices [15]. Therefore, it is essential to investigate their mechanical properties under various physical conditions.

To characterize the mechanical behavior of silicon nanowires, it is desirable to understand their tensile deformation properties under different loading conditions. Sohn and co-workers experimentally demonstrated the impact of size on various mechanical properties of Si NW [16]. Zhu *et al.* studied Si NWs' deformation and fracture mechanisms using scanning electron microscopy (SEM) [17]. They showed that the Young's modulus decreased and fracture strength increased with the decrease in the diameter of the nanowire. Tang *et al.* combined transmission electron microscopy and molecular dynamics (MD) simulations to reveal the impacts of diameter, stress state, and loading condition during tensile testing [18]. Over the past few decades, numerous experimental studies have characterized the mechanical properties of

Corresponding Author: S. S. Sarangi **Email**: sssarangi_phy@vssut.ac.in

Si NWs [18-20]. However, due to their small size, tensile testing of NWs requires sophisticated instrumentation, and it is challenging to precisely apply and measure external loads and strain at the nanoscale.

MD simulation is a computational tool for controlling external loads while examining the effects of a variety of external parameters, such as temperature, size, and strain rate. Hence, it can be used to examine the mechanical characteristics of NWs at the atomic scale [21-23]. Ivashchenko *et al.* investigated the influence of strain rate on the deformation mechanisms of Si NWs and concluded that failure strength rises linearly with a rise in the strain rate [24]. Jing *et al* highlighted the significant impact of strain rate, temperature, and size on the tensile mechanical properties of Si NWs [25]. Kang *et al* reported that the fracture mechanism of Si NWs depends on both temperature and size [26]. Moreover, theoretical simulations have also shown that Young's modulus for Si NWs increases with diameter and decreases with rising temperature [26, 27]

This study aims to provide a comprehensive understanding of the effects of strain rate and temperature on the stress-strain deformation and mechanical properties of ultra-thin Si NWs. In this context, MD simulations were conducted using modified embedded atom method (MEAM) potentials to examine the uniaxial tensile mechanical properties of a cylindrical, diamond cubic Si NW with a diameter of 3 nm across a temperature range of 10-700 K and strain rates varying from 0.0005 to 0.05 ps^{-1}. Various mechanical properties (yield strength, yield strain, fracture strain, and Young's modulus) were calculated by analyzing stress and potential energy variation with respect to strain. To address the scarcity of quantitative data and establish a theoretical basis for the applicability of Si NWs, this study further investigates the influence of temperature and strain rate on mechanical properties by analyzing atomic-level stress and strain variations.

2. Methodology

Large-scale Atomic/Molecular Massively Parallel Simulator (LAMMPS) software was used to carry out the MD simulations [28]. For the bulk Si crystal simulation, a diamond-structured bulk Si box containing 8000 atoms was created. The dimensions of the simulation box are 5.43 nm along the X, Y, and Z axes, representing the lattice directions [1 0 0], [0 1 0], and [0 0 1], respectively. Periodic boundary conditions (PBCs) were applied along the three directions to obtain the bulk structure.

For the NW studies, a cylindrical diamond cubic Si NW with a length of 10 nm (along the Z-axis) and a diameter of 3 nm containing 3567 atoms was created. Here, PBC is applied only along the Z-axis (the direction of applied strain), while shrink-wrapped boundary conditions are applied along the X and Y axes to ensure the one-dimensional NW structure.

The NW is divided into three distinct regions along its length: two grip regions, each 1 nm long at either end, where atoms are fixed to their lattice points, and a central deformable region, 8 nm in length, which contains mobile atoms. These regions are illustrated in Fig. 1, which shows a schematic representation of the initial structure of the Si NW.

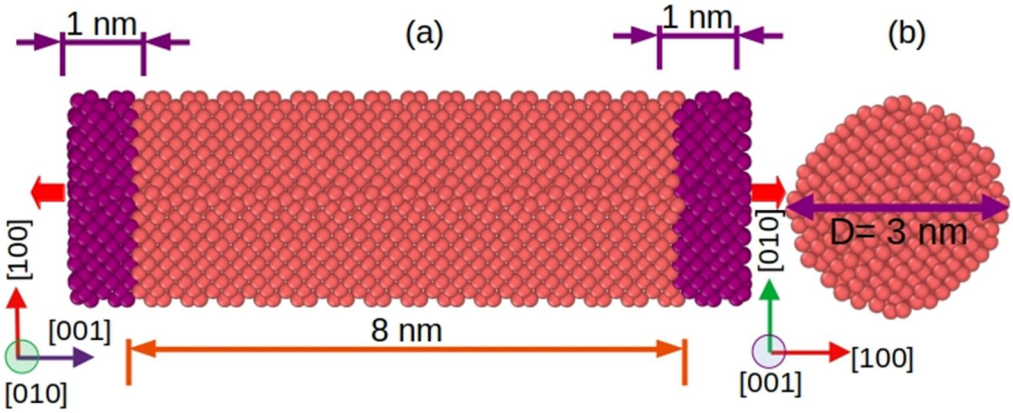

FIG. 1. (a) Side (lateral) view (b) top (transverse) view of a schematic diagram of the initial structure of the Si NW. Red horizontal arrows indicate the direction of application of tensile strain.

To begin the simulation at a given temperature, velocities are randomly assigned to the atoms according to a Gaussian distribution function. Then, the system is equilibrated for 1 ns in the NPT ensemble and the temperature is controlled by a Nosé-Hoover thermostat [29, 30]. After the equilibration period, a uniaxial tensile load at predetermined strain rates is applied along the Z-axis to create yielding and fracture in the NVT ensemble. The production time is about 1 ns. Velocity-Verlet algorithm is used for the calculations and the time step of integration is 1 fs. Visualization is carried out by using the Open Visualization Tool (OVITO) [31].

The NW is stretched along the Z-direction, and the corresponding component of the uniaxial tensile stress tensor is calculated by:

$$\sigma^{zz} = \frac{1}{\Omega}\left(-\sum_i m_i v_i^z v_i^z + \frac{1}{2}\sum_i \sum_{i \neq j} F_{ij}^z r_{ij}^z\right) \quad (1)$$

where Ω is the volume of the system, m_i is the mass, v_i is the velocity of the atom i, and F_{ij} and r_{ij} are the force and distance of separation between atoms i and j. The tensile strain along the Z-direction, e_{zz}, is determined by:

$$e_{zz} = \frac{L_z - L_0}{L_o} \quad (2)$$

where L_z is the instantaneous length under tension and L_0 is the initial length of the NW.

Interatomic potential plays a pivotal role in MD simulations and selection of it is crucial. Baskes extensively developed MEAM potential parameters to extend the embedded atom model (EAM) to account for bonding directionality [32-34]. Here, MEAM parameters developed by Lee et al. [32] are used for Si-Si interactions. In the MEAM model, the total energy is represented as:

$$E = \sum_i \left[F_i(\bar{\rho}_i) + \frac{1}{2}\sum_{j(\neq i)} S_{ij}\phi_{ij}(R_{ij})\right] \quad (3)$$

where F_i denotes the embedding function, ρ_i represents the background electron density at site i, S_{ij} is the screening function, and $\varphi_{ij}(R_{ij})$ stands for the pair interaction term between atoms i and j separated by a distance R_{ij}.

3. Results and Discussion

3.1. Simulation of the Bulk Si Crystal

The variation of stress with respect to strain is commonly used to calculate various mechanical properties of materials. Figure 2 depicts the stress-strain graph for bulk silicon at 300 K and 0.005 ps^{-1} strain rate.

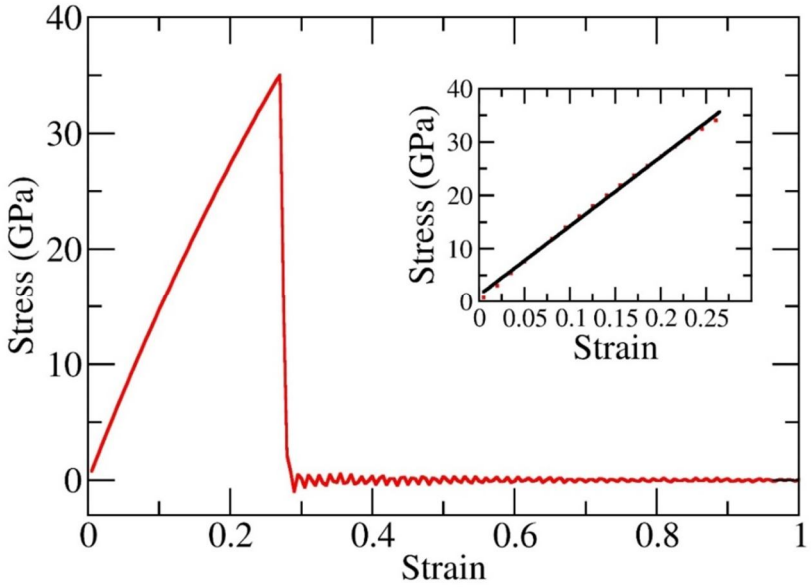

FIG. 2. Variation of stress with respect to strain for bulk silicon at 300 K temperature and strain rate of 0.005ps^{-1}. The inset shows a linear fit for the calculation of Young's modulus.

The figure illustrates that stress initially increases linearly with strain, indicating elastic deformation. In the elastic region, stress reaches a peak of 34.96 GPa (yield strength) at a strain of 0.270 (yield strain). Beyond this point, stress rapidly drops to zero as strain increases, indicating fracture. The slope of the stress-strain curve in the elastic region gives the Young's modulus, shown in the inset of Fig. 2. The calculated Young's modulus for bulk silicon at 300 K and a strain rate of 0.005 ps^{-1} is 129.6

GPa, closely matching the experimentally measured value of 130 GPa [35].

The effects of strain rate and temperature on the uniaxial tensile mechanical properties of Si NW are explained in the following sub-sections.

3.2 Effect of Strain Rate on Si NW

The nanowire is initially energy-minimized and then thermally relaxed at 300 K. After full relaxation, the Si NW is subjected to tensile loading along the axial direction (Z-axis) at different strain rates ranging from 0.0005 to 0.05 ps^{-1}. The corresponding stress vs. strain curves are shown in Fig. 3. It is observed from the graph that, for all strain rates, stress initially varies linearly with strain, indicating elastic deformation. The curves in this linear region are almost overlapping, which means Young's modulus is nearly independent of the strain rate. Beyond the elastic region, stress abruptly decreases, indicating fracture and confirming the brittle nature of the Si NW, as noted by other researchers [17, 20, 21].

The strain rate significantly influences the stress-strain curves beyond the elastic limit. Notably, as the strain rate increases, both fracture strain and yield strength increase. Table 1 provides the estimated values of Young's modulus, yield strength, yield strain, and fracture strain at each strain rate.

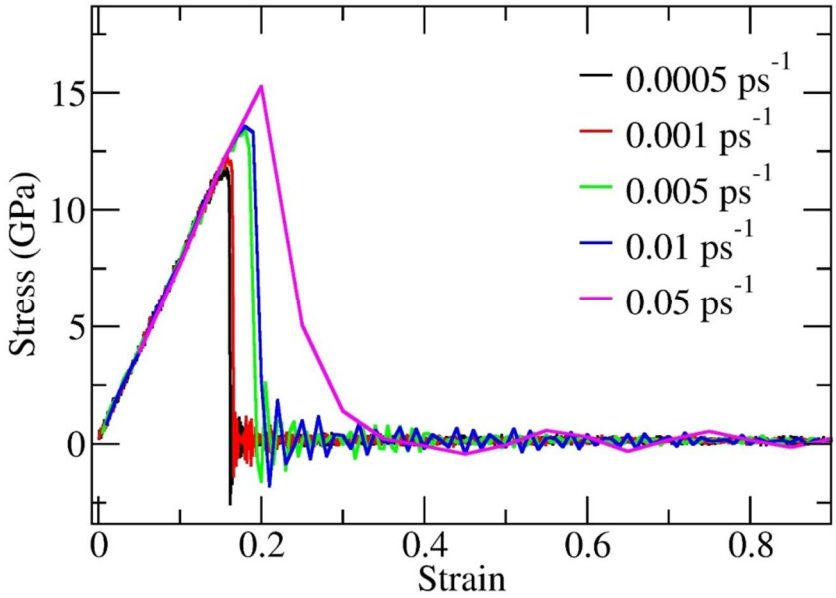

FIG. 3. Stress vs. strain curves of Si NWs at 300 K for different strain rates.

TABLE 1. The calculated values of mechanical properties at various strain rates for the Si NW at 300 K.

Strain rate (ps^{-1})	Young's modulus (GPa)	Yield strength (GPa)	Yield strain	Fracture strain
0.0005	77.73	11.7993	0.155	0.161
0.001	77.086	12.2578	0.156	0.165
0.005	75.85	12.480	0.175	0.187
0.01	77.453	13.452	0.18	0.205
0.05	76.773	15.2636	0.2	0.386

Figure 4 depicts the variation in potential energy of the Si NW as a function of strain for different strain rates at 300 K. Initially, potential energy rises linearly with strain, then drops steeply before gradually rising again. The first drop in the potential energy curve indicates the breaking of bonds and disruption of the crystal structure of the Si NW. It is also observed that the first drop in the potential energy curves shifts towards higher strain values with the increase in strain rate, which is consistent with the first peak positions of the corresponding stress-strain curves.

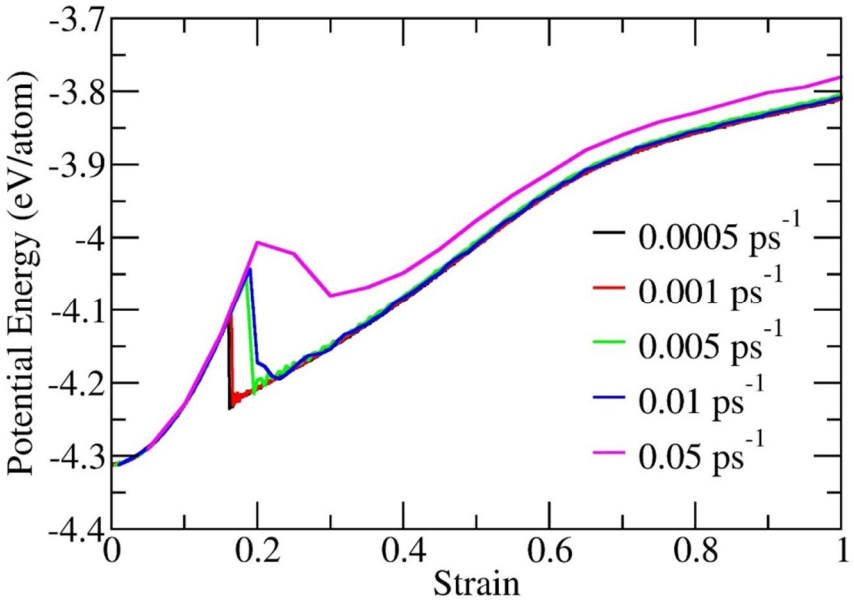

FIG. 4. Potential energy vs. strain curves at various strain rates of the Si NW at 300 K.

3.3 Effect of Temperature on Si NW

Kinetic energy determines the momentum and thermal excitations of the system, whereas potential energy assists in the investigation of the mechanical characteristics. Figure 5 depicts potential energy vs. strain curves for the Si NW at various temperatures ranging from 10 to 700 K. The elastic area of the potential energy curve increases monotonically with respect to strain, then dips rapidly, indicating the end of the elastic zone. Finally, when strain increases, the potential energy approaches a limiting value. Breaking of NW occurs when the potential energy value decreases below this limit. It is observed that with an increase in temperature, the potential energy of the system increases, and the strain at which the first peak appears also shifts to the left side of the graph (Fig. 5).

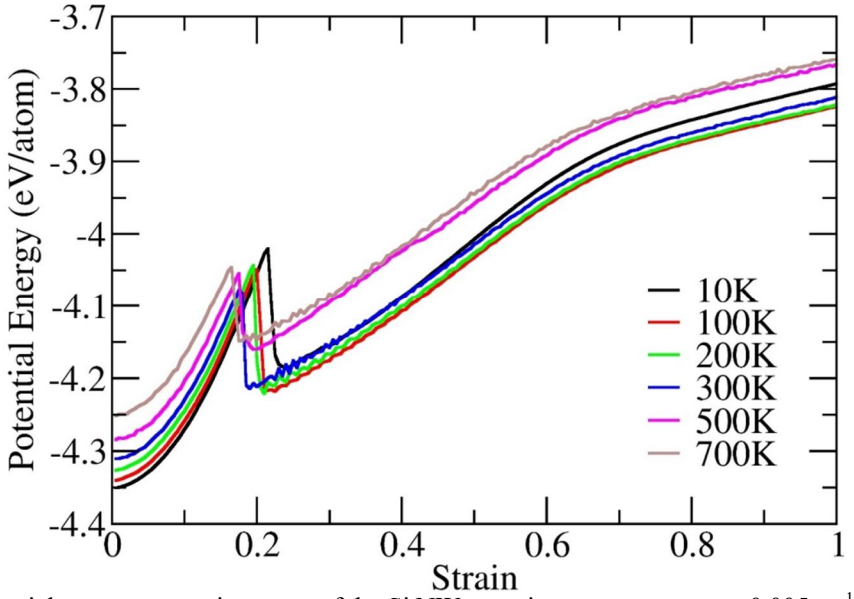

FIG. 5. Potential energy vs. strain curves of the Si NW at various temperatures at 0.005 ps^{-1} strain rate.

The temperature has a significant impact on the nanowire's tensile deformation behavior. To characterize the temperature effect on the mechanical properties of the Si NW, the stress versus strain curves in a temperature range of 10-700 K at 0.005 ps^{-1} strain rate are obtained and shown in Fig. 6. It is observed that the deformation of the NW gets accelerated with increase in temperature. Because greater temperatures cause atoms to oscillate more, massive dislocations are formed in weaker nanowires. As a result, the higher temperature causes the nanowire to fail prematurely. The attractive force between Si atoms decreases as temperature rises, causing atoms to drift from their equilibrium positions. Hence, the stress on the nanowire reduces at the same strain, resulting in lower Young's modulus and decreased yield strength, yield strain, and fracture strain. At higher temperatures and the same strain level, the number of displaced atoms and lattice defects rises, causing the NW to reach its ultimate stress point more quickly, thus decreasing yield strength. Thermal softening is evident as tensile stress decreases with temperature.

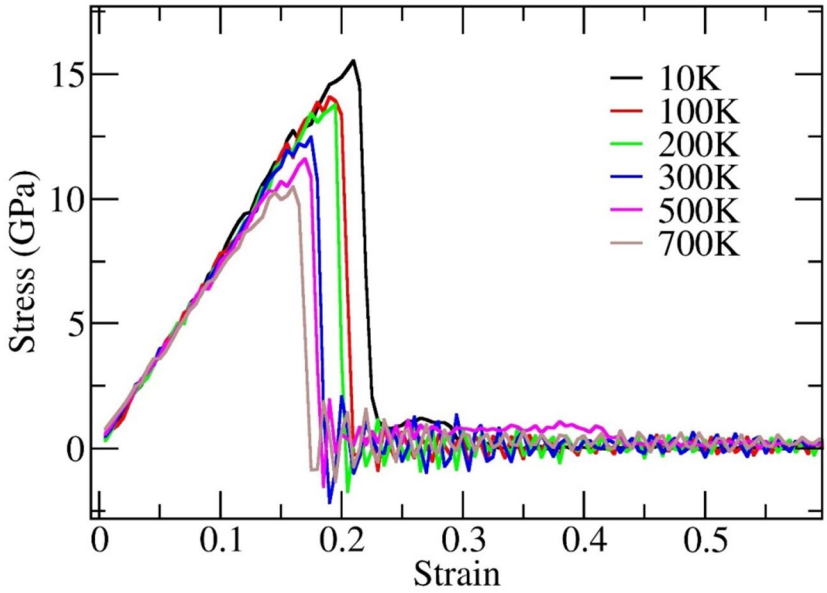

FIG. 6. Stress vs. strain curves of the Si NW for different temperatures at 0.005 ps^{-1} strain rate.

Figure 7 illustrates atomic configurations in the Si NW during tensile deformation at 300 K and 0.005 ps^{-1} strain rate. In Fig. 7(a), the Si NW, initially in a diamond cubic crystal structure, is shown after relaxation without loading. At a strain of 0.155, the NW reaches its elastic deformation limit (the first peak in the stress-strain graph), appearing elongated with a narrowed middle, as seen in Fig. 7(b). Plastic deformation begins beyond yield strain; at this stage, the NW surface fractures, planes slide along the cracking area, and atoms shift from their equilibrium positions. Figure 7(c) shows the NW at fracture strain (0.187), where it has broken into two separate parts. Table 2 lists the calculated mechanical properties of the Si NW at different temperatures.

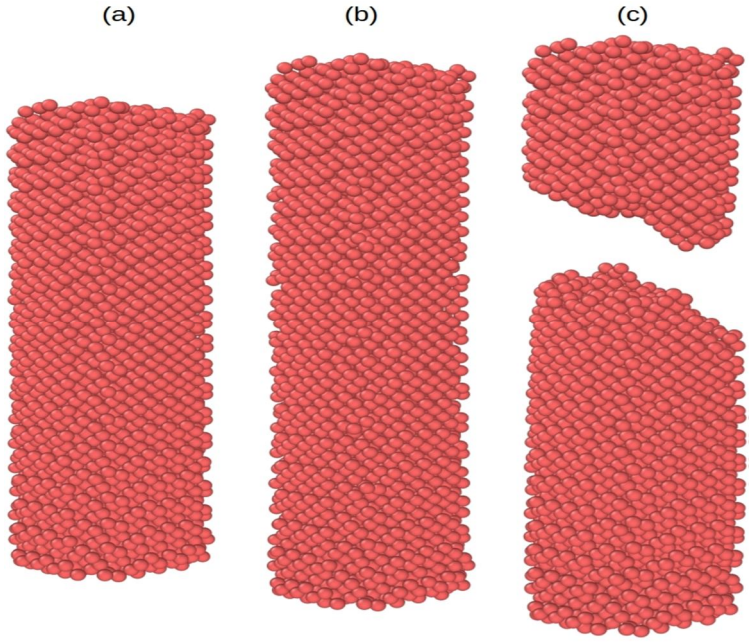

FIG. 7. Atomic configurations of the Si NW at 300K and 0.005 ps^{-1} strain rate (a) Original state, strain = 0. (b) Tensile state, Strain = 0.155. (c) Fracture state, strain = 0.187.

TABLE 2. The quantitative data on mechanical properties at various temperatures for the Si NW 0.005 ps^{-1} strain rate.

Temperature (K)	Young's modulus (GPa)	Yield strength (GPa)	Yield strain	Fracture strain
10	79.036	15.528	0.210	0.304
100	77.021	14.064	0.195	0.205
200	76.89	13.752	0.190	0.203
300	75.85	12.480	0.175	0.187
500	71.984	11.617	0.170	0.183
700	67.812	10.489	0.160	0.174

4. Conclusion

In this research work, the impact of strain rate and temperature on the mechanical properties of Si NWs was explored using MD simulations with the MEAM potential. The results reveal that strain rate and temperature distinctly influence various mechanical properties of the NWs. It is observed from our results that the yield strength, yield strain, and fracture strain increase with an increase in strain rate, whereas Young's modulus remains unaffected. Temperature has an equally important influence on the mechanical characteristics of the Si NW as it affects both the elastic and plastic characteristics profoundly. With an increase in temperature, Young's modulus, yield strength, yield strain, and fracture strain of the NW are found to decrease. These results show that with an increase in strain rate and decrease in temperature, the strength of the Si NW increases. Other factors, including size and orientation, also influence the mechanical properties of NWs, and we are currently exploring these in further research. The precise numerical values obtained in this study can aid experimentalists and guide future research in silicon nanomaterial applications.

Acknowledgment

The authors are thankful to the honorable vice chancellor of VSSUT, Burla, India, for providing the necessary facilities to carry out this research.

References

[1] Lieber, C. M., MRS Bull., 28 (7) (2003) 486.

[2] Cui, Y., Wei, Q., Park, H., and Lieber, C. M., Science, 293 (2001) 1289.

[3] Beckman, R. et al., Science, 310 (5747) (2005) 465.

[4] Canham, L. T., Appl. Phys. Lett., 57 (1990) 1046.

[5] Sarangi, S.S. et al., Indian J. Phys., 91 (2017) 853.

[6] Samantaray, M. P. and Sarangi, S. S., Mater. Proc., 46 (20) (2021) 10861.

[7] Samantaray, M. P. and Sarangi, S. S., Indian J. Phys., 96 (2022) 2285.

[8] Samantaray, M. P. and Sarangi, S. S., Int. Jour. Nanosci., 22 (1) (2023) 2250052-SA119.

[9] Ahmad, R., Mahmoudi, T., Ahn, M. S., and Hahn, Y.B., Biosens. Bioelectron, 100 (2018) 312.

[10] Buitrago, E., Badia, M. F. B., Georgiev, Y. M., Yu, R., Lotty, O., Holmes, J. D., Nightingale, A. M., Guerin, H. M., and Ionescu, A. M., Sens. Actuators B Chem., 199 (2014) 291.

[11] Čalnerytė, D., Rimavičius, V., and Barauskas, R., Acta Mech., 230 (2019) 1907.

[12] Ziegler, A. and Luisier, M., IEEE Trans. Electron. Devices, 65 (4) (2018) 1298.

[13] Lee, S., Kim, K., Kang, D. H., Meyyappan, M., and Baek, C. K., Nano Lett., 19 (2019) 747.

[14] Li, H.-P. and Zhang, R.-Q., Chin. Phys. B., 27 (3) (2018) 036801.

[15] Zhou, G., Xu, L., Hu, G., Mai, L., and Cui, Y., Chem. Rev., 119 (20) (2019) 11042.

[16] Sohn, Y. S., Park, J., Yoon, G., Song, J., Jee, S. W., Lee, J. H., Na, S., Kwon, T., and Eom, K., Nanoscale Res. Lett., 5 (2010) 211.

[17] Zhu, Y., Xu, F., Qin, Q., Fung, W. Y., and Lu, W., Nano Lett., 9 (11) (2009) 3934.

[18] Tang, D. M., Ren, C. L., Wang, M. S., Wei, X., Kawamoto, N., Liu, C., Bando, Y., Mitome, M., Fukata, N. and Golberg, D., Nano Lett., 12 (4) (2012) 1898.

[19] Han, X. D., Zheng, K., Zhang, Y. F., Zhang, X. N., Zhang, Z., and Wang, Z. L., Adv. Mater., 19 (2007) 2112.

[20] Gordon, M. J., Baron, T., Dhalluin, F., Gentile, P., and Ferret, P., Nano Lett., 9 (2) (2009) 525.

[21] Barik, S. and Sarangi, S. S., Mater. Proc., 56 (1) (2022) 60.

[22] Sarangi, S. S., Mater. Proc., 41 (2) (2021) 413.

[23] Barik, S. and Sarangi, S. S., Mol. Simul., 49 (4) (2023) 377.

[24] Ivashchenko, V. I., Turchi, P. E. A., and Shevchenko, V.I. Phys. Rev. B, 75 (8) (2007) 085209.

[25] Jing, Y. H., Meng, Q. Y., and Zhao, W., Physica E., 41 (4) (2009) 685.

[26] Kang, K. and Cai, W., Int. J. Plast., 26 (9) (2010) 1387.

[27] Zhao, D., Li, J., and Zhang, L., Crystals, 11 (9) (2021) 1010.

[28] Plimpton, S., J. Comp. Phys., 117 (1) (1995) 1.

[29] Nose, S., J. Phys. Condens. Matter, 2 (1990) SA115.

[30] Hoover, W. G., Phys. Rev. A, 31 (3) (1985) 1695.

[31] Stukowski, A., Model. Simul. Mater. Sci. Eng., 18 (1) (2009) 015012.

[32] Lee, B.-J., Calphad, 31 (1) (2007) 95.

[33] Baskes, M. I., Mater. Chem. Phys., 50 (2) (1997) 152.

[34] Lee, B. J., Shim, J. H. and Baskes, M. I., Phys. Rev. B, 68 (14) (2003) 144112.

[35] Hopcroft, M. A., Nix, W. D., and Kenny, T. W., J. Microelectromech. Syst., 19 (2) (2010) 229.

Volume 17, Number 4, 2024. pp. 469-481

Jordan Journal of Physics

ARTICLE

Two–Dimensional Electron-Hole GaAs System in the Static Fluctuation Approximation

Mohamed K. Al-Sugheir[a], **Heba J. Alasali**[b], **Mouath G. Shatnawi**[a] and **Ghassan A. Alnawashi**[a]

[a] *Department of Physics, Faculty of Science, The Hashemite University, 13115, Zarqa, Jordan.*

[b] *Department of Physics, Science Faculty, Isra University, 11622, Amman, Jordan.*

Doi: **https://doi.org/10.47011/17.4.10**

Received on: 30/03/2023; *Accepted on: 26/04/2023*

Abstract: The energy spectrum, particle distribution, internal energy, and specific heat capacity of a two-dimensional electron-hole GaAs system were investigated within the framework of the static fluctuation approximation. The study explored the influence of temperature, dielectric thickness, and dielectric constant on these properties. It was found that the interaction potential had a more pronounced effect on the energy spectrum and distribution of holes than on those of electrons. The results also revealed that the interaction potential effect on internal energy and specific heat capacity of the system occurs at temperatures less than the Fermi temperature. Additionally, the study found that at low temperatures, the system exists in a bound state, whereas at high temperatures, it transitions to a scattering state.

Keywords: Static fluctuation approximation, Two-dimensional electron-hole GaAs system, Energy spectrum, Particle distribution, Heat capacity.

PACS: 65.40. Ba, 71.10. Ca, 71.35. Ee, 73.63.Hs.

1. Introduction

A two-dimensional electron-hole system is a fascinating model with controllable interactions, comprising two parallel layers separated by a distance [1-9]. One layer contains electrons and the other contains holes. The energy spectrum of this system shows that it behaves like an ideal gas if transitions to higher energy states are ignored [1]. The system also exhibits superconductivity due to the pairing of electrons and holes [2]. This system can be analyzed by applying an electric field to double quantum wells [3, 6]. The phases of this system were studied using variational wave functions [9].

Examples of two-dimensional systems are two graphene layers [5, 10, 11], two-dimensional semiconductors [12, 13] and coupled quantum wells [5, 14, 15]. Graphene bilayers can exhibit a Kosterlitz-Thouless temperature as high as room temperature if they have a high number density ($> 10^{13}$ cm^{-2}) and a small interlayer distance (< 2nm) [10]. This indicates that some of these systems can be superfluid near room temperature. This is also possible for double trilayer and quadlayer graphene sheets [11]. Theoretically, the dielectric function of electron-hole plasma was derived using random phase approximation [12]. The exciton energy states in coupled quantum wells were studied by solving the Schrodinger equation for the GaAs/AlGaAs system [15]. The results showed that the Coulomb correlations can create a degenerate

Corresponding Author: Mohamed K. Al-Sugheir **Email**: msugh@hu.edu.jo

electron-hole liquid when the average distance between the particles is smaller than the size of the exciton [14]. The exchange interaction between electrons and holes was found to be the major barrier for generating entangled photon pairs in semiconductor quantum dots [13].

A two-dimensional electron-hole system is a remarkable system that shows various phenomena such as electron-hole plasma [16], phase transitions from exciton gas to electron-hole plasma [17], and exciton condensate in semiconductor quantum well [18]. Due to its extraordinary behavior, this system has drawn significant research interest over the decades leading to the discovery of many applications [9-18].

A two-dimensional electron-hole system is a useful model for many real systems such as coupled quantum wells and graphene layers [6, 19-23]. One of the interesting phases in this system is the Mott insulator [17], where the system remains insulating despite having a band structure that allows conduction. The phase transition from Mott insulator to electron-hole plasma was studied in quasi-equilibrium [17]. The experimental analysis of the phase diagram of indirect excitons for GaAs/AlGaAs showed that unbound electron-hole plasma appears when the temperature of the system increases [20].

The two-dimensional electron-hole system was studied using the mean field approximation [5, 18]. The results showed that the phase transition is affected by the interlayer interaction and the number density of the system. The SFA is an approximation that can account for the quantum fluctuations that are ignored in the mean field approximation. These fluctuations are more important in low-dimensional systems. While much prior work has focused on the system's electric and magnetic properties, we were specifically interested in studying the thermodynamic properties of the two-dimensional electron-hole system, an area with limited research.

In this work, the macroscopic properties of the two-dimensional electron-hole system are derived from its microscopic properties. This can be done in the framework of the SFA. The SFA was used for various systems ranging from weak to strong interactions [24-34], such as the two-dimensional Ising model [25], liquid helium-4 [24], liquid helium-3 [26], and ^{3}He-HeII [27].

2. Basics of Static Fluctuation Approximation.

The main idea of the SFA is to replace the square of the local field operator with its mean value [24]. This means that the true quantum mechanical spectrum of this operator is replaced with a distribution around its mean value [24-26].

The SFA is used to investigate how the interaction potential parameters, number density, and temperature affect the system's thermodynamic properties, including occupation number, energy spectrum, total energy of the system, and specific heat capacity. These properties depend on the temperature, number density, dielectric interlayer thickness, and dielectric constant of the system. The SFA is applied for the first time to electron-hole systems. For that, a symmetric case is considered in this work, where the electrons and holes have the same number density. This symmetry simplifies the Hamiltonian, as the asymmetric case requires additional terms to account for imbalanced densities between electrons and holes.

According to the main assumption of the SFA, the Hamiltonian $\widehat{H}$ can be expressed as a linear combination of the local field operator $\hat{E}_{k,\sigma}$ and the number of particles operator $\hat{n}_{k,\sigma} = \hat{c}^{+}_{\boldsymbol{k},\sigma}\hat{c}_{\boldsymbol{k},\sigma}$ [24, 26],

$$\widehat{H} = \sum_{\boldsymbol{k},\sigma} \hat{E}_{k,\sigma}\hat{c}^{+}_{\boldsymbol{k},\sigma}\hat{c}_{\boldsymbol{k},\sigma}, \tag{1}$$

where $\hat{c}^{+}_{\boldsymbol{k},\sigma}$ and $\hat{c}_{\boldsymbol{k},\sigma}$ are the creation and annihilation operators of electrons and holes. Here, σ refers to the particle type and k is the wave number of a specific state.

The Heisenberg representation of the creation operator $\hat{c}^{+}_{k,\sigma}(\tau)$ is given by:

$$\hat{c}^{+}_{k,\sigma}(\tau) = \exp(\tau\widehat{H})\hat{c}^{+}_{k,\sigma}(0)\exp(-\tau\widehat{H}), \tag{2}$$

where $\tau \equiv it$. The creation operator in Heisenberg picture obeys the equation of motion:

$$\frac{d\hat{c}^{+}_{k,\sigma}(\tau)}{d\tau} = \left[\widehat{H}, \hat{c}^{+}_{\boldsymbol{k},\sigma}(\tau)\right], \tag{3}$$

where $\tau = it$. The creation and annihilation operators for Fermi system have the following anticommutation relations:

$$\left\{\hat{c}^{+}_{\boldsymbol{k},\sigma}, \hat{c}_{\boldsymbol{p},\sigma_1}\right\} = \delta_{\boldsymbol{k},\boldsymbol{p}}\delta_{\sigma,\sigma_1} \tag{4a}$$

$$\{\hat{c}_{\boldsymbol{p},\sigma}, \hat{c}_{\boldsymbol{q},\sigma_1}\} = 0. \quad (4b)$$

In the SFA, the local field operator is assumed to be Hermitian and commutes with the creation and annihilation operators [24-26]. Based on this assumption and using Eqs. (1)-(4), we can express the local field operator as [26]

$$\hat{E}_{k,\sigma} = \{\hat{c}_{\boldsymbol{k},\sigma}, [\hat{H}, \hat{c}^{+}_{\boldsymbol{k},\sigma}(\tau)]\}. \quad (5)$$

The grand Hamiltonian describing the two-dimensional electron-hole system in second quantization can be written as [5]:

$$\hat{H} = \sum_{k,\sigma}(\varepsilon_\sigma(k) - \mu_\sigma)\hat{c}^{+}_{k,\sigma}\hat{c}_{k,\sigma} + \sum_{k,q,p} V(k)\hat{c}^{+}_{k-q,h}\hat{c}_{k-p,h}\hat{c}^{+}_{q,e}\hat{c}_{p,e}, \quad (6)$$

where $\varepsilon_\sigma(k) = \frac{\hbar^2 k^2}{2m^*_\sigma}$ is the single particle energy, h is Planck's constant ($\hbar = h/2\pi$ Dirac's constant) and m^*_σ is the effective mass of either the electron or hole. μ_e (μ_h) is the chemical potential of the electron (hole) system. $V(k)$ in Eq. (6) is the attractive electron-hole interaction defined by the two-dimensional Fourier image of the screened electron-hole attraction [5, 35, 36]:

$$V(k) = -\frac{\bar{U}\, exp(-kd)}{k + 2(a_e^{-1} + a_h^{-1}) + 4(1 - exp(-2kD))/(ka_e a_h)}. \quad (7)$$

Here, d is the dielectric interlayer thickness, $\bar{U} = Ke^2 n/2\varepsilon$ is the potential strength, K is Coulomb's constant, e is the electronic charge, n is the electron and hole number density, and ε is the dielectric constant of the system, $a_{e,h} = \frac{\hbar^2 \varepsilon}{Ke^2 m^*_{e,h}}$, where m^*_e and m^*_h are the effective masses of electron and hole, respectively. The electron-electron and hole-hole interactions are included in the effective mass in the kinetic energy term based on the effective mass approximation. Also, the spin of electrons and holes is neglected here because we are not interested in magnetization effects [5]. For a neutral electron-hole system, the densities of electrons and holes should be equal.

The grand local field operators of electrons and holes are determined from Eq. (5) and Eq. (6):

$$\hat{E}_{\boldsymbol{k},e} = \varepsilon_e(k) - \mu_e + \sum_q V(|q-k|)\hat{n}_{q,h} \quad (8)$$

and

$$\hat{E}_{\boldsymbol{k},h} = \varepsilon_h(k) - \mu_h + \sum_q V(|q-k|)\hat{n}_{q,e}. \quad (9)$$

In the SFA, the quadratic fluctuations in the local field operator are replaced by their mean value [24, 26]. The true quantum energy spectrum is replaced with a distribution around the mean value of the local field operator:

$$\Delta\hat{E}^2_{k,\sigma} = <\Delta\hat{E}^2_{k,\sigma}> = \phi^2_{k,\sigma} \quad (10)$$

The so-called long-range equation of Fermi system was derived [26]:

$$\langle\hat{n}_{k,\sigma}\hat{A}\rangle = \eta_{0,\sigma}(k)\langle\hat{A}\rangle + \eta_{1,\sigma}(k)\langle\Delta\hat{E}_{k,\sigma}\hat{A}\rangle, \quad (11)$$

where $\hat{A}$ is an arbitrary operator that commutes with the creation and annihilation operators. The functions $\eta_{0,\sigma}(k)$ and $\eta_{1,\sigma}(k)$ are given by [25]:

$$\eta_{0,\sigma}(k) = \frac{1}{2}\left\{\frac{1}{exp[\beta(\langle\hat{E}_{k,\sigma}\rangle + \phi_{k,\sigma})]+1} + \frac{1}{exp[\beta(\langle\hat{E}_{k,\sigma}\rangle - \phi_{k,\sigma})]+1}\right\} \quad (12)$$

$$\eta_{1,\sigma}(k) = \frac{1}{2\phi_{k,\sigma}}\left\{\frac{1}{exp[\beta(\langle\hat{E}_{k,\sigma}\rangle + \phi_{k,\sigma})]+1} - \frac{1}{exp[\beta(\langle\hat{E}_{k,\sigma}\rangle - \phi_{k,\sigma})]+1}\right\}, \quad (13)$$

where the parameter $\beta = \frac{1}{k_B T}$, with k_B being the Boltzmann's constant and T absolute temperature [37]. The long-range equation is a generator equation.

Choosing $\hat{A} = 1$, in Eq. (11) the particle distribution is obtained:

$$\langle\hat{n}_{k,\sigma}\rangle = \eta_{0,\sigma}(k) + \eta_{1,\sigma}(k)\langle\Delta\hat{E}_{k,\sigma}\rangle. \quad (14)$$

Due to the symmetry in the fluctuations of $\Delta\hat{E}_{k,\sigma}$, the mean value $\langle\Delta\hat{E}_{k,\sigma}\rangle$ vanishes. Therefore, the particle distribution becomes

$$\langle\hat{n}_{k,\sigma}\rangle = \eta_{0,\sigma}(k). \quad (15)$$

It is more convenient to rewrite Eq. (11) in terms of the deviations of the occupation-number operator:

$$<\Delta\hat{n}_{k,\sigma}\hat{A}> = \eta_{1,\sigma}(k) <\Delta\hat{E}_{k,\sigma}\hat{A}>. \quad (16)$$

Now, it is possible to obtain the close set of coupled nonlinear integral equations. Choosing $\hat{A} = \Delta\hat{E}_{k,\sigma}$ in Eq. (16), we obtain the quadratic fluctuations in the grand local field operator $\Delta\hat{E}^2_{k,\sigma}$:

$$\eta_{1,\sigma}(k)\phi^2_{k,\sigma} = <\Delta\hat{n}_{k,\sigma}\Delta\hat{E}_{k,\sigma}>. \quad (17)$$

Using Eqs. (8), (9), and (17), the quadratic fluctuations in the grand local field operator for electrons and holes can be written as:

$$\eta_{1,e}(k)\phi_{k,e}^2 = \sum_{\boldsymbol{q}} V(|\boldsymbol{q}-\boldsymbol{k}| < \Delta\hat{n}_{k,e}\Delta\hat{n}_{\boldsymbol{q},h} >, \quad (18)$$

$$\eta_{1,h}(k)\phi_{k,h}^2 = \sum_{\boldsymbol{q}} V(|\boldsymbol{q}-\boldsymbol{k}| < \Delta\hat{n}_{k,h}\Delta\hat{n}_{q,e} >. \quad (19)$$

Choosing $\sigma \equiv e$ in Eq. (16) to refer to electrons and using $\hat{A} = \Delta\hat{n}_{q,h}$, we get the pair correlation function $< \Delta\hat{n}_{k,e}\Delta\hat{n}_{q,h} >$,

$$\begin{aligned} < \Delta\hat{n}_{k,e}\Delta\hat{n}_{q,h} > &= \eta_{1,e}(k) < \Delta\hat{E}_{k,e}\Delta\hat{n}_{q,h} > \\ &= \eta_{1,e}(k)\sum_{\boldsymbol{p}} V(|\boldsymbol{k}-\boldsymbol{p}|) < \Delta\hat{n}_{p,h}\Delta\hat{n}_{q,h} >. \\ &= \eta_{1,e}(k)\sum_{\boldsymbol{p}} V(|\boldsymbol{k}-\boldsymbol{p}|)\,(\langle\Delta\hat{n}_{p,h}{}^2\rangle\delta_{p,q} + < \\ &\Delta\hat{n}_{p,h}\Delta\hat{n}_{q,h} >_c) \end{aligned} \quad (20)$$

Choosing $\sigma \equiv e$ in Eq. (16) and $\hat{A} = \Delta\hat{n}_{q,e}$, where $q \neq k$ we get the pair correlation function $< \Delta\hat{n}_{k,e}\Delta\hat{n}_{q,e} >_c$, the index c denoting the true correlation function $q \neq k$.

$$\begin{aligned} < \Delta\hat{n}_{k,e}\Delta\hat{n}_{q,e} >_c &= \eta_{1,e}(k) < \Delta\hat{E}_{k,e}\Delta\hat{n}_{q,e} > \\ &= \eta_{1,e}(k)\sum_{p} V(|k-p|) < \Delta\hat{n}_{p,h}\Delta\hat{n}_{q,e} >. \end{aligned} \quad (21)$$

Choosing $\sigma \equiv h$ in Eq. (16) and $\hat{A} = \Delta\hat{n}_{q,h}$, where $q \neq k$ we get the pair correlation function $< \Delta\hat{n}_{k,h}\Delta\hat{n}_{q,h} >_c$.

$$\begin{aligned} < \Delta\hat{n}_{k,h}\Delta\hat{n}_{q,h} >_c &= \eta_{1,h}(k) < \Delta\hat{E}_{k,h}\Delta\hat{n}_{q,h} > \\ &= \eta_{1,h}(k)\sum_{\boldsymbol{p}} V(|\boldsymbol{k}-\boldsymbol{p}|) < \Delta\hat{n}_{p,e}\Delta\hat{n}_{q,h} >. \end{aligned} \quad (22)$$

The closed system of coupled nonlinear integral equations consisting of $\langle\hat{E}_{k,e}\rangle$, $\langle\hat{E}_{k,h}\rangle$, $\langle\hat{n}_{k,e}\rangle$, $\langle\hat{n}_{k,h}\rangle$, $\phi_{k,e}$, $\phi_{k,h}$, $\langle\Delta\hat{n}_{p,e}\Delta\hat{n}_{q,h}\rangle$, $< \Delta\hat{n}_{k,h}\Delta\hat{n}_{q,h} >_c$ and $< \Delta\hat{n}_{k,e}\Delta\hat{n}_{q,e} >_c$ can be solved numerically by Gaussian quadrature point method [25, 38]. The energy in our calculations is in units of eV.

3. Results and Discussion

In this work, the effect of temperature T, dielectric thickness d, and dielectric constant ε on the distribution and energy spectrum of electrons and holes, internal energy, and specific heat capacity of the GaAs system were examined. Although the effective masses of electrons (m_e^*) and holes (m_h^*) are T-dependent, for convenience we assumed them to be constant across the examined temperature range of 1–50 K. Here, we used $m_h^* = 0.45m_e$ and $m_e^* = 0.067m_e$ [39, 40], where m_e is the electron mass. In temperatures below 150 K, the effective mass of the electron remains nearly constant, close to $m_e^* = 0.067m_e$ [41].

The distribution of electrons and holes at various temperatures is shown in Figs. 1 and 2, respectively. At T = 1 K, both distributions display a step-like behavior, with a high occupation probability (≈ 1) for states below the Fermi momentum k_f. The Fermi temperatures of electrons and holes are 41.5 and 6.2 K, respectively. At T = 1 K, all holes are in the ground state with $k < k_f$. As the temperature increases to be greater than the Fermi temperature, some particles are excited to states above the Fermi level. This depletion from the ground state to excited states increases as the temperature increases. At T = 25 K, the probability of occupying the zero-momentum state is approximately 0.88 for electrons and 0.49 for holes, situating this temperature below the Fermi temperature for electrons but above that for holes. By T = 50 K, most holes are in higher energy states, reflecting their excitation above the Fermi temperature, while electrons still predominantly occupy lower energy states due to their higher Fermi temperature.

The energy spectrum for electrons and holes is the expectation value of the local field operator which is given by

$$\langle\hat{E}_{\boldsymbol{k},e}\rangle = \varepsilon_e(k) + \sum_q V(|q+k|)\langle\hat{n}_{q,h}\rangle, \quad (23)$$

and

$$\langle\hat{E}_{\boldsymbol{k},h}\rangle = \varepsilon_h(k) + \sum_{\boldsymbol{q}} V(|\boldsymbol{q}+\boldsymbol{k}|)\langle\hat{n}_{q,e}\rangle. \quad (24)$$

Figures 3 and 4 show how the energy spectra of electrons and holes change with temperature. The results indicate that the energy of states below the Fermi level is T-dependent. At high-energy states, $k > k_f$, the kinetic energy term is dominant, while the interaction term significantly influences the low-energy states. The interaction potential is attractive and inversely related to k. The system is bound for $k < k_f$ and in a scattering state for $k > k_f$. The temperature effect in the interaction term comes from the distribution of particles. As temperature rises, more particles are excited to states with $k > k_f$, diminishing the influence of the attractive potential with higher k.

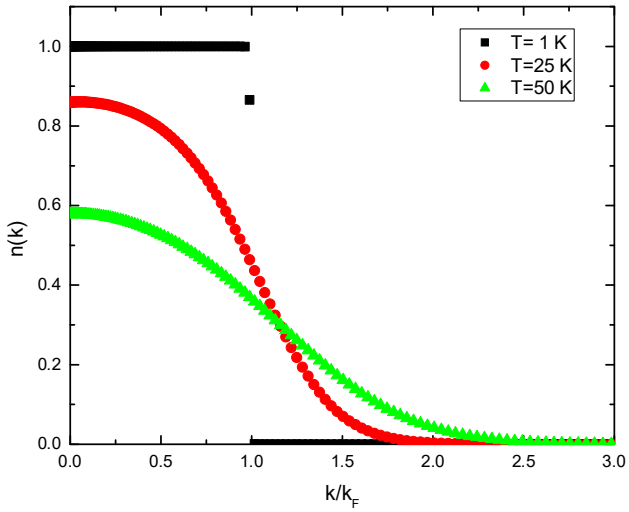

FIG. 1. The electron distribution as a function of k/k_f at values of $\varepsilon = 3$, $d = 5nm$, number density $n = 1x10^{11}\ cm^{-2}$, $m_h^* = 0.45m_e$, and $m_e^* = 0.067m_e$.

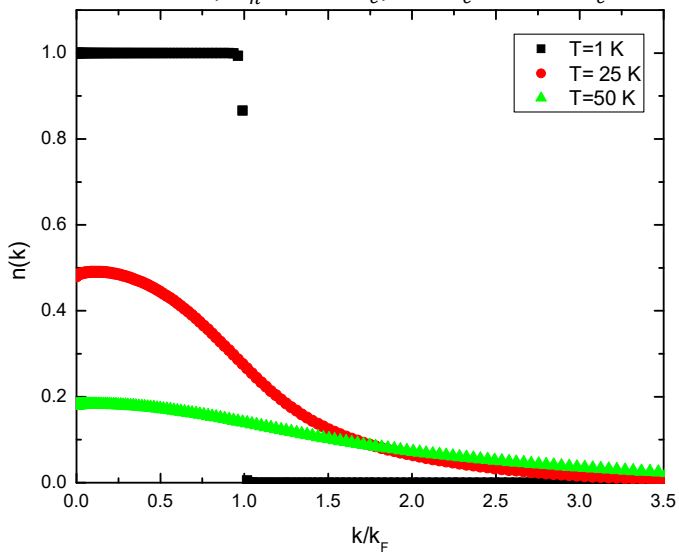

FIG. 2. The hole distribution as a function of k/k_f at values of $\varepsilon = 3$, $d = 5nm$, number density $n = 1x10^{11}\ cm^{-2}$, $m_h^* = 0.45m_e$, and $m_e^* = 0.067m_e$.

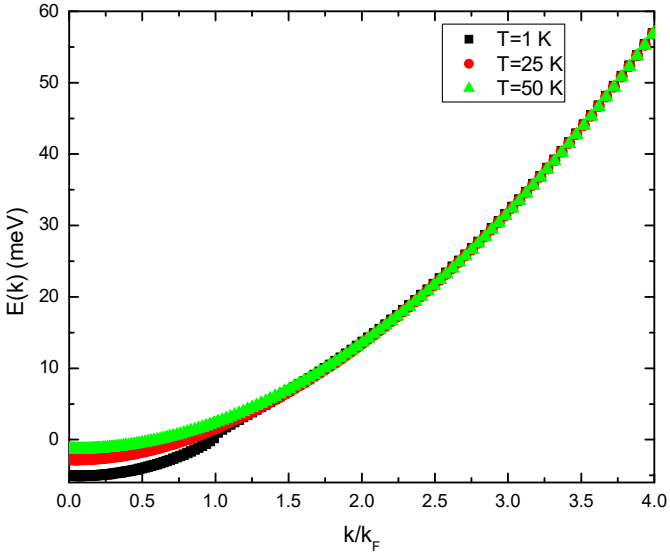

FIG. 3. The electron energy spectrum as a function of k/k_f at values of $\varepsilon = 3$, $d = 5nm$, number density $n = 1x10^{11}\ cm^{-2}$, $m_h^* = 0.45m_e$, and $m_e^* = 0.067m_e$.

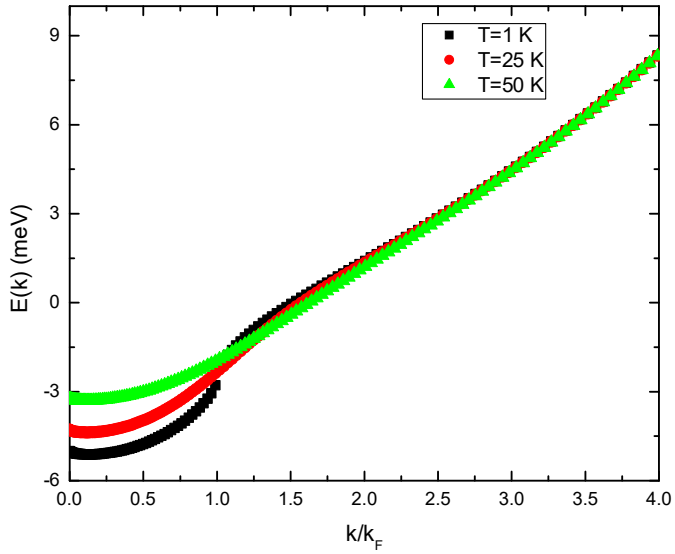

FIG. 4. The hole energy spectrum as a function of k/k_f at values of $\varepsilon = 3$, $d = 5nm$, number density $n = 1x10^{11}\ cm^{-2}$, $m_h^* = 0.45m_e$ and $m_e^* = 0.067m_e$.

The electron and hole distributions at T = 25 K with different dielectric interlayer thicknesses d are shown in Figs. 5 and 6, respectively. Results indicate that the electron distribution is not sensitive to d, while the hole distribution in the lowest states is shifted upward as the dielectric interlayer thickness decreases, where the attractive potential decreases as d increases (the attractive potential is proportional to e^{-kd}). Given that the effective masses of electrons and holes are $0.067m_e$ and $0.45m_e$, respectively, electrons possess higher kinetic energy than holes. Therefore, the attractive potential influences the hole distribution more than the electron distribution.

The energy spectra of electrons and holes at T = 25 K are presented in Figs. 7 and 8, respectively. The results indicate that the energy spectrum of electrons exhibits a parabolic dependence on momentum, where the kinetic energy of the electrons is dominant in the higher energy states. It is only shifted downward as the interaction potential increases (d decreases). The spectrum of the hole energy (Fig. 8) is more influenced by the interaction term in the local field operator, as holes have a greater effective mass than electrons. Therefore, holes in the lowest states become more bound due to the effect of the attractive potential. In both cases, the interaction potential affects mainly the lowest states up to states with momentum comparable to the Fermi momentum.

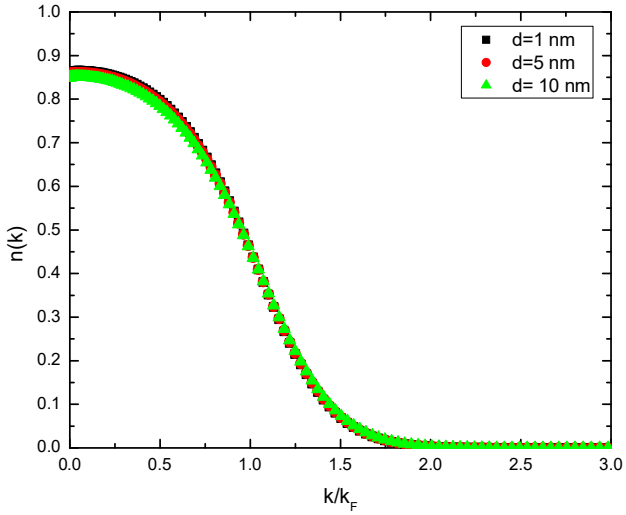

FIG. 5. The electron distribution as a function of k/k_f at values of $T = 25$ K, $\varepsilon = 3$, number density $n = 1x10^{11}\ cm^{-2}$, $m_h^* = 0.45m_e$, and $m_e^* = 0.067m_e$.

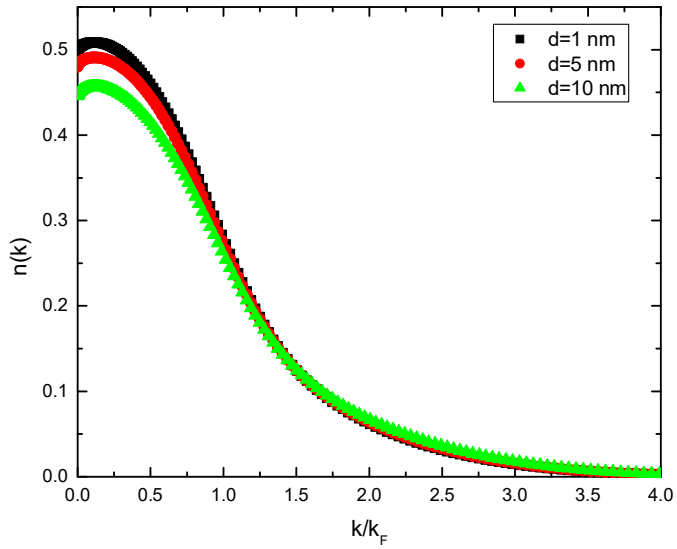

FIG. 6. The hole distribution as a function of k/k_f at values of $T = 25$ K, $\varepsilon = 3$, number density $n = 1x10^{11}\ cm^{-2}$, $m_h^* = 0.45m_e$, and $m_e^* = 0.067m_e$.

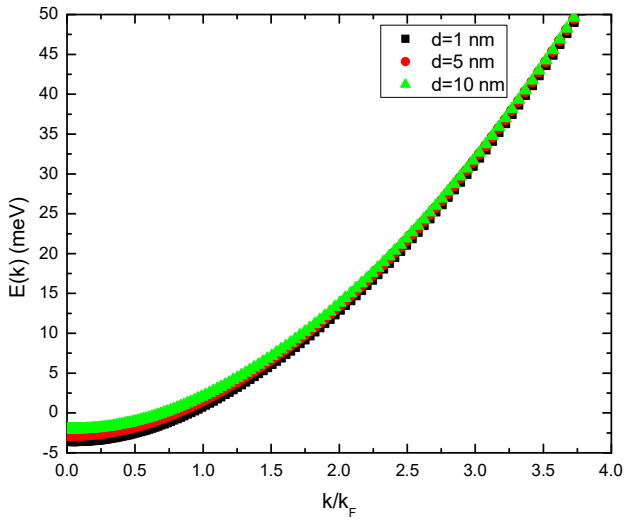

FIG. 7. The electron energy spectrum as a function of k/k_f at values of $T = 25$ K, $\varepsilon = 3$, number density $n = 1x10^{11}\ cm^{-2}$, $m_h^* = 0.45m_e$, and $m_e^* = 0.067m_e$.

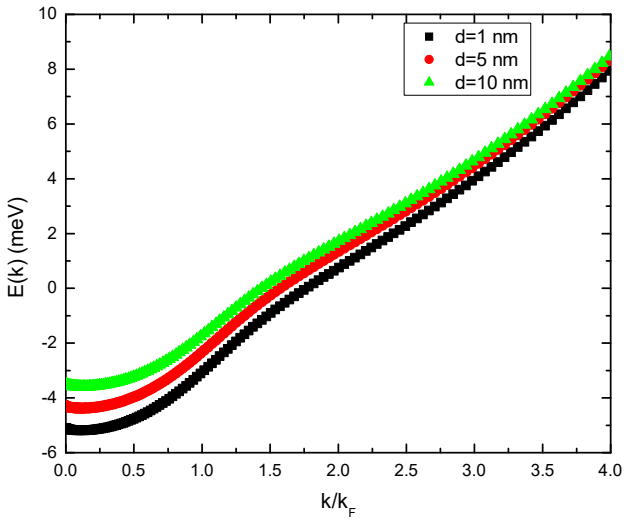

FIG. 8. The hole energy spectrum as a function of k/k_f at values of $T = 25$ K, $\varepsilon = 3$, number density $n = 1x10^{11}\ cm^{-2}$, $m_h^* = 0.45m_e$, and $m_e^* = 0.067m_e$.

The effect of the dielectric constant on the electron and hole distributions is shown in Figs. 9 and 10. The figures show that as the dielectric constant increases, the probability of finding a particle in states with momentum below the Fermi momentum decreases. The pair potential is inversely proportional to the dielectric constant, so the system is more attractive as the dielectric constant decreases. The distribution of holes is more sensitive to the dielectric constant than that of electrons, as electrons have higher kinetic energy. The results show that the Fermi temperature of the system increases as the dielectric constant decreases, where the probability of having a particle in a state with $k < k_F$ increases as the dielectric constant decreases.

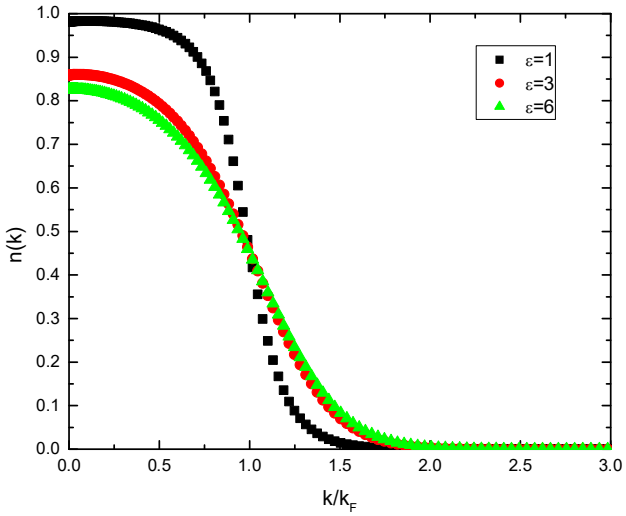

FIG. 9. The electron distribution as a function of k/k_f at values of $T = 25$ K, $d = 5nm$, number density $n = 1x10^{11}\ cm^{-2}$, $m_h^* = 0.45m_e$, and $m_e^* = 0.067m_e$.

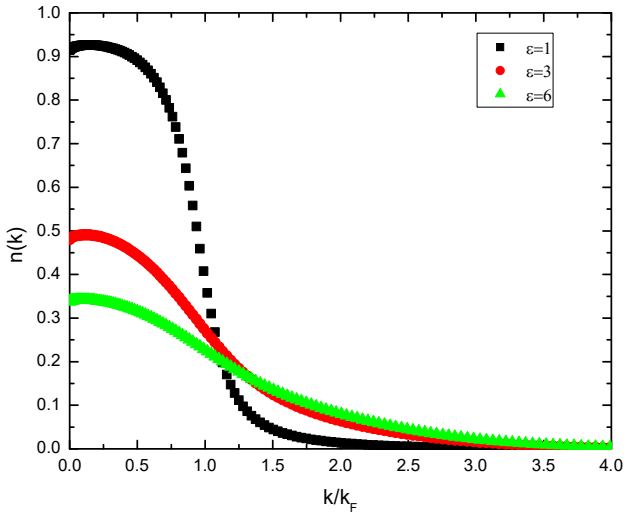

FIG. 10. The hole distribution as a function of k/k_f at values of $T = 25$ K, $d = 5nm$, number density $n = 1x10^{11}\ cm^{-2}$, $m_h^* = 0.45m_e$, and $m_e^* = 0.067m_e$.

Figures 11 and 12 present the energy spectrum of electrons and holes across different dielectric constants. The results indicate that the spectrum of both electrons and holes behaves like a non-interacting system at high momentum states, $k > k_F$, where the kinetic energy is dominant in the local field operator. In low momentum states, $k < k_F$, the energy spectrum is shifted downward with increasing the pair potential (the dielectric constant decreases). This result indicates that the pair potential affects mainly the low-lying energy states, which is proportional to e^{-kd}.

The influence of the interaction potential on the internal energy per particle, $\frac{U}{N}$, and specific heat capacity, $\frac{C_A}{Nk_B}$, is examined. Figure 13 shows how $\frac{U}{N}$ varies with the dielectric interlayer

thickness. $\frac{U}{N}$ has the same behavior for any value of thickness. The interaction potential affects $\frac{U}{N}$ mainly at low temperatures ($T < T_F$, where T_F is the Fermi temperature). As temperature rises, $\frac{U}{N}$ becomes similar across thickness values because the kinetic energy becomes dominant. Figure 14 shows how $\frac{C_A}{Nk_B}$ depends on temperature for different values of the thickness of the dielectric interlayer. The results indicate that $\frac{C_A}{Nk_B}$ increases with T until it reaches a maximum value at $T = T_F$ and then decreases to the classical value of a two-dimensional non-interacting system at high temperatures. The "bump" in $\frac{C_A}{Nk_B}$ suggests an order-disorder transition, shifting from a more ordered low-temperature quantum regime to a less ordered high-temperature classical regime.

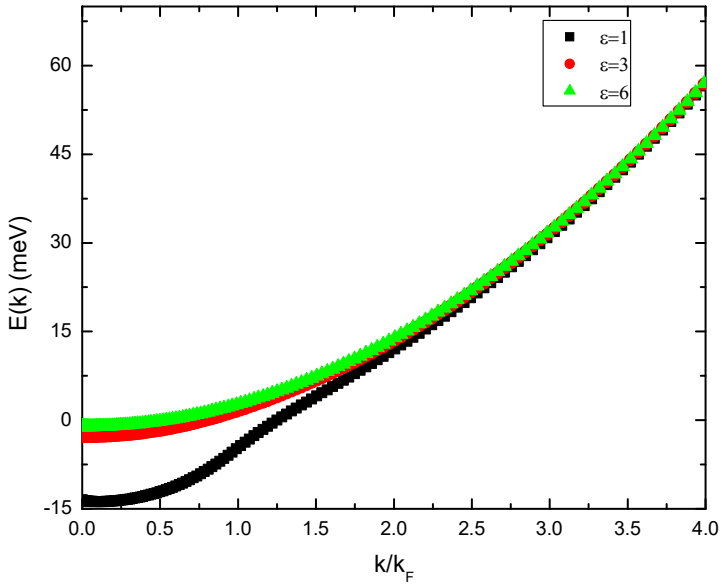

FIG. 11. The energy spectrum of electrons as a function of k/k_f at values of $T = 25$ K, $d = 5nm$, number density $n = 1x10^{11}\ cm^{-2}$, $m_h^* = 0.45m_e$, and $m_e^* = 0.067m_e$.

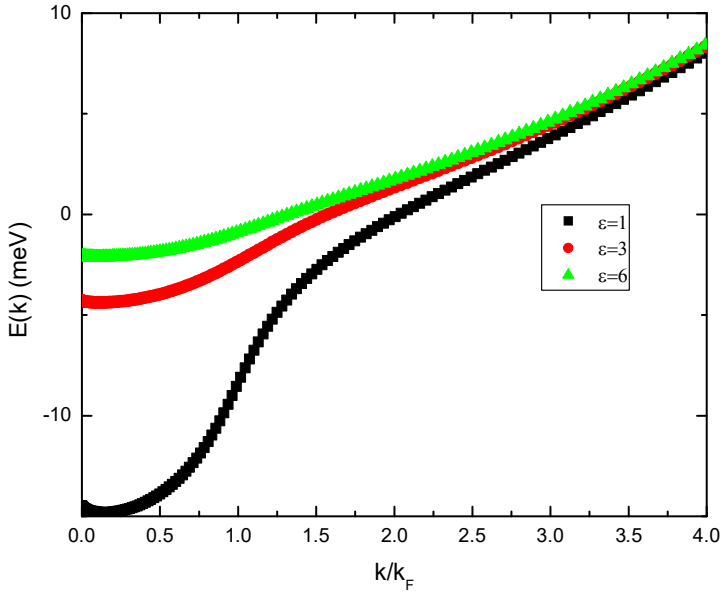

FIG. 12. The hole spectrum as a function of k/k_f at values of $T = 25$ K, $d = 5nm$, number density $n = 1x10^{11}\ cm^{-2}$, $m_h^* = 0.45m_e$, and $m_e^* = 0.067m_e$.

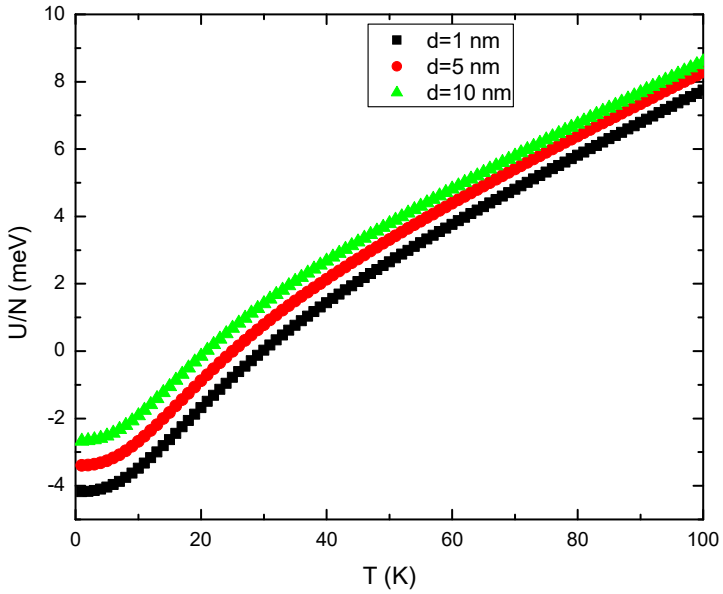

FIG. 13. The energy of the system as a function of temperature at values of $\varepsilon = 3$, number density $n = 1x10^{11}\ cm^{-2}$, $m_h^* = 0.45m_e$, and $m_e^* = 0.067m_e$.

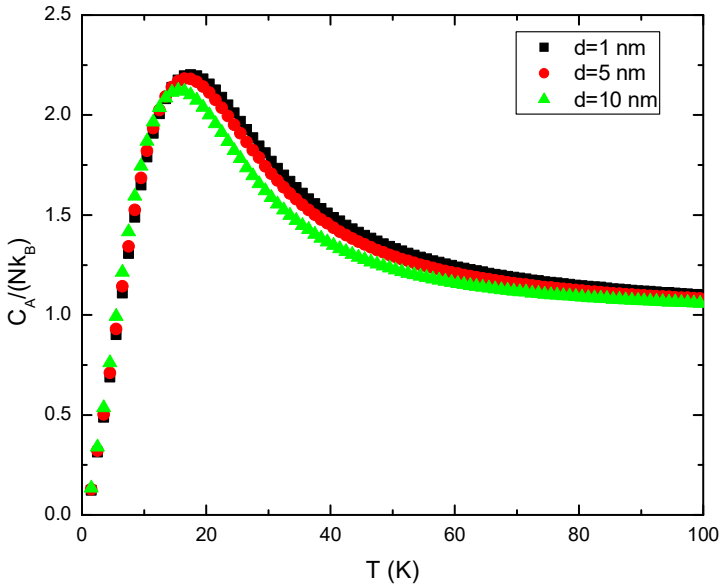

FIG. 14. The specific heat capacity $C_A/(Nk_B)$ as a function of temperature at values of $\varepsilon = 3$, number density $n = 1x10^{11}\ cm^{-2}$, $m_h^* = 0.45m_e$, and $m_e^* = 0.067m_e$

The effect of the dielectric constant on $\frac{U}{N}$ is illustrated in Fig. 15. The results indicate that the interaction potential affects $\frac{U}{N}$ at low temperatures. $\frac{U}{N}$ is negative at low temperatures, where the interaction term in the local field operator becomes dominant. It is well known that as the dielectric constant increases the interaction potential decreases. Therefore, $\frac{U}{N}$ is more negative in the quantum regime (low temperatures) as the dielectric constant decreases. In the classical regime (high temperatures), $\frac{U}{N}$ is slightly dependent on the dielectric constant. Figure 16 shows $\frac{C_A}{Nk_B}$ for different values of the dielectric constant. $\frac{C_A}{Nk_B}$ increases with T until it reaches a maximum value at $T = T_F$. At high temperatures, it approaches the value of a two-dimensional non-interacting system. The results of $\frac{C_A}{Nk_B}$ indicate that the Fermi temperature increases as the interaction increases (dielectric constant decreases).

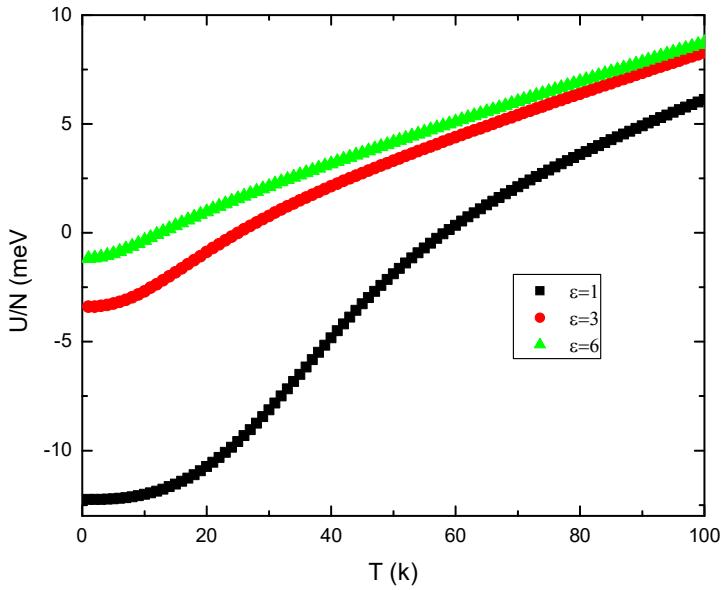

FIG. 15: The energy of the system as a function of temperature at values of $d = 5nm$, number density $n = 1x10^{11}\ cm^{-2}$, $m_h^* = 0.45m_e$, and $m_e^* = 0.067m_e$.

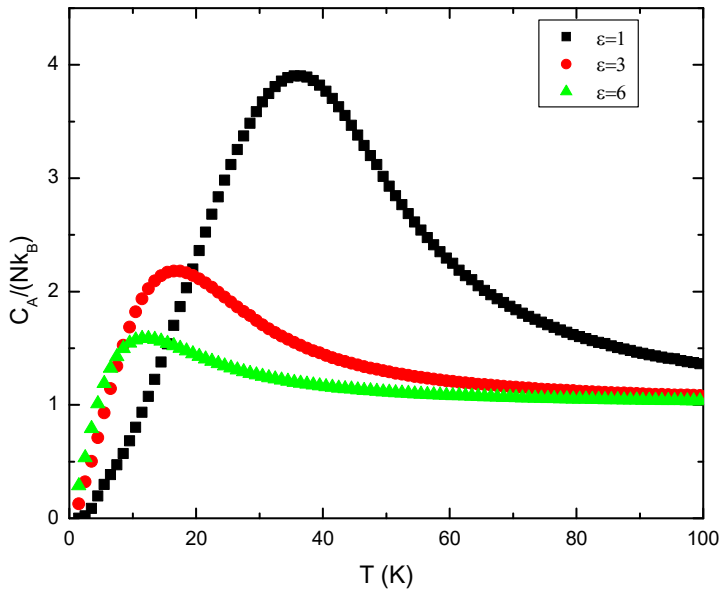

FIG. 16. The specific heat capacity $C_A/(Nk_B)$ as a function of temperature at values of $d = 5nm$, number density $n = 1x10^{11}\ cm^{-2}$, $m_h^* = 0.45m_e$, and $m_e^* = 0.067m_e$.

4. Conclusion

The static fluctuation approximation (SFA) technique was applied successfully to calculate the distribution and energy spectrum of the two-dimensional electron-hole GaAs system. The influence of temperature, dielectric interlayer thickness, and the dielectric constant on these quantities was examined. The results indicate that the interaction term in the local field operator affects these quantities at low-momentum states. The internal energy per particle and specific heat capacity of the GaAs system were also investigated. The system acts like a nearly ideal, non-interacting gas at high temperatures or high momentum. The dielectric constant has a stronger effect on the results than the dielectric interlayer thickness.

The SFA goes well beyond the mean-field approach and has been applied over a wide range of systems ranging from strongly to weakly interacting systems. However, just like other perturbative theories, it is most suitable for weakly interacting or dilute systems. To improve the present framework of the SFA, we could reformulate it to include higher orders of fluctuations.

References

[1] Lerner, I. V. and Lozovik, Y. E., Sov. Phys. JETP, 53 (1981) 763.

[2] Shevchenko, S. I., Phys. Rev. Lett., 72 (1994) 3242.

[3] Yoshioka, D. and MacDonald, A. H., J. Phys. Soc. Jpn., 59 (1990) 4211.

[4] Lai, C. W., Zoch, J., Gossard, A. C., and Chemla, D. S., Science, 303 (2004) 503.

[5] Berman, O. L., Kezerashvili, R. Y., and Ziegler, K., Physica E, 71 (2015) 7.

[6] Kvon, Z. D., Olshanetsky, E. B., Kozlov, D. A., and Dvoretskii, S. A., JETP Lett., 87 (2008) 502.

[7] Huijben, M., Brinkman, A., Koster, G., Rijnders, G., Hilgenkamp, H., and Blank, D.H.A., Adv. Mater., 21 (2009) 1665.

[8] Lozovik, Y. E., Ogarkov, S. L., and Sokolik, A. A., Phys. Rev. B, 86 (2012) 045429.

[9] Tiene, A., Levinsen, J., Parish, M. M., MacDonald, A. H., Keeling, J., and Marchetti, F. M., Phys. Rev. Res., 2 (2020) 023089.

[10] Min, H., Bistrizer, R., Su, J. J., and MacDonald, A. M., Phys. Rev. B, 78 (2008) 121401.

[11] Zarenia, M., Perali, A., Neilson, D., and Peeters, F. M., Sci. Rep., 4 (2014) 7319.

[12] Semkat, D., Stolz, H., Kraeft, W-D., and Fehske, H., J. Phys. Condens. Matter, 33 (2021) 475501.

[13] Kadantsev, E. S. and Hawrylak, P., J. Phys.: Conf. Ser., 248 (2010) 012018.

[14] Babichenko, V. S. and Polishchuk, I. Y., JETP Lett., 97 (2013) 628.

[15] Sivalertporn, K., Phys. Lett. A, 380 (2016) 1990.

[16] Ryzhii, V., Satou, A., and Otsuji, T., J. Appl. Phys., 101 (2007) 024509.

[17] Asano, K. and Yoshioka, T., J. Phys. Soc. Jpn., 83 (2014) 084702.

[18] Zhu, X., Littlewood, P. B., Hybertsen, M. S., and Rice, T. M., Phys. Rev. Lett., 74 (1995) 1633.

[19] Butov, L. V., Zrenner, A., Abstreiter, G., Böhm, G., and Weimann, G., Phys. Rev. Lett., 73 (1994) 304.

[20] Stern, M., Garmider, V., Umansk, V. Y., and Bar-Joseph, I., Phys. Rev. Lett., 100 (2008) 256402.

[21] Lozovik, Y. E. and Sokolik, A. A., JETP Lett., 87 (2008) 55.

[22] Liu, M., Yin, X., and Zhang, X., Nano Lett., 12 (2012) 1482.

[23] Sorianello, V., Midrio, M., and Romagnoli, M., Opt. Expr., 23 (2015) 6478.

[24] Al-Sugheir, M. K., Ghassib, H. B., and Nigmatullin, R. R., Int. J. Theor. Phys., 40 (2001) 1033.

[25] Nigmatullin, R. R., Khamzin, A. A., and Ghassib, H. B., Solid State Commun. 113 (2000) 257.

[26] Al-Sugheir, M. K. and Ghassib, H. B., Int. J. Theor. Phys., 41 (2002) 705.

[27] Al-Sugheir, M. K., Int. J. Theor. Phys., 43 (2004) 1527.

[28] Ghulam, N. M., Ghassib, H. B., and Al-Sugheir, M.K., Phys. Rev. C, 75 (2007) 64317.

[29] Al-Sugheir, M. K., Al-Khzon, H. A., Al-Maghrabi, M., and Alna'washi, G. A., Acta Phys. Pol. A, 122 (2012) 704.

[30] Alhami, E. M., Ghassib, H. B., and Al-Sugheir, M. K., Acta Phys. Pol. A, 127 (2015) 1648.

[31] Al-Khzon, H. and Al-Sugheir, M. K., Eur. Phys. J. B, 94 (2021) 192.

[32] Al-Sugheir, M. K. and Mqbel, F. F., Can. J. Phys., 99 (2021) 841.

[33] Al-Khzon, H. and Al-Sugheir, M. K., Int. J. Mod. Phys. B, 35 (2021) 2150059.

[34] Al-Khzon, H. and Al-Sugheir, M. K., Phys. B, 571 (2019) 18.

[35] Lozovik, Y. E. and Yudson, V. I., Sov. Phys. JETP, 44 (1976) 389.

[36] Lozovik, Y. E. and Yudson, V. I., Sov. Phys. JETP, Lett., 22 (1975) 26.

[37] Feynman, R. P., "Statistical Mechanics", (Benjamin, Reading Massachusetts, 1972).

[38] Burden, R. L. and Faires, J. D., "Numerical Analysis", 5th Ed., (PWS publishing company, Boston, 1993).

[39] Tang, J., Cao, S., Gao, Y., Sun, Y., Geng, W., Williams, D. A., Jin, K., and Xu, X., Appl. Phys. Lett., 105 (2014) 041109.

[40] Hillmer, H., Forchel, A., Hansmann, S., Morohashi, M., and Lopez, E., Phys, Rev. B, 39 (1989) 10901.

[41] Hazama, H., Sugimasa, T., Imachi, T., and Hamaguchi, C., JPSJ, 55 (1986) 1282.

Volume 17, Number 4, 2024. pp. 483-495

Jordan Journal of Physics

ARTICLE

Simulated Transimpedance Amplifier Performance Analysis through Channel Length Modification for Fiber Optics Applications

Asmaa Z. Al-Kawaz and **Muhammed S. H. Alsheikhjader**

Department of Physics, College of Science, University of Mosul, Iraq.

Doi: **https://doi.org/10.47011/17.4.11**

Received on: 01/04/2023; *Accepted on: 07/06/2023*

Abstract: A proposed transimpedance amplifier was simulated using channel length modification. The amplifier consists of a feedforward input stage followed by a common gate-common source (CG-CS) configuration. A series of channel lengths (45, 90, and 130 nm) in complementary metal-oxide semiconductor (CMOS) technology was implemented for comparative performance analysis within the same proposed topology. There are two key advantages of this study. First, the trade-off between gain and bandwidth, as well as the input-referred noise current, remains applicable when the channel length is increased from 45, 90, and 130 nm. Second, power consumption decreases as the channel length increases for the same topology. The total power consumption series (0.621, 0.29, and 0.175 mW) corresponds to the above channel length series. Corresponding bandwidths of (1.69, 1.35, and 1.10 GHz) were reported, with respective transimpedance amplifier (TIA) gains of (44.78, 46.39, and 47.94 dBΩ). The input-referred noise current was reduced to (15.24, 10.77, and 9.40 $pA/\sqrt{H_z}$) for the channel lengths of 45, 90, and 130 nm, respectively, aligning with the trends observed in bandwidth and TIA gain.

Keywords: Transimpedance amplifier, Feedforward, Front-end preamplifier, RGC.
Keywords: Transimpedance amplifier, Feedforward, Front-End preamplifier, RGC.
PACS: 85.40.-e, 07.50.Ek, 84.30.-r.

1. Introduction

Fiber optic networks are meeting the demands for high-speed (Gb/s) systems of communications which are rapidly growing. A comparative analysis of a transimpedance amplifier (TIA) using 45 and 180 nm inductorless CMOS process was achieved in which a single-ended current-mode TIA in the form of N similar TIAs in parallel configuration was conducted [1]. A 45 nm silicon-on-insulator (SOI) CMOS process was demonstrated in the form of a 40 Gb/s optical transceiver that consists of a TIA where a feedback resistor is connected between the gate and drain of NMOS and PMOS transistors [2]. A two-phase TIA was implemented in 45 nm CMOS, featuring a regulated cascode (RGC) and an inverted cascode output stage [3]. A 5 Gbps TIA in a 90 nm CMOS process that employs an active RGC structure at the input stage leading to low input resistance which was followed by a level shifter and a common source structure to achieve high transimpedance at low supply voltage was introduced [4]. A modified RGC TIA followed by a closed loop gain stage with an added level shifter circuit to the booster of a conventional RGC circuit was proposed in the 90 nm CMOS process [5]. A TIA with three cascaded stages in the form of common source amplifiers utilizing capacitive degeneration and inductive peaking in a 90 nm CMOS process was introduced [6]. A conventional RGC TIA employing a cascode inverter as proposed local feedback was implemented in 130 nm CMOS technology [7]. A 2.5 Gbit/s TIA was realized in 130 nm CMOS technology that involved using a common source (CS) amplifier with active inductive peaking [8].

Corresponding Author: Muhammed S. H. Alsheikhjader **Email**: mohammedsubhi@uomosul.edu.iq

A 64-Gbaud TIA in 130 nm SiGe process was implemented. The topology involved a π–network broadband technique and shunt-shunt RC feedback to achieve high gain and a wide bandwidth [9]. A double cascode TIA with inductive peaking and shunt-shunt negative feedback was realized in a 130 nm RF CMOS process for 10 Gbps optoelectronic receivers [10].

1.1 Feedforward Transimpedance

The common gate topology of transistor M_2 enables it to function as a source follower because it is a part of a feedback loop, as illustrated in Fig. 1(a). At low frequencies, resistor R_2 is comparable to the total TIA gain. The input resistance is represented by Eq. (1) [11], if the loop at the M_2 gate is broken, and assuming that body effect and channel length modulation are disregarded:

$$R_{in} = \frac{1}{g_{m2}}\left(\frac{1}{1+g_{m1}R_1}\right) \quad (1)$$

where g_{m1} and g_{m2} are the transconductance parameters of transistors M_1 and M_2, respectively. The feedback loop lowers the input resistance, extending the bandwidth as a result. The circuit in Fig. 1(a) can be redrawn as shown in Fig. 1(b), which is essentially a feedforward amplifier that drives the gate of transistor M_2, which is in a common-source formation.

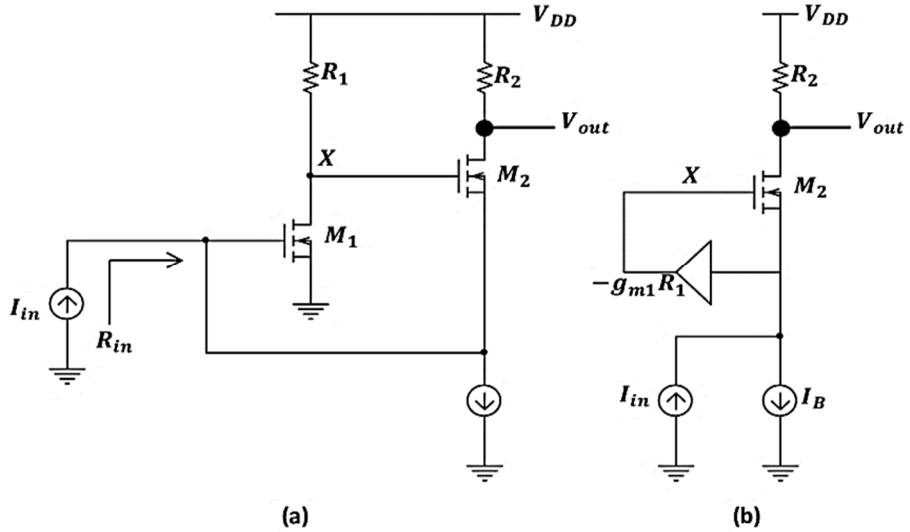

FIG. 1. (a) TIA in a feedback form, (b) Amplifier inserted in feedforward path [11].

1.2 Regulated Cascode TIA

In common-gate (CG) configurations, the impact of large input parasitic capacitance on bandwidth can be mitigated. However, it is difficult to totally isolate this capacitance when the CG topology is used as an input stage. Power consumption constraints also limit the transconductance parameter g_m of the NMOS transistor. The noise performance is normally deteriorated by a small g_m. The RGC input mechanism provides a valuable solution by enhancing g_m effectively. This RGC amplifier input node sits at virtual ground enabling wider bandwidths [12]. The RGC schematic circuit is shown in Fig. 2. where the photodiode current is turned into an amplified voltage at the drain of transistor M_2. Local feedback through transistor M_1 with R_b at its drain reduces input impedance equivalent to the same amount of its own voltage gain. The TIA gain is equal to R_F. The RGC input impedance is $(1 + g_{m1}R_b)$ times smaller than in the CG configuration.

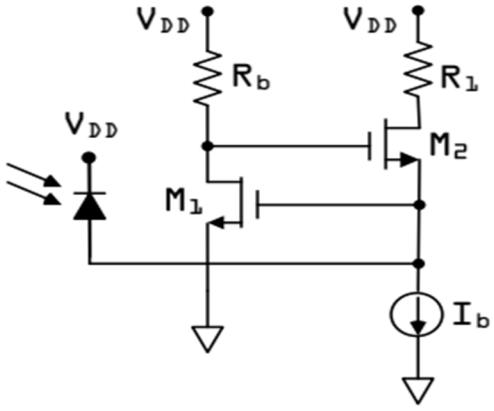

FIG. 2. A typical regulated cascode TIA [12].

The pole in the local feedback of Fig. 2 is a pole zero in the transfer function, leading to frequency peaking at $1/[2\pi R_b(C_{gs2} + C_{db1})]$, where C_{gs2} and C_{db1} are the gate-to-source

capacitance of transistor M_2 and the drain-to-bulk capacitance of transistor M_1, respectively. In order to avoid peaking, two options are possible: either the resistance or the gate width of transistor M_2 can be reduced. When R_b is reduced, then the input transconductance g_m is reduced almost in a linear manner. The input transconductance is reduced at a slower pace when the width of transistor M_2 is decreased. This can lead to an increase in the contribution of channel thermal noise from transistor M_2 as a result of smaller g_{m2} [12]. These RGC configuration challenges are noted in other studies [13-15].

This work aims to investigate the effects of channel length modification on a proposed TIA topology, focusing on the trade-off between gain and bandwidth, input-referred noise, and power consumption reduction as channel length increases.

2. Proposed TIA Topology

The schematic in Fig. 3 illustrates a current gain provider in the form of an input feedforward stage followed by a transimpedance gain provider in a common-gate common-source (CG-CS) arrangement. Nodes X and Y in the input stage must have sufficient voltage headroom to permit a measurable drain current for amplifier transistors M_1 and M_3. The DC level rise at node X through the pass transistor M_2 overcomes this voltage headroom. As a result, transistor M_1's drain-to-source voltage is also given the ability to have sufficient headroom. This input stage setup builds upon previously published designs [16].

As for the CG-CS stage, it is a modified form of the transconductance parameter g_m boosting mechanism. The drain of transistor M_{10} at node B provides enough gate-to-source voltage headroom for transistor M_9. Hence, a boosted g_m for transistor M_9 enables lower input impedance at node $in2$, expanding the bandwidth of the CG-CS stage. Interestingly, the low input impedance of this stage represents a low load for the input feedforward stage. The CS high input impedance at node A is in parallel with the source limited and finite input impedance of transistor M_9.

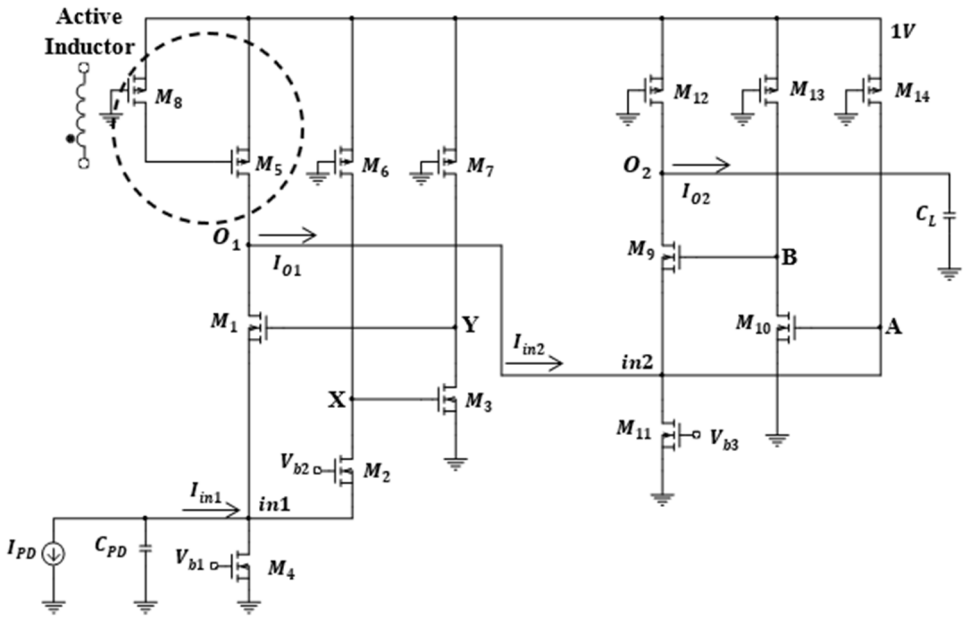

FIG. 3. Proposed TIA topology.

For the input stage, the small signal model is represented in Fig. 4. The input current I_{in1} that enters node $in1$ is a fraction of the photodiode current I_{PD} since some of it vanishes through the photodiode capacitance C_{PD}. The current source as an active inductor impedance is illustrated as Z_{AI}. The drain current of transistor M_1 is governed by the voltage difference between nodes Y and $in1$, while the drain current of transistor M_3 is governed by the voltage swing on node X. Gate biasing for transistor M_4 provides a stable path for drain current o M_1.

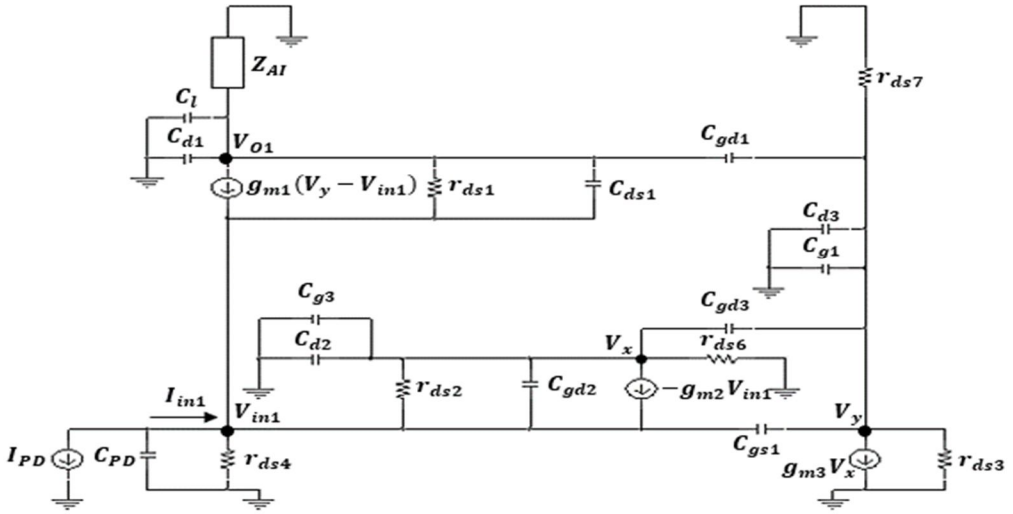

FIG. 4. Small-signal model of the feedforward input stage.

The small-signal model analysis is governed by KCL equations is represented as follows. In this analysis, g_{mx} is the transconductance representation as per numbered transistors, g_{mbx} is the bulk transconductance parameter, g_{dx} is the output conductance, while C_{dx} and C_{gx} are the total drain and gate capacitances, respectively. Gate-to-drain capacitances are given as C_{gdx}, while gate-to-source capacitance is represented as C_{gs1}. The total input capacitance $C_{in,tot1} = C_{PD} + C_{s1} + C_{s2} + C_{d4}$ is dominated by the photodiode capacitance.

$$I_{in1} = V_{in1}\big(g_{m1} + g_{mb1} + g_{ds1} + g_{m2} + g_{mb2} + g_{ds2} + g_{ds4} + sC_{in,tot1}\big) - V_X\, g_{ds2} - V_Y\big(g_{m1} + sC_{gs1}\big) - V_{O1}\, g_{ds1} \quad (2a)$$

$$0 = V_X\left(g_{ds6} + g_{ds2} + s\big(C_{d2} + C_{g3}\big)\right) - V_Y sC_{gd3} - V_{in1}(g_{m2} + g_{mb2} + g_{ds2}) \quad (2b)$$

$$0 = V_Y\left(g_{ds7} + g_{ds3} + s\big(C_{d3} + C_{g1}\big)\right) - V_X\big(g_{m3} - sC_{gd3}\big) - V_{O1}sC_{gd1} - V_{in1}\, s\, C_{gs1} \quad (2c)$$

$$0 = V_{O1}\big(Y_{AI} + g_{ds1} + s(C_{d1} + C_L)\big) + V_Y\big(g_{m1} - sC_{gd1}\big) - V_{in1}(g_{m1} + g_{mb1} + g_{ds1}) \quad (2d)$$

The voltage gain of the input stage circuit is deduced as:

$$A_{v1} = \frac{V_{O1}}{V_{in1}} = \frac{g_{m1}(1+|A_{M2}A_{M3}|)+g_{mb1}+g_{ds1}}{Y_{AI}+g_{ds1}+s(C_{d1}+C_L)} \quad (3)$$

Here, A_{M2} is the voltage gain of transistor M_2 and A_{M3} is the voltage gain of transistor M_3. The active inductor load admittance Y_{AI} is defined through the inversion of active inductor impedance as follows [17]:

$$Z_{AI} = \frac{r_{o8}C_{gs5}s+1}{g_{m5}+C_{gs5}s} \quad (4)$$

From Eq. (3), the TIA gain of the input stage is:

$$Z_{TIA1} = Z_{in1}A_{v1} = \frac{A_{v1}}{P+sC_{eq1}} \quad (5)$$

The input impedance of the input stage is given as:

$$Z_{in1} = \frac{1}{P+sC_{eq1}} \quad (6)$$

where P is worked out as:

$$P = g_{m1}(1 + |A_{M2}A_{M3}|) + g_{ds2}(1 - A_{M2}) + g_{ds1}(1 - A_{v1}) + g_{mb1} + g_{m2} + g_{mb2} + g_{ds4} \quad (7)$$

The equivalent input capacitance is defined as $C_{eq1} = \big[C_{i,tot1} + |A_{M2}A_{M3}|C_{gs1}\big]$, while the output impedance of the input stage is as follows:

$$Z_{O1} = \frac{1}{Y_{AI}+g_{ds1}+s\big(C_{d1}+C_L+C_{ds1}+C_{gd1}\big)} \parallel Z_{in2} \quad (8)$$

The term Z_{in2} will be addressed later within the CG-CS stage. The current gain for the input stage is expressed as:

$$\frac{I_{O1}}{I_{in1}} = \frac{Z_{TIA1}}{Z_{O1}} \quad (9)$$

The f_{-3dB} bandwidth of the proposed TIA topology is therefore worked out as:

$$f_{-3dB} = \frac{P}{2\pi C_{eq1}} \quad (10)$$

The combinational topology of CG-CS has the CS configuration with a gate that draws no current (at low frequencies), hence, a current gain of infinity (theoretically) can be exhibited.

The high input impedance of the CS core is in parallel with the CG input terminal which has far lower input impedance. Voltage headroom through the gate-to-source voltage of transistor M_{10} is easily overcome since node $in2$ carries the DC voltage from node O_1 and a fraction of the DC budget supply of 1V. The small-signal model of the CG-CS stage is shown in Fig. 5.

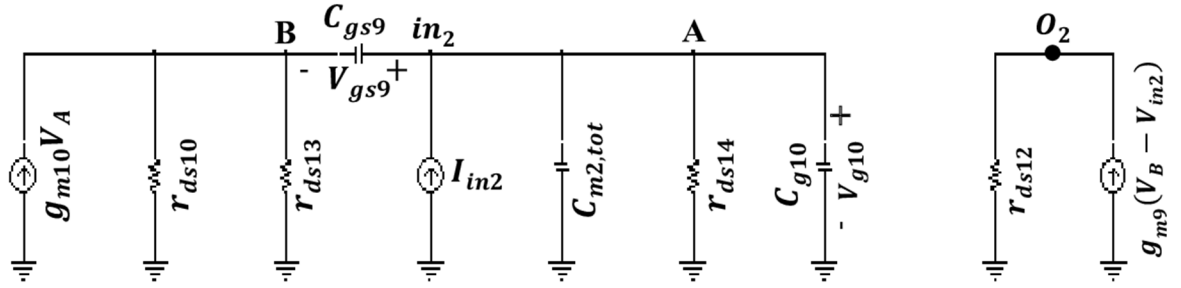

FIG. 5. Small-signal model of the CG-CS stage.

$$I_{in2} = V_{in2}\left(g_{m9} + g_{mb9} + g_{ds9} + g_{ds11} + C_{in2,tot}\right) - V_B\left(g_{m9} + sC_{gs9}\right) - V_{O2}(g_{ds9} + sC_{ds9}) \quad (11a)$$

$$0 = V_A\left(g_{ds14} + s\left(C_{d14} + C_{g10}\right)\right) - V_B sC_{gd10} - V_{in2} sC_{g10} \quad (11b)$$

$$0 = V_B\left(g_{ds13} + g_{ds10} + s\left(C_{d10} + C_{g9} + C_{d13}\right)\right) - V_A\left(g_{m10} - sC_{gd10}\right) - V_{O2} sC_{gd9} \quad (11c)$$

$$0 = V_{O2}\left(g_{ds12} + g_{ds9} + s(C_{d9} + C_{d12})\right) + V_B\left(g_{m9} - sC_{gd9}\right) - V_{in2}\left(g_{m9} + g_{mb9} + g_{ds9} + sC_{gd9}\right) \quad (11d)$$

where $C_{in2,tot} = C_{O1} + C_{s9} + C_{d11} + C_{g10}$ as $C_{O1} = C_{d1} + C_{d5}$. There is no actual gain from node $in2$ to node A, it is rather a transfer of impedance. However, for the sake of representation, the following formula is worked out based on Eq. (11b):

$$A_{in2A} = \frac{V_A}{V_{in2}} = \frac{sC_{g10}}{g_{ds14} + s\left(C_{d14} + C_{g10}\right)} \quad (12)$$

Voltage gain from node A to node B is represented as:

$$A_{AB} = \frac{V_B}{V_A} = \frac{g_{m10}}{g_{ds13} + g_{ds10} + s\left(C_{d10} + C_{g9} + C_{d13}\right)} \quad (13)$$

The voltage gain of the CG-CS stage is introduced as:

$$A_{v2} = \frac{g_{m9}(1 + |A_{in2A}A_{AB}|) + g_{mb9} + g_{ds9}}{g_{ds12} + g_{ds9} + s(C_{d9} + C_{d12})} \quad (14)$$

The input impedance of the CG-CS stage is manifested as follows which was indicated back in Eq. (8):

$$Z_{in2} = \frac{1}{Q + sC_{eq2}} \quad (15)$$

Whereas fractional Q is given as:

$$Q = g_{m9}(1 + |A_{in2A}A_{AB}|) + g_{mb9} + g_{ds9} + g_{ds11} - A_{v2}g_{ds9} \quad (16)$$

The equivalent input capacitance for the CG-CS stage is $C_{eq2} = C_{in2,tot} + |A_{in2A}A_{AB}|C_{gs9}$, while the CG-CS TIA gain is:

$$Z_{TIA2} = \frac{V_{O2}}{I_{in2}} = Z_{in2}A_{v2} \quad (17)$$

The overall TIA gain for the proposed topology is:

$$Z_{TIA} = \frac{I_{O1}}{I_{in1}} \times \frac{V_{O2}}{I_{in2}} \quad (18)$$

where $I_{O1} = I_{in2}$ in which a current gain of the input stage is multiplied by the TIA gain of the CG-CS stage as in the above equation.

3. Noise Analysis

The following equation is based upon an experimental common formula [16], however with a unique expression that describes the mean square channel thermal noise voltage (spectral density) at transistor M_1's drain:

$$\overline{V_{no,d1}^2} = 4kT\alpha g_{m1}(Z_{TIA1} - Z_{O1})^2 \quad (19)$$

where $\alpha = \gamma(g_{d0}/g_m)$, as γ is the channel thermal noise coefficient, and g_{d0} is the zero bias drain conductance. The drain of transistor M_2 mean square channel thermal noise voltage is:

$$\overline{V_{no,d2}^2} = 4kT\alpha g_{m2}\left(Z_{TIA1} - Z_X\frac{A_{v1}}{A_{M2}}\right)^2 \quad (20)$$

Here, $A_{v1}/A_{M2} = V_{O1}/V_X$, where Z_X is the impedance at node X. The mean square channel thermal noise voltage at the drain of transistor M_3 is:

$$\overline{V_{no,d3}^2} = 4kT\alpha g_{m3}\left(Z_{TIA1} - Z_Y \frac{A_{v1}}{A_{M2}A_{M3}}\right)^2 \quad (21)$$

Here, $A_{v1}/(A_{M2}A_{M3}) = V_{O1}/V_Y$, where Z_Y is the impedance at node Y. An update to the approach from prior literature [16] incorporates short channel effects [18] for the mean square induced gate noise voltage (spectral density) of transistor M_1. The expression for the mean square induced gate noise voltage is:

$$\overline{V_{no,g1}^2} = 4kT\delta \frac{(\omega C_{gs1})^2}{5g_{d01}}\left(Z_{TIA1} - Z_Y \frac{A_{v1}}{A_{M2}A_{M3}}\right)^2 \quad (22)$$

where δ is the gate noise coefficient. The shunt conductance (g_g) is redefined here as $\left[(\omega C_{gs1})^2/5g_{d01}\right]$. Previously, it was considered as $[(\omega C_O)^2/g_{d01}]$, where C_O represented the gate-oxide capacitance. The mean square induced gate noise voltages (for transistors M_2 and M_3) are:

$$\overline{V_{no,g2}^2} = 4kT\delta \frac{(\omega C_{gs2})^2}{5g_{d02}}(Z_{TIA1})^2 \quad (23)$$

$$\overline{V_{no,g3}^2} = 4kT\delta \frac{(\omega C_{gs3})^2}{5g_{d03}}\left(Z_X \frac{A_{v1}}{A_{M2}}\right)^2 \quad (24)$$

The common form of the overall gate and drain noise contribution is defined as [16]:

$$\overline{V_{no,Mx}^2} = \overline{V_{no,dx}^2} + \overline{V_{no,gx}^2} + 2|c|\sqrt{\overline{V_{no,dx}^2}.\overline{V_{no,gx}^2}} \quad (25)$$

where c is the cross-correlation coefficient (drain-to-gate noise). Transistor M_4 noise voltage contribution is defined in this work as:

$$\overline{V_{no,M4}^2} = 4kT(Z_{TIA1})^2 g_{ds4} \quad (26)$$

The noise voltage contribution of the PMOS current sources (M_5 and M_8), as well as transistors M_6 and M_7, is uniquely defined in this work as:

$$\overline{V_{no,r}^2} = 4kT\left(Z_O^2 Y_{AI} + Z_x^2 g_{ds6}\left(\frac{V_o}{V_x}\right)^2 + Z_y^2 g_{ds7}\left(\frac{A_{v1}}{A_{M2}A_{M3}}\right)^2\right) \quad (27)$$

The total noise contribution based on integrated mean square noise voltage (spectral density) is:

$$\overline{V_{no}^2} = \overline{V_{no,M1}^2} + \overline{V_{no,M2}^2} + \overline{V_{no,M3}^2} + \overline{V_{no,M4}^2} + \overline{V_{no,r}^2} \quad (28)$$

As a result, the input-referred noise current is given by the following common formula:

$$\overline{I_{in}^2} = \frac{\overline{V_{no}^2}}{(Z_{TIA1})^2} \quad (29)$$

4. Results

Channel length modifications using 45, 90, and 130 nm scales for the proposed TIA circuit topology (Fig. 3) are presented with corresponding TIA gain in Fig. 6(a). Ranging from 45, 90, and 130 nm scale, as the f_{-3dB} bandwidth is reduced, the TIA gain increases. Specifically, bandwidths of 1.68, 1.35, and 1.10 GHz correspond to 44.78, 46.39, and 47.94 dBΩ, respectively. Similar ohmic TIA gain behavior is manifested in Fig. 6(b). For the same bandwidths of 1.68, 1.35, and 1.10 GHz the respective ohmic gains are 173.434, 208.74, and 259.70 Ω, respectively.

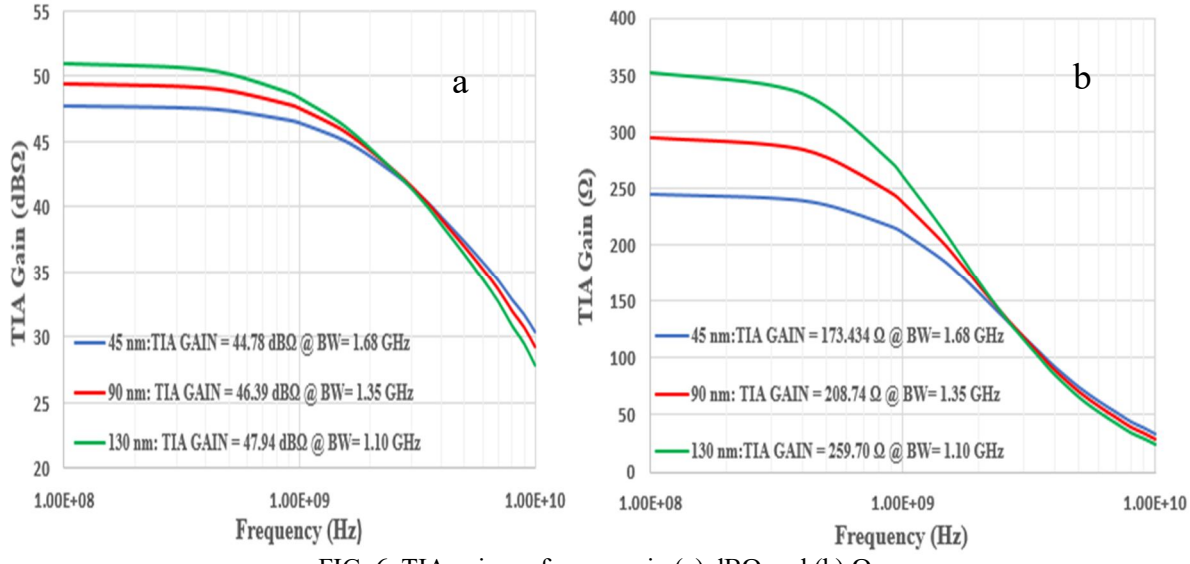

FIG. 6. TIA gain performance in (a) dBΩ and (b) Ω.

The reduction in bandwidth—1.68, 1.35, and 1.10 GHz—correlates directly with a rise in input impedance, as shown in Fig. 7, where the input impedance values are 230.93, 288.22, and 349.19 Ω for the channel lengths of 45, 90, and 130 nm, respectively. In contrast, the input-referred noise current (spectral density), shown in Fig. 8, decreases inversely to the input impedance. Specifically, the noise current reduces to 15.24 $pA/\sqrt{H_z}$, 10.77 $pA/\sqrt{H_z}$, and 9.40 $pA/\sqrt{H_z}$. This inverse relationship between input impedance and input-referred noise highlights a trade-off where increasing the channel length leads to a reduction in noise current, further impacting the bandwidth as a result.

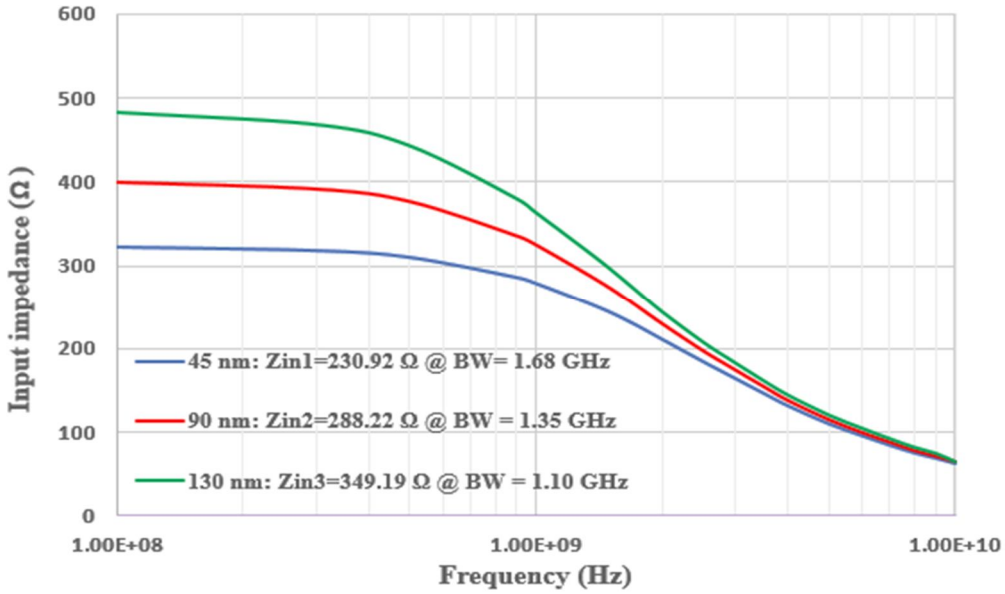

FIG. 7. Input impedance frequency dependence as per each channel length.

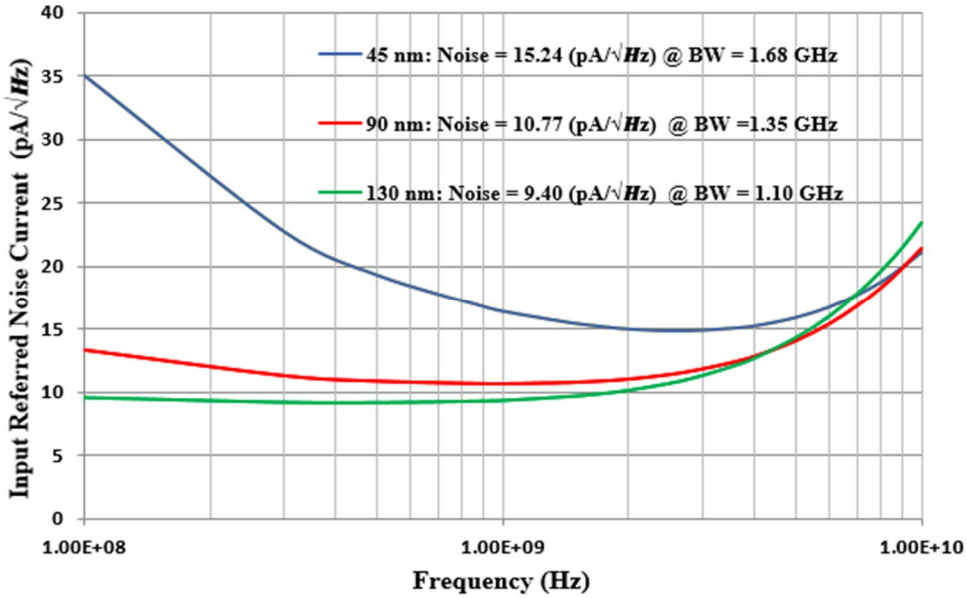

FIG. 8. Input referred noise current spectral density as per each channel length.

The total power consumption is confined to 0.621, 0.29, and 0.175 mW for the channel lengths of 45, 90, and 130 nm, respectively (Fig. 9). In addition, an individual transistor consumption is also shown. The most power-consuming transistors are M_6, $M_{12,}$ and M_{14}. The 45 nm scale consumes more than twice the power of the 90 nm scale and over three times the power of the 130 nm scale.

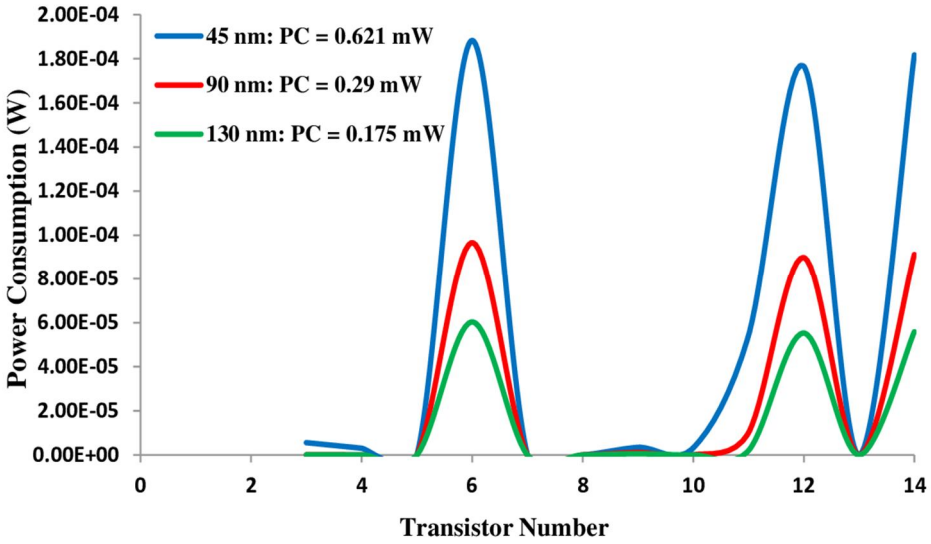

FIG. 9. Power consumption as per each transistor number for the channel length series (45, 90, and 130 nm).

The simulated active inductor impedance, based on extracted data, exhibits a frequency response that somewhat resembles the behavior of a spiral inductor. As shown in Fig. 10, an impedance divergence is observed in the 45 nm scale when compared to the 90 nm and 130 nm scales. This divergence arises from the onset of overlap between the depletion layers extending from the drain towards the source, an effect known as drain-induced barrier lowering (DIBL), which results from short-channel effects. To facilitate a clearer representation, a low frequency of 5 Hz is used.

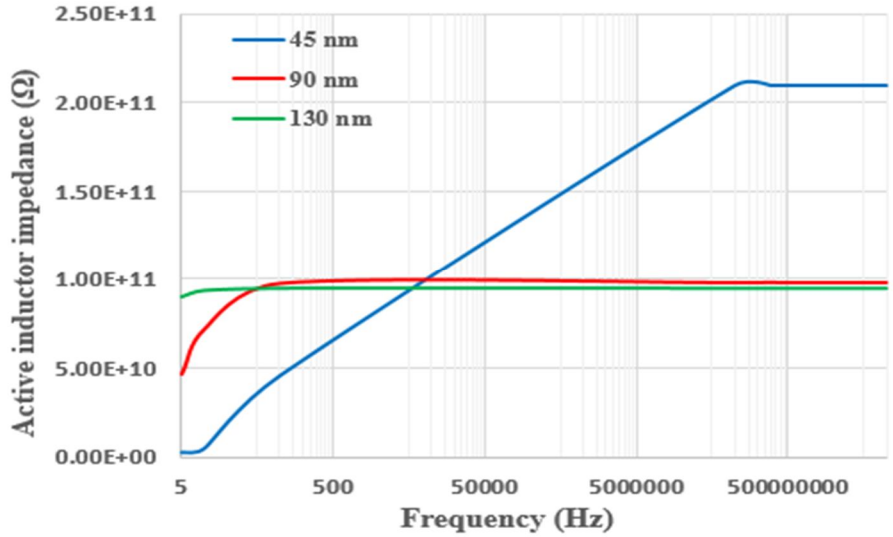

FIG. 10. Calculated active inductor impedance for the channel length series (45, 90, and 130 nm).

The eye diagram for the 45 nm TIA topology is presented in Fig. 11(a). The measure of jitter is around 0.07 ns which is the time variation of zero crossing, while the best time to sample is around 0.4 ns which is the decision point in which the most open part of the eye is equivalent to the best SNR. The signal-to-noise ratio at the sampling point is equivalent to 24.5 mV. The slope corresponds to a change in voltage swing of 15 mV versus a change of 0.09 ns. This slope is relatively small which indicates the sensitivity to timing error. As in the 90 nm scale for the same TIA topology, shown in Fig. 11(b), the measure of jitter is around 0.04 ns, while the best time to sample is around 0.45 ns. The signal-to-noise ratio at the sampling point is equivalent to 32 mV. The slope corresponds to a change in voltage swing of 10 mV versus a change of around 0.04 ns. Regarding the 130 nm scale for the same TIA topology, shown in Fig. 11(c), the

measure of jitter is around 0.04 ns, while the best time to sample is around 0.47 ns. The signal-to-noise ratio at the sampling point is equivalent to 36 mV. The slope corresponds to a change in voltage swing of 8 mV versus a change of around 0.03 ns. The bandwidth series (1.68, 1.35, and 1.10 GHz) and the vertical and horizontal eye openings shown in Fig. 11 indicate very limited intersymbol interference (ISI) in random data transmission. Although the bandwidth is lower at the 90 nm and 130 nm scales, corresponding to 1.35 GHz and 1.10 GHz respectively, a 1.5 Gb/s input bit sequence was applied for comparative performance purposes.

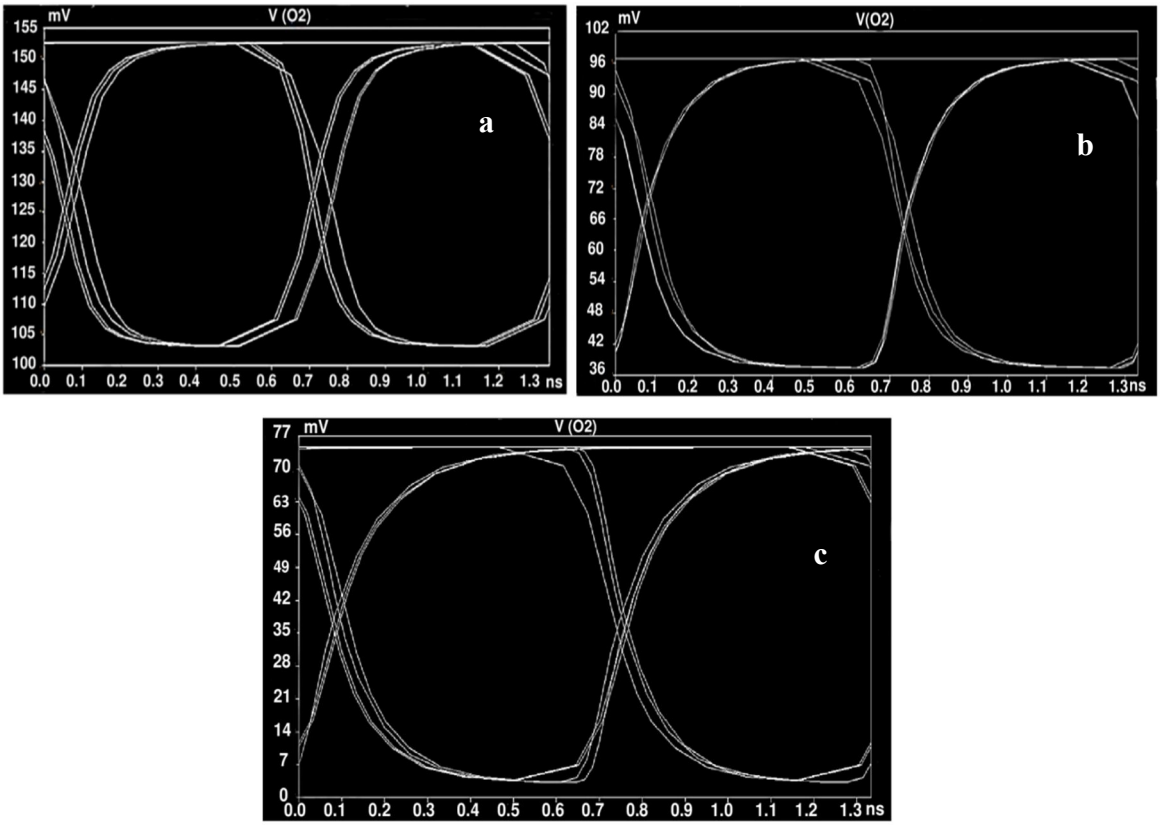

FIG. 11. Eye diagram using bit sequencing at 1.5 Gb/s for : (a) 45 nm scale, (b) 90 nm scale, and (c) 130 nm scale.

For the 45 nm scale, Table 1 illustrates a clear trade-off in TIA gain, bandwidth, and input-referred noise, showing balanced performance. In related literature, the lowest reported power consumption is 0.01 mW [3], though the supply voltage is unspecified. When comparing the power consumption of 0.621 mW achieved in this study with other references [4,19], it becomes evident that, while the gain level of 44.78 dBΩ in this work is moderately lower, the achieved power efficiency offers a competitive advantage in application-specific contexts, particularly given the f_{-3dB} bandwidth of 1.68 GHz.

TABLE 1. Comparative performance for 45 nm scale in relation to other literature.

Ref.	[4]	[19]	[3]	This Work
Year	2010	2018	2022	2023
CMOS Technology	45 nm	45 nm	45 nm	45 nm
TIA Gain (dBΩ)	55	74.4	140	44.78
Bandwidth	30	23	10 MHz	1.68 GHz
Input Referred Noise ($pA/\sqrt{Hz}$)	20.47	12	4.6	15.24
Power Consumption (mW)	9	36.6	0.01	0.621
DC Supply Voltage (V)	1	1	-	1

Table 2 provides a balanced comparison between this work and the cited literature [20-21]. There is an indirect relationship between power consumption and bandwidth, which highlights the trade-off between bandwidth and TIA gain. The power consumption level of 0.29 mW in this work is more than three times lower than that reported in the comparative literature [20, 21]. However, the f_{-3d} bandwidth in the comparative studies is over five times higher, with results for TIA gain and input-referred noise being closer, given that a 1.2V DC supply voltage is applied in that literature [20]. Due to the mentioned trade-off relationships, other studies [22] appear to focus on different applications other than power consumption reduction as a key advantage. The same approach is followed in Table 3 in which there are some divergent results between this work and the cited literature [7, 23] in terms of TIA gain. Given the compromise of achieving a low power consumption of just 0.175 mW in this work, this divergence is expected. However, it is important to note that a 1.5 V DC supply budget is applied in the referenced studies [7, 23], compared to the 1V used in the proposed TIA topology. The high power consumption reported in the cited literature [24] is associated with high input-referred noise, which represents a significant difference from this work, especially since no specific DC supply voltage is indicated in that context.

TABLE 2. Comparative performance for 90 nm scale in relation to other literature.

Ref	[20]	[21]	[22]	This Work
Year	2019	2020	2021	2023
CMOS Technology	90 nm	90 nm	90 nm	90 nm
TIA Gain (dBΩ)	50.5	41	39.8	46.39
Bandwidth (GHz)	7.3	6.5	24.8	1.35
Input Referred Noise ($pA/\sqrt{H_Z}$)	13.7	33.4	50	10.77
Power Consumption (mW)	1	1.67	11.6	0.29
DC Supply Voltage (V)	1.2	1	-	1

TABLE 3. Comparative performance with other literature for 130 nm scale.

Ref	[7]	[23]	[24]	This Work
Year	2015	2019	2021	2023
CMOS Technology	130 nm	130 nm	130 nm	130 nm
TIA Gain (dBΩ)	52.4	59.885	66	47.94
Bandwidth (GHz)	8.2	6.9	40	1.10
Input Referred Noise ($pA/\sqrt{H_Z}$)	1.94 μArms	7.925	9.4	9.40
Power Consumption (mW)	3.6	0.872	142	0.175
DC Supply Voltage (V)	1.5	1.5	-	1

5. Discussion

In the input stage shown in Fig. 3, the active inductor is configured using two PMOS structures (transistors M_5 and M_8). In this configuration, the conditions of having a single MOSFET operating in saturation as a current source do not apply, yet the active inductor can still maintain a stable voltage at node O_1 given the fact that channel length modulation parameter $\lambda \neq 0$. The drain terminal of transistor M_5 can draw a DC current and present high impedance. The significant impedance of the active inductor behaves like an ideal current source, exhibiting nearly infinite small-signal resistance.

Theoretically, the highest possible voltage gain for transistor M_1 is given by $(-g_{m1}r_{O1})$. However, the output node resistance of transistor M_1 is determined by the parallel combination of its own output resistance (represented by the active inductor impedance at low frequencies and the input resistance of the second CG-CS stage. A key advantage of having the active inductor current source is its ability to alleviate the trade-off between voltage gain and the voltage headroom $(V_{GS1} - V_{th})$ so far as transistor M_1 is concerned.

The degeneration output resistance of transistor M_4 sustains a fraction of the input voltage at node $in1$. From the perspective of the

CG configuration, the photodiode input signal is delivered as a current, causing the voltage at node $in1$ to increase by ΔV_{in1}. Consequently, the gate-to-source voltage of transistor M_1 decreases by similar amount, leading to a reduction in drain current by $g_{m1}\Delta V_{in1}$ and consequently, an increase in output voltage at node O_1. The input pole magnitude described in Eq. (1) is maximized within the CG structure by maximizing g_{m1}, which can be achieved by increasing the drain current. This leads to higher gate-to-source and minimum allowable drain-to-source voltages for transistors M_1 and M_4, respectively, along with an increased voltage drop across the active inductor impedance Z_{AI} at the DC level. The 1V supply voltage is sufficient to support these voltage headroom requirements. Interestingly, Z_{AI} is extremely high across the bandwidth series (1.68, 1.35, and 1.10 GHz), and even at lower frequencies as shown in Fig. 10. This high level of Z_{AI} contributes to the suppression of input-referred noise and prevents the magnitude of Z_{TIA1} from falling. The biasing of transistor M_4 is set high enough to allow a reasonably elevated drain-to-source voltage, thereby reducing noise and drain capacitance. Despite the challenging constraints, a broadband topology with a reasonably high transimpedance gain was achievable in this work, even with a low supply voltage of 1V.

The CG drawbacks were overcome since transistor M_1 not only serves as active feedback but is also in a CG configuration. The first CG drawback is that the noise scales in a direct way with $C_{in,tot1}$ and frequency; as $sC_{in,tot1}$ increases, a significant fraction of the noise contributed by transistor M_1 does not circulate inside it but instead flows from the output node O_1. The second drawback, which is often expected, is that the noise contributed to the input by the DC component of Z_{AI} rises as $|sC_{in,tot1}|$ becomes comparable to g_{m1}. This is typically observed since the TIA gain tends to decrease as the signal frequency approaches the input pole.

Within the CG-CS stage, the low input impedance of the CG core (ignoring the high CS input impedance) enables a wider bandwidth of the CG-CS topology, accommodating the time constant of the output node O_1 from the input feedforward stage. The combined CG-CS output impedance is determined by how low is the output conductance of transistors M_{12} and M_{13}. Given the high output resistances of transistors M_9 and M_{10}, it was not possible to neglect channel length modulation. The CG stage on its own suffers from a trade-off between gain and overdrive voltage, the drain resistance of transistor M_9 is high enough to achieve a considerable voltage gain.

With regard to channel length modification effects on input impedance and TIA gain, the upward direction in channel lengths (45, 90, and 130 nm) for the identical proposed TIA topology leads to increases in both TIA gain and input impedance as illustrated in Fig. 6 and Fig. 7. According to Eq. (6), the increase in input impedance (with increasing channel length) is attributed to the decrease in g_{m1} (transconductance of transistor M_1). This decrease in g_{m1} occurs due to the narrower variation in gate-to-source voltage and, subsequently, a reduced variation in drain current for transistor M_1 as channel length increases. Similarly, the decrease in the transconductance parameter g_{m2} for the pass transistor M_2 affects input impedance in the same manner as observed in transistor M_1. Subsequently, an increase in input impedance contributes to the increase in TIA gain of the input stage (Z_{TIA1}) according to Eq. (5). The term $|A_{M2}A_{M2}|$ plays an important role in determining the input stage voltage gain (A_{v1}), which has an inverse relation with input impedance as described in Eq. (5). For a single transistor, there is a proportional relationship between channel length L and voltage gain A_v, expressed as $|A_v| \propto \sqrt{2\mu_n C_{OX} WL/I_D}$ [17]. This relationship remains true when generalized to the proposed circuit topology. Therefore, a higher voltage gain means a higher TIA gain across the channel length series (45, 90, and 130 nm).

Regarding the effects of channel length modification on bandwidth and input-referred noise, the increase in input impedance associated with the channel length series results in reduced bandwidth, lower input-referred noise, and lower power consumption. To be more precise, the DC input resistance is given by $1/P$ according to Eq. (6), hence, the f_{-3dB} bandwidth is governed by this resistance alongside the equivalent input parasitic capacitance C_{eq1}. Therefore, the rise in input impedance shown in Fig. 7 across the channel length series (45, 90, and 130 nm) leads to a reduction in bandwidth (1.68, 1.35, and 1.10 GHz). From the perspective of input-referred

noise shown in Fig. 8, the rise in input impedance along the channel length series causes an increase in Z_{TIA1} gain according to Eq. (5). Given the square Z_{TIA1} term in Eq. (29), this inevitably leads to a reduction in input-referred noise current along the series. The inverse relationship between $\overline{I_{in}^2}$ and $(Z_{TIA1})^2$ as in Eq. (29) may not be straightforward, since the total integrated mean square noise voltage spectral density contribution $\overline{V_{no}^2}$ also contains $(Z_{TIA1})^2$ in various terms. However, the impact of $\overline{V_{no}^2}$ is minimized. For instance, in Eq. (19), the term $(Z_{TIA1} - Z_{O1})^2$ clearly indicates the subtraction of the input stage output impedance Z_{O1}, especially since $g_{ds1} \gg Y_{AI}$ as in Eq. (8), considering that the active inductor impedance Z_{AI} is extremely high at the bandwidth series (1.68, 1.35, and 1.10 GHz) shown in Fig. 10.

In terms of the effects of channel length modification on power consumption reduction, the upward trend in channel length correlates with the output resistance of each individual transistor, since $r_O = (\lambda I_D)^{-1}$. Given that $\lambda \propto L^{-1}$ and considering the channel length series (45, 90, and 130 nm), a new form of channel length modulation arises for the proposed TIA circuit topology. The series power consumption (0.621, 0.29, and 0.175 mW) shown in Fig. 9 corresponds to the aforementioned channel length series, which is attributed to the rise in output resistance of each transistor. PMOS current sources, such as transistors M_6, M_{12} and M_{14}, exhibit higher power consumption compared to other transistors. For transistor M_6, an additional drain current is drawn due to the biasing of transistor M_2 in a degenerative configuration, where its source is connected to the drain of the biasing transistor M_4, resulting in an extra drain current. Transistor M_{12} also has a degeneration path through the drain of transistor M_{11}, and similarly for transistor M_{14}. Based on the above argument, it is valid to say that the 45 nm scale indicates the highest power consumption, although it is still far lower than values reported in other literature. It is also possible that there was an overlap in the depletion regions between the drain and source in the 45 nm scale, which could have led to higher output resistance due to short-channel effects, specifically drain-induced barrier lowering (DIBL).

In the comparative performance analysis tables, an important concept emerges regarding the trade-offs among TIA gain, bandwidth, and input-referred noise. This trade-off is evident in the 45 nm scale literature presented in Table 1, as well as in the rest of the channel length series (45, 90, and 130 nm) for the proposed TIA topology shown in Fig. 3. For application-specific criteria, power consumption reduction does not exactly and fully follow the trends observed in the comparative literature presented in Tables 1, 2, and 3, as the channel length increases from 45, 90, and 130 nm. This discrepancy is due to the selective nature of certain applications that may relax the original trade-offs in TIA gain, bandwidth, and input-referred noise. Nonetheless, the general principle that power consumption reduces with increasing channel length (for similar or different topologies) remains valid in most cases.

Conclusion

A proposed TIA was designed, analyzed, and simulated with channel length modification. It was found that a trade-off between gain, bandwidth, and input-referred noise current can still apply as the channel length is increased from 45, 90, and 130 nm. In addition, power consumption reduction occurred with the upward modification of channel length for the same topology.

References

[1] Raut, A., Bhagat, N., and Rathod, S. S., Int. J., 2 (10) (2013) 1022.

[2] Kim, J. and Buckwalter, J. F., IEEE J. Solid-St. Circ., 47 (3) (2012) 615.

[3] Muthukumaranm B. and Ramachandranm B., J. Phys.: Conf. Ser., IOP Publishing, 2335 (1) (2022) 012039.

[4] Saffari, R., Dolatshahi, M., and Zohoori, S, 28th IEEE Conf. Electrical Engineering, (ICEE), Iran, (2020), 1-5.

[5] Zohoori, S. and Dolatsahi, M., Int. J. Circ. Theor. App., 46 (12) (2018) 2217.

[6] Khaki, A. M. Z., Omoomi, M., and Borzabadi, E., 24th IEEE Conf. Electrical Engineering (ICEE), Iran, (2016), 1055-1059.

[7] Atef, M. and Abd-Elrahman, D., Nat. Radio Sci. Conf. (NRSC), Egypt, (2015), 363-370.

[8] Atef, M. and Abd-Elrahman, D., 21st Int. Conf., Mix. Design Integr. Circuit Sys., Poland, (2014), 103-107.

[9] Wu, M. Z., Hong, S., Su, H. M., and Hsu, S.S., IEEE MTT-S Int. Microwave Symp. (IMS), USA, (2021), 393-396.

[10] Ponchet, A. F., Bastida, E. M., Finardi, C. A., Panepucci, R. R., Tenenbaum, S., Finco, S., and Swart, J. W., 29th Symp. Integr. Circuit Sys. Design (SBCCI), Brazil, (2016).

[11] Razavi, B., "Design of Integrated Circuits For Optical Communications", 2nd Ed., (A John Wiley & Sons, Inc. Publication, New Jersey, 2012), 124-26.

[12] Hammoudi, E., Imad, B., and Mohamed, D., IEEE Int. Conf. Complex Sys. (ICCS), Morocco, (2012), 1-6.

[13] Park, S. M. and Yoo, H., IEEE J. Solid-St. Circ., 39 (1) (2004) 112.

[14] Park, S. M., Lee, J., and Yoo, H., IEEE J. Solid-St. Circ., 39 (6) (2004) 971.

[15] Chen, W. Z., Cheng, Y. L. and Lin, D. S., IEEE J. Solid-St. Circ., 40 (6) (2005) 1388.

[16] Kromer, C., Sialm, G., Morf, T., Schmatz, M.L., Ellinger, F., Erni, D. and Jäckel, H., IEEE J. Solid-St. Circ., 3 (6) (2004) 885.

[17] Razavi, B., "Fundamentals of Microelectronics", Review Ed., (A John Wiley & Sons, Inc., Publication, New Jersey, 2006), 575-576.

[18] Youssef, A. A. and Haslett, J., "Nanometer CMOS RFICs for Mobile TV Applications", (Springer Science & Business Media, 2010), 17-18.

[19] Xie, Y., Li, D., Liu, Y., Liu, M., Zhang, Y., Wang, X., and Geng, L., IEEE Int. Symp. Circuits Sys. (ISCAS), Italy, (2018).

[20] Soltanisarvestani, R., Zohoori, S., and Soltanisarvestani, A., Intl. J. Electron., 107 (3) (2020) 444.

[21] Honarmand, S., Pourahmadi, M., Shayesteh, M., and Abbasi, K., J. Circuit. Sys. Comp., 30 (06) (2021) 2150110.

[22] Jou, J. J., Shih, T. T., Peng, C. C., Hsu, H. W., and Ye, X. Y., J. Semicond. Tech. Sci., 21 (5) (2021) 304.

[23] Elbadry, M. M., Makkey, M. Y., Abdelgawad, M., and Atef, M., Elsevier, Microelectr. J., (2019).

[24] Inac, M., Dziallas, G., Fatemi, A., Gerfers, F., and Malignaggi, A., 15th IIEEE European Microwave Integr. Circuit Conf. (EuMIC), Netherlands, (2020), 292-295.

Volume 17, Number 4, 2024. pp. 497-504

Jordan Journal of Physics

TECHNICAL NOTE

Level and Potential Radon (^{222}Rn) Radiation Risk in Groundwater Samples at Jimba-Oja, Northcentral Nigeria

Toafeeq O. LAWAL[a], **Habeeb A. SHITTU**[a], **John S. Abayomi**[b] and **Funmilayo AYEDUN**[c]

[a] *Physics Department, University of Ilorin, Ilorin, Kwara state, Nigeria.*

[b] *Deptartment of Science Laboratory Technology, Kwara State Polytechnic, Ilorin, Nigeria.*

[c] *Pure and Applied Science Department, National Open University of Nigeria.*

Doi: **https://doi.org/10.47011/17.4.12**

Received on: 19/11/2022; *Accepted on: 21/03/2023*

Abstract: Radon (^{222}Rn) concentration in groundwater was investigated using the Rad7 detector. This investigation was necessary due to the impact of a new mining company in Jimba-Oja, which may affect the surface water supply, potentially percolating into subsurface water sources. Nine (9) samples were collected from hand-pump wells and analyzed in the laboratory. The estimated radon concentration ranged from 3.08 Bq. L^{-1} to 9.18 Bq. L^{-1} with an average value of 5.00 BqL^{-1}. The average AED for groundwater ingestion by adults, children, and infants was calculated at 36.50, 54.75, and 63.88 $\mu Sv.y^{-1}$, respectively. The average AED_{total} values were 162.50 $\mu Sv.y^{-1}$ for adults, 180.75 $\mu Sv.y^{-1}$ for children, and 189.88 $\mu Sv.y^{-1}$ for infants. The results indicate that the AED for infants exceeds the permissible limit of 100 $\mu Sv.y^{-1}$, while the values for children and adults remain within the recommended limit of 200 $\mu Sv.y^{-1}$. Thus, the health risk from radiological exposure is within allowable limits for children and adults but poses a potential risk for infants. Although ^{222}Rn concentrations in groundwater samples are low, are currently low, there may still be probabilistic effects on local inhabitants over time. To monitor ^{222}Rn levels, we recommend repeating these measurements in the same wells and season within the next two years to ensure consistency and detect any changes in radon levels.

Keywords: Radon (^{222}Rn) concentration, Groundwater, Jimba-Oja, Dose rate.

Introduction

^{222}Rn a naturally occurring radioactive gas originating from the disintegration of the ^{238}U series, is a natural radioactive element found within layers of the Earth [1]. ^{222}Rn has a half-life of up to 3.82 days, after which it quickly decays, producing a short-lived radioactive element polonium-218 and emitting a series of radioactive elements, as illustrated in Fig. 1 [2]. ^{222}Rn is a chemical element with the symbol Rn and an atomic number of 86. It is a colorless, odorless, and tasteless noble gas that is radioactive and soluble in water. It is a product of radium-226, which has a half-life of 1,602 years and originates from the uranium series via alpha decay. This makes it one of the main sources of radiation risk in homes, caves, water, and the environment. When radon is mixed with other atmospheric particles such as aerosols and dust and is inhaled, it can damage the lungs [3]. Alpha, beta, and gamma radiation are emitted

Corresponding Author: Toafeeq Olanrewaju LAWAL **Email**: lawal.to@unilorin.edu.ng

during the radioactive decay chain of ^{222}Rn. This decay chain starts with the alpha decay of ^{222}Rn, producing polonium-218 with an energy of 5.49 MeV and a half-life of 3.1 minutes, which makes it useful in tracing the early history of groundwater. Other decay products, namely lead (Pb-214), bismuth (Bi-214), polonium (Po-214), lead (Pb-210), bismuth (Bi-210), polonium (Po-210), thallium (Ti-206), and lead (Pb-210) are shown in Fig. 1 along with their half-lives, energies, and emitted radiation types.

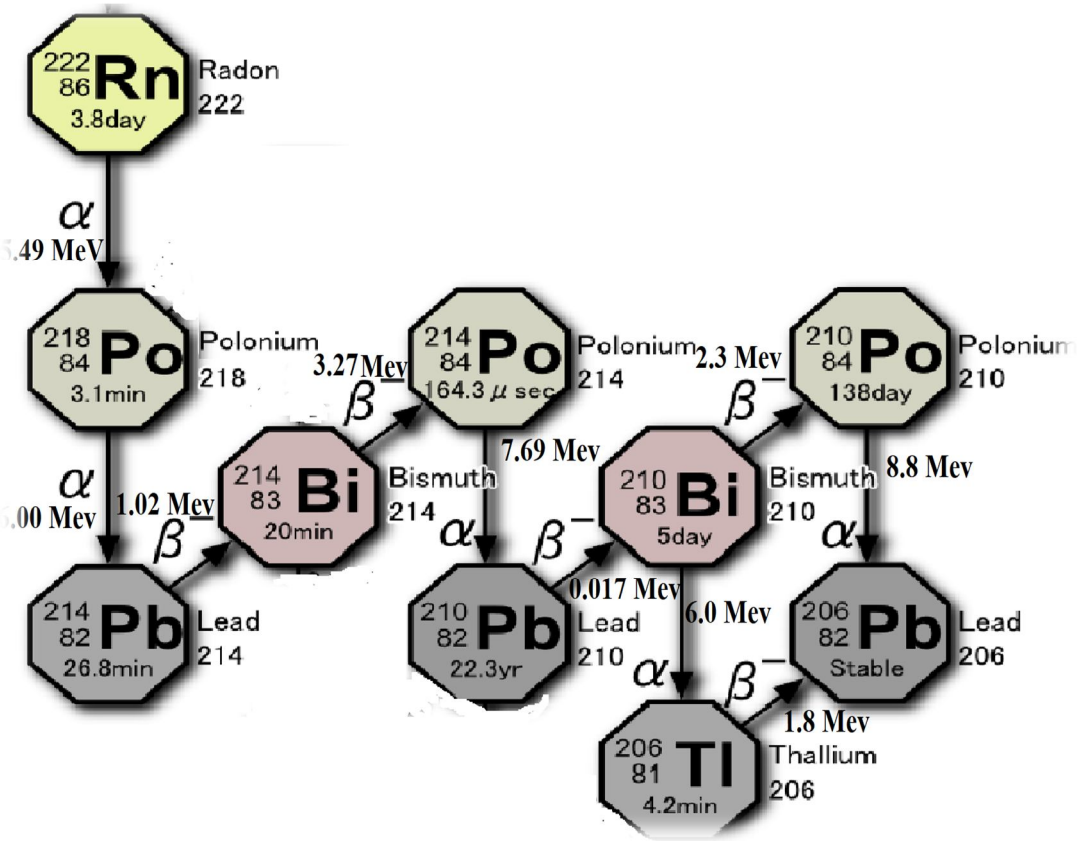

FIG. 1. The decay series from radon-222 to lead-206 (stable) [13].

Studies have reported that natural ^{222}Rn and its decay products are responsible for over fifty percent of the overall effective dose of ionizing radiation received by the global population from natural sources [2, 4]. Concentrated ^{222}Rn in groundwater can be attributed to factors such as radium/uranium levels in surrounding rocks, lithology, presence of shear zones, degree of metamorphism, and soil porosity [5]. This means that ^{222}Rn concentrations in geological environments vary depending on the activity concentration of radium in the host rocks present in the area. The concentration and associated risk of ^{222}Rn increase with higher levels of radium and uranium in groundwater [4, 5].

Water, an essential resource for living organisms, is estimated to amount to nearly a billion cubic meters on Earth [6]. Groundwater is particularly important as a primary source for domestic use, especially in Africa [4, 7]. However, this untreated water source is vulnerable to contamination from geological rocks and the decay of radioactive elements, which can lead to varying degrees of radiation hazards for residents [4]. Many researchers around the world have reported ^{222}Rn concentrations in surface and groundwater. For instance, [3] investigated ^{222}Rn concentrations in ground and surface water samples in Sankey Tank and Mallathahalli Lake, using a Durridge RAD-7 analyzer. They reported average radon activities ranging from 11.6 ± 1.7 to 381.2 ± 2.0 Bq. L^{-1} for surface water and 1.50 ± 0.83 to 18.9 ± 1.59 Bq. L^{-1} for groundwater. In another study, ^{222}Rn concentrations were measured in groundwater in the Ashanti region of Ghana using an AB-5 detector [8]. They obtained average ^{222}Rn values ranging from 0.51 to 46.16 Bq. L^{-1}. [6] determined concentrations of ^{222}Rn gas in selected bottled and sachet water from a major market of Ile-Ife, Nigeria using a RAD 7 device made by Durridge, USA. They found

^{222}Rn concentrations for bottled samples between 0.00 and 9.4493 Bq. L^{-1} (average: 2.4428 Bq L^{-1}) and for sachet samples between 0.0479 and 0.5068 Bq L^{-1} (average: 0.2492 Bq L^{-1}). These results were deemed safe for household use.

Another study assessed the annual effective dose of ^{222}Rn in drinking water from an abandoned mining site in Oyun, Nigeria, reporting ^{222}Rn concentrations from 21.03 to 44.95 Bq L^{-1} (average: 35.86 Bq L^{-1}) [9], which exceed the United Nations Scientific Committee on the Effects of Atomic Radiation's recommended limit of 11.1 Bq L^{-1} [10]. These findings underscore the need to monitor water quality to protect public health from potential radiation hazards linked to radioactive decay [11]. Given the establishment of a new mining company in Jimba-Oja, assessing ^{222}Rn levels in the area's groundwater is especially relevant.

Area of Study

The area of study, Jimba-Oja, is located southwest of Ilorin, the state capital of Kwara State which is about 21 km from the state capital (Fig. 2). Geologically, the area lies within the Precambrian basement complex, which has been extensively described by several authors [15,16]. This part of the country consists predominantly of migmatite gneiss and the schist belt formations. The area of study is made up of about 60% rocks within the migmatite-gneiss-quartzite complex. The rocks include granite gneiss, banded gneiss, migmatite gneiss, and banded iron formations. The schist belts, which are generally localized to the southwestern part of Nigeria, contain younger meta-sediments primarily concentrated in the central part of the study area, as depicted in the geological map (Fig. 3).

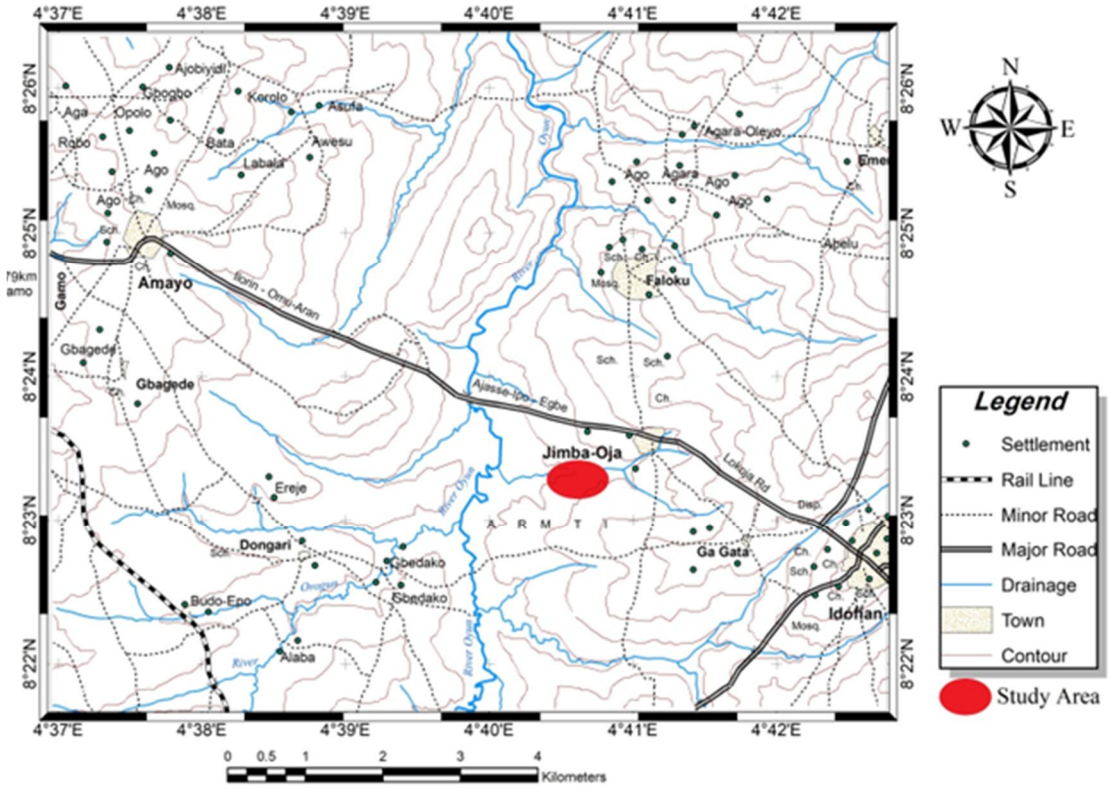

FIG. 2. Topographical map showing the area of study [17].

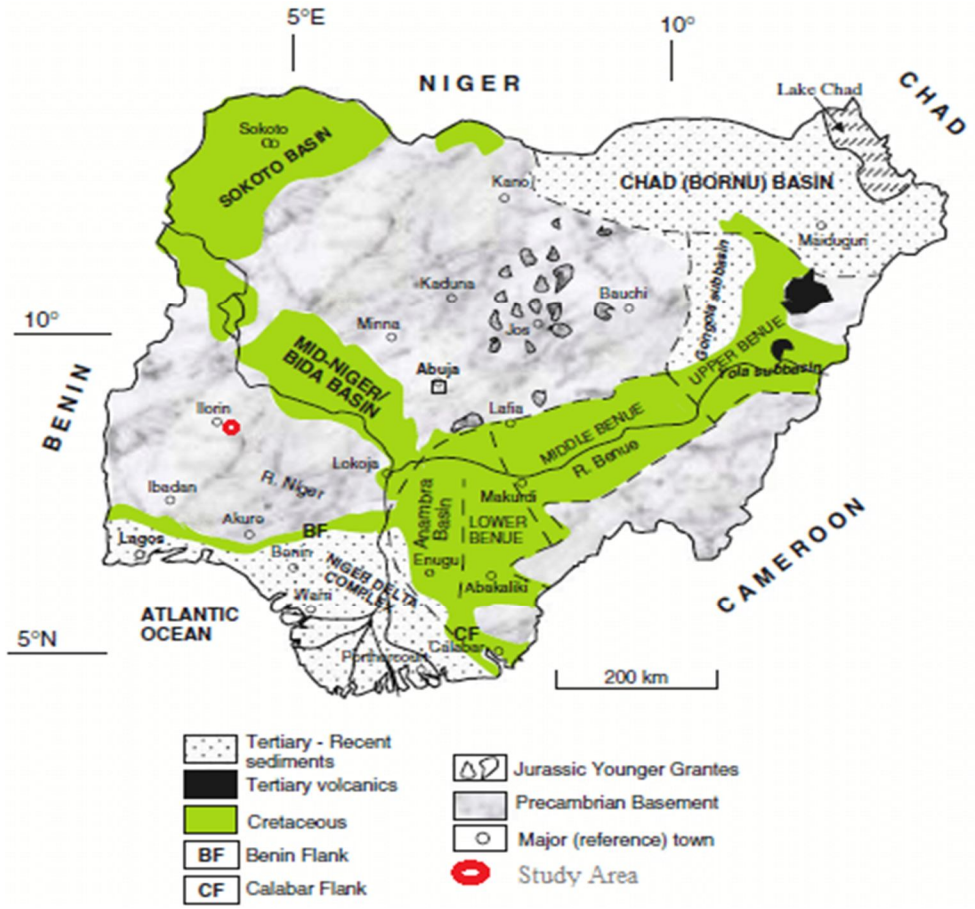

FIG. 3. Nigeria geological map showing the area of study [18].

Methodology

Nine groundwater samples were randomly collected from sites near KAM Wire Company, where the water sources serve domestic purposes for the local inhabitants. Samples were taken as early as possible from their sources to prevent agitation by the inhabitants. Each sample was drawn from hand pump wells after allowing the water to run from the pump for 10 to 15 minutes before collection to prevent radon mixing [4, 9]. The water was collected below the surface and filled to the brim of a 250 mL plastic bottle. Bubbles were removed, and each bottle was sealed tightly with a detector water kit to prevent radon loss due to degassing [9].

In the lab, a Rad-7 detector, manufactured by Durridge Company, Inc., was used to measure radon (^{222}Rn) concentrations [19]. The RAD7 operates as an aerated, closed-loop system comprising: (a) the RAD7 monitor, (b) a desiccant tube supported by a retort stand, and (c) a watertight aerator (Fig. 4). Based on alpha particle disintegration, the detector uses a solid-state sensor to identify alpha particles with varying energy levels [3, 19]. This solid-state detector converts alpha particle energy into electrical signals, enabling the identification of disintegration products from ^{222}Rn to ^{218}Po and ^{214}Po, each emitting particles at unique energy levels (Fig. 1). Radon concentration was measured using a radon-in-air monitor (RAD7) coupled with a specially fabricated closed-loop aeration system that released radon gas from the water, maintaining constant air and water volumes independent of flow rate. This closed-loop system ensures that air and water volumes remain consistent, regardless of flow fluctuations. After 15 to 20 minutes, radon concentration levels in the groundwater samples were accurately assessed through energy-specific windows, which filter out interference and maintain low background counts for precise radon measurement [12].

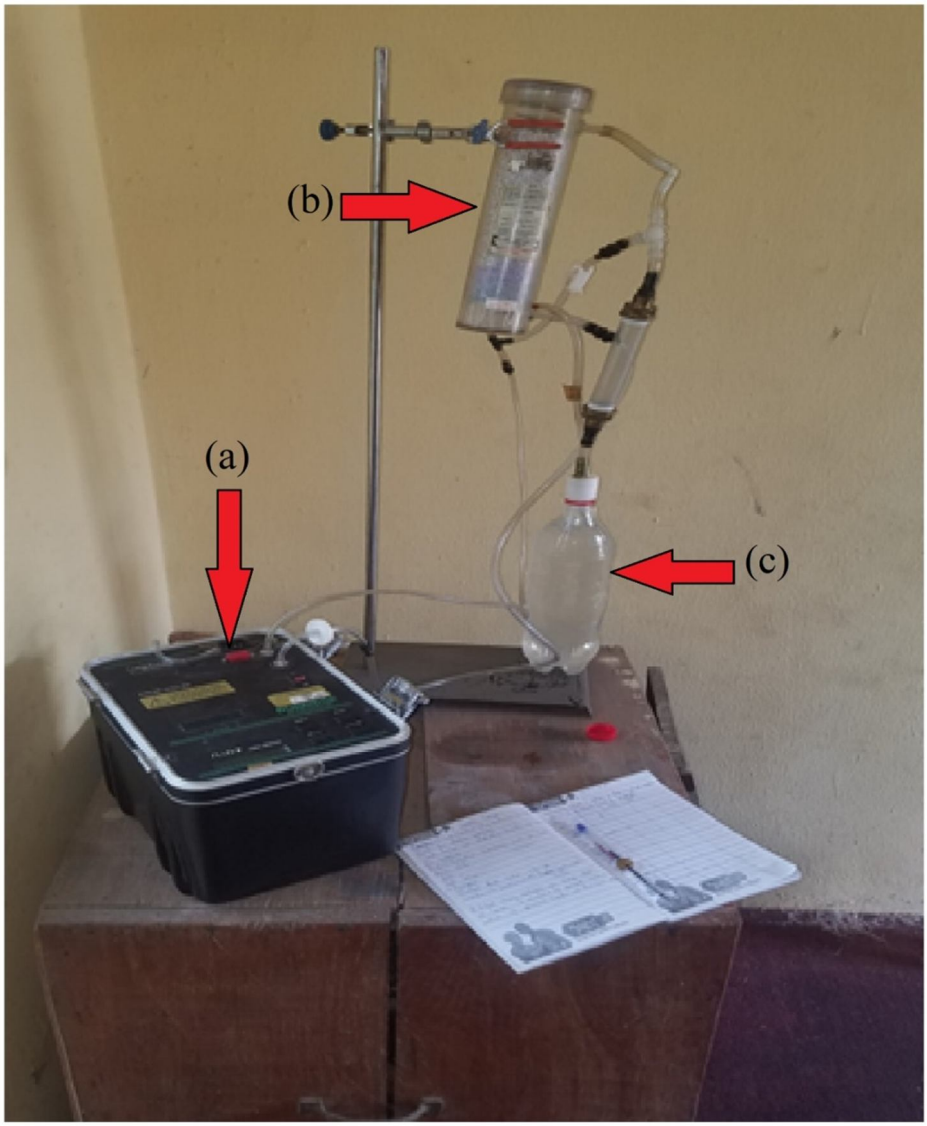

FIG. 4. A typical RAD-7 radon detector: (a) a Rad-7 monitor, (b) a desiccant tube supported by a retort stand, and (c) a watertight aerator [9, 19].

To assess the level of exposure among different age groups (infants, children, and adults), the annual effective dose (AED) from both inhalation and ingestion is a central aspect of radiological protection. It sums up various exposure levels into a single value that reflects the overall risk, making the concept practical for radiological safety, despite its complexity. The total annual effective doses (AED $_{total}$) were calculated due to the potential for ^{222}Rn gas to enter homes via air when water is used for domestic purposes.

The mathematical expression for AED$_{ingestion}$ rate (μSvy^{-1}) of groundwater is given as [9]:

$$\text{AED}_{ing} = T * K * C_{Rn} * C_w \quad (1)$$

where T is time span in a year, K is the dose per unit consumption from the ingested water, which varies among different age groups (infants, children, and adults), C_w is daily water consumption, also varying by age group, and C_{Rn} is the concentration of ^{222}Rn in each of the samples obtained from the laboratory.

To calculate the AED from inhalation, the following expression is used [9]:

$$\text{AED}_{inh} = Dose\ Conversion\ Factor\ (DCF) * O * C_{Rn} * F \quad (2)$$

where O is the mean indoor occupancy time per individual and F is the equilibrium factor between ^{222}Rn and the offspring (0.4).

Finally, the total annual effective dose AED_{total} can be expressed mathematically as[9]:

$$AED_{total} = AED_{ing} + AED_{inh} \quad (3)$$

Results and Discussion

The laboratory investigation of ^{222}Rn samples is summarized in Table 1. This table includes labeled samples (1–9), as well as the latitude, longitude, and elevation of the study area, alongside the activity concentrations of ^{222}Rn gas and their associated errors. The results indicate that the concentration of ^{222}Rn ranges from a minimum value of 3.08 Bq. L^{-1} in Well 4 to a maximum value of 9.18 Bq. L^{-1} in Well 9.

The observed levels of ^{222}Rn concentrations in groundwater are primarily influenced by the activity concentration of Radium-226 in the host rock and its distribution within the rock cycle. Generally, activity concentrations of Radium-226 are relatively low in rocks such as gneiss, while they tend to be higher in sandstones and weathered granite rocks [4]. Consequently, the low values of ^{222}Rn concentrations recorded in this study can be attributed to the presence of granite-gneiss, banded-gneiss, migmatite-gneiss, and banded iron formations in the area.

TABLE 1. ^{222}Rn concentrations for each water sample.

Water Samples	Latitude (^{0}N)	Longitude (^{0}E)	Elevation (M)	Radon (^{222}Rn) [Bq. L^{-1}]	Error±
WELL 1	8.3731	4.665	344	3.97	0.64
WELL 2	8.3645	4.6021	347	5.09	0.92
WELL 3	8.3942	4.6011	349	3.33	0.76
WELL 4	8.3983	4.681	346	3.08	0.73
WELL 5	8.3977	4.682	348	5.44	0.94
WELL 6	8.3042	4.6815	347	5.26	0.94
WELL 7	8.3823	4.6805	349	4.61	0.88
WELL 8	8.3897	4.671	346	5.04	0.92
WELL 9	8.3055	4.6801	345	9.18	1.20
Min.				3.08	0.64
Max.				9.18	1.20
Mean				5.00	0.88
S.D				1.68	0.15

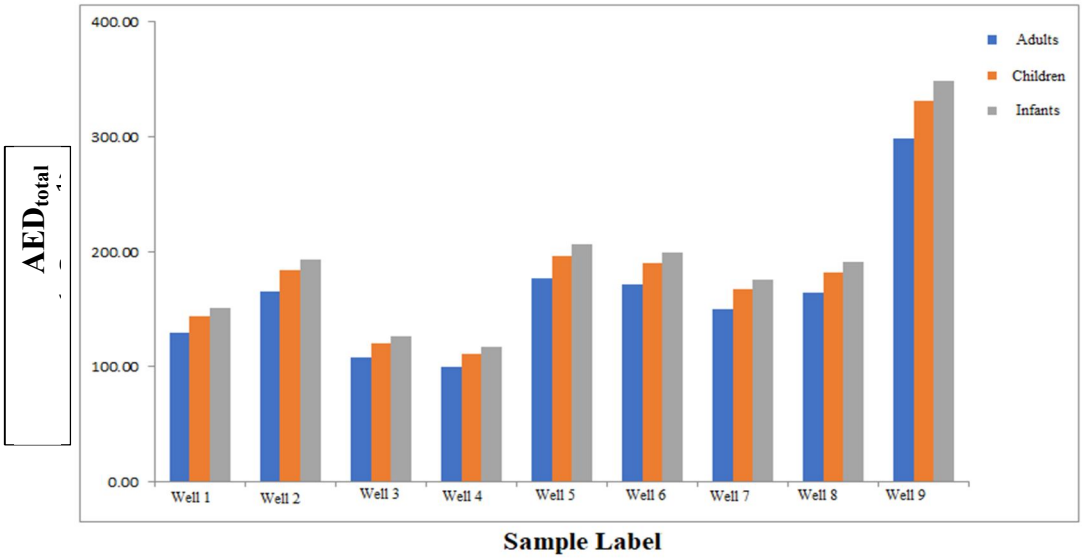

FIG. 5. Estimated total AED ($\mu Sv.y^{-1}$) for all age groups.

Additionally, the level of radon hazards among different age groups was assessed using Eqs. (1), (2), and (3). For Eq. (1), 365 days were used to represent the time span throughout the year. K varies by age group: it is 7 x 10^{-8} SvBq^{-1} for infants, 2 x 10^{-8} SvBq^{-1} for children, and 10^{-8} SvBq^{-1} for adults [9]. C_w also differs among age groups: infants are expected to consume 0.5 liters, children 1.5 liters, and adults 2.0 liters a day. C_{Rn} is the concentration ^{222}Rn in each of the samples obtained from the laboratory [11]. For Eq. (2), the dose conversion factor (DCF) was set at 9 ($\mu Sv.y^{-1}$), with an average indoor occupancy time of 7,000 hours per year and an equilibrium factor (F) of 0.4 [20]. Equation (3) provides the total annual effective dose (AED) by summing the values from both equations. Table 2 presents the results, including

columns for AED via ingestion and inhalation, along with the total AED for each age group (infants, children, and adults). The average AED values for water ingestion are 63.88, 54.75, and 36.50 $\mu Sv.y^{-1}$ for infants, children, and adults, respectively. The inhalation values range from 77.62 to 231.34 μSvy^{-1}, with a mean value of 126.00 μSvy^{-1}.

TABLE 2. Estimated AED from ingestion and inhalation, along with the total AED for all age groups (infants, children, and adults).

Water Samples	AED $_{ingested}$ $(\mu Sv.y^{-1})$			AED $_{inh}$ $(\mu Sv.y^{-1})$	AED $_{TOTAL}$ $(\mu Sv.y^{-1})$		
	Infants	Children	Adults		Infants	Children	Adult
WELL 1	50.72	43.47	28.98	100.04	150.76	143.52	129.03
WELL 2	65.02	55.74	37.16	128.27	193.29	184.00	165.43
WELL 3	42.54	36.46	24.31	83.92	126.46	120.38	108.23
WELL 4	39.35	33.73	22.48	77.62	116.96	111.34	100.10
WELL 5	69.50	59.57	39.71	137.09	206.58	196.66	176.80
WELL 6	67.20	57.60	38.40	132.55	199.75	190.15	170.95
WELL 7	58.89	50.48	33.65	116.17	175.06	166.65	149.83
WELL 8	64.39	55.19	36.79	127.01	191.39	182.20	163.80
WELL 9	117.27	100.52	67.01	231.34	348.61	331.86	298.35
Min.	39.35	33.73	22.48	77.62	116.96	111.34	100.10
Max.	117.27	100.52	67.01	231.34	348.61	331.86	298.35
Average	63.88	54.75	36.50	126.00	189.88	180.75	162.50

The AED_{total} calculated using Eq. (3) shows variations in the estimated dose rates among different age groups, as illustrated in Fig. 5. The average values obtained are 189.88 $\mu Sv.y^{-1}$ for infants, 180.75 $\mu Sv.y^{-1}$ for children, and 162.50 $\mu Sv.y^{-1}$ for adults (Table 2). These values indicate that the estimated dose for infants exceeds the recommended permissible limit of 100 $\mu Sv.y^{-1}$, while the values for children and adults are within the acceptable limit of 200 $\mu Sv.y^{-1}$ [21]. This suggests that the health risks associated with radiological hazards are acceptable for children and adults, but pose a significant risk for infants. It is crucial to ensure that infants receive proper care, as their systems and organs are still developing. Greater attention should be given to the water consumption of this age group to prevent potential adverse effects from radiological hazards, including cancer and skin diseases. Furthermore, it is important to note that the results may not be directly linked to the mining company; rather, they could be attributed to naturally occurring radioactive elements that have leached into the groundwater.

Conclusion

An investigation into the levels and potential radon radiation risks of randomly selected groundwater samples from Jimba-Oja, Kwara State, was conducted using a Rad-7 electronic detector in the laboratory. This study aimed to provide baseline information on ^{222}Rn concentrations across different age groups, particularly in light of the newly established KAM iron and steel company in the area. The results indicate that the mean ^{222}Rn concentration is low compared to the recommended value [21, 22]. However, the total annual effective dose (AED) for infants was found to be higher than the recommended limit, while the doses for children and adults remained within acceptable levels.

It is recommended that this measurement be repeated across all seasons to determine if the newly established KAM Iron and Steel Company has any radiological impact on these age groups. Additionally, ^{222}Rn should be assessed in all sources of drinking water throughout the state and the country. This approach would enable the establishment of state or national maximum permissible limits for all age groups, safeguarding public health from radiological pollution. Although the values obtained serve as baseline data for this area, the presence of the KAM Iron and Steel Company may pose radiological hazards in the future. Currently, however, the groundwater in this area is safe for drinking and domestic use, as the average ^{222}Rn values from this study are below recommended limits [21, 22].

References

[1] Ali, A. A., Qusay, B. M., Noor, A. J., and Hassan A. M., Jordan J. Phys., 15 (4) (2022) 353.

[2] Mustafa, A. and Daniel, K., Int. J. Radiat. Biol., 1 (85) (2009) 57.

[3] Ravikumar, P. and Somashekar, R. K., Int. J. Environ. Sci. Technol., 3 (2013) 247.

[4] Nguyen, D. C., Marek, D., Pawel, J., Jakub, N., Kazimierz, R., Monika, S., and Przemyslaw, W., Taylor & Francis, 2011 (2011) 415.

[5] Adegun, I. K., Anyaegbuna, B. E., and Olayemi, O. A., IOP C. Ser. Earth Env., 1378 (2019) 1.

[6] Oni, E. A., Adagunodo, T. A., Adegbite, A. A., and Omeje, M., IOP C. Ser. Earth Env., 655 (2021) 012092.

[7] Olawepo, A. O., Fatoyinbo, A. A., Ali, I., and Lawal, T. O., Afr. Rev. Phys., 8 (45) (2013) 317.

[8] Noah, K. A. D., Patrick, A. P., Eric Clement, D. K. A., David, D. W. and Anthony, A. A., J. Radioanal. Nucl. Chem., 317 (2018) 675.

[9] Orosun, M. M., Ajibola., T. B., Ehinlafa, O. E., Issah, A. K., Salawu, B. N., Ishaya, S. D., Ochommadu, K. K., and Adewuyi, A. D., Pollution, 8 (1) (2022) 181.

[10] United Nations Scientific Committee on the Effects of Atomic Radiation, UNSCEAR 2019 Report. Report to the General Assembly Scientific Annexes A and B, (2020) 220-254.

[11] Usikalu, M.R., Olatinwo, V., Akpochafor, M., Aweda, M.A., Giannini, G. and Massimo, V., IOP Conf. Series: J. of Phys.: Conf. Series, 852 (2017) 012028.

[12] Malakootian, M. and Nejhad, Y. S., Iran. Int. J. Radiat. Res., 15 (1) (2017) 81.

[13] Gillmore G. K., Crockett, R. G. M. and Przylibski, T. A., Nat. Hazards Earth Syst. Sci., 10 (2010) 2051.

[14] Khalaf., Q. and Hayder., S., H. Journal of Physics: Conference Series 2114 (2021) 012062.

[15] Lawal, T. O., Arab. J. Geos., 13 (16) (2020) 1.

[16] Fatoyinbo, A. A., Lawal, T. O., Yussuf, A. H., and Fawale, O., Jordan J. Phys., 3 (15) (2022) 247.

[17] Abdullahi, A. B. and Feyisetan, T. O. https://www.researchgate.net/project/Geology-of-JIMBA-OJA-ARMTI-Southwestern-Nigeria.

[18] Obaje, N. G., Springer, 120 (2009) 1.

[19] Somashekar, R. K. and Ravikumar, K., J. Radioanal. Nucl. Chem., 285 (2010) 343.

[20] Khalaf, Q. and Hayder, S. H., J. Phys.: Conf. Ser., 2114 (2021) 012062.

[21] USEPA, Air and Radiation Report EPA (2008), 402 – 424.

[22] WHO, "Guidelines for Drinking Water Quality", 4th Ed., (World Health Organization, Geneva, 2011), 245-250.

Volume 17, Number 4, 2024. pp. 505-516

Jordan Journal of Physics

ARTICLE

On the Optimization of the Transmission Performance of a Broadband A-Sandwich Radome Wall Structure

Manal M. Al-Ali[a], **A. M. Al-Khateeb**[a], **Abd Alghany Jaradat**[a] and **S. H. Mahmood**[b]

[a] *Department of Physics, Yarmouk University, Irbid, Postal Code 21163, Jordan.*
[b] *Department of Physics, The University of Jordan, Amman, Postal Code 11942, Jordan.*

Doi: **https://doi.org/10.47011/17.4.13**
Received on: 23/08/2023; *Accepted on: 28/11/2023*

Abstract: In this work, the microwave propagation characteristics of a planar A-sandwich broadband radome wall structure (Glass epoxy/PU foam/Glass epoxy) were investigated using the characteristic matrix formalism. Theoretical results were compared with those from COMSOL Multiphysics software under varying parameters. At optimal thickness values of the skin (d_1) of the Glass epoxy and the core (d_2) of the PU foam layers, zero reflectance and minimal absorbance (< 2%) were observed at normal incidence, leading to a highly transparent sandwich structure with > 98% transmittance at 3 GHz. Optimization of the core thickness revealed significant improvement in transmittance versus frequency and angle of incidence. The A-sandwich with a skin layer thickness of 0.60 mm and a core layer thickness of 5 mm exhibited high transmittance for a broad frequency band, extending to the X-band at normal incidence. Also, the A-sandwich exhibited high transparency at all angles of incidence for electromagnetic waves with frequencies at the center of the S-band and the X-band. These results demonstrate the feasibility of optimizing planar A-sandwich as a broadband, high-performance radome wall structure for a wide range of frequencies and angles of incidence.

Keywords: A-sandwich radomes, Characteristic matrix, Transmittance, TE and TM waves

1. Introduction

A radar dome (radome) wall constructed from dielectric-dielectric or dielectric-metal combinations is usually used to shield and protect transmitting and receiving antennas and electronic equipment against environmental damage [1–12]. The high performance of the enclosed antenna requires a radome wall with excellent transmission at operating frequencies. Consequently, extensive efforts were devoted to the design of radomes for broadband antenna operation [13–17].

Reflection losses and aberration caused by the radome wall depend on the dielectric constant and the loss tangent of the materials involved in the construction. Therefore, to minimize the impact of the radome on the performance of the antenna, combinations that lead to high absorption should be avoided. In addition, depending on the operational requirements of the antenna, the shape and thickness profile of the radome are also important parameters to meet the structural and environmental requirements [11, 17]. Different structures of the radome wall are usually considered, including thin dielectric walls, half wavelength walls, A-sandwich, B-sandwich, C-sandwich, and multilayered structures [15, 16, 18–20].

Corresponding Author: Manal M. Al-Ali **Email**: manal.alali@yu.edu.jo

The A-sandwich structure, satisfying both the mechanical and electrical requirements, is a practical choice for weather radar radomes [13, 19, 21]. Additionally, A- sandwich designs are used in a wide range of applications [2, 22]. A typical structure consists of two resin glass-fiber skin layers with a dielectric constant near 4 and a loss tangent of0.015, along with a core material, such as honeycomb or foam, with a dielectric constant near 1.15 and a loss tangent of 0.002 [23, 24]. The performance of a high-quality sandwich radome depends on the number of layers, the shape of the radome wall, the thicknesses of skin and core materials, and the overall thickness profile of the structure [1, 2, 5, 6].

The overall reflection, transmission, and absorption response can usually be obtained by adopting the scattering or the propagation matrices, the propagation of the impedances at the interfaces in analogy to transmission lines, or the propagation of the reflection responses [3, 4, 6, 25]. These techniques with forward and backward layer recursions are of most importance for the investigation of wave propagation problems in dielectric thin films, radome wall design, and layered structures. A transfer (transition) matrix relates the electromagnetic fields at two different interfaces (it relates input to output fields), which can be arranged into a scattering matrix that relates the corresponding incoming to outgoing field amplitudes [26–28]. The elements of the scattering matrix (S-parameters) are used widely in the characterization of two- and multi-port networks at microwave frequencies.

In looking for a perfect transmitter with ignorable reflection and absorption responses, we adopt in this article a combination of dielectric materials to construct a planar A-sandwich consisting of a PU Foam dielectric core slab between two identical Glass epoxy skin slabs on either side. The reflection and transmission coefficients are evaluated within the frame of the global characteristic matrix approach [3, 25]. The propagation characteristics of the A-sandwich design with different choices of skin and core layer thicknesses are analyzed, and an optimal sandwich structure is suggested for broadband operation at all angles of incidence.

In this article, theoretical results will be compared with those from COMSOL Multiphysics software. COMSOL Multiphysics is based on the finite element method. It is used to solve and simulate a wide range of physics and engineering problems, in particular, coupled phenomena and multiphysics [29–34]. The effects of skin and core slab thicknesses on the transmission, reflection, and absorption behaviors with the increase of the incident wave frequency and angle of incidence will be investigated by considering representative numerical analysis from theory and simulations. In particular, we are looking for the feasibility of optimizing the A-sandwich radome wall for both TE and TM modes for a broadband high performance at all angles of incidence. The article is organized as follows: In Sec. II we present the geometry and model equations used in characterizing the A-sandwich radome performance. A conventional field-matching technique is used for deriving the global characteristic matrix and the corresponding reflection and transmission coefficients. In Sec. III, we present the transmittance, the reflectance, and the absorbance of electromagnetic waves by the A-sandwich with different layer thicknesses and discuss the dependencies of the performance of the A-sandwich on the frequency and the angle of incidence. Finally, we present the main conclusions of this study in Sec. IV.

2. Model Equations

Figure 1 shows the A-sandwich geometry with free space serving as the input and output media. When the radius of curvature of the radome wall is significantly larger than the wavelength of the incident wave, the radome wall can be treated as a planar multilayer structure with an infinite extent in the *xy*-plane and with finite width in z [6]. We use for the A-sandwich panel two Glass epoxy (G) slabs with $\varepsilon_r = 4$ and a loss tangent $\tan \delta_e = 0.015$, having thicknesses $d_1$and d_3. The core layer consists of PU foam (F), with $\varepsilon_r = 1.15$, $\tan \delta_e = 0.002$, and slab thickness d_2 [23, 24].

The characteristic matrix formalism and its relation to impedance propagation are presented below, along with derivations of expressions for the global reflection ρ and transmission τ coefficients in terms of the elements of the global matrix of a laminated medium [3, 4]. Then we apply the results to analyze the three slabs of the A-sandwich radome wall structure.

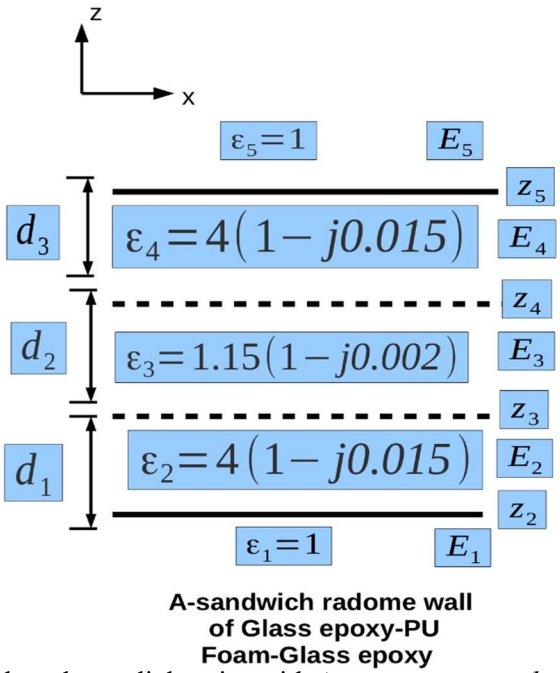

FIG. 1. A-radome wall of three lossy dielectrics with $\Delta z2 = z3 - z2 = d1$, $\Delta z3 = z4 - z3 = d2$, and $\Delta z4 = z5 - z4 = d3$.

Let the plane of incidence be the xz-plane such that $\vec{k}_0 = k_0 \sin\theta_1\, \hat{x} + k_0 \cos\theta_1\, \hat{z}$, where θ_1 stands for the angle of incidence on the first interface. For the transverse electric (TE) mode, the electric field is perpendicular to the plane of incidence such that $\vec{E} = E_y \hat{y}$, whereas the magnetic field is in the plane of incidence such that $\vec{H} = H_x \hat{x} + H_z \hat{z}$.

Considering the y-independent plane wave solution with a typical layer between z_{m-1} and z_m [3], the time-harmonic fields inside the m^{th}-layer of the multilayered structure are given by,

$$E_y = \left(A_m e^{-j\phi_m} + B_m e^{j\phi_m}\right) e^{j(\omega t - k_m x \sin\theta_m)} \quad (1)$$

$$H_x = -\frac{1}{\eta_m}\left(A_m e^{-j\phi_m} - B_m e^{j\phi_m}\right) e^{j(\omega t - k_m x \sin\theta_m)} \quad (2)$$

$$\phi_m = k_m (z - z_m) \cos\theta_m, \quad (3)$$

$$\eta_m = \frac{\omega\mu_m}{k_m} \sec\theta_m\,, k_m^2 = \omega^2 \mu_m \epsilon_m \quad (4)$$

where ω is the frequency of the incident wave, $\mu_m$and $\epsilon_m$are the permeability and permittivity of the m^{th}-layer, respectively, and θ_m is the refraction angle at the m^{th} interface relating the layers m and $m-1$. The continuity of E_y at all interfaces implies $k_m \sin\theta_m = k_0 \sin\theta_1$ for all m-values, namely,

$$\cos\theta_m = \sqrt{1 - \frac{sin^2\theta_1}{\epsilon_m}}, m = 2, 3, 4. \quad (5)$$

At the interface $z = z_m$, the field components $E_y = E_m$ and $H_x = H_m$ are as follows:

$$E_m = (A_m + B_m) e^{j(\omega t - k_m x \sin\theta_m)}, \quad (6)$$

$$H_m = -\frac{1}{\eta_m}(A_m - B_m) e^{j(\omega t - k_m x \sin\theta_m)}. \quad (7)$$

Similarly, at $z = z_{m-1}$, the field values E_{m-1} and H_{m-1}, are given by

$$E_{m-1} = \left(A_m e^{j\Delta\phi_m} + B_m e^{-j\Delta\phi_m}\right) e^{j(\omega t - k_m x \sin\theta_m)}, \quad (8)$$

$$H_{m-1} = -\frac{1}{\eta_m}\left(A_m e^{j\Delta\phi_m} - B_m e^{-j\Delta\phi_m}\right) e^{j(\omega t - k_m x \sin\theta_m)}, \quad (9)$$

$$\Delta\phi_m = k_m (z_m - z_{m-1}) \cos\theta_m = k_m \Delta z_m \cos\theta_m. \quad (10)$$

Upon solving Eqs. (6) and (7) simultaneously for A_m and B_m in terms of E_m and H_m, we get

$$2A_m = (E_m - \eta_m H_m) e^{-j(\omega t - k_m x)\sin\theta_m}, \quad (11)$$

$$2B_m = (E_m + \eta_m H_m) e^{-j(\omega t - k_m x)\sin\theta_m}, \quad (12)$$

By substituting A_m and B_m into Eqs. (8) and (9), we obtain the following relation between the

input fields (E_{m-1}, H_{m-1}) and the output (E_m, H_m) in matrix form, namely,

$$\begin{pmatrix} E_{m-1} \\ H_{m-1} \end{pmatrix} = \begin{pmatrix} \cos\Delta\phi_m & -j\eta_m \sin\Delta\phi_m \\ -\frac{j}{\eta_m}\sin\Delta\phi_m & \cos\Delta\phi_m \end{pmatrix}, \quad (13)$$

$$= \begin{pmatrix} k_{11} & k_{12} \\ k_{21} & k_{22} \end{pmatrix} \begin{pmatrix} E_m \\ H_m \end{pmatrix}, \quad (14)$$

where k_m stands for the ij^{th} element of the characteristic transmission matrix of the m^{th} layer. Note that E_{m}, H_{m}, $E_{\text{m-1}}$, and $H_{\text{m-1}}$ are the fields on both sides of the m^{th} interface, thus, relating the fields in both layers m and $m-1$. The incident transverse magnetic (TM) mode with $\vec{E}$ being parallel to the plane of incidence can be treated in the same manner without any difficulty. The only change in the above formalism for transverse magnetic waves is to replace the slab intrinsic impedance $\eta_m^{TM} = \frac{\omega\mu_m}{k_m}\sec\theta_m$ by $\eta_m^{TM} = \frac{\omega\mu_m}{k_m}\cos\theta_m$.

A repeated application of the above matrix in a recursive order results in the following relation between the input and the output fields:

$$\begin{pmatrix} E_1 \\ H_1 \end{pmatrix} = \prod_{m=2}^{M} \begin{pmatrix} k_{11} & k_{12} \\ k_{21} & k_{22} \end{pmatrix} \begin{pmatrix} E_M \\ H_M \end{pmatrix}, \quad (15)$$

where $M = 5$ for the A-sandwich under consideration. Note that $M = 2$ and $M = 3$ correspond to a single interface and a slab, respectively. The above product of slab matrices defines the global matrix K of the whole multilayered structure which relates the fields on either side of the structure. Accordingly, we write

$$\begin{pmatrix} E_1 \\ H_1 \end{pmatrix} = \begin{pmatrix} K_{11} & K_{12} \\ K_{21} & K_{22} \end{pmatrix} \begin{pmatrix} E_M \\ H_M \end{pmatrix}, \quad (16)$$

$$E_1 = K_{11}E_M + K_{12}H_M, \quad (17)$$

$$H_1 = K_{21}E_M + K_{22}H_M. \quad (18)$$

In what follows, we express the fields E_1,H_1, E_M, and H_M in terms of the amplitudes of A_1, B_1, A_M, and B_M by using Eqs. (6) and (7). Accordingly, we obtain,

$$A_1 + B_1 = K_{11}(A_M + B_M) + \frac{K_{12}}{\eta_M}(B_M - A_M), \quad (19)$$

$$\frac{B_1 - A_1}{\eta_1} = K_{21}(A_M + B_M) + \frac{K_{22}}{\eta_M}(B_M - A_M), \quad (20)$$

Upon solving Eqs. (19) and (20) simultaneously, we put the result in the following matrix form:

$$\begin{pmatrix} A_1 \\ B_1 \end{pmatrix} = \begin{pmatrix} u_{11} & u_{12} \\ u_{21} & u_{22} \end{pmatrix} \begin{pmatrix} A_M \\ B_M \end{pmatrix}. \quad (21)$$

Here, the elements of the u-matrix are as follows:

$$u_{11} = \frac{1}{2}\left(K_{11} - \frac{1}{\eta_M}K_{12} - \eta_1 K_{21} + \frac{\eta_1}{\eta_M}K_{22}\right) \quad (22)$$

$$u_{12} = \frac{1}{2}\left(K_{11} + \frac{1}{\eta_M}K_{12} - \eta_1 K_{21} - \frac{\eta_1}{\eta_M}K_{22}\right) \quad (23)$$

$$u_{21} = \frac{1}{2}\left(K_{11} - \frac{1}{\eta_M}K_{12} + \eta_1 K_{21} - \frac{\eta_1}{\eta_M}K_{22}\right) \quad (24)$$

$$u_{22} = \frac{1}{2}\left(K_{11} + \frac{1}{\eta_M}K_{12} + \eta_1 K_{21} + \frac{\eta_1}{\eta_M}K_{22}\right) \quad (25)$$

To obtain the microwave propagation characteristics of the A-sandwich of Fig. 1, we assume vacuum as the medium on both sides of the A-sandwich. Applying the above results for five media $M = 5$ with four interfaces, waves will be transmitted in the output medium without any further reflection since the output medium is a free space with an intrinsic impedance $\eta_{M=5} = Z_0$ and extends to infinity. The characteristic matrix K_5 is the unit matrix, therefore, the input as well as the output media will not alter the electromagnetic fields' (E_5 and H_5) transmission through the topmost vacuum layer $M = 5$.

The ratio of the globally transmitted to incident electric field amplitudes defines the global transmission coefficient τ of the A-sandwich structure, which is simply $A_M/A_1 = 1/u_{11}$. On the other hand, using the relation $B_1 = u_{21}A_M = u_{21}\tau A_1$, the ratio of the globally reflected to incident electric field amplitudes $B_1/A_1 = \tau u_{21}$ defines the global reflection coefficient. Accordingly, using Eqs. (22) and (24) we obtain the following relations for these coefficients,

$$\rho = \frac{K_{11} - K_{22} + Z_0 K_{21} - K_{12}/Z_0}{K_{11} + K_{22} - Z_0 K_{21} - K_{12}/Z_0} \quad (26)$$

$$\rho = \frac{2}{K_{11} + K_{22} - Z_0 K_{21} - K_{12}/Z_0} \quad (27)$$

Here, $Z_0 = 377$ is the vacuum impedance and $K_{\alpha\beta}$ is the $\alpha\beta^{th}$-element of the global 2×2 -characteristic matrix K of the A-sandwich, namely, $K = K_2K_3K_4$. The matrices K_2 and K_4 are the characteristic matrices of the skin layers, and K_3 is the characteristic matrix of the core layer. For the transverse electric (TE) wave incident at an angle θ_1, the relevant parameters for the analysis of the A-sandwich performance are defined as follows:

$$K_2 = \begin{pmatrix} \cos\Delta\phi_2 & -j\eta_2 \sin\Delta\phi_2 \\ -\frac{j}{\eta_2}\sin\Delta\phi_2 & \cos\Delta\phi_2 \end{pmatrix}, \quad (28)$$

$$K_3 = \begin{pmatrix} \cos\Delta\phi_3 & -j\eta_3 \sin\Delta\phi_3 \\ -\frac{j}{\eta_3}\sin\Delta\phi_3 & \cos\Delta\phi_3 \end{pmatrix}, \quad (29)$$

$$K_4 = \begin{pmatrix} \cos\Delta\phi_4 & -j\eta_4 \sin\Delta\phi_4 \\ -\frac{j}{\eta_4}\sin\Delta\phi_4 & \cos\Delta\phi_4 \end{pmatrix}, \quad (30)$$

$$\Delta\phi_2 = \frac{\omega}{c_0}\sqrt{\varepsilon_2}\,\Delta z_2 \cos\theta_2\,, \eta_2 = \frac{Z_0}{\sqrt{\varepsilon_2}}\sec\theta_2, \quad (31)$$

$$\Delta\phi_3 = \frac{\omega}{c_0}\sqrt{\varepsilon_3}\,\Delta z_3 \cos\theta_3\,, \eta_3 = \frac{Z_0}{\sqrt{\varepsilon_3}}\sec\theta_3, \quad (32)$$

$$\Delta\phi_4 = \frac{\omega}{c_0}\sqrt{\varepsilon_4}\,\Delta z_4 \cos\theta_4\,, \eta_4 = \frac{Z_0}{\sqrt{\varepsilon_4}}\sec\theta_4, \quad (33)$$

where c_0 is the free space speed of light. For identical lower and upper media, the reflectance R, transmittance T, and absorbance A can be calculated as follows [25]:

$$T = \tau\tau^*, R = \rho\rho^*, A = 1 - R - T, \quad (34)$$

where τ^* and ρ^* stand for the complex conjugate of the transmission and reflection coefficients, respectively.

3. Results and Discussion

In this section, we provide numerical examples of the propagation characteristics of the A-sandwich. For all numerical examples, the skin Glass epoxy (G) slab thicknesses are equal, i.e. $\Delta z_2 = d_1$, $\Delta z_4 = d_3 = d_1$, and the thickness of the core PU foam (F) slab is $\Delta z_3 = d_2$. The complex relative permittivity of the skin Glass epoxy slabs is $\varepsilon_2 = \varepsilon_4 = 4\,(1 - j0.015)$, while that of the core foam layer is $\varepsilon_4 = 1.15\,(1 - j0.002)$[23, 24]. Figures 2-4 illustrate the transmittance, reflectance, and absorbance of 3 GHz normally incident waves versus the ratio of core slab thickness to the free space wavelength λ_0. To investigate the effect of the G-layer thickness, calculations were performed for $d_1 = d_3$ within the range of 0.60-0.70 mm.

The curves of Fig. 2 show the transmittance at normal incidence versus the normalized core thickness d_2/λ_0 for different Glass epoxy slab thicknesses d_1. The theoretical transmittance curves presented in this work align perfectly with those obtained from COMSOL Multiphysics software for all parameters at normal incidence. All curves show that the A-sandwich structure under consideration is primarily transparent to electromagnetic waves in the S-band at all layer thicknesses under consideration, with a minimum transmittance of ~96%. In COMSOL simulation, the A-sandwich model is studied for one unit cell with applied Floquet boundary conditions that describe the periodicity. The Floquet periodicity can be used to model infinite periodic structures and models involving plane waves interacting with periodic structures [35, 36].

However, the transmittance exhibited a periodic behavior as d_2 increased, with a slight decrease in successive periods. The period of $0.4660\lambda_0$ is precisely half the wavelength in the core medium with $\varepsilon_3 = 1.15$. Also, the reflectance exhibited similar periodic behavior with the same period as d_2 increases, and the reflectance minima coincide with the transmittance maxima (Fig. 3). The first transmittance maximum (with the highest transmittance of ~99%) occurs at $d_1 = 0.60$ mm and $d_2 \approx 3.0$ cm. The first transmittance maximum revealed an almost perfectly transparent structure with negligible reflection and only < 1% absorption as indicated by Figs. 2-4. The subsequent increase of d_2 by a multiple of half wavelength in the core material reproduced the transmittance maxima and reflection minima, as seen in Figs. 2 and 3. Evidently, the maximum values of the transmittance are almost independent of the value of d_1, which is a consequence of the vanishing effect of d_1 on the reflectance minima and the negligibly small increase of the absorbance with the increase of d_1, being ~ 0.1% across the whole range of d_1. However, the effect of d_1 on the minimum values of the transmittance is more pronounced owing to the more tangible increase of the maximum reflectance with the increase of d_1 leading to a reduction in the transmittance. Nevertheless, this reduction is still negligibly small for practical applications (< 1%). On the other hand, the small monotonic decrease (~ 1%) of the transmittance maximum value with the increase of d_2 from $0.3\lambda_0$ to $1.2\lambda_0$ is a result of the increase of absorption in progressively thicker layers of the core material.

Noteworthy, the periodic behavior of the transmittance in Fig. 2 and the reflectance in Fig. 3 are due to the dependence of K_3 from Eq. (29) on ϕ_3. The sine and cosine of $\Delta\phi_3$ vary with $d_2 = n\lambda$ and $d_2 = (n + 1/2)\lambda$ between +1 and -1, respectively, giving the periodic behavior of the transmittance and the reflectance as defined in Eq. (27).

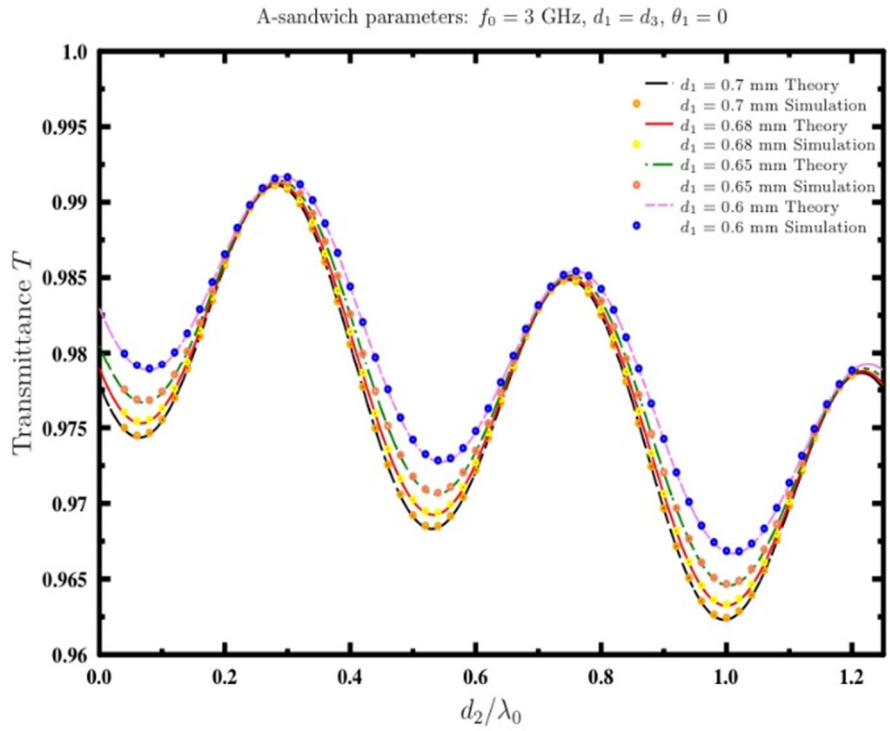

FIG. 2. Transmittance from theory and simulation for symmetric G-F-G unit cell.

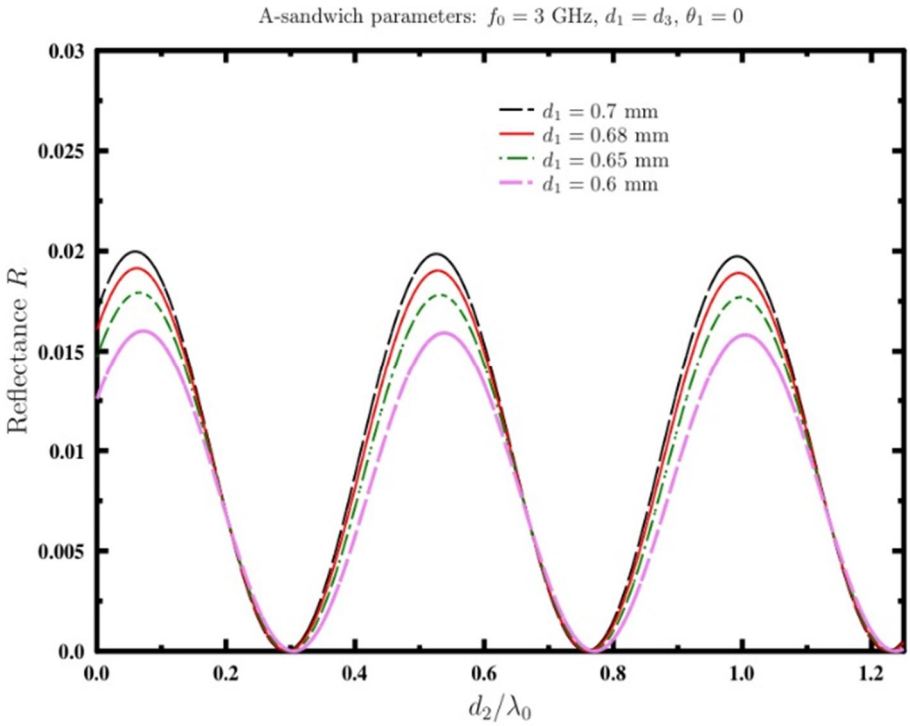

FIG. 3. Reflectance for symmetric G-F-G unit cell.

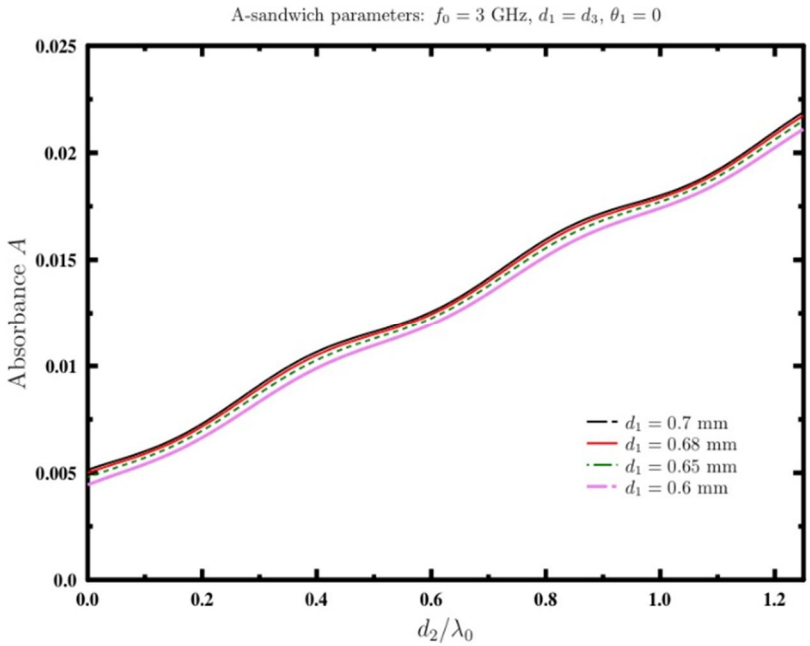

FIG. 4. Absorbance for symmetric G-F-G unit cell.

It is obvious from the above results that a skin thickness of d_1 = 0.60 mm provides better performance compared to larger values of d_1. Also, it is evident that the transmittance did not change appreciably with increasing core thickness d_2. However, the analysis of the propagation characteristics of the A-sandwich versus frequency in the range of 0-18 GHz, covering the S-band (2− 4 GHz) and the X-band (8 −12 GHz), reveals optimal performance at lower core thickness values. Figure 5 shows the frequency dependence of the transmittance at normal incidence for two A-sandwiches with d_1 = 0.60 mm, the first having d_2 = 0.5 cm and the second with d_2 = 3.0 cm. Obviously, at d_2 = 0.5 cm the A-sandwich maintains a high transmittance (above 95%) up to 14 GHz, beginning to degrade at frequencies higher than 12 GHz, reaching 77% at 18 GHz. In comparison, the transmittance of the A-sandwich with a core thickness of 3.0 cm exhibits oscillations in this frequency range, and a lower transmittance across the X-band and up to 15 GHz. The transmittance of this sandwich drops down to below 90% in the central region of the X-band, and down to 67% at 18 GHz. However, a slight improvement in performance is observed in a narrow frequency range of around 16 GHz.

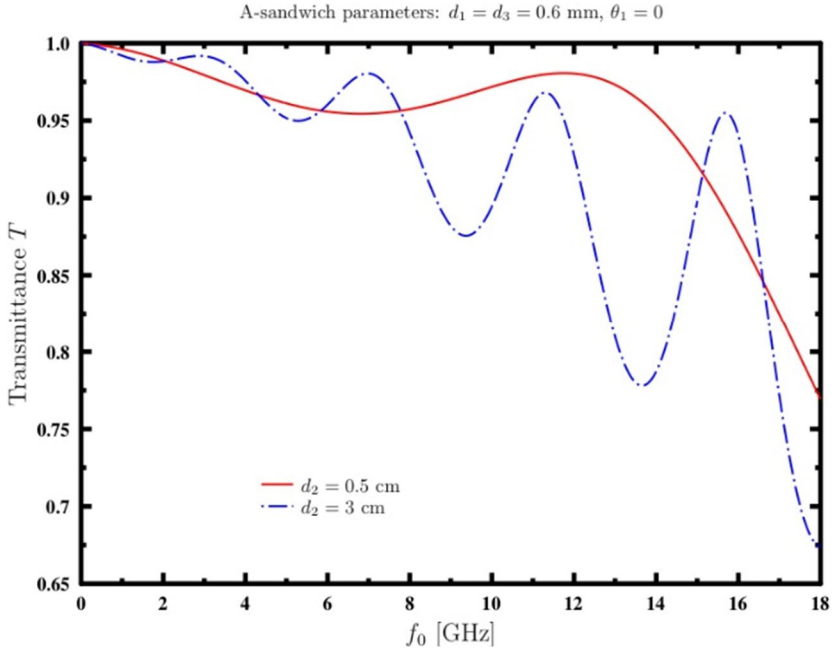

FIG. 5. Transmittance for symmetric G-F-G unit cell.

The fluctuations observed in Fig. 5 represent periodic oscillations in transmittance due to the dependence of $\Delta\phi_3$ on ωd_2. Accordingly, as the core thickness d_2 increases, the frequency range for a single oscillation period decreases. The superior performance of the A-sandwich with a core thickness of 0.5 cm is demonstrated by its low reflectance and absorbance across the X-band (Fig. 6). Conversely, the sharp increase in reflectance at higher frequencies is the primary factor responsible for the decline in transmittance for frequencies above 12 GHz.

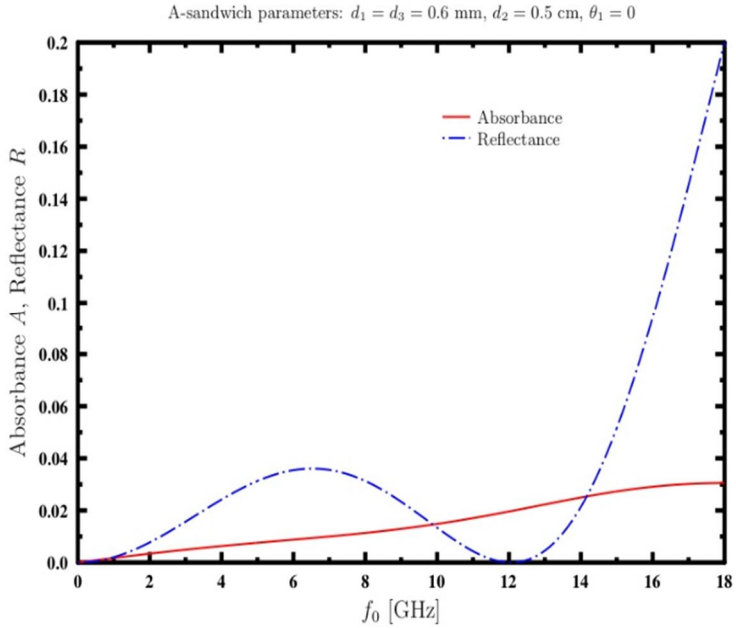

FIG. 6. Absorbance and reflectance for symmetric G-F-G unit cell.

To investigate the performance of the A-sandwich at arbitrary angles of incidence, the dependence of the transmittance on the angle of incidence was evaluated at the center of the S-band (3 GHz) and the center of the X-band (10 GHz) for the sandwiches with d_2 = 0.5 cm and d_2 = 3.0 cm. Figures 7 reveals high transmittance (> 92%) at 3 GHz for the sandwiches with d_2 = 0.5 and 3.0 cm up to an incident angle of 60°. At higher angles, the transmittance of both sandwiches drops rapidly to zero at grazing incidence, but the rate of decrease of the 3.0-cm sandwich is faster. At 10 GHz (Fig. 8), the 0.5-cm sandwich exhibits similar behavior, but with a faster decrease of transmittance with the increase of the angle of incidence, exhibiting 75% at 60°. However, the 3.0-cm sandwich exhibits a slow drop from 90% to a local minimum of 82% at 30° and subsequently increases to a maximum of 96% at ~ 52°, and then decreases rapidly to zero at grazing incidence. This sandwich exhibits higher transmittance than the 0.5 cm sandwich in the angular range of 45°-63°, but at higher angles, the transmittance dropps to zero at a faster rate. Accordingly, the sandwich with d_1 = 0.60 mm and d_2 = 0.5 cm can be suggested as a highly transparent radome wall for broadband electromagnetic waves at all angles of incidence. The behavior of the transmittance at the two different d_2 values in Figs. 7 and 8 is due to the dependence on $\Delta\phi_3$ which is proportional to $\omega d_2 \cos\theta_3$. As θ_3 increases above zero (normal incidence), the value of $\Delta\phi_3$ decreases leading to the observed behavior for d_2 = 3 cm.

Finally, we evaluated the transmission characteristics of the A-sandwich with d_1 = 0.60 mm and d_2 = 0.5 cm for perpendicular (TE) and parallel (TM) polarizations. At low angles of incidence, the sandwich revealed similar behaviors of the transmittance versus frequency with high transparency for both polarization modes in a broad frequency range (not shown for brevity). However, the frequency-dependent transmittance of the two modes showed different behaviors at higher angles of incidence. Figures 9 and 10 show representative curves of the transmittance versus frequency at an incident angle of 30°. Evidently, the A-sandwich revealed a high transparency (more than 90%) for both polarization modes up to 16 GHz, above which the transmittance starts decreasing rapidly. However, the transmittance of the TE mode was generally lower than the TM mode across the frequency range up to the end of the Ku band (18 GHz).

The average transmittance curves for both polarization modes at an angle of incidence $\theta_1 = \frac{\pi}{6}$ are shown in Fig. 10. By decomposing an incident wave into TE and TM wave modes, the average transmittance is obtained from $T_{av} = \frac{1}{2}(T_{TE} + T_{TM})$ [25]. Figure 10 shows that the theoretical results closely align with the simulation results, demonstrating almost identical transmittance values up to 18 GHz.

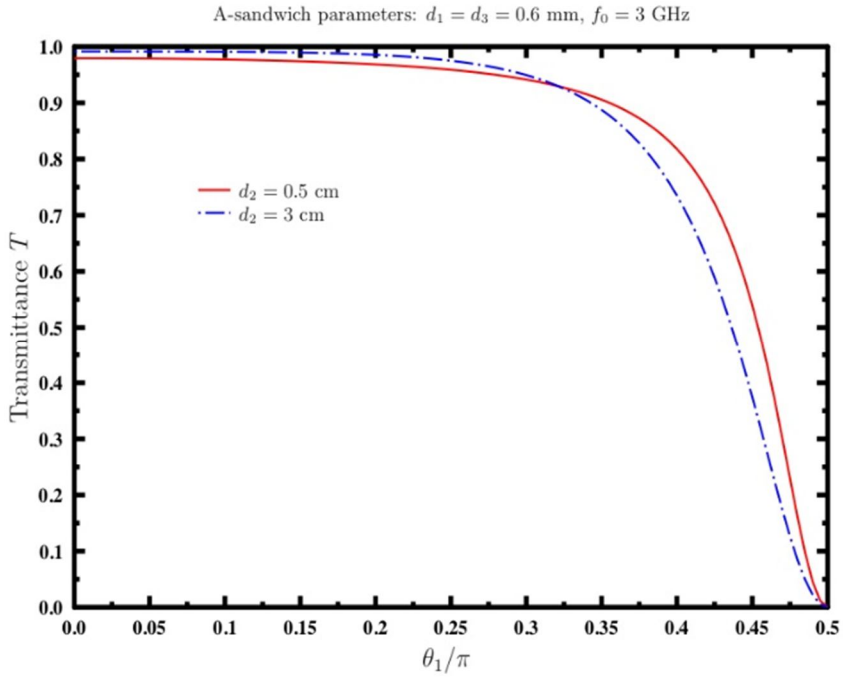

FIG. 7. Transmittance for symmetric G-F-G unit cell.

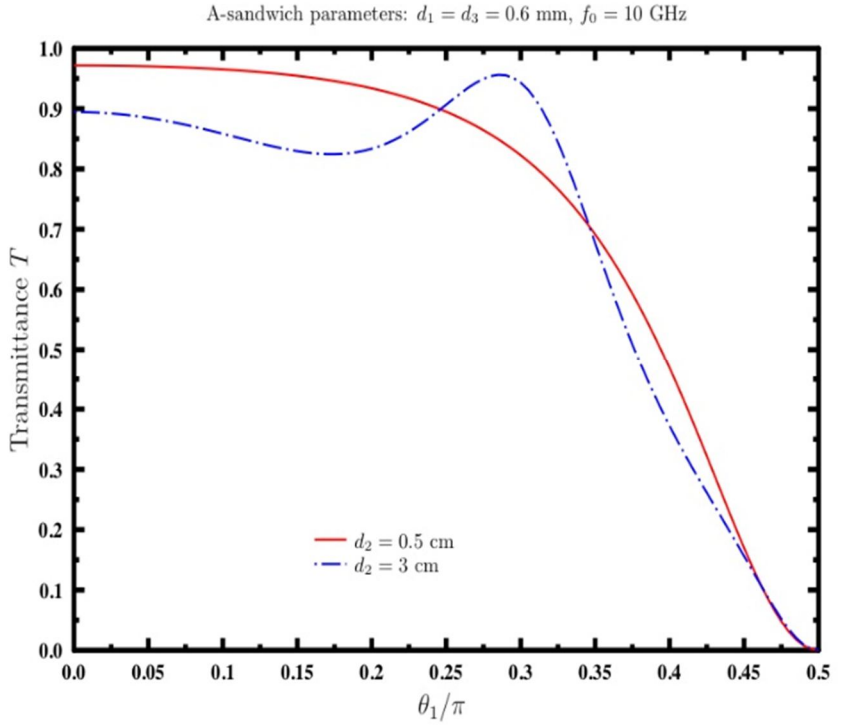

FIG. 8. Transmittance for symmetric G-F-G unit cell.

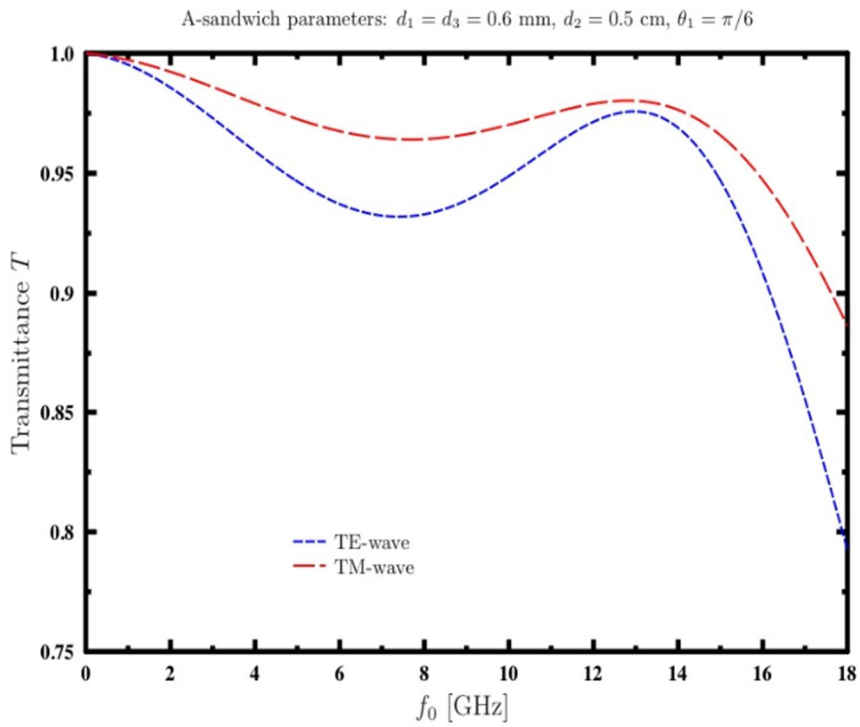

FIG. 9. Transmittance for symmetric G-F-G unit cell.

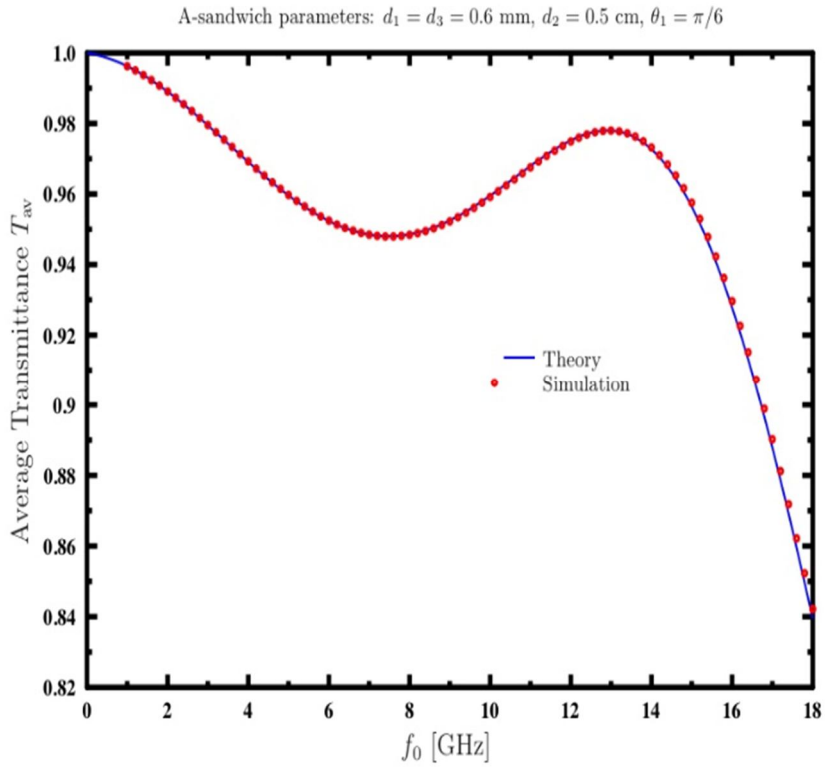

FIG. 10. Average transmittance from theory and simulation for symmetric G-F-G unit cell.

4. Conclusions

We investigated the propagation characteristics of the A-sandwich constructed from two identical skin Glass epoxy slabs and a core PU foam slab. The effects of slab thicknesses on transmission, reflection, and absorption behaviors were analyzed as the incident wave frequency and angle of incidence increased, utilizing representative numerical analyses derived from both theoretical models and simulations. The A-sandwich, with a skin layer thickness d_1 ranging from 0.60 to 0.70 mm and a core layer thickness d_2 of up to 12 cm, exhibited high transparency at 3 GHz normal

incidence conditions. However, the dependencies of the transmittance on the frequency and angle of incidence revealed a superior broadband performance of the A-sandwich with a lower core thickness compared to that with a higher core thickness, as demonstrated by the transmittance curves of the sandwiches with $d_1 = 0.60$ mm and core thicknesses of 0.5 and 3.0 cm. Generally speaking, the sandwich with a core thickness of 0.5 cm exhibited a high transparency, exceeding 95% at normal incidence across the frequency range from the S-band the X-band. Also, a high transmittance $\geq$ 92% at 3 GHz was observed for this sandwich at angles of incidence up to 60°. Even though the sandwich exhibited a small decrease of the transmittance at 10 GHz to the range of 98 – 82% at angles of incidence up to 55°, its performance is still of considerable practical importance. In addition, the A-sandwich exhibited a high performance for both TE and TM modes in a broad frequency range. These results from both theory and simulation indicate the feasibility of optimizing the A-sandwich radome wall for a broadband high performance in a wide range of angles of incidence. Further optimization of the skin and core layer thicknesses may provide only slight improvements in the A-sandwich transmission characteristics compared to the configuration we proposed for optimal performance. However, the mechanical strength of the radome wall constructed from the proposed A-sandwich should be investigated to ensure durability, robustness, and applicability for practical applications.

References

[1] Kozakoff, D. J., "Analysis of Radome-Enclosed Antennas", 2nd Ed., (Boston-London: Artech House, 2010).

[2] Cady, W., Karelitz, M. and Turner, L., "Radar Scanners and Radomes", MIT Radiation Laboratory Series Vol. 26, (McGraw-Hill, New York, 1948).

[3] Jones, D. S., "The Theory of Electromagnetism", (Pergamon Press Ltd., New York, 1964).

[4] Cornbleet, S., "Microwave Optics", (New York: Academic Press, 1976).

[5] Rudge, A. W., Milne, K., Olver, A. D., and Knight, P. "The Handbook of Antenna Design", Vol. 2, (Peter Peregrinus Ltd., London, UK, 1983).

[6] Shavit, R., "Radome Electromagnetic Theory and Design", 1st Ed., (John Wiley & Sons Ltd., 2018).

[7] Yurchenko, V. B., Altintas, A., and Nosich, A. I., IEEE Trans. Antennas Propag., 47 (1999) 668.

[8] Sunil, S., Venu, K. S., Vaitheeswaran, S. M., and Raveendranath, U., Microw. Opt. Techn. Lett., 30 (2001) 350.

[9] Nair, R. U. and Jha, R. M., Electron. Lett., 43 (15) (2007) 787.

[10] Nair, R. U., Neelam, A. and Jha, R. M., Appl. Electromagn. C. (AEMC), (2009), 1.

[11] Nair, R. U. and Jha, R. M, IEEE Trans. Antennas Propag., 57 (2009) 3664.

[12] Mei, Z., Xu, Y., Bai, J., and Cui, T., IEEE Trans. Opt. Express, 20 (2012) 16955.

[13] Sunil, C., Daniel, A., Rao, B. S., Kumar, V. S. and Sarkar, M., IEEE Indian C. Antenn. Propag. (InCAP) - Hyderabad, India (2018) 16.

[14] Nair, R. U., Shashidhara, S. and Jha, R. M., IEEE Antenn. Wirel. Propag. Lett., 11 (2012) 854.

[15] Lee, K., Chung, Y., Hong, I. and Yook, J., IEEE Antennas and Propagation Society International Symposium, (2010), pp.1-4.

[16] Duxian, W., J. Electron., 11 (4) (1994) 332.

[17] Lee, K. W., Chung, Y. C., Hong, I. P. et al., IEEE Antennas and Propagation Society Int. Symp. (APSURSI), Toronto, Canada, (2010), pp. 1-4.

[18] Walton, J. D., "Radome Engineering Handbook: Design and Principles", Vol. 1, (New York: M. Dekker, 1970).

[19] Choi, I., Kim, J. G., Lee, D. G., and Seo, I. S., Compos. Sci. Technol., 71 (14) (2011) 1632.

[20] Nazari, F., Taherkhani, M., Mokhtari, M., Aliakbarian, H., and Shekoofa, O., IET Sci. Meas. Technol., 14 (2020) 808.

[21] Zhou, L., Pei, Y. and Fang, D., IEEE Antenn. Wirel. Pr., 15 (2015) 218.

[22] Jasik, H., “Antenna Engineering Handbook”, (McGraw-Hill, New York, 1961).

[23] Mahima, P., Suprava, M., Vandana, S., Yazeen, M. P. S., and Nair, R. U., "Electromagnetic Performance Analysis of Graded Dielectric Inhomogeneous Radomes", (Springer Briefs in Applied Sciences and Technology, Springer, Singapore, 2018).

[24] Yazeen, P. S. M., Vinisha, C. V., Vandana, S., Suprava, M., and Nair, R. U., "Broadbanding Techniques for Radomes", (Springer Briefs in Electrical and Computer Engineering, Springer Nature Singapore Pte Ltd. 2020).

[25] Pedrotti, F. L., Pedrotti, L. M., and Pedrotti, L.S., "Introduction to Optics", 3rd Ed., (Cambridge University Press, 2017).

[26] Pozar, D. M., "Microwave Engineering", 4th Ed., (John Wiley & Sons, New York, 2012).

[27] Dobrowolski, J. A., "Microwave Network Design Using the Scattering Matrix", (Artech House, Boston/London 2010).

[28] Benson, F. A. and Benson, T. M., "Fields, Waves and Transmission Lines", 1st Ed., (Springer-Science, Business Media, B. V. 1991).

[29] COMSOL, "COMSOL Multiphysics 4.3 Users Guide", (2012).

[30] De Vita, F., Di Marco, S., Costa, F., and Turchi, P., "Design of a Stealthy Antenna Using COMSOL Multiphysics", (Excerpt from the Proceedings of the 2012 COMSOL Conference in Milan).

[31] Cross, L. W. and Almalkawi, M. J., "Scan Angle Stability of a Second-Order Plasma-Switched Frequency Selective Surface", (Excerpt from the Proceedings of the 2013 COMSOL Conference in Boston).

[32] Lu, Y., Chen, J., Li, J., and Xu, W., Materials, 15(2) (2022) 640.

[33] Ali, N. M. and Ali, T. A., Appl. Phys. B, 129 (2023) 15.

[34] Cai, F. and Ko, Z., Photonics, 10 (2023) 643.

[35] Guillod, T., Kehl, F., and Hafner, C., Prog. Electromagn. Res., 137 (2013) 565.

[36] Alaverdyan, S. A., Kabanov, I. N., Komarov, V. V., and Meschanov, V.P., IEEE T. Microw. Theory, 63 (8) (2015) 2509.

الجداول: تعطى الجداول أرقاما متسلسلة يشار إليها في النص. ويجب طباعة كل جدول على صفحة منفصلة مع عنوان فوق الجدول. أما الحواشي التفسيرية، التي يشار إليها بحرف فوقي، فتكتب أسفل الجدول.

الرسوم التوضيحية: يتم ترقيم الأشكال والرسومات والرسومات البيانية (المخططات) والصور، بصورة متسلسلة كما وردت في النص.

تقبل الرسوم التوضيحية المستخرجة من الحاسوب والصور الرقمية ذات النوعية الجيدة بالأبيض والأسود، على ان تكون أصيلة وليست نسخة عنها، وكل منها على ورقة منفصلة ومعرفة برقمها بالمقابل. ويجب تزويد المجلة بالرسومات بحجمها الأصلي بحيث لا تحتاج إلى معالجة لاحقة، وألا تقل الحروف عن الحجم 8 من نوع Times New Roman، وألا تقل سماكة الخطوط عن 0.5 وبكثافة متجانسة. ويجب إزالة جميع الألوان من الرسومات ما عدا تلك التي ستنشر ملونة. وفي حالة إرسال الرسومات بصورة رقمية، يجب أن تتوافق مع متطلبات الحد الأدنى من التمايز (1200 dpi Resolution) لرسومات الأبيض والأسود الخطية، و 600 dpi للرسومات باللون الرمادي، و300 dpi للرسومات الملونة. ويجب تخزين جميع ملفات الرسومات على شكل (jpg)، وأن ترسل الرسوم التوضيحية بالحجم الفعلي الذي سيظهر في المجلة. وسواء أرسل المخطوط بالبريد أو عن طريق الشبكة (Online)، يجب أرسال نسخة ورقية أصلية ذات نوعية جيدة للرسومات التوضيحية.

مواد إضافية: تشجع المجلة الباحثين على إرفاق جميع المواد الإضافية التي يمكن أن تسهل عملية التحكيم. وتشمل المواد الإضافية أي اشتقاقات رياضية مفصلة لا تظهر في المخطوط.

المخطوط المنقح (المعدّل) والأقراص المدمجة: بعد قبول البحث للنشر وإجراء جميع التعديلات المطلوبة، فعلى الباحثين تقديم نسخة أصلية ونسخة أخرى مطابقة للأصلية مطبوعة بأسطر مزدوجة، وكذلك تقديم نسخة إلكترونية تحتوي على المخطوط كاملا مكتوبا على Microsoft Word for Windows 2000 أو ما هو استجد منه. ويجب إرفاق الأشكال الأصلية مع المخطوط النهائي المعدل حتى لو تم تقديم الأشكال إلكترونيا. وتخزن جميع ملفات الرسومات على شكل (jpg)، وتقدم جميع الرسومات التوضيحية بالحجم الحقيقي الذي ستظهر به في المجلة. ويجب إرفاق قائمة ببرامج الحاسوب التي استعملت في كتابة النص، وأسماء الملفات على قرص مدمج، حيث يعلَم القرص بالاسم الأخير للباحث، وبالرقم المرجعي للمخطوط للمراسلة، وعنوان المقالة، والتاريخ. ويحفظ في مغلف واقٍ.

حقوق الطبع

يُشكِّل تقديم مخطوط البحث للمجلة اعترافاً صريحاً من الباحثين بأنّ مخطوط البحث لم يُنْشَر ولم يُقَدَّم للنشر لدى أي جِهَة أخرى كانت وبأي صيغة ورقية أو إلكترونية أو غيرها. ويُشترط على الباحثين ملء أنموذج يَنُصُّ على نقْل حقوق الطبع لتُصبح ملكاً لجامعة اليرموك قبل الموافقة على نشر المخطوط. ويقوم رئيس التحرير بتزويد الباحثين بإنموذج نقل حقوق الطبع مع النسخة المُرْسَلَة للتنقيح. كما ويُمنع إعادة إنتاج أيِّ جزء من الأعمال المنشورة في المجلّة من دون إذن خَطِّيٍّ مُسْبَق من رئيس التحرير.

إخلاء المسؤولية

إن ما ورد في هذه المجلة يعبر عن آراء المؤلفين، ولا يعكس بالضرورة آراء هيئة التحرير أو الجامعة أو سياسة اللجنة العليا للبحث العلمي أو وزارة التعليم العالي والبحث العلمي. ولا يتحمل ناشر المجلة أي تبعات مادية أو معنوية أو مسؤوليات عن استعمال المعلومات المنشورة في المجلة أو سوء استعمالها.

الفهرسة: المجلة مفهرسة في:

Scopus	**Emerging Sources Citation Index (ESCI)** Journal Impact Factor 2022 0.7
ULRICHSWEB GLOBAL SERIALS DIRECTORY	

معلومات عامة

المجلة الأردنية للفيزياء هي مجلة بحوث علميّة عالمية متخصصة مُحكمة تصدر بدعم من صندوق دعم البحث العلمي والابتكار، وزارة التعليم العالي والبحث العلمي، عمان، الأردن. وتقوم بنشر المجلة عمادة البحث العلمي والدراسات العليا في جامعة اليرموك، إربد، الأردن. وتنشر البحوث العلمية الأصيلة، إضافة إلى المراسلات القصيرة Short Communications، والملاحظات الفنية Technical Notes، والمقالات الخاصّة Feature Articles، ومقالات المراجعة Review Articles، في مجالات الفيزياء النظرية والتجريبية، باللغتين العربية والإنجليزية.

تقديم مخطوط البحث

تقدم المخطوطات إلكترونيًا عن طريق موقع المجلة: https://jjp.yu.edu.jo/index.php/jjp

ويجري تحكيمُ البحوثِ الأصيلة والمراسلات القصيرة والملاحظات الفنية من جانب مُحكِّمين اثنين في الأقل من ذوي الاختصاص والخبرة. وتُشَجِّع المجلة الباحثين على اقتراح أسماء المحكمين. أما نشر المقالات الخاصّة في المجالات الفيزيائية النَشِطَة، فيتم بدعوة من هيئة التحرير، ويُشار إليها كذلك عند النشر. ويُطْلَب من كاتب المقال الخاص تقديم تقرير واضح يتّسم بالدقة والإيجاز عن مجال البحث تمهيداً للمقال. وتنشر المجلةُ أيضاً مقالات المراجعة في الحقول الفيزيائية النشطة سريعة التغيُّر، وتُشَجّع كاتبي مقالات المراجعة أو مُستَكتبيها على إرسال مقترحٍ من صفحتين إلى رئيس التحرير. ويُرْفَق مع البحث المكتوب باللغة العربية ملخص (Abstract) وكلمات دالة (Keywords) باللغة الإنجليزية.

ترتيب مخطوط البحث

يجب أن تتم طباعة مخطوط البحث ببنط 12 نوعه Times New Roman، وبسطر مزدوج، على وجه واحد من ورق A4 (21.6 × 27.9 سم) مع حواشي 3.71 سم ، باستخدام معالج كلمات ميكروسوفت وورد 2000 أو ما استُجِدَ منه. ويجري تنظيم أجزاء المخطوط وفق الترتيب التالي: صفحة العنوان، الملخص، رموز التصنيف (PACS)، المقدّمة، طرق البحث، النتائج، المناقشة، الخلاصة، الشكر والعرفان، المراجع، الجداول، قائمة بدليل الأشكال والصور والإيضاحات، ثَمَّ الأشكال والصور والإيضاحات. وتُكْتَب العناوين الرئيسة بخطٍ **غامق**، بينما تُكْتَب العناوين الفرعية بخطٍ *مائل*.

صفحة العنوان: وتشمل عنوان المقالة، أسماء الباحثين الكاملة وعناوين العمل كاملة. ويكتب الباحث المسؤول عن المراسلات اسمه مشارا إليه بنجمة، والبريد الإلكتروني الخاص به. ويجب أن يكون عنوان المقالة موجزا وواضحا ومعبرا عن فحوى (محتوى) المخطوط، وذلك لأهمية هذا العنوان لأغراض استرجاع المعلومات.

الملخص: المطلوب كتابة فقرة واحدة لا تزيد على مائتي كلمة، موضحة هدف البحث، والمنهج المتبع فيه والنتائج وأهم ما توصل إليه الباحثون.

الكلمات الدالة: يجب أن يلي الملخص قائمة من 4-6 كلمات دالة تعبر عن المحتوى الدقيق للمخطوط لأغراض الفهرسة.

PACS: يجب إرفاق الرموز التصنيفية، وهي متوافرة في الموقع http://www.aip.org/pacs/pacs06/pacs06-toc.html.

المقدمة: يجب أن توضّح الهدف من الدراسة وعلاقتها بالأعمال السابقة في المجال، لا أن تكون مراجعة مكثفة لما نشر (لا تزيد المقدمة عن صفحة ونصف الصفحة مطبوعة).

طرائق البحث (التجريبية / النظرية): يجب أن تكون هذه الطرائق موضحة بتفصيل كاف لإتاحة إعادة إجرائها بكفاءة، ولكن باختصار مناسب، حتى لا تكون تكرارا للطرائق المنشورة سابقا.

النتائج: يستحسن عرض النتائج على صورة جداول وأشكال حيثما أمكن، مع شرح قليل في النص ومن دون مناقشة تفصيلية.

المناقشة: يجب أن تكون موجزة وتركز على تفسير النتائج.

الاستنتاج: يجب أن يكون وصفا موجزا لأهم ما توصلت إليه الدراسة ولا يزيد عن صفحة مطبوعة واحدة.

الشكر والعرفان: الشكر والإشارة إلى مصدر المنح والدعم المالي يكتبان في فقرة واحدة تسبق المراجع مباشرة.

المراجع: يجب طباعة المراجع بأسطر مزدوجة ومرقمة حسب تسلسلها في النص. وتكتب المراجع في النص بين قوسين مربعين. ويتم اعتماد اختصارات الدوريات حسب نظام Wordlist of Scientific Reviewers.

Subscription Form

Jordan Journal of PHYSICS

An International Peer-Reviewed Research Journal issued by the Support of the Scientific Research and Innovation Support Fund

Published by the Deanship of Research & Graduate Studies, Yarmouk University, Irbid, Jordan

Name: ..... الأسم:

Specialty:..... التخصص:

Address: ..... العنوان:

P.O. Box:..... صندوق البريد:

City & Postal Code: ..... المدينة/الرمز البريدي:

Country: ..... الدولة:

Phone: ..... رقم الهاتف:

Fax No:..... رقم الفاكس:

E-mail:..... البريد الإلكتروني:

No. of Subscription: ..... عدد الإشتراكات:

Method of Payment:..... طريقة الدفع:

Amount Enclosed:..... المبلغ المرفق:

Signature: ..... التوقيع:

Cheques should be paid to Deanship of Research and Graduate Studies - Yarmouk University.

I would like to subscribe to the Journal
For

- One Year
- Two Years
- Three Years

One Year Subscription Rates

	Inside Jordan	Outside Jordan
Individuals	JD 8	€ 40
Students	JD 4	€ 20
Institutions	JD 12	€ 60

Correspondence

Subscriptions and Sales:

Prof. Mahdi Salem Lataifeh
Deanship of Research and Graduate Studies
Yarmouk University
Irbid – Jordan
Telephone: 00 962 2 711111 Ext. 2075
Fax No.: 00 962 2 7211121

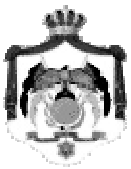

المملكة الأردنية الهاشمية

جامعة اليرموك

المجلة الأردنية

للفيزياء

مجلة بحوث علمية عالمية متخصصة محكّمة

تصدر بدعم من صندوق دعم البحث العلمي والابتكار

المجلد (17)، العدد (4)، تشرين الأول 2024م / ربيع الثاني 1446هـ

المجلة الأردنية

للفيزياء

مجلة بحوث علمية عالمية محكّمة

المجلد (17)، العدد (4)، تشرين الأول 2024م / ربيع الثاني 1446هـ

المجلة الأردنية للفيزياء: مجلة علمية عالمية متخصصة محكّمة تصدر بدعم من صندوق دعم البحث العلمي والإبتكار، عمان، الأردن، وتصدر عن عمادة البحث العلمي والدراسات العليا، جامعة اليرموك، إربد، الأردن.

ترسل البحوث إلى العنوان التالي:

الأستاذ الدكتور مهدي سالم لطايفة

رئيس تحرير المجلة الأردنية للفيزياء

عمادة البحث العلمي والدراسات العليا، جامعة اليرموك

إربد ، الأردن

هاتف 7211111 2 962 00 **فرعي** 2075

E-mail: *jjp@yu.edu.jo* **Website**: *http://Journals.yu.edu.jo/jjp*